An Analysis of Magnetohydrodynamic Waves and Oscillations in the Solar Corona
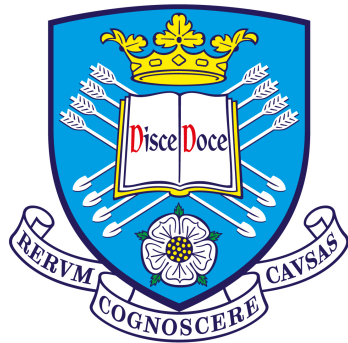
Farhad Allian

Dr. Rekha Jain

School of Mathematics & Statistics

The University of Sheffield

A thesis submitted in partial fulfilment for the degree of
Doctor of Philosophy

July 2021

For my mother, for giving me the life she never had.

Acknowledgements

The devil is in the details, they say; and I have learned that the pursuit of science contains many devils. But, fortunately, I have had the right people by my side throughout this time to help me keep them at bay.

Firstly, I would like to thank my academic supervisor, Dr. Rekha Jain, for her unquestioning support throughout these past four years, and for her patience in allowing me to immerse myself in this vast and captivating field of research. I will always remember the hours and hours of conversations and insightful discussions. My thanks also goes out to our collaborator, Prof. Bradley Hindman, for answering all of my incessant signal processing questions. I would also like to thank my advisor of studies, Dr. Yi Li, for providing me with hopeful advice and encouragement throughout the years. Thank you to my examiners, Dr. Viktor Fedun and Dr. Richard Morton, whose comments greatly improved the quality of this thesis.

My gratitude extends to everyone I have had the pleasure of meeting in the School of Mathematics and Statistics, in particular to Prof. Caitlin Buck and Dr. Dimitrios Roxanas. Thank you to all of those who made the H23 office a warm and welcoming environment: Matt Allcock, Fionnlagh Dover and Samuel Skirvin, to name only a few.

To my closest friends, Greg, Jason, Kyle and Marc, all of who embarked on our own separate journeys but nonetheless remained as close, I'm grateful for our friendships. Special thanks go out to Alex and Carys, for reminding me that the bad days never last. I would also like to say a heartfelt thank you to my better half, Bryony, for your support throughout this time. I am equally grateful for the love and support from my mother and sister. I couldn't have done this without any of you.

Declaration of Authorship

I hereby declare that except where specific reference is made to the work of others, the contents of this thesis are original and have not been submitted in whole or in part for consideration for any other degree or qualification in this, or any other university. This thesis is my own work and contains nothing which is the outcome of work done in collaboration with others, except as specified in the text. This thesis contains fewer than 80,000 words including appendices, bibliography, footnotes, tables and equations.

Farhad Allian

July 2021

Scientific Contributions

Peer-reviewed Published Articles

1. <u>Allian F</u>., Jain R., & Hindman, B.W., (2019), 'A New Analysis Procedure for Detecting Periodicities within Complex Solar Coronal Arcades', *ApJ*, **880**, 3.

2. <u>Allian F</u>. and Jain R., (2021), 'The Need for New Techniques to Identify the High-frequency MHD Waves of an Oscillating Coronal Loop', *Astron. Astrophys.*, **650**, A91.

Conferences, Seminars and Public Outreach

1. BUKS, Waves and Instabilities in the Solar Atmosphere, 03/09/18 - 07/09/18.
   Instituto de Astrofísica de Canarias, La Laguna, Tenerife, Spain.
   <u>Contributed poster</u>: *Oscillations in a Solar Coronal Arcade.* Related to Chapter 3.

2. AOGS, MHD Waves in Solar Magnetic Structures, 28/07/19 - 02/08/19.
   SUNTEC Convention & Exhibition Centre, Singapore.
   <u>Contributed talk</u>: *Detecting Periodicities in Complex Coronal Arcades.* Related to Chapter 3.

3. Applied Mathematics Colloquium, 04/12/19.
   The University of Sheffield, Sheffield, UK.
   <u>Contributed talk</u>: *Transverse Waves in Solar Coronal Loops.* Related to Chapters 3 and 4.

4. UK Solar Physics Nugget, 30/09/19.
   <u>Contributed blog</u>. Related to Chapter 3.

Abstract

Loops of hot plasma trace the invisible magnetic field lines of the Sun's dynamic corona. These structures are known to host various magnetohydrodynamic (MHD) waves and oscillations and are believed to play a crucial role in long-standing problems, such as the enigmatic heating of the solar corona. Recent high-resolution observations have galvanised interest in understanding the nature of these loops. Often, coronal loops are observed to oscillate in response to an expulsion of energy from solar flares, with frequencies of around 1–10 mHz. Current efforts are aimed at determining the physical parameters of the loops that are otherwise unmeasurable by virtue of seismology. However, before seismic inversions can be successfully executed, it is imperative to fully understand the observed wave signals emitted from these structures, including the techniques used for their analyses. Using multiple observations, we develop a novel technique for detecting periodicities within complex coronal arcades. Key applications include loop oscillations with a poor image contrast whereby the inherent waveform is revealed. Next, we ask whether it is possible to identify high-frequency wave signals from an oscillating loop using two common spectral methods. We demonstrate that the spectrum of a loop oscillating with a single frequency contains power at frequencies that are integer multiples of the fundamental frequency. These frequencies are completely artificial and arise owing to the inability of the methods to distinguish the periodic but non-sinusoidal signals from coronal waveforms. This study highlights simple cases where the methods themselves fail, and calls for more robust procedures, including 3D MHD simulations, to confidently reveal such high frequencies. Finally, we investigate a rare event of transverse oscillations induced by consecutive flares. We find evidence of a loop exhibiting a change in frequency during the observation and discuss the possibility of multiple simultaneous excitation sources.

Contents

List of Figures

List of Tables

List of Acronmys

1

Introduction

> "If I have seen further, it is by standing upon the shoulders of giants."
>
> — Sir Isaac Newton to Robert Hooke

In a letter to his fellow scientist, Sir Isaac Newton humbly attributed his many scientific accomplishments to that of his predecessors, acknowledging that his discoveries would not have been possible without their endeavours. The answers to the questions we seek are arguably derived from the foundations — whether it be theoretical or experimental — that have been built by the visionaries of our past. Just as Newton did with Descartes and Hooke, I have looked upon my giants and climbed. By honouring those before me, I hope that my work can pave the way for others after me.

1.1   The Anatomy of the Sun

1.1.1   How does the Sun Shine?

The birth and evolution of the Sun as we know it today began around 4.6 billion years ago. In fact, it is believed that our entire solar system, including the Earth, was also formed during the same epoch. The Sun, in particular, is known to have formed from the collapse of a massive concentration of interstellar gas. As more particles coalesced due to an accumulating gravitational force, the core of the gas began to form a hot and dense protostar. Once the core became dense enough, individual sub-atomic nuclei were then forced to overcome their mutual electrostatic repulsion, igniting the extreme and energetic conditions for nuclear fusion. During this process, it is known that hydrogen atoms are fused to produce helium nuclei and, in turn, expel vast amounts of energy governed by Albert Einstein's mass-energy equivalence (Einstein 1905),

$$E = mc^2, \tag{1.1}$$

where m is the mass and c is the speed of light. This energy conversion is believed to occur only within 20% of the solar radius $R_\odot$, creating temperatures of $\sim$15.7 million K and densities of $\sim$150.0 g cm^{-3}. Due to these extreme conditions, a hot and ionized state of matter called plasma permeates throughout the solar interiors. Stars like our Sun owe their existence to the fusion of nuclei within their cores, generating their primary source of energy.

However, the precise physical processes behind nuclear fusion were not well established until the 1920s when British astrophysicist Sir Arthur Eddington suggested that stars could create energy within their cores from such chemical reactions (Eddington 1926). Several years later, the pioneering work of Nobel laureate Hans Bethe (Bethe 1939), alongside Eddington's efforts, laid the foundations of theoretical astrophysics, and fuelled the development of stellar nucleosynthesis. Their theory describes the generation of energy within the solar core as an intricate chain of thermonuclear reactions, governed by the three-step proton-proton reaction[1] (p-p cycle). More specifically, the entire p-p cycle entails the fusion of four hydrogen $\left(^1_1\text{H}\right)$ nuclei (i.e. four protons), yielding a helium atom $\left(^4_2\text{He}\right)$ with remnants of two positrons $\left(\text{e}^+\right)$, two electron neutrinos (ν_e) and two high-energy photons (γ). The net output of the entire p-p cycle can be summarised as follows:

$$4\,^1_1\text{H} \rightarrow\, ^4_2\text{He} + 2\,\text{e}^+ + 2\,\nu_e + 2\,\gamma + \text{Q}, \tag{1.2}$$
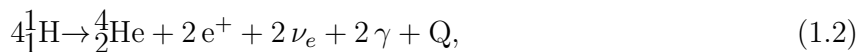
where $Q \simeq 26.73$ MeV is the total binding energy produced in accordance of Equation (1.1). During this production, energy is mainly carried by the photons and neutrinos. Since the

---

[1] The primary source of energy of more massive stars is generated by the Carbon-Nitrogen-Oxygen cycle.

neutrinos interact weakly with matter, they are estimated to traverse the Sun in seconds and reach the Earth in only $\sim$8 minutes (Carroll and Ostlie 2007). Thus, confirmation of the Sun's primary energy source relied solely on capturing these elusive neutrinos.

The detection of solar neutrinos was the only direct experimental evidence for Eddington and Bethe's theory of stellar nucleosynthesis. In early experiments – such as the historic Kamiokande (Fukuda et al. 1996) and GALLEX/SAGE (Hampel et al. 1999; Abdurashitov et al. 2009) – the number of detected neutrinos was around one-third of that predicted by the Standard Solar Model, indicating an inherent flaw existed in the physics. This so-called solar neutrino problem was later solved by virtue of next-generation instruments, namely, the Sudbury Neutrino Observatory (Ahmad et al. 2001) and Super-Kamikoande (Abe et al. 2011). These revolutionary experiments were able to shed first light on this fundamental problem; demonstrating that neutrinos have mass and are able to change flavours[2] during their transit from the Sun. More recently, the Borexino experiment (Borexino Collaboration et al. 2014, 2018) was able to detect the full energy spectrum of solar neutrinos regimes and demonstrate that 99% of the Sun's energy is generated directly by the p-p cycle. Ultimately, our Sun feeds from the energy produced by complex thermonuclear reactions within its core, enabling it to light up our solar system for another 4 billion years.

1.1.2 Energy Transport in the Radiative and Convective Zones

Of course, the vast energy produced by such nuclear processes in the core must be transported somewhere and somehow. Within the solar interior, two distinct surrounding regions are defined by the physical mechanisms which dictate how this energy is transported, namely, the radiative and convective zones.

In the radiative zone, which extends over $0.31R_\odot \leq r \leq 0.714R_\odot$ (Carroll and Ostlie 2007), energy is mainly transported by photon diffusion due to frequent collisions with the surrounding plasma. As the density and temperature drops with increasing distance from the core, photons are continuously scattered resulting in $\sim$250,000 years for a single photon escape (Mitalas and Sills 1992). When the hindering plasma becomes too opaque – due to the change in density, temperature and ionization states of atoms – radiative transport becomes less efficient and convection takes over as the dominant mechanism of energy transport (e.g. Phillips 1992). The convective zone is defined over the region $0.71R_\odot \leq r \leq 1.0R_\odot$ wherein energy is transported by the turbulent movement of plasma, forming a circular convection current. The heated plasma ascends due to its buoyancy, expels its energy to its surroundings and finally descends to repeat the convective cycle. Physically, convection occurs only when the temperature gradient exceeds the adiabatic temperature gradient. This leads to the visible and physical region of the Sun, called the photosphere, where the convective cells can

---

[2] More commonly known as neutrino oscillations between electron- (ν_e), muon- (ν_μ) and tau- neutrinos (ν_τ).
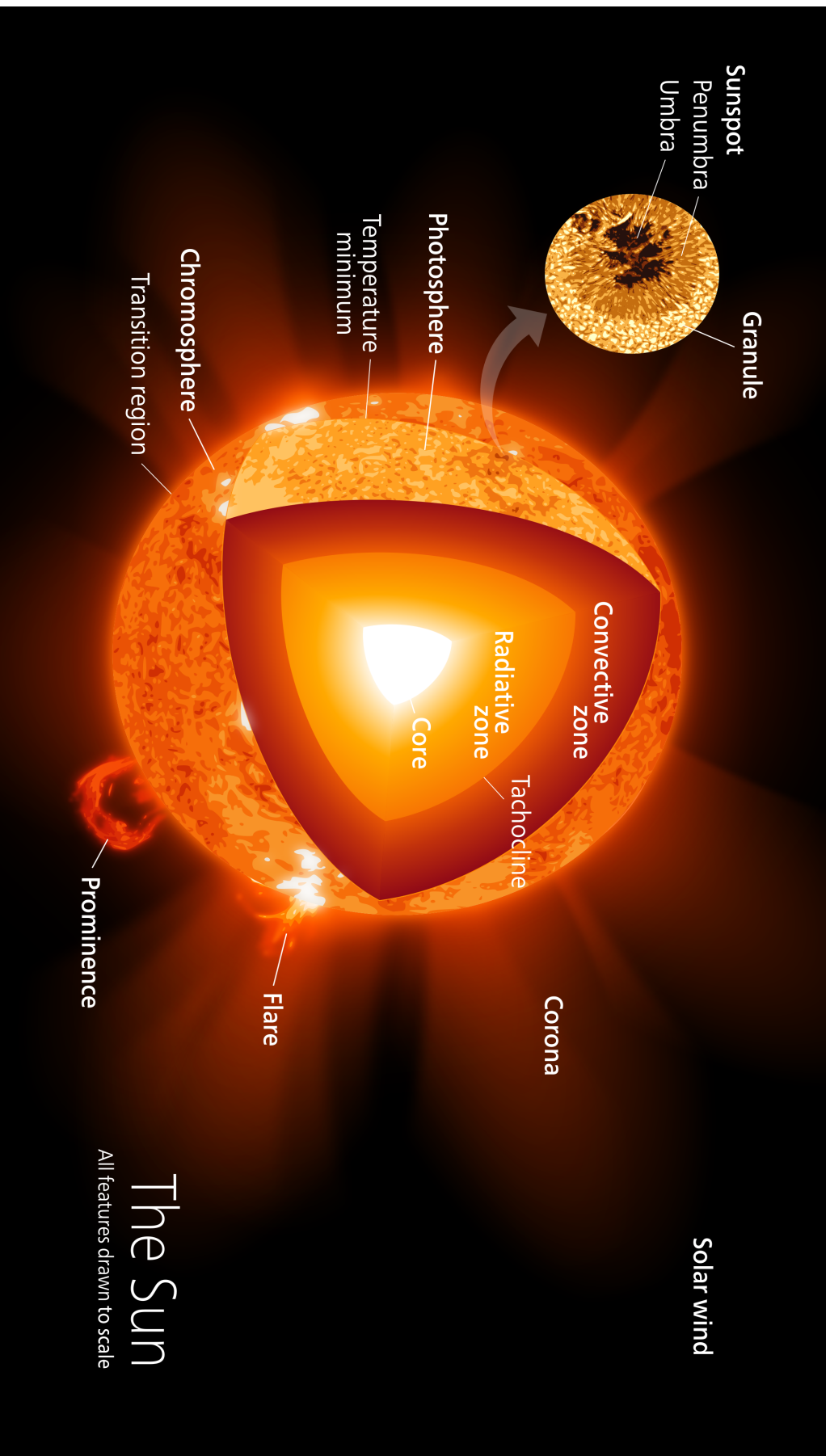
Figure 1.1: A schematic diagram highlighting some main features of the Sun's interiors and exteriors. The solar interior consists of distinct regions, namely, the core, radiative zone, tachocline and convective zone. The visible exterior are the photosphere, chromosphere and corona. Intense concentrations of magnetic field lines are grouped together in sunspots, which are enhanced by strong shearing exhibited within the tachocline. The sunspot's umbra appears darker than its surrounding penumbra due to suppression of its thermal energy. Image credit: Kelvinsong (2012).

be readily identified as granules and large-scale flows.

1.1.3 Tachocline

Interestingly, the radiative and convective zone are separated by a thin, intermediate layer called the tachocline (Spiegel and Zahn 1992). Within this region, a sharp change in velocity between the rigid rotation of the radiative zone and the differentially rotating convective zone causes a strong shear. It is currently hypothesised that the shearing exhibited within this layer plays an important role in generating, or at least enhancing, the Sun's magnetic field through a dynamo process (Ossendrijver 2003). With a rotation period of 25 days at its equator and 36 days at the poles, this differential rotation is believed to wrap and wind up magnetic field lines like a coil. Intense concentrations of magnetic fields can then rise and pierce through the solar surface, suppressing the convection and thermal radiation from below, forming what are formally known as sunspots (Hale 1908) (see Section 1.2.1). However, a detailed mechanism regarding the origin of the solar dynamo remains unknown and is currently an ongoing area of research. Arguably, the origin of the Sun's magnetic energy lies at the heart of solar and stellar astrophysics (e.g. Baliunas 2004).

At this point, it is worth highlighting that since the solar interiors are opaque to electromagnetic radiation, direct observations cannot be made. Therefore, all knowledge of the Sun's internal structure are purely derived from theoretical models, or through helioseismology – the study of the solar interiors using the propagation of acoustic waves generated by convective turbulence. Although this particular notion may seem unintuitive at first, we will see that, in fact, various types of waves and oscillations pervade the Sun.

1.1.4 Helioseismology and the Sun's 5-minute Oscillations

The idea that the Sun may be able to host waves and oscillations was not proposed until the early 1960s. Leighton et al. (1962) first discovered that regions of the photosphere were oscillating with a period of about 5 minutes ($\sim$3 mHz). It was at this time that Leighton et al. (1962) realised the diagnostic potential of such detections by noting that these oscillations offer 'a new means of determining certain local properties of the solar atmosphere'. Further theoretical and observational studies demonstrated that the observed oscillatory motions are actually the superposition of several global resonant modes of the Sun that arise from broadband convective sources (e.g. Ulrich 1970; Leibacher and Stein 1971; Deubner 1975). The reference model of (global) helioseismology describes the Sun's oscillatory modes as the resonance formed by spherical harmonics (see the left panel of Figure 1.2). These oscillations in the solar interiors come in two flavours: global acoustic waves (p-modes), for which pressure is the restoring force, or gravity modes (g-modes), where the restoring force is predominantly buoyancy. The p-modes have a dominant periodicity of 5 minutes (ranging
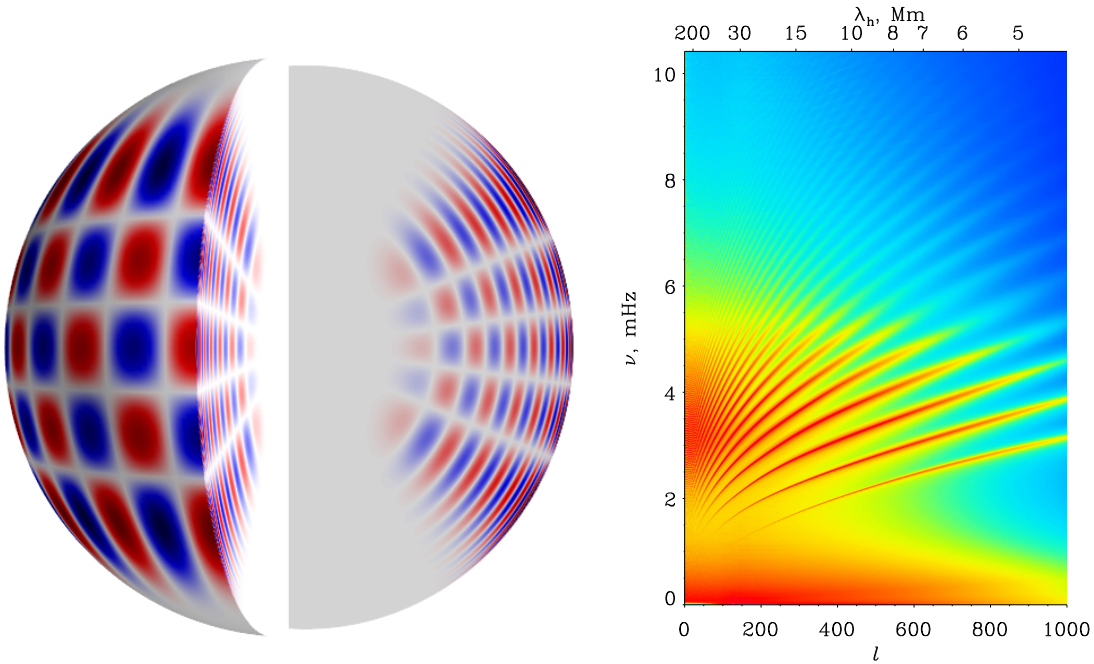
Figure 1.2: Examples of the Sun's global acoustic oscillations. Left panel: an illustration of p-modes described by spherical harmonics of various orders throughout the solar interior. The red (blue) regions correspond to areas on the solar surface where waves are propagating outward (inward) Image credit: Warrickball (2017). Right panel: Power spectrum of the solar interior measured by the SOHO/MDI instrument. The bottom (top) horizontal axis corresponds to the angular (spatial) wave modes. The strongest frequency, shown in red, occurs at about 3 mHz (5 minutes) and arise due to p-modes. Image courtesy of SOHO/MDI science teams.

from 3-10 minutes) and are formed by waves that propagate throughout the entire solar interior (right panel of Figure 1.2). The wave interference enables p-modes to form normal modes, providing a measure of the properties inside the inaccessible solar interior. It has also been suggested that p-modes may weakly penetrate the outer solar atmosphere (see Cally 2017; Morton et al. 2019). In addition to those mentioned in previous sections, such as the solar neutrino problem and the discovery of the tachocline, another major discovery of helioseismology came from Gough (1977), who suggested that the convection zone was substantially deeper than what models predicted (also see the reviews by Basu and Antia 2008; Kosovichev 2012). Thus, the entire Sun is singing and its harmonies are subtly encoded into the vibrations of its music.

1.1.5 Photosphere

The photosphere is the first layer of the Sun wherein photons are finally allowed to escape without being absorbed, enabling a direct observation in the visible-light continuum (Car-

roll and Ostlie 2007). It is therefore considered to be the 'surface' of the Sun and serves as a benchmark for mathematical calculations, such as its radius, effective temperature and wavelength. Its emission of light ranges from the ultraviolet (UV), through the visible spectrum and even into infrared. In particular, measurements of the photospheric spectral flux demonstrate that its emission follows that of a theoretical blackbody governed by Planck's law. From this, an effective temperature of the solar photosphere is estimated to be ∼5800K.

Although the spectral flux of the solar photosphere appears continuous, the presence of absorption lines, including Fraunhofer lines, provide evidence for the presence of various chemical elements (Carroll and Ostlie 2007). Since the solar interiors are almost in thermodynamic equilibrium, Kirchoff's laws suggest that absorption lines should be present in locations of the photosphere where it is cooler than the internal continuum regions. However, this argument does not hold in the outer layers such as the chromosphere, since non-thermal equilibrium effects take place. The advantage of such spectroscopic techniques lie in their diagnostic potential of photospheric structures that are otherwise inaccessible, such as temperature and velocity fields, chemical composition/abundance and magnetic properties. A specific example is the spectral line measurements of the continuous convective movement of photospheric granules. In such cases, spectral line profiles can be broadened due to the motions of granulations along the line of sight, and their characteristic widths, and sometimes asymmetries, provides insight into the physical effects that are present on the photosphere.

Another advantage of spectroscopy is the ability to directly measure the photospheric magnetic field strength through the Zeeman effect (Zeeman 1897). This quantum mechanical phenomenon describes the splitting of atomic energy levels in the presence of a magnetic field, where the separation between the chemical components along the wavelength is proportional to the magnetic field strength. In particular, Hale (1908) was the first astronomer to find pronounced Zeeman splitting in heavy chemical elements (such as iron) within the spectrum of sunspots, revealing their magnetic properties for the first time. Typical sunspot observations show that the dark umbra of a sunspot is surrounded by a relatively lighter penumbra, indicating a hotter but highly magnetic ($|\mathbf{B}| \sim 3000$G) and cooler but less magnetic ($|\mathbf{B}| \sim 1000$G) region, respectively. Commonly, sunspots form in pairs of opposite polarity and are separated by an inversion line, but they can also develop into complex multi-polar arrangements. Since the discovery of sunspots, the Sun has served as a gateway to the exploration of cosmic magnetic fields, including their role in various astrophysical plasmas.

In addition, the underlying principle of the Zeeman Effect is how magnetogram detectors measure the line-of-sight component of the magnetic field over the solar photosphere. From this technique, an entire magnetic field vector can also be constructed using the polarisation of the spectral line components (Carroll and Ostlie 2007; Priest 2014). Unfortunately, such methods can primarily be applied to observations of photospheric structures, such as

sunspots, since their magnetic fields are strong ($\sim$kG) enough to cause the Zeeman splitting. In relatively weak magnetic field regions (tens of G), measurements are typically based on the Hanle Effect (Hanle 1924): the modification of the linear polarization of a spectral line in the presence of a magnetic field. Distinctively, the Hanle Effect does not create the polarization of spectral lines unlike the Zeeman splitting, but requires its presence through radiation scattering processes. Physical properties of the Hanle Effect has enabled solar physicists to further constrain the photospheric magnetic field strengths, and to find evidence for such weak fields occupying the background of the photosphere (Stenflo 1982).

1.1.6 Chromosphere

Above the photosphere lies the chromosphere, a layer that bridges the relatively cool solar surface and the extremely heated, tenuous transition region and corona. Analyses of the chromospheric light indicates that the plasma density drops by a factor of 10^4 and the temperature begins to increase with altitude with respect to the photospheric temperature minimum, from 4400 K to $20{,}000$ K (Phillips 1992; Carroll and Ostlie 2007).

Whilst the photosphere contains mainly absorption spectra, the chromosphere is primarily dominated by emission spectra. Although visible wavelengths are not usually seen against the bright solar disk in the chromosphere, they can be best observed near the solar limb for a few seconds before and after a total eclipse; this is known as a flash spectrum. During this short time, the outer edge of the chromosphere transitions from a glowing rosy red halo to a vibrant blue, due to emission from the Hα ($\lambda \sim 656.3$ nm) and Hβ ($\lambda \sim 486.1$ nm) Balmer series of the hydrogen atom, respectively. This observational property led Lockyer (1868) to give the chromosphere its name (derived from the Greek words for 'sphere of colour').

In the chromosphere, many different types of plasma structures are sculpted by magnetic fields. For instance, the chromosphere is known to host the diminutive but ubiquitous grass-like spicules, and the swirling fiery clouds of plasma called prominences[3]. An individual spicule may have a lifetime of only 15 minutes, but exist in many locations of the solar surface. On the other hand, prominences can last for several weeks and span a large portion of the chromosphere (Priest 2014). Of course, the physical processes behind the formation and dynamics of such structures are undoubtedly different. However, by harvesting the various emitted spectra from the solar atmosphere, it is possible to further constrain the properties of these structures, such as their temperature and origin. This presents a particularly fascinating fact that many (if not all) structures in the outer atmosphere appear to coexist with the much hotter and outer layer of the corona, suggesting a sudden and non-uniform merging of these layers. As a matter of fact, this is precisely what historical observations

---

[3] The nomenclature given for prominences when viewed on the solar disk are 'filaments'.
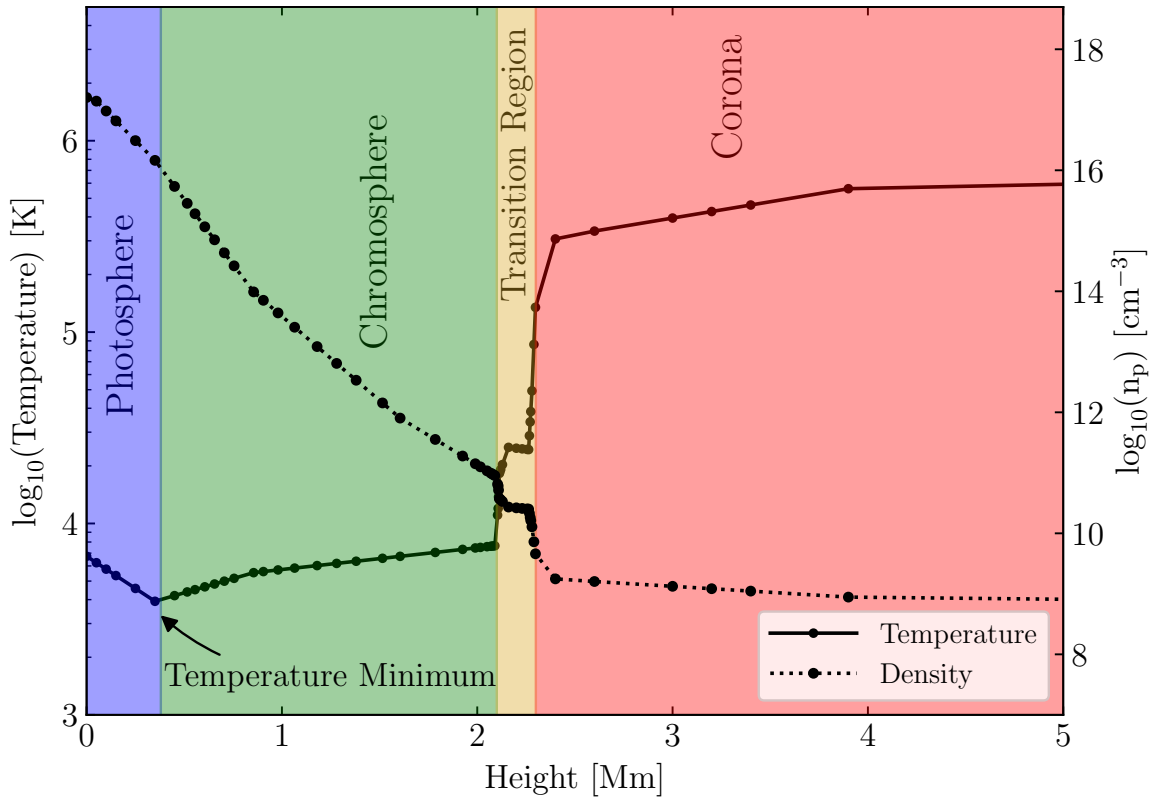
Figure 1.3: Temperature (solid line) and proton number density (dotted) profiles of the solar exteriors as a function of height from the photosphere, based on the semi-empirical models of Vernazza et al. (1981) and McWhirter et al. (1975). The smooth lines are first-order spline interpolations of the measured data points. The shaded colours denote the regions of the solar exteriors. The temperature minimum originates at the upper photosphere at approximately 4400 K and reaches around $20,000$ K with decreasing density at the upper chromosphere. A sharp temperature increase of more than an order of magnitude in only 50 km defines the transition region. In the corona, temperatures reach as high as 10^6 K.

have shown.

1.1.7 Transition Region

Prior to the 1940s, it was thought that the temperature decreases with height above the photosphere in accordance of the second law of thermodynamics – only in the presence of external work can a region become hotter. However, the first spectroscopic measurements of the Sun's atmosphere showed that it is dominated by emission lines (Grotrian 1939; Edlen 1943). In particular, Grotrian (1939) identified emission lines from the forbidden transitions of Fe XIV, Fe X and Ca XV. Edlen (1943) later found four additional important emission lines from Fe XI, Ca XII and Ca XIII. The presence of such high ionization atomic states implied extreme temperatures in its atmosphere. Soon after this, McWhirter et al. (1975) and Vernazza et al. (1981) derived a semi-empirical model of the solar atmosphere

from such emission lines at various heights (see Figure 1.3). This model demonstrates that the temperature slowly rises from the photospheric temperature minimum to the upper chromosphere, and then abruptly increases only within 100 km. This is more commonly known as the transition region. In this narrow layer, plasma temperatures rise from 10^4 to more than 10^5 K, while densities decrease by nearly eight orders of magnitude. Clearly, this sudden and intense heating cannot be solely due to thermodynamic processes and must therefore be accompanied by some additional mechanism. As we will see, it is speculated that the Sun's magnetic energy may play a vital role in the heating of its atmosphere. Additionally, this model has served as the base solar atmospheric model for many solar simulations (e.g. Fedun et al. 2011; Mumford and Erdélyi 2015; Gent et al. 2019).

1.1.8 Corona

Even more mysterious than the transition region is the Sun's corona. The corona (Latin for 'crown') forms the outermost layer of the Sun from the upper transition region, expanding far into the solar wind. The sheer magnitude and inhomogeneity of the solar corona can be appreciated during a total eclipse (Priest 2014), as shown in Figure 1.4. Within the corona, magnetic fields dominate the plasma dynamics, with closed field lines originating near the limb and open field lines extending further out by the stretching of the continuous outwardly-flowing solar wind. The corona's region of influence can extend far into the solar system, and even beyond the orbit of Pluto.

Average temperatures of coronal plasmas are about $1-2$ MK, however, substantially higher temperatures of $6-10$ MK can also be measured in flaring regions (Priest 2014). As introduced above, this (seemingly) paradoxical property of the corona – formally known as the coronal heating problem – is believed to violate the laws of thermodynamics. For over 60 years, the exact mechanisms that create and maintain the multi-million degree corona have remained unknown. However, two distinct hypotheses are often in contention: the first is known as magnetic reconnection; a topological reconfiguration of field lines which produce extreme heating by the direct conversion of magnetic energy to thermal energy (e.g. Priest 1986). The second is magnetohydrodynamic (MHD) wave dissipation; this idea suggests that energy can be transported and dissipated through the propagation of magnetic waves (Priest 2014)[4]. Despite the distinction, both mechanisms share a common connection: magnetism. It is currently agreed that the origin for such extreme temperatures must be primarily due to the Sun's magnetic activity and, consequently, the governing physics is not violated.

Although the coronal heating problem still remains largely unsolved, advancements have been made. There has recently been a paradigm shift regarding the Sun's origin of heating. Aschwanden et al. (2007) argue that observations do not show evidence for heating in the

---

[4] Historically, wave-based mechanisms are often referred to as Alternating Current (AC), whereas a conversion of magnetic to thermal energy is termed as Direct Current (DC).
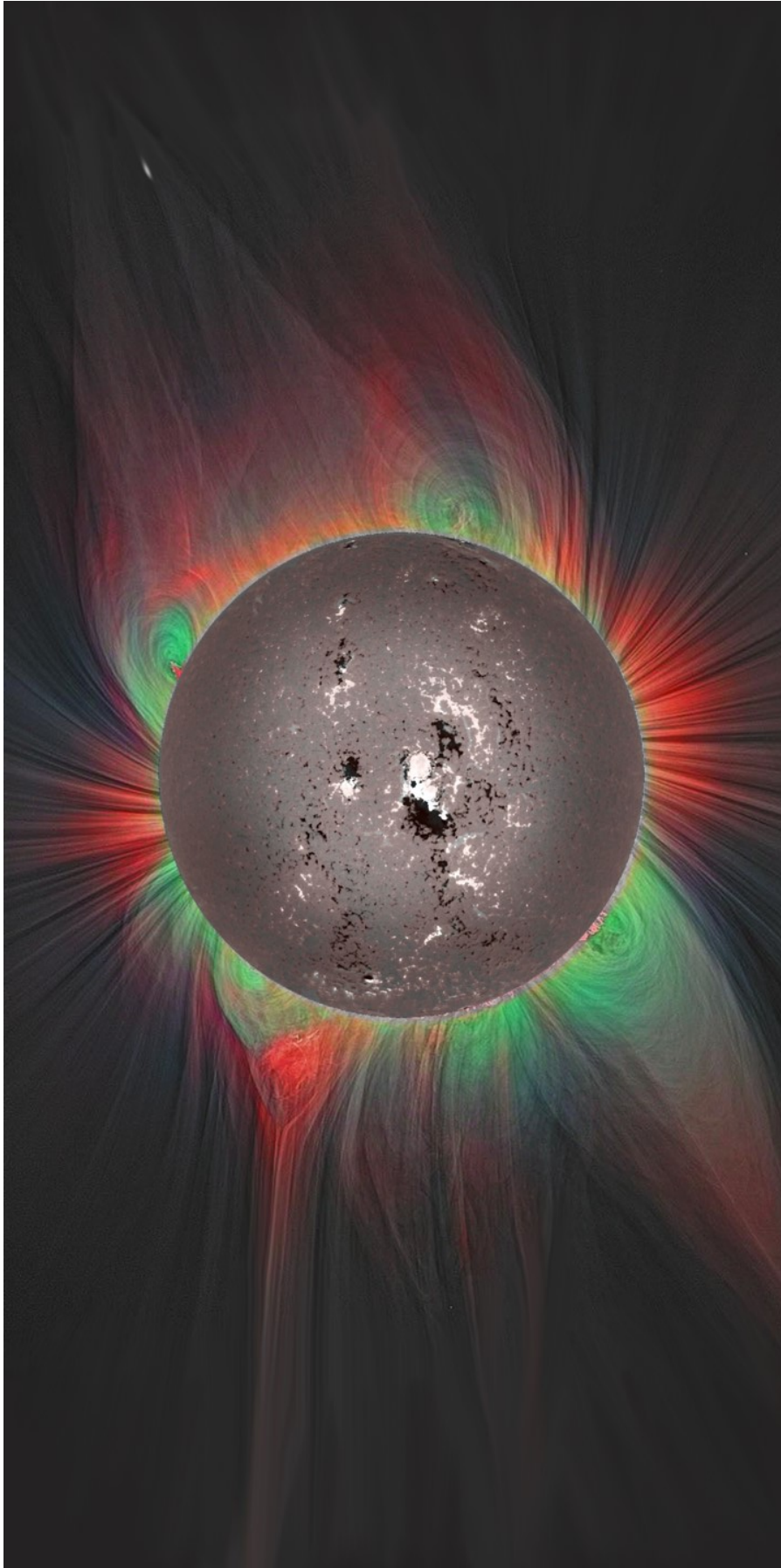
Figure 1.4: The highly inhomogeneous solar corona as a false-coloured image. Hot plasma is traced along the invisible magnetic field lines. Open field lines are shown in red, whereas the closed field lines are in green. The composite image is a magnetogram of the line-of-sight magnetic field configuration. The white and black polarities correspond to outward and inward field lines, respectively. Image credit: Druckmüller, M. and National Science Foundation/NSO (2013)

corona, but instead in the transition region and upper chromosphere from which the material is directly transported up into the corona. This underlying process is known as chromospheric evaporation (Neupert et al. 1968). Aschwanden et al. (2007) suggest that such a heating mechanism may be dominant in quiet Sun regions, however, excludes open magnetic field configurations such as the extended solar wind. In such a scenario, the question would not be "how does one heat the corona?" but "how does one heat the chromosphere?" Further studies have shown that coronal heating is only a few percent of chromospheric heating (Priest 2014). In all likelihood, a mixture of various mechanisms, such as reconnection and waves, may play a role in heating different regions of the solar atmosphere and, therefore, a unique solution to this particular problem should not be expected. This does not, however, imply that the problem at hand is unworthy of pursuit. The solar corona is still full of many mysteries, only waiting to be solved.

It should be emphasised that, in contrast to the photosphere, the corona's magnetic field is resistant to spectroscopic measurements. This is primarily because the magnetic field strength of the corona is relatively weak. As a consequence of this unfortunate fact, magnetic properties of coronal structures can only be estimated using extrapolations and inversions techniques. This thesis does not directly explore the issue of coronal heating and inversion methods. However, it is hoped that the techniques and results presented in this work will provide a valuable tool for identifying and analysing oscillatory regions in which the coronal structures reside, enabling further progress in the field.

1.2 Solar Phenomena

1.2.1 The Sunspot and Solar Magnetic Cycles

The Sun is host to many different structures and phenomena. Traditionally, these have been categorised into two classes: quiet and active. During a quiet Sun period, the Sun's magnetic influence is comparably low. The active Sun, on the other hand, is far more interesting. In this magnetically dominated period, the Sun consists of extremely energetic phenomena such as sunspots, solar flares and other transient events, which are essentially superposed onto the quiet Sun background. This section introduces some of the key phenomena that is frequently observed.

The Sun fluctuates on all timescales that are physically attainable from current observational methods, ranging from sub-second intervals to centuries. Importantly, these timescales can provide insight into the physical properties, such as the possible sources, which can be in action at the time of observation. Historical observations have shown that the Sun can exhibit many different types, such as periodic, chaotic and even stochastic variations (e.g. Goldreich and Keeley 1977; Usoskin et al. 2007; Hathaway 2010). An obvious example of
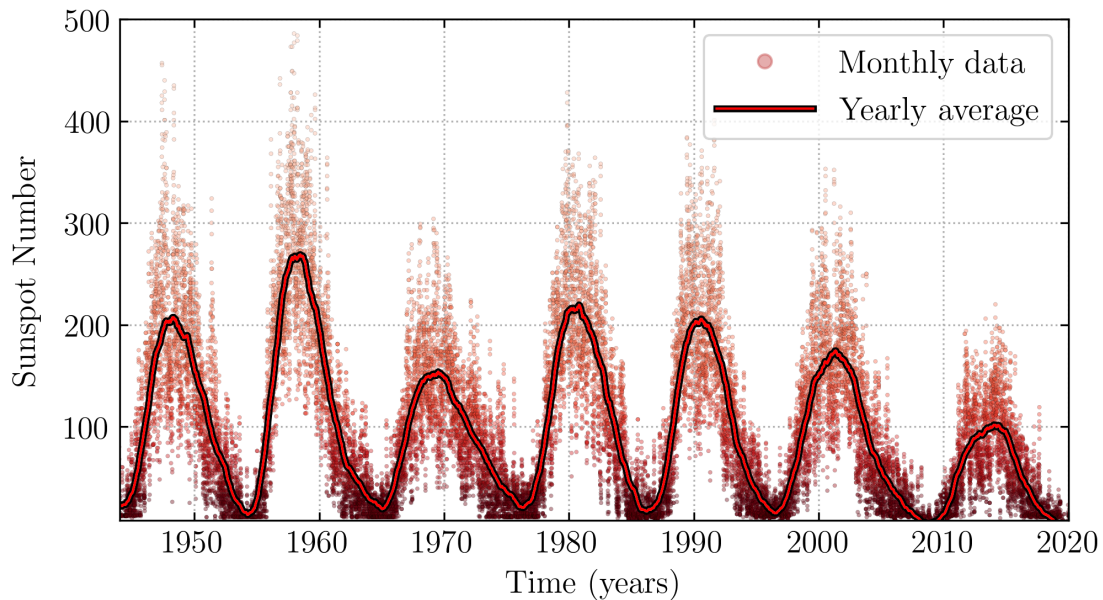
Figure 1.5: Variability of the number of sunspots spanning over 7 solar cycles, from cycle 18 to 24. The scatter plots show the distribution of monthly sunspot numbers, ranging from a few to several hundreds, and the solid red line shows a running average of the original data. A clear periodic pattern is observed, corresponding to the ∼11 year cycle of magnetic activity. At the time of writing, it is believed that the Sun is at the end of cycle 24 and is in its ascending phase of its 25th cycle. The sunspot data were obtained the SILSO database maintained by the Royal Observatory of Belgium, Brussels (http://www.sidc.be/silso/datafiles).

the Sun's variability is its period of rotation, which are 25 days and 36 days at its equator and poles, respectively.

Another fundamental temporal variation in which the Sun exhibits is its ∼11 year cycle, namely, the sunspot cycle. More specifically, this refers to the local magnetic activity driven by the solar dynamo which waxes and wanes in strength during this period. Temporal variations are typically observed in radio, optical, UV and X-ray wavelengths, but more clearly by the canonical indication of magnetic activity from the number of sunspots (Hathaway 2010). Figure 1.5 shows an example of the sunspot number as a function of time, from 1940 until the present year, where a clear periodicity of about 11 years can be observed. Each cycle has a maximum and a minimum, which correspond to active and quiet Sun periods, respectively. At times of solar maxima, magnetic activity, such as the presence of sunspots and ARs, is substantially greater than those of solar minima. The strength and duration of a particular solar cycle also determines the types of structures present in the solar atmosphere. The Sun's magnetic cycle, however, is more rigorously defined as two sunspot cycles, which includes the reversal of its global magnetic field in each hemisphere and thus requires approximately 22 years to complete (Babcock 1961).

The sunspot cycle, and thereby the overall magnetic activity of the Sun, also has imperative consequences for life on Earth. At times of high activity, the Sun is prone to various high-energy particles that are transported through the interplanetary magnetic field by the continuous outflow of the solar wind. At the Earth, such physical interactions can be hazardous to technologies, the climate and even human welfare. A drastic, historical example is from the Maunder Minimum, which was a period of extreme low solar activity from AD 1650 to 1715 (e.g. Eddy 1976, and references therein.) In solar physics literature, and wider discourse, this period is often linked to the Little Ice Age experienced on Earth during the 13th to 20th centuries (e.g. Mann et al. 2009). However, recent studies have demonstrated that such cold climate conditions on Earth are unlikely to be a direct cause of low solar activity (e.g. Lockwood et al. 2010; Owens et al. 2017). The Sun's magnetic variations are, thus, of great scientific intrigue and importance to many ongoing areas of research.

1.2.2 Active Regions

The magnetised realm surrounding an area of strong magnetic activity on the Sun is broadly categorised as an active region (AR) (see the recent reviews by van Driel-Gesztelyi and Green 2015; Toriumi and Wang 2019). The formation and evolution of ARs is believed to strongly depend on the coexistence of the solar dynamo within the tachocline, and the Sun's differential rotation. Current dynamo models attribute the observed formation of ARs to the process of magnetic buoyancy (e.g. Dikpati and Gilman 2007). It is postulated that the Sun's differential rotation produces twisting, toroidal magnetic fields from its global poloidal field, producing buoyant magnetic loop-like structures that can emerge in the photosphere where the magnetic flux is strong enough. A schematic diagram of this flux emergence process is shown in Figure 1.6. ARs vary in size, lifetimes and magnetic field strength (Toriumi and Wang 2019). They form at latitudes of $\pm 30°$ and then migrate towards with the solar equator until an eventual solar minimum is reached (Hathaway 2010). This evolution is best visualised in the form of the so-called solar 'butterfly' diagram of sunspots, as first reported by Maunder (1904).

Although a sunspot can be categorised as an AR, the converse is generally not true. In fact, the magnetic configuration of ARs are generally much more spatially elongated than that of a sunspot observed in optical wavelengths. An example of an AR exhibiting a sunspot is shown in Figure 1.7. For ARs that do show sunspots, they are typically observed with a bipolar magnetic configuration, which is clearly structured into two islands of opposite polarity in each hemisphere, but can also merge and mould into complex multi-polar arrangements, emitting radiation in multiple wavelengths. For this reason, van Driel-Gesztelyi and Green (2015) argue that the general definition of ARs should be extended to include '...all observable phenomena preceding, accompanying and following the birth of sunspots including radio-, X-, EUV- and particle emission'. Consequently, such a definition aids the
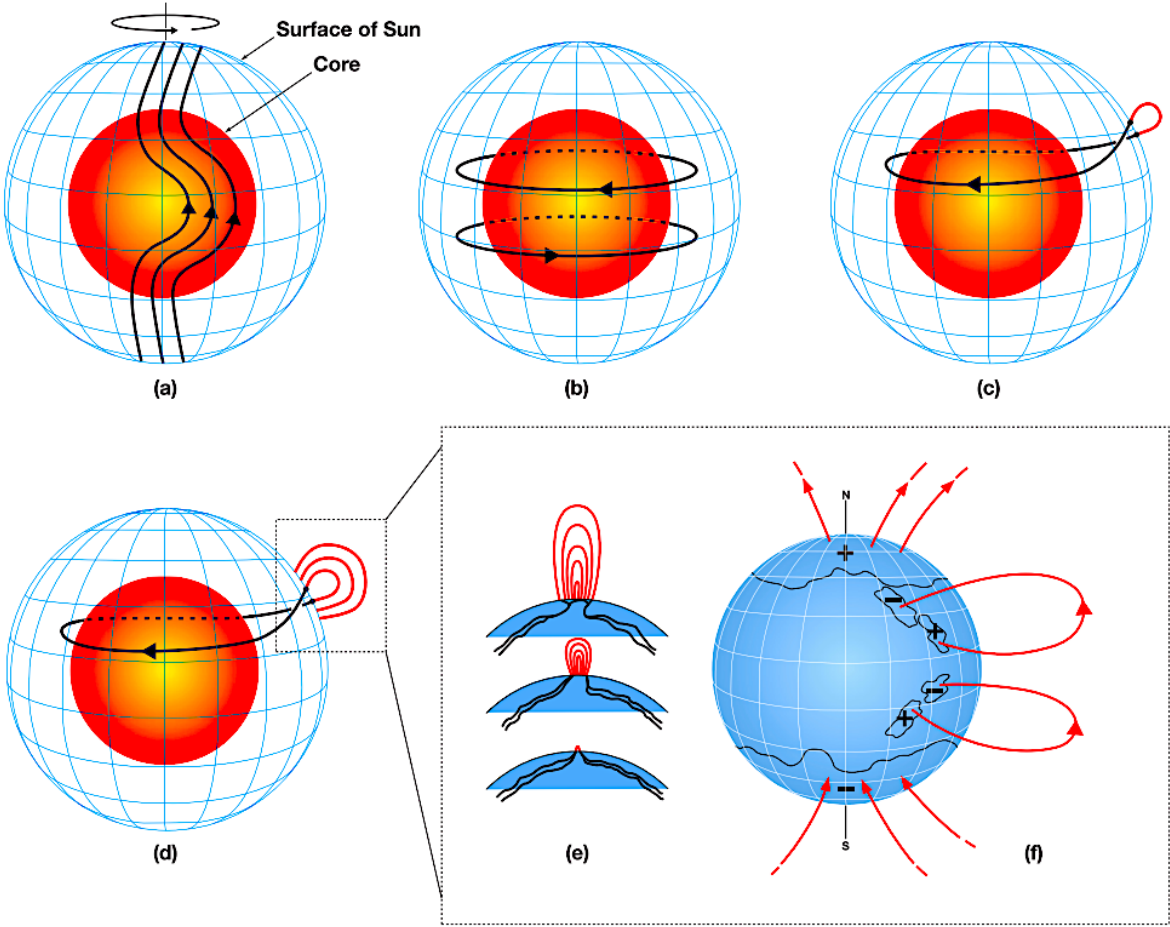
Figure 1.6: Schematic diagram of the solar dynamo process responsible for creating ARs. The red region represents the Sun's radiative zone and the blue contours is the photosphere. The solar dynamo is believed to originate within the tachocline, between the two layers. (a) Differential rotation causes a shearing of the Sun's global, poloidal magnetic field. (b) A toroidal field is then produced due to this shearing. (c) In regions of strong magnetic flux, buoyant, twisting loop-like structures pierce through the photosphere where sunspots are also formed. (d,e) Additional flux emergence and development. (f) Magnetic flux spreads out due to the decay of sunspots towards the equator. Reproduced from Dikpati and Gilman (2007).

explanation of the diverse solar phenomena observed in wavelengths associated with the upper atmosphere, such as solar flares, Coronal Mass Ejections (CME), jets, surges and other energetic phenomena.

1.2.3 Solar Flares

Solar flares are one of the most energetic events in the entire solar system. In only tens of minutes, a flare can expel energy in the range of $10^{28} - 10^{32}$ erg, emitting radiation across the entire electromagnetic spectrum, from radio to γ-rays (e.g. Benz 2008). They are commonly observed to originate from ARs and in frequent succession within periods of solar maxima.
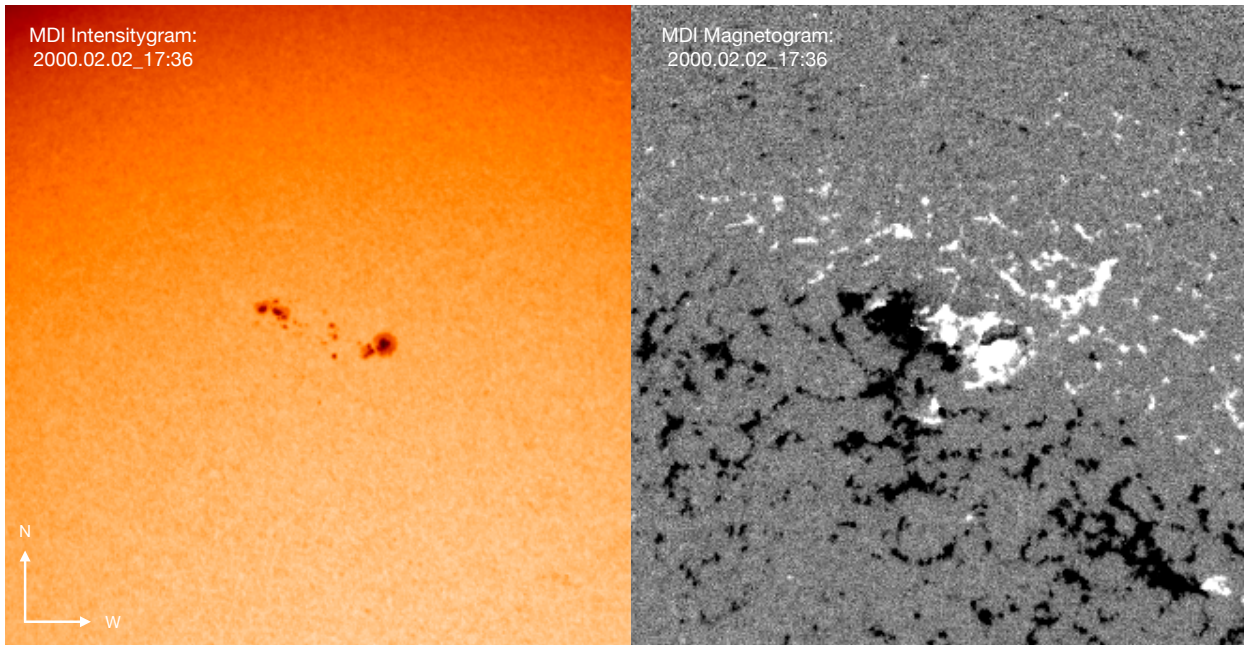
Figure 1.7: Typical observations of a sunspot in white-light (left) and its corresponding magnetogram (right) observed by SOHO/MDI during the peak of the previous solar cycle on 2000 February 02. The sunspot correspond to the strongest magnetic field concentration that is observed in the magnetogram. However, the entire AR spans a significantly wider portion of the solar surface, almost occupying the entire field-of-view. Here, the magnetic configuration is bipolar, with the white (black) colours corresponding to positive (negative) field lines. Note, in the white-light image on the left, the solar limb appears darker due to an observational effect called 'limb darkening', which can be removed. These images can be found on http://soi.stanford.edu/data/. Image credit: SOHO/MDI science teams.

During a flare, plasma temperatures can reach as high as several tens of millions Kelvin. The sudden release of energy from a flare can be currently best understood from the standard model of a solar flare (or the CSHKP model, named after Carmichael 1964; Sturrock 1966; Hirayama 1974; Kopp and Pneuman 1976). Essentially, this 2D model describes the sudden energy release from a flare as a results of the conversion of its magnetic energy, which is triggered by the 'reconnection' of the magnetic field lines, to radiative, kinetic, thermal and non-thermal energy (also see the review by Fletcher et al. 2011). Current efforts are aimed at generalising the standard flare model to account for 3D effects (e.g. Aulanier et al. 2012) and predicting the occurrence of imminent flares Kusano et al. (2020).

The first solar flare was discovered in optical white-light by Carrington (1859), and independently by Hodgson (1859), in September 1895 during Solar Cycle 10. This was also coincidentally the most powerful solar flare ever recorded in history. Since then, the advancement of detectors has enabled further investigation into the characteristics and physical properties of flares, and other impulsive transients in the solar atmosphere (Schrijver 2009; Benz 2017). For instance, the time-scales of flaring activity are now known to be represen-
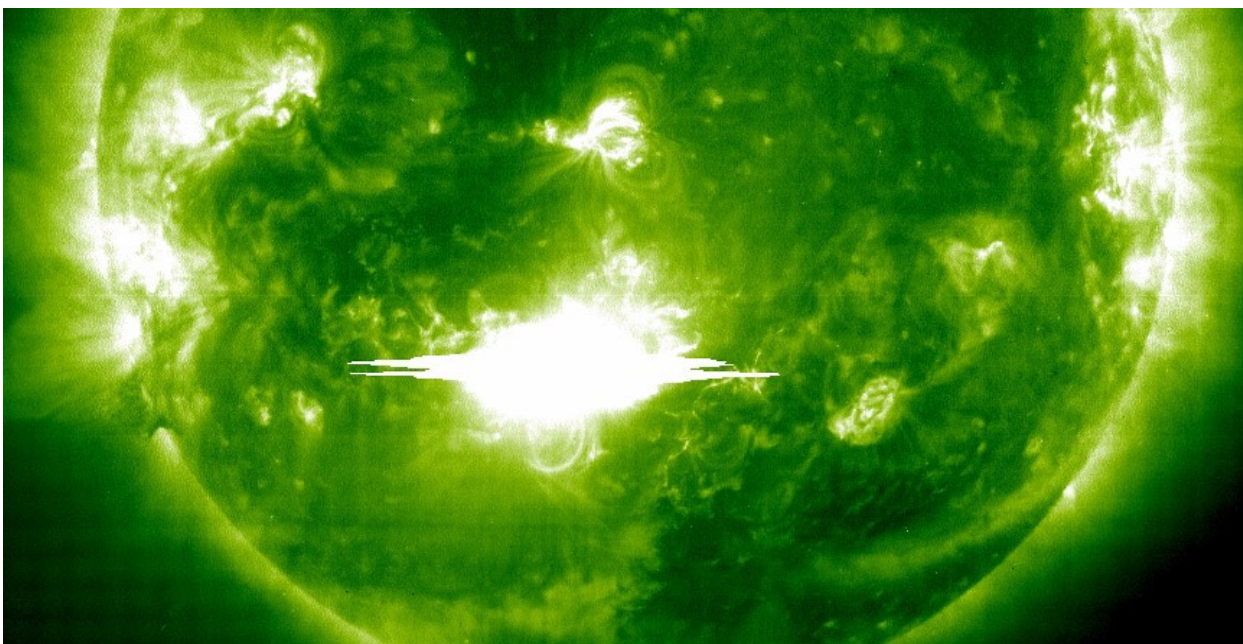
Figure 1.8: Example of an EUV observation of a thunderous solar flare observed by SOHO/EIT in the 195 Å waveband corresponding to temperatures of around 1.5 MK. The intense energy from the flare causes a saturation of the detector's CCD pixels that pierces across the observational field of view. Credit: SOHO/EIT science teams.

tative of the underlying physical mechanisms that can be present. During an observation, one can distinguish between several phases of a solar flare (e.g. Murphy et al. 1987). In the 'pre-flare' phase, there is a gradual increase in Extreme Ultraviolet (EUV/X-ray emission from the heated plasma where the flaring activity occurs. The 'impulsive' phase of the flare consists of a sudden acceleration of energetic charged particles through reconnection events, lasting only up to a few minutes, and can be observed in radio, microwave, X-ray and gamma-ray wavelengths. Following this, a 'decay' phase can be observed where the photon emission eventually plateaus back to some low-level intensity. Although these definitions are generally subjective, studying the morphology of flares can be important for shedding light into the underlying mechanisms and oscillations observed in the solar corona.

1.2.4 Coronal Loops and Arcades

Coronal loops are arguably the building blocks of the solar atmosphere because they exist in both quiet Sun and ARs (see the reviews by Benz 2008; Reale 2014). They are best observed in EUV images as vibrant, arched arcades of hot plasma that delineate the local magnetic field lines. However, they can also be observed in soft X-ray wavelengths and in Doppler images (Peres et al. 2000; Morton et al. 2019). Topologically, their footpoints are anchored into photospheric regions of opposite magnetic polarity found near the edges of ARs, giving rise to their dipolar shape. The typical lifetime of a loop system can range from
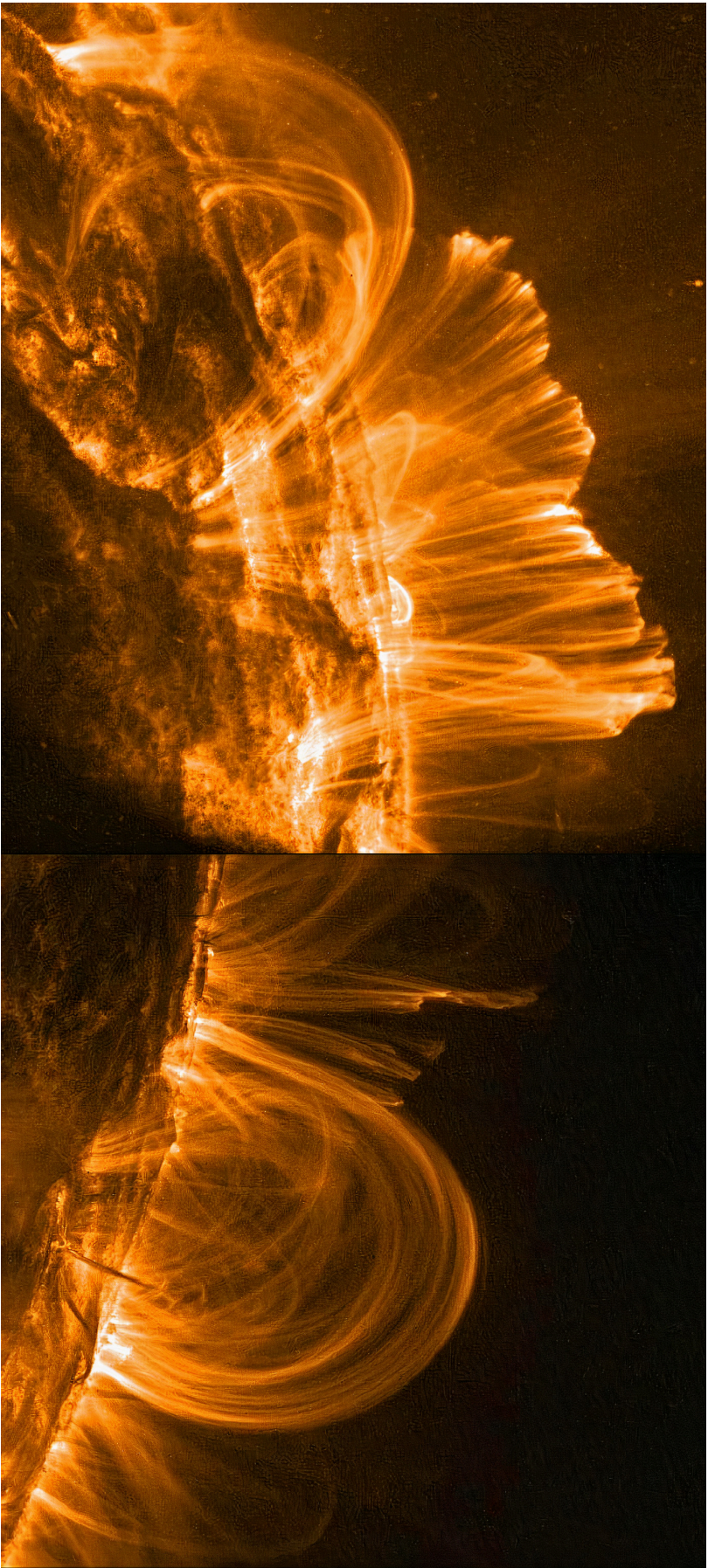
Figure 1.9: The elegant coronal loops of plasma traced by local magnetic field lines in the solar atmosphere. These structures are common examples of magnetically dominated ARs when viewed in coronal wavelengths. The bright locations along segments of the loops indicate regions of intense heating and the dark regions correspond to areas of relatively cool temperatures. Both images were observed by TRACE in the 171 Å waveband on November 6 1999. Image courtesy of LMSAL, TRACE and NASA science teams.

several hours to days (Antiochos et al. 2003; Warren et al. 2010, 2011). Since the 1970s, their conspicuous observational properties have spurred the development of coronal studies and have served as the focal point of unlocking the key to the dynamics, magnetic activity and heating of the Sun (e.g. Brueckner and Bartoe 1974; Kopp and Pneuman 1976; Levine and Withbroe 1977).

Coronal loop arcades are essentially manifestations of closed magnetic field configurations where cross-field thermal diffusion is strongly inhibited due to the dominant role of the magnetic field and strong ionisation levels (Aschwanden et al. 2002). Their luminosity observed in EUV images is primarily due to upflows of dense, evaporated plasma from impulsive heating events that stays trapped within individual field lines, which can be clearly viewed in Figure 1.9. However, the plasma confinement can become leaky for loops reaching altitudes greater than one solar radius since the thermal pressure takes over as the dominant force (Gary 2001; Aschwanden et al. 2002). Depending on the rate of energy input at the loop footpoints, which is expected to be spatially and temporally sporadic, coronal loops can coexist in a range of temperatures. Thus, studying coronal loops proffer the opportunity of investigating the fundamental problem of the heating of the solar atmosphere.

In the context of coronal heating studies, an important question to ask is whether an observed loop is multi-thermal. If a loop does not exist within a single (or narrow) temperature band, then it may suggest that the visible loop is contingent and consists of thinner strands below the detector's spatial resolution, which behave in unison. Due to the optically thin nature of coronal wavelengths, this should be expected in most cases, since what we define as a 'coronal loop' is probably just a preferentially bright segment of a larger magnetic arcade, which is illuminated by local heating processes. For instance, Schmelz et al. (2001) performed a simultaneous, multi-wavelength analysis of AR loops, using two independent detectors, and found that their temperature distributions are inconsistent with isothermal plasma along the loop length and line-of-sight. Schmelz et al. (2001) proposed that neither instrument observes a single, isolated loop, but rather unresolved bundles of loops below their detector's resolution.

The following next-generation instrument, namely the Transition Region and Coronal Explorer (TRACE, Handy et al. 1999), revealed the fine-structuring of coronal loops like never before (see Figure 1.9). The discovery of the strong inhomogeneity of the solar corona precipitated a tumult of observational studies, with the aim of solving the elusive coronal heating problem (see Bray et al. 1991, and references therein). Aschwanden and Nightingale (2005) reported on the first quantitative analysis (234 samples) of the multi-threaded structure of loops using TRACE, and concluded that majority (84%) are spatially-resolved, monolithic and isothermal structures. On the contrary, the work by Mulu-Moore et al. (2011) investigated the same AR studied by Aschwanden and Nightingale (2005) and found that the evolution of these loops are, in fact, inconsistent with a single cooling strand. Mulu-

Moore et al. (2011) suggested that such loops are both multi-stranded and multi-thermal, and that the majority of loops observed by TRACE are not spatially resolved. Clearly, despite progress in understanding the solar atmosphere, these basic physical properties of corona loops remain largely debated.

However, progress on the definitive resolved widths of coronal loops has been made. For instance, Aschwanden and Peter (2017) explored the distribution of coronal loop widths using simultaneous observations and Monte Carlo simulations to determine a diagnostic criterion and discriminate whether loops are resolved. Their analysis predicted a most-likely width value of ∼550km. An investigation by Williams et al. (2020a) into the faint emission loop structures using the recently launched High-Resolution Coronal Imager (Hi-C, Rachmeler et al. 2019) found evidence of low-emission loops beneath the capabilities of current instruments. Following this study, Williams et al. (2020b) reported evidence for multiple 'hidden' loop strands that may exist along the observational line-of-sight, shedding further light into the likely nature of coronal loops.

1.3 Standing Transverse Oscillations of Coronal Loops

1.3.1 Large Amplitude Oscillations

Prior to any imaging observations, it was theorised that coronal loops can act as waveguides and exhibit various types of oscillations. In July 1998, the EUV detector onboard TRACE recorded the first spatially-resolved motion of coronal loop oscillations (Aschwanden et al. 1999; Nakariakov et al. 1999; Wills-Davey and Thompson 1999). These loops were observed to sway back and forth in a direction perpendicular to the loop plane, immediately following a outburst of energy from a solar flare, before decaying and returning to an initial equilibrium. Aschwanden et al. (1999) interpreted these oscillations as standing (fundamental) modes and measured an average periodicity of 4.6 minutes, displacement amplitude of 4.1 Mm and decay time of about 19.7 minutes. These values are comparable to those independently reported by Nakariakov et al. (1999). Their displacement amplitudes are also typically observed to rapidly damp within only a few cycles before falling below the detector's spatial resolution (Aschwanden et al. 2002) (see Figure 1.10). Possible causes for the observed damping will be discussed in Section 1.4.3.

The majority of loop oscillations that have been observed possess a horizontal polar-isation (perpendicular to the loop plane), though scarce reports of vertically polarised oscillations (parallel to the loop plane) exist in the literature (e.g. Wang and Solanki 2004; Verwichte et al. 2006; Aschwanden 2011; White et al. 2012). In general, vertically polarised oscillations are rare because their excitation requires the driver to be located near the loop centre (Selwa et al. 2011). Aschwanden (2011) studied a rare event of vertically polarised
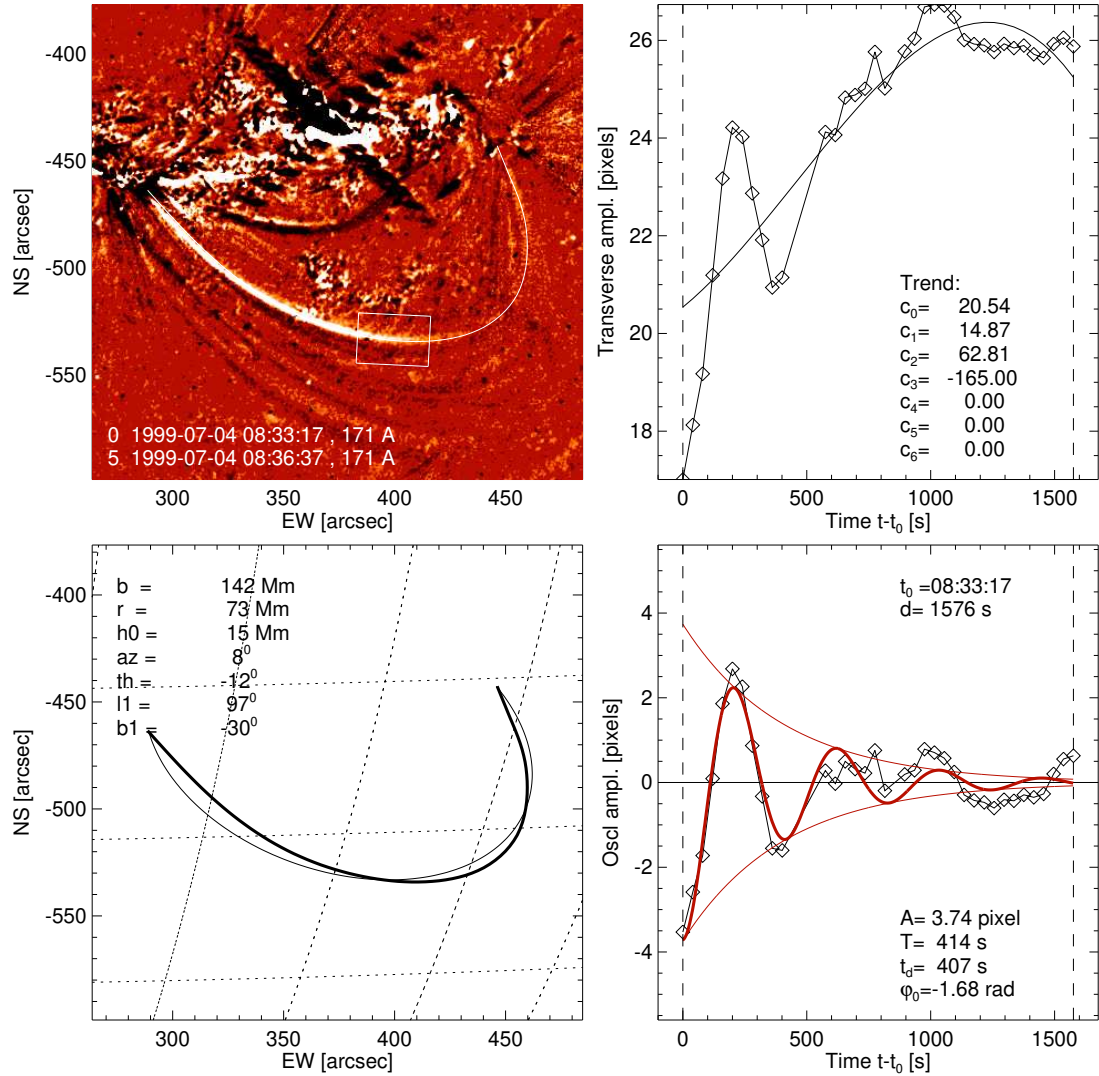
Figure 1.10: Analysis of flare-induced transverse loop oscillations observed by TRACE in the 171 Å waveband on 1999 July 4. The top left panel is a base difference (subtracted 3-minutes) image of the entire field of region containing the loop. The bright pixels show regions where oscillations exist. The top right panel shows a time series of the loop's positions of peak brightness. The bottom left panel shows the reconstructed loop by assuming a semi-circular model. The bottom right panel shows the detrended data (diamonds) and the solid red line is the expected damped sinusoid fit to the data. For this loop, the amplitude and period of oscillation are 3.74 pixels and 6.9 minutes, respectively. Figure from Aschwanden et al. (2002).

loop oscillations driven by a nearby CME and found that their cross-sectional behaviour was coupled with density perturbations, which could not be explained by the then-current theoretical models (see Section 1.4). Furthermore, if a driver perturbs the loops asymmetrically, we can also expect to detect higher-order modes or a combination of multiple frequency modes (Aschwanden et al. 2002). It is generally necessary to estimate the 3D geometry of

the loop for verification of such modes (Verwichte et al. 2004; Verwichte et al. 2006)

Although it is accepted that loops can be perturbed by nearby flares/CMEs, their precise physical roles in exciting oscillations are unknown. For instance, from the TRACE observations, Schrijver et al. (2002) suggested that transverse loop oscillations are likely to be driven rather than free oscillations. Following this, Aschwanden et al. (2002) suggested that the time-profiles of loop oscillations do not follow simple harmonic behaviour and may indicate the presence of complicated propagating waves. Though it is generally assumed that observations of loop oscillations are standing waves, it is often difficult to verify that they are not the response of a transient wave (e.g. Verwichte et al. 2004). A statistical study of 28 cases by Hudson and Warmuth (2004) showed that the timings of the majority of events (12) are consistent with the idea that loop oscillations result from the passage of a large-scale wave originating from the flaring epicentre. Uralov (2003) proposed that the observed oscillatory behaviour of loops are not oscillations, but are remnants of an oscillatory wake from a flare-generated blast wave. A more recent study by Zimovets and Nakariakov (2015) investigated transverse loop oscillations from 58 events spanning four years from 2010 to 2014. They found that 95% of events were excited by some lower coronal eruption/ejection that deviated the loops from an initial equilibrium. Those authors also reported that 91% of the events were associated with flaring activity. Clearly, these studies highlight the necessity of further investigating the underlying mechanisms of transverse coronal loop oscillations.

1.3.2   Small Amplitude Oscillations

Since the discovery of flare-induced loop oscillations, recent observational efforts have revealed transverse oscillations in the absence of any obvious source, namely, the small amplitude oscillations of coronal loops. These oscillations do not appear to exhibit a temporal decay and are often referred to as "decayless" oscillations (Anfinogentov et al. 2013, 2015; Nisticò et al. 2013). Anfinogentov et al. (2015) conducted a statistical analysis of 21 non-flaring ARs in the 171 Å bandpass of SDO/AIA in order to estimate the regularity of this phenomenon. The average amplitude in the loop displacement is estimated to be 0.17 Mm, with periods ranging from 1.5 to 10 minutes. The nature of the driver of these oscillations remains unknown and various models have been suggested. In contrast to the impulsively-generated, large amplitude regime, these oscillations are not connected to energetic sources and do not exhibit any significant decay (Anfinogentov et al. 2013, 2015). Their displacement amplitudes are an order of magnitude lower than that of the large amplitude (decaying) case and, in some cases, are observed to grow with time (Wang et al. 2012). Figure 1.11 shows typical examples of large (top panel) and small amplitude (bottom panel) loop oscillations. Nisticò et al. (2013) demonstrated that a loop can exhibit small amplitude oscillations with the same periodicity (within the observational error bars) both before and after any flaring activity. A statistical analysis by (Anfinogentov et al. 2015) investigated 21 ARs and found
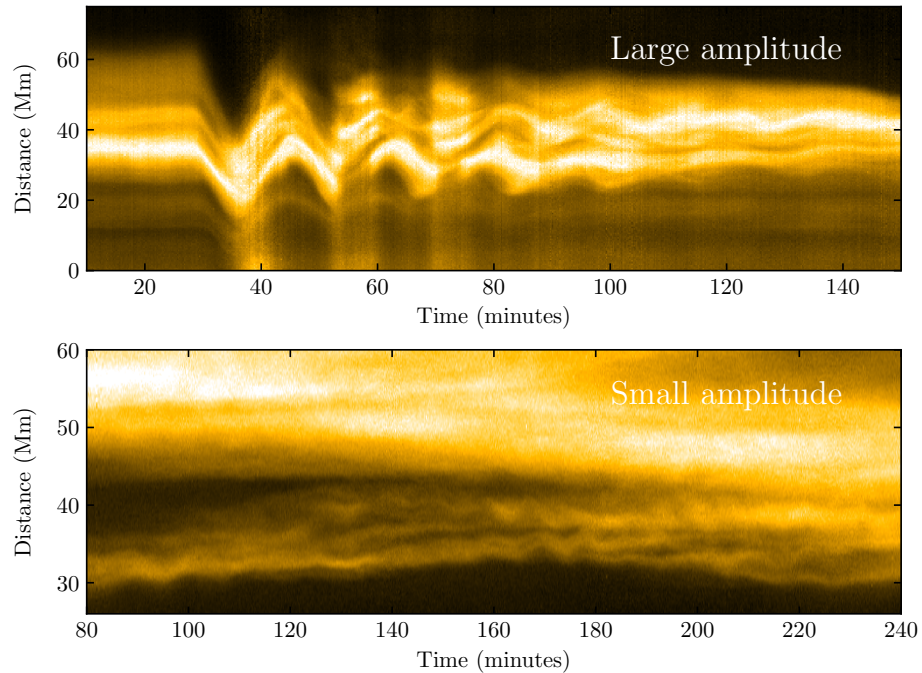
Figure 1.11: Examples of the two classes of transverse coronal loop oscillations. Top panel: Large amplitude (≈ 5 Mm) oscillations excited by a nearby flare on 2013 July 08. Bottom panel: Small amplitude (≈ 1 Mm) oscillations from a different event that persist without a significant amplitude decay. Both images are observed in the 171 Å waveband, corresponding to plasma temperatures of around 1 MK.

that small-amplitude oscillations are prevalent in almost all loop systems. As in the large amplitude case, the excitation mechanism is unknown, though it is suggested that wave leakage of p-modes can be ruled out (Nakariakov et al. 2016).

Studies of propagating Alfvénic waves in the corona have also received significant attention in recent times (e.g. Tomczyk and McIntosh 2009; Morton et al. 2015). These wave modes are found to be more common throughout the corona and are therefore strong candidates the heating of the solar atmosphere. Observations of persistent fluctuations, regularly observed in Doppler velocity, show waves propagating at Alfvénic speeds along the curved magnetic field lines of coronal loops. Similar to the decaying and decayless standing regime of transverse loop oscillations, their excitation mechanism for propagating waves remains unknown, though some studies have argued that p-modes can act as a possible source (e.g. Cally 2017; Morton et al. 2019).

From such observations of waves and oscillations, it is often desirable to compare the wave parameters to theoretical models, with the objective of estimating the local plasma properties. The next section will introduce the basic theory required to understand the oscillatory nature of these magnetic loops in the solar corona.

1.4 Theory of Ideal Magnetohydrodynamics

1.4.1 Basic Ideal MHD

MHD is a theoretical framework that governs the dynamics of electrically conducting fluids in the presence of magnetic fields. It is essentially a combination of James Clerk Maxwell's equations of electromagnetism (Maxwell 1865) and fluid mechanics, and is the mathematical underpinning of solar physics. This framework was first introduced by Nobel laureate Hannes Alfvén in an attempt to address the enigmatic coronal heating problem (Alfvén 1942). Alfvén (1942) was the first to propose the existence of an 'electromagnetic-hydrodynamic' wave, which could carry energy from the photosphere to the corona and solar wind, transferring heat between the two media. This magnetic wave, now coined the Alfvén wave, is a purely magnetic, transverse wave in which the magnetic field lines act as the only restoring force, analogous to waves on an elastic string. Arguably, the study of MHD waves in the solar corona is unique in two important ways: Firstly, it represents the only astrophysical laboratory in which we can spatially resolve the plasma structures of interest and, secondly, the Sun exhibits the most powerful and prolific plasma processes than any other terrestrial laboratory. General introductions to MHD with solar applications can be found in several textbooks (e.g. Goedbloed and Poedts 2004; Aschwanden 2004; Priest 2014).

In essence, MHD is a macroscopic, low-frequency and single-fluid theory of magnetised plasmas. In the context of solar physics, appropriate assumptions can be made, thereby reducing the complexity of the governing equations. For instance, the typical approach of studying the behaviour of waves and oscillations in the corona requires the plasma to be a perfect conductor and therefore non-ideal effects, such as resistivity, can be neglected. However, occasionally, extended models or even a kinetic theory approach may be required beyond the ideal MHD framework (e.g. Chen 2016). For the purposes of this thesis, we will only consider the theory of ideal MHD. This theory is applicable to the corona because the time scales at which plasmas advect is much larger than their diffusion.

The basic equations governing the dynamics of coronal plasmas can be described by the set of ideal MHD equations:

$$\frac{\partial \rho}{\partial t} + \nabla \cdot (\rho \mathbf{v}) = 0, \qquad \text{(Mass Contunity)} \tag{1.3}$$

$$\rho \frac{D\mathbf{v}}{Dt} = -\nabla P + (\mathbf{J} \times \mathbf{B}) + \mathbf{F}, \quad \text{(Momentum)} \tag{1.4}$$

$$\frac{\partial \mathbf{B}}{\partial t} = \nabla \times (\mathbf{v} \times \mathbf{B}), \quad \text{(Ideal Induction)} \tag{1.5}$$

$$\nabla \cdot \mathbf{B} = 0, \quad \text{(Solenoidal Constraint)} \tag{1.6}$$

$$\mathbf{E} = -\mathbf{v} \times \mathbf{B}, \quad \text{(Ideal Ohm's Law)} \tag{1.7}$$

$$\mathbf{J} = \nabla \times \mathbf{B}/\mu_0, \quad \text{(Ampère's Law)} \tag{1.8}$$

$$\frac{D}{Dt}\left(\frac{P}{\rho^\gamma}\right) = 0, \quad \text{(Adiabatic Energy)} \tag{1.9}$$

$$P = \frac{\rho k_B T}{m}. \quad \text{(Ideal Gas Law)} \tag{1.10}$$

Here, $\nabla \equiv (\frac{\partial}{\partial x_1}, \ldots, \frac{\partial}{\partial x_n})$ is the spatial derivative operator, ρ is the plasma density, $\mathbf{v}$ is the velocity, $D/Dt = \partial/\partial t + \mathbf{v} \cdot \nabla$ is the convective derivative, P is the thermal gas pressure, γ is the ratio of specific heats ($= 5/3$ for an ideal, monatomic gas with 3 degrees of freedom), $\mathbf{B}$ is the magnetic field, $\mathbf{E}$ is the electric field, k_B is the Boltzmann constant, m is the ion mass, T is the temperature, $\mathbf{J}$ is the current density, μ_0 is the permeability constant of free space and $\mathbf{F}$ represents other external forces. The most important property of ideal MID is Alfvén's frozen-in theorem (Alfvén 1942), which states that the magnetic field lines behave as if they move with the plasmas that are perfect conductors[5]. In other words, field lines that initially contain plasmas will always do so in ideal MHD.

The first of the equations of ideal MHD, namely the mass continuity in Equation (1.3), describes the conservation of the fluid mass within a closed system. The flow is said to be incompressible if and only if $\nabla \cdot \mathbf{v} = 0$ and the advection terms vanish in the convective derivative. The momentum equation is the second of the fluid equations used in the MHD framework and can be understood simply as Newton's second law of motion. In particular, from this equation it is clear to see that the coupling of electromagnetism and fluid mechanics introduces a magnetic (or Lorentz) force term that does not exist otherwise. To show this, we

---

[5] Mathematically, this is written as $\frac{d}{dt}\int_S \mathbf{B} \cdot \mathbf{n}\, dA = 0$ where S is a surface that contains a closed curve.

can consider a magneto-static case of the momentum equation with a stationary equilibrium, in the absence of time-dependence quantities, flows and external forces:

$$-\nabla P + \frac{1}{\mu_0}(\nabla \times \mathbf{B}) \times \mathbf{B} = \mathbf{0}. \tag{1.11}$$

Equation (1.11) can be further simplified using a basic vector identity[6] to give the following:

$$-\nabla P \underbrace{-\nabla\left(\frac{|\mathbf{B}|^2}{2\mu_0}\right)}_{\text{magnetic pressure gradient}} + \underbrace{\left(\frac{(\mathbf{B} \cdot \nabla)\mathbf{B}}{\mu_0}\right)}_{\text{magnetic tension}} = \mathbf{0}. \tag{1.12}$$

Hence, the presence of the Lorentz force results in a sum of two magnetic but distinct components. The first term represents the magnetic pressure gradient, which acts perpendicular to the magnetic field lines and resists compression. The second term is the magnetic tension, which exists due to the presence of curved field lines. The purpose of magnetic tension is essentially to straighten the field lines towards an initial equilibrium. As we will see, both of these forces are paramount for the study of coronal loop oscillations.

It is also instructive to explore the relative strengths of the two pressure gradients in the context of solar physics. For simplicity, we can consider a straight, uniform and static magnetic field configuration, which results in zero magnetic tension. The non-dimensional measure of which pressure gradient dominates a region is given by the (plasma) β parameter:

$$\beta \equiv \frac{\text{gas pressure}}{\text{magnetic pressure}},$$
$$= \frac{P}{|\mathbf{B}|^2/2\mu_0}. \tag{1.13}$$

As the focus of this thesis is on coronal ARs, we can anticipate by simple order of magnitude estimations that $\beta \ll 1$ within these regions. In other words, magnetic fields are expected to dominate the plasma dynamics in the solar atmosphere and in particular within coronal loop arcades and thermal pressure effects may be safely neglected.

In the case of a uniform field, Equation (1.12) can be rewritten as the gradient of total pressure: $-\nabla(P + |\mathbf{B}|^2/2\mu_0) = 0$. In other words, any variation in magnetic pressure must be balanced by the gas pressure and, as a result, uniform field configurations must satisfy total pressure equilibrium:

$$P_i + \frac{|\mathbf{B}_i|^2}{2\mu_0} = P_e + \frac{|\mathbf{B}_e|^2}{2\mu_0}, \tag{1.14}$$

---

[6] $\nabla(\mathbf{a} \cdot \mathbf{b}) = (\mathbf{a} \cdot \nabla)\mathbf{b} + (\mathbf{b} \cdot \nabla)\mathbf{a} + \mathbf{a} \times (\nabla \times \mathbf{b}) + \mathbf{b} \times (\nabla \times \mathbf{a})$.

where the subscripts i and e refer to the interior and exterior of a specified region, respectively. This basic magneto-static model of a slab geometry can be exploited to deduce why sunspots appear darker than their surroundings within photospheric observations (see Aschwanden 2004, Chapter 6, p. 248).

The main message of this section is that the plasma dynamics are strongly coupled to the magnetic field in the framework of ideal MHD (see the above discussion on the frozen-in theorem). As previously discussed, due to the relatively weak magnetic field strengths in the corona, spectroscopic measurements remain insufficient to probe magnetically dominated regions. Yet, observations of the Sun have revealed irrefutable evidence that magnetic waves and oscillations exist throughout the entire solar atmosphere. Naturally, then, one can ask whether it is possible to combine the framework of MHD and observations to infer about the inaccessible properties of the solar corona. The next two subsections introduce the mathematical formulations of MHD waves in uniform and non-uniform plasmas, which are commonly used to test the aforementioned hypothesis.

1.4.2 MHD Waves in Uniform Plasmas

Waves and oscillations are ubiquitous in nature and pervade our entire universe. From the vibrations of individual atomic nuclei to the gravitational waves emitted from coalescing black holes, it is well known that waves are primary candidates through which energy can be transferred between bodies. For instance, electromagnetic waves are a type of transverse waves, that is, the electric and magnetic fields oscillate perpendicular to the direction of the wave's propagation, and can propagate naturally within a vacuum, gas, liquid and even a solid. Longitudinal (acoustic) disturbances, on the other hand, propagate only in the direction parallel to the wave in the form of compressions or rarefactions. Further types of waves can be introduced by introducing a magnetic field (e.g. Alfvén 1942). As we have already described, the Sun is covered by magnetic fields and, consequently, those mentioned above and various other types of waves and disturbances are expected to permeate throughout the solar atmosphere.

In order to study MHD wave propagation, a standard technique is to examine the case of linear and small perturbations to the plasma parameters introduced above. Mathematically, we consider the following perturbed quantities:

$$\rho(\mathbf{r}, t) = \rho_0 + \rho_1(\mathbf{r}, t), \quad \mathbf{v}(\mathbf{r}, t) = \mathbf{v}_0 + \mathbf{v}_1(\mathbf{r}, t), \quad P(\mathbf{r}, t) = P_0 + P_1(\mathbf{r}, t), \quad \mathbf{B}(\mathbf{r}, t) = \mathbf{B}_0 + \mathbf{B}_1(\mathbf{r}, t).$$

Here, the subscripts 0 and 1 denote the background and perturbed quantities, respectively. It is assumed that the plasma exhibits no background flow (i.e. $\mathbf{v}_0 = \mathbf{0}$) and that the magnitude of all perturbed quantities are much less than the background (i.e. $|\mathbf{B}_1| \ll |\mathbf{B}_0|$).

The equilibrium magnetic field is also uniform and is oriented along the z-axis of a Cartesian coordinate system, $\mathbf{B} = B_0\hat{\mathbf{z}}$.

It is instructive to firstly introduce the idealised case of an unbounded and uniform plasma. We begin by writing the perturbed quantities as $\propto \exp\left(i(\mathbf{k} \cdot \mathbf{r} - \omega t)\right)$, where $\mathbf{k} = (k_x, k_y, k_z)$ is the wavevector and ω is the angular frequency, such that the temporal derivatives yield terms of $\partial/\partial t \mapsto -i\omega$ and the spatial derivatives yield $\nabla \mapsto i\mathbf{k}$. The aim of this analysis is to find the dispersion relation, which expresses ω as a function of $\mathbf{k}$, or in other words, the phase speed of the waves. Note, however, the only property which cannot be analysed from this approach is the wave amplitude, which requires non-linear studies (e.g. Terradas and Ofman 2004). A complete mathematical derivation can be found in standard textbooks (Aschwanden 2004; Priest 2014).

Following this simple procedure, we obtain the dispersion relations for MHD waves in uniform plasmas:

$$\underbrace{\left[\omega^2 - k^2 v_A^2 \cos^2(\theta)\right]}_{\text{Alfvén wave}} \underbrace{\left[\omega^4 - k^2\left(c_s^2 + v_A^2\right)\omega^2 + k^4 c_s^2 v_A^2 \cos^2(\theta)\right]}_{\text{Fast and slow magnetoacoustic waves}} = 0, \tag{1.15}$$

where θ is the angle defined by the wavevector and equilibrium magnetic field, $c_s = \sqrt{(\gamma P/\rho)}$ is the acoustic sound speed. The first and most important solution of Equation (1.15) is the (shear) Alfvén wave (see Alfvén 1942), which propagates at the Alfvén (phase) speed $v_A = |\mathbf{B}|/\sqrt{\mu_0\rho}$. The Alfvén mode is a purely magnetic, transverse wave, which propagates with a phase (Alfvén) speed v_A along the magnetic field line without perturbing the plasma density or pressure and, thus, is incompressible. Hence, magnetic tension acts as the only restoring force. Furthermore, the second term is quadratic in ω^2 and as a result its solution yields two distinct dispersion relations corresponding to two unique waves; the fast and slow magnetoacoustic waves. These two modes are both magnetic and acoustic in nature and therefore magnetic pressure and gas pressure play an important role. The positive root of ω^2 corresponds to the case where magnetic pressure and gas pressure act in concert (fast wave), whereas the negative root results in both forces acting in opposition (slow wave). From Equation (1.15), it can also be inferred that the fast mode is the only wave that can propagate transverse to the magnetic field.

Thus, within a homogeneous and unbounded plasma, each MHD wave can be decoupled and easily identified. However, in reality, no such wave will exist in isolation within solar plasmas. One important piece of observational evidence is that the solar corona, including coronal loops, is highly inhomogeneous. Therefore, it is natural to extend this framework and seek for a model that can better describe the oscillatory phenomena that are routinely observed. The next section will introduce the basic theory of transverse coronal loop oscillations as the natural modes of an inhomogeneous, magnetic, cylindrical waveguide.

1.4.3 Eigenmodes of a Non-uniform Magnetic Cylinder and their role in Coronal Seismology

The idea of combining MHD wave theory and observations to estimate the properties of the solar corona was not proposed until the 1970s. This was first introduced by Uchida (1970), who theoretically investigated the behaviour of magnetic waves, suggested that it may be possible to acquire 'a new means of obtaining information about the magnetic field in the corona which is inaccessible by conventional methods of astronomical magnetic field measurements'. Independent of Uchida (1970), Roberts et al. (1984) exploited waves and oscillations produced by a magnetic flux tube as demonstrated by Edwin and Roberts (1983), and proposed that a combination of theory and observations may provide 'a valuable diagnostic tool for in situ conditions in the corona'. These pioneering studies gave birth to the field of coronal seismology (see the reviews by Roberts 2000; Nakariakov and Verwichte 2005; De Moortel and Nakariakov 2012)

In many ways, the field of coronal seismology has natural similarities to helioseismology (see Section 1.4). However, there are also stark contrasts between the two disciplines. For instance, helioseismology builds on the propagation of acoustic waves within a dense and homogeneous medium, whereas coronal MHD seismology relies on the ability of distinguishing, in the best of cases, between three MHD waves in a homogeneous medium. As we shall see, the non-uniformity of plasmas introduces even more types of magnetic waves and their properties are strongly dependant on the geometry of the waveguide.

The purpose of this subsection is to provide a basic introduction to the well-established mathematical formalism of coronal loop oscillations commonly used in seismic studies, as developed by the seminal works of Edwin and Roberts (1983), Roberts et al. (1984) and Spruit (1982). The theoretical model begins by describing an equilibrium state in the form of a magnetic cylinder of radius, r_0 and length L. In this state, all background quantities are constant across the flux tube. The magnetic field is also constant ($\mathbf{B} = B_0\hat{\mathbf{z}}$) and is oriented parallel to the z-axis of the cylinder with respect to a cylindrical coordinate system, (r, ϕ, z). The plasma quantities with subscripts i and e denote the interior and exterior of the waveguide, respectively. An illustration of this model is shown in Figure 1.12. Moreover, as we have already demonstrated that coronal ARs are magnetically dominated, we neglect gas pressure effects and consider a zero-β environment (this is also known as the cold plasma approximation e.g. Chen (2016)). Reviews of MHD wave propagation in non-uniform media can be found in Nakariakov and Verwichte (2005) and Ruderman and Erdélyi (2009).

We now proceed in a similar manner to the previous subsection by considering a plane wave ansatz in the ideal MHD equations (Equations 1.3 – 1.6), and introducing the plasma displacement vector, $\boldsymbol{\xi}$, as $\boldsymbol{v}_1 \equiv \partial\boldsymbol{\xi}/\partial t$. Firstly, the components of the Induction equation (Equation (1.5)) can be written as:
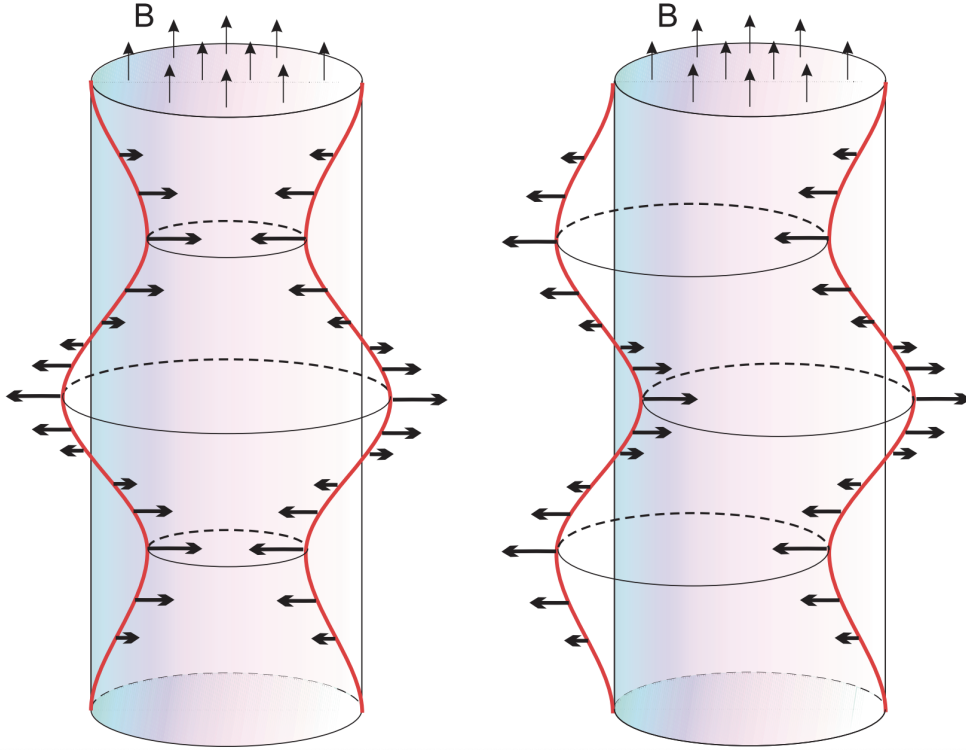
Figure 1.12: An illustration of the two main MHD wave modes of a cylindrical flux tube. The left image shows the $m = 0$ (sausage) mode and is characterised by an axisymmetric, periodic 'breathing in and out' of the wave guide, producing a compression in the pressure and magnetic field. The right panel shows the $m = 1$ mode, which is the only wave that causes a non-axisymmetric, transverse displacement of the entire waveguide. This mode, in contrast to the sausage mode, does not alter the tube's cross-section. Here, the red lines show the perturbed geometry of the tube and the thick black arrows represent the direction of the plasma displacement vector, $\boldsymbol{\xi}$. The thin black arrows overlaid on the top of the tube convey the direction of the background magnetic field, which is taken parallel to the axis of the tube, i.e. $\mathbf{B} = B_0 \hat{\mathbf{z}}$. Image from Morton et al. (2012).

$$B_{1r} = B_0 \frac{\partial \xi_r}{\partial z}, \tag{1.16}$$

$$B_{1\phi} = B_0 \frac{\partial \xi_\phi}{\partial z}, \tag{1.17}$$

$$P = -\frac{B_0^2}{\mu_0 r} \left(\frac{\partial (r \xi_r)}{\partial r} + \frac{\partial \xi_\phi}{\partial \phi} \right). \tag{1.18}$$

Similarly, the Momentum equation (Equation 1.4) can be rewritten as,

$$\rho_0 \frac{\partial^2 \boldsymbol{\xi}}{\partial t^2} = \frac{1}{\mu_0} (\nabla \times \boldsymbol{B}_1) \times \boldsymbol{B}_0, \tag{1.19}$$

where $\boldsymbol{B}_1 = \nabla \times (\boldsymbol{\xi} \times \boldsymbol{B}_0)$ from Equation (1.5). This can now be written as a system of wave equations in component form:

$$\frac{\partial^2 \xi_r}{\partial t^2} - v_A^2 \frac{\partial^2 \xi_r}{\partial z^2} = -\frac{1}{\rho_0} \frac{\partial P}{\partial r}, \tag{1.20}$$

$$\frac{\partial^2 \xi_\phi}{\partial t^2} - v_A^2 \frac{\partial^2 \xi_\phi}{\partial z^2} = -\frac{iP}{r\rho_0}, \tag{1.21}$$

$$\frac{\partial^2 \xi_z}{\partial t^2} = 0, \tag{1.22}$$

where we have introduced $P = B_0 B_{1z}/\mu_0$ as a magnetic pressure due to the field perturbation (see Ruderman and Erdélyi 2009).

Next, all variables are Fourier decomposed proportional to $\exp(i(-\omega t + m\phi + kz))$ where m is an integer ($m = 0, 1, 2, \dots$) that describes the azimuthal behaviour of the oscillating flux tube. Modes with $m = 0$ are termed sausage waves, which causes an axisymmetric perturbation to the waveguide. There also exists torsional Alfvén waves that similarly do not perturb the boundary. The $m = 1$ mode produces a displacement of axis of the plasma structure and modes with $m \geqslant 2$ are called fluting waves. For the purposes of this thesis, we will only examine the behaviour of the $m = 1$ azimuthal mode, or commonly called a 'kink' wave, which is the only mode that causes a non-axisymmetric, transverse displacement of the entire waveguide as viewed in observations (see Figure 1.12). Hence, the above equations are reduced to the following forms:

$$\left(\omega^2 - k^2 v_A^2\right) \xi_r = \frac{1}{\rho_0} \frac{dP}{dr}, \tag{1.23}$$

$$\left(\omega^2 - k^2 v_A^2\right) \xi_\phi = \frac{iP}{r\rho_0}, \tag{1.24}$$

$$-\omega^2 \xi_z = 0, \tag{1.25}$$

$$B_{1r} = iB_0 k \xi_r, \tag{1.26}$$

$$B_{1\phi} = iB_0 k \xi_\phi, \tag{1.27}$$

$$P = -\frac{B_0^2}{\mu_0 r} \left(\frac{d(r\xi_r)}{dr} + i\xi_\phi\right). \tag{1.28}$$

Finally, Equations (1.23) - (1.28) can be combined to yield the following governing equation,

$$\frac{d^2P}{dr^2} + \frac{1}{r}\frac{dP}{dr} + \left(\kappa_\alpha^2 - \frac{1}{r^2}\right)P = 0, \tag{1.29}$$

where $\kappa_\alpha^2(\omega) = \omega^2/v_{A\alpha}^2 - k^2$ and $\alpha = i, e$. Equation (1.29) is a Bessel equation, which describes the behaviour of MHD wave propagation within a cylindrical flux tube. This equation can be solved either numerically or analytically in order to obtain the dispersion relations. Here, we derive the solution of Equation (1.29) analytically by imposing the standard boundary conditions. The first of these is that the total pressure perturbation must be continuous inside and outside the waveguide (Equation 1.14). This must also be true for the radial component of the plasma displacement, which acts perpendicular to the boundary. Lastly, for physical solutions, the wavefield parameters must be regular at $r = 0$ and vanish as $r \to \infty$. In other words, we expect the waves to decay with radius outside the tube and so the condition $\kappa_e^2 > 0$ must be fulfilled. On the other hand, κ_i^2 can generally have any sign and so waves within the tube can be either evanescent or oscillatory, termed surface and body modes, respectively (see Roberts 1981). For the purposes of this thesis, we are interested in wave propagation inside the waveguide and so we may take $\kappa_i^2 < 0$. Thus, we obtain two linearly independent eigenfunctions written as,

$$P(r) = \begin{cases} C_i J_1\left(\kappa_i r_0\right) & r < r_0, \\ C_e K_1\left(\kappa_e r_0\right) & r \geq r_0, \end{cases} \tag{1.30}$$

where C_i and C_e are constants, J_1 is the Bessel function of the first kind and K_1 is the modified Bessel function of the second kind. Both Bessel functions are of order 1. An algebraic expression for both C_i and C_e can be obtained by imposing pressure continuity at $r = r_0$. Now, all other eigenfunctions can be obtained using Equations (1.23) - (1.25). Applying the boundary conditions to the solutions of the Bessel equation leads to the dispersion relation for magnetoacoustic waves in a cylindrical waveguide (Edwin and Roberts 1983; Roberts et al. 1984):

$$\frac{\rho_i\left(\omega^2 - v_{Ai}^2 k^2\right)}{\kappa_i}\frac{J_1(\kappa_i r_0)}{J_1'(\kappa_i r_0)} - \frac{\rho_e\left(\omega^2 - v_{Ae}^2 k^2\right)}{\kappa_e}\frac{K_1(\kappa_e r_0)}{K_1'(\kappa_e r_0)} = 0, \tag{1.31}$$

where the prime denotes a derivative with respect to the argument of the Bessel function. The existence and behaviour of wave modes described by these transcendental equations are determined by the physical equilibrium parameters. As we are interested in wave propagation under coronal conditions, then it follows from Equation (1.14) that a loop can trap MHD waves if the external Alfvén speed is greater than the internal (i.e. $v_{Ai} < v_{Ae}$ and $\rho_i > \rho_e$).

The top panel of Figure 1.13 shows a typical dispersion diagram of magnetoacoustic waves within an inhomogeneous coronal loop. The wave solutions presented here are a specific and simpler case (zero-β, $m = 1$ mode) of the generalised dispersion relations studied in previous works (e.g. Edwin and Roberts 1983; Roberts et al. 1984; Ruderman and Roberts
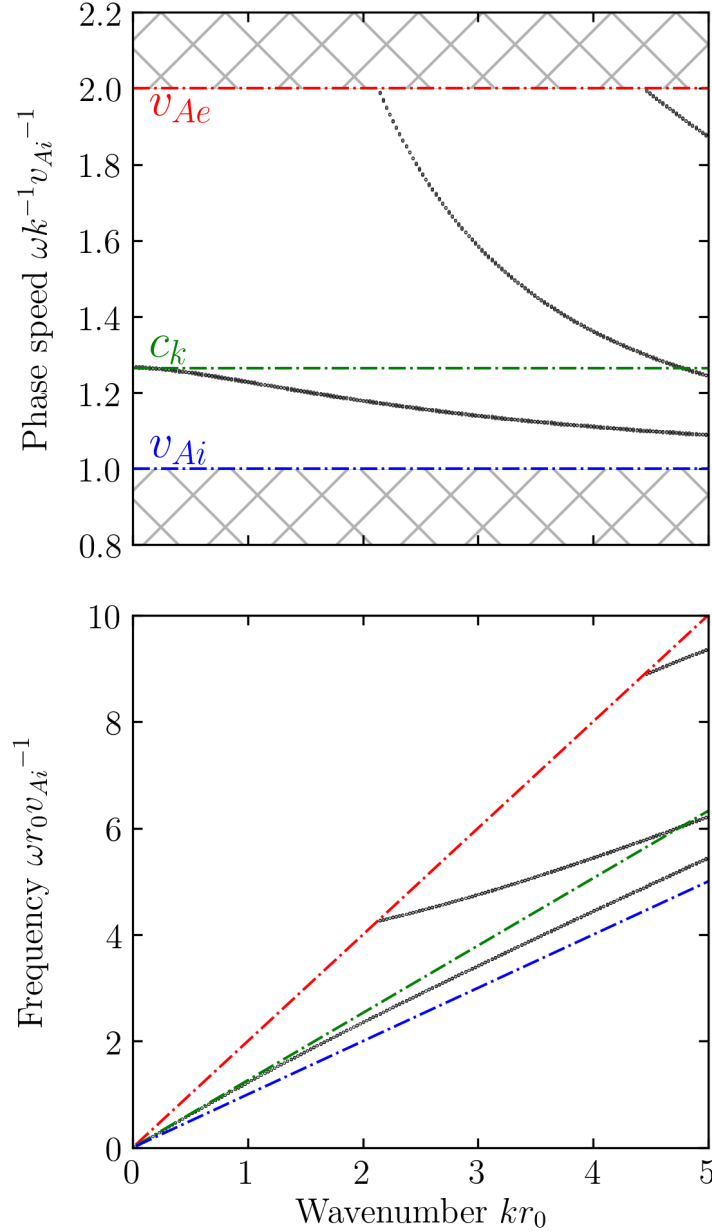
Figure 1.13: Dispersion diagram for fast MHD waves trapped within an isolated waveguide under coronal conditions ($B_i = B_e$, $\rho_i/\rho_e = 3$). Top panel: Wave phase speed normalised with respect to the internal Alfvén speed as a function of dimensionless wavenumber. The hatched lines indicate regions where waves are evanescent and hence no real solution exists. Solutions to the dispersion relation Equation (1.31) are discrete and exist only within the range $v_{Ai} < v < v_{Ae}$. Bottom panel: Corresponding frequency-wavenumber diagram. The red and blue lines indicate the external and internal Alfvén speeds, respectively. The green line indicates the theoretical kink mode.

2006). It is clear from Figure 1.13 that this waveguide only exhibits body modes under coronal conditions. In analogy to the uniform case, these modes are often classed as 'fast' MHD waves because they exist in the range $v_{Ai} < v < v_{Ae}$. We also include the corresponding

wavenumber-frequency diagram in the bottom panel of Figure 1.13, as this is often overlooked in theoretical studies. Evidently, both panels in Figure 1.13 demonstrate the dispersive nature of fast MHD waves and their associated cut-off frequencies below which waves cannot propagate (hatched lines). It is also clear from both panels that there is only one eigenmode solution that exists for all wavenumbers. Some authors also refer to this as the 'global fundamental mode' (see Ruderman and Erdélyi 2009). Furthermore, it is also clear that this mode exhibits a comparatively stronger dispersion and does not have any nodes in the longitudinal direction. In the long wavelength limit ($kr_0 \ll 1$), the phase speed of this wave is defined as the kink speed, c_k, where:

$$c_k = \left(\frac{2}{1 + \rho_e/\rho_i} \right)^{1/2} v_{Ai}. \tag{1.32}$$

The kink speed is essentially an averaged Alfvén speed within the two inhomogeneous media and has been extensively studied due to its seismological capabilities (e.g. Spruit 1981; Roberts 1981; Roberts et al. 1984). It must also be noted that, due to the symmetrical geometry of the straight tube model, there is no preferred direction of the kink mode oscillations and so the wave solutions are degenerate. This is a strong dissimilarity of the distinct frequencies of the horizontal and vertical polarised oscillations, which are commonly observed (refer to Section 1.3) and highlights the necessity for consulting multi-dimensional geometries for a more accurate interpretation and is discussed below.

It is also commonly assumed that the loop footpoints are line-tied into the dense lower atmosphere, such that only standing waves exist as $k = n\pi/L$, where n is an integer that describes the mode of oscillation: $n = 1$ is the fundamental mode, $n = 2$ is the first overtone and so on. In tandem with observational data, this approach is then used to estimate the properties of the loop by comparing the observed loop's frequency of oscillation with the theoretical kink mode (see Aschwanden et al. 1999; Nakariakov et al. 1999). The primary objective of Aschwanden et al. (1999) and Nakariakov et al. (1999) was to demonstrate the utility of coronal seismology by estimating the physical properties of the loop, as initially suggested by Roberts et al. (1984). Based on the same observations, and assuming the fundamental kink mode, Nakariakov and Ofman (2001) also estimated a magnetic field strength of $|\mathbf{B}| = 13 \pm 9$ G. Note, the field strengths of active region loops estimated through seismology have now been shown to be considerably lower (around 30 times) than those estimated from spectropolarimetry analyses (Kuridze et al. 2019).

In cases where higher order modes can be observed, Díaz et al. (2004) initially suggested that the longitudinal structuring may be analysed in terms of the period ratio between the fundamental and first overtone. Since then, several theoretical and observational studies have focused on obtaining information on the longitudinal structuring of a loop, such as the plasma density (see Andries et al. 2009). For example, Andries et al. (2005) suggested

any wave that exhibits dispersion, such as those arising naturally in the magnetic flux tube due its finite cross-section, then the period ratio contains information about the plasma structuring. Verwichte et al. (2004) investigated the oscillatory behaviour of a post-flare loop arcade using TRACE and reported the presence of a loop's fundamental and first overtone. Using the frequencies reported by Verwichte et al. (2004) and the magnetic cylinder model, Van Doorsselaere et al. (2007) estimated a coronal density scale height of 109 Mm. Verth et al. (2007) demonstrated that density stratification induces the anti-nodes of a loop's first overtone to shift towards the loop footpoints.

Additionally, the strong attenuation of loop oscillations that is commonly observed (see the top panel of Figure 1.11) has been explained using several mechanisms, such as phase mixing (Ofman and Aschwanden 2002), wave leakage (Smith et al. 1997; Brady and Arber 2005), resonant absorption (Goossens et al. 2002; Ruderman and Roberts 2002; Hindman and Jain 2018), the wake of a travelling disturbance (Uralov 2003; Terradas et al. 2005) and by a wave interference effect (Hindman and Jain 2014). Over the years, resonant absorption has received significantly more attention for the cause of wave damping in coronal loops. Resonant absorption is essentially a mode conversion process whereby energy is transferred from global transverse waves to local Alfvénic waves (Hindman and Jain 2018). Mathematically, this conversion arises due to a singularity where the two aforementioned modes share the same frequency within the governing MHD equations. Recently, Hindman and Jain (2015, 2018) demonstrated that fast MHD waves can be fully trapped by the magnetic field in an arcade and wave leakage is not necessarily an essential process for resonant absorption. Separately, the assumptions behind ideal MHD has led some studies to suggest that resonant absorption is merely a mathematical artefact, as it is mutually inconsistent with a kinetic description of plasmas (Bellan 1994, 1996). Nevertheless, ideal MHD remains a consistently used framework in the modelling of coronal loop oscillations.

However, the basic cylinder model, which has served as the theoretical paradigm for seismic studies, has recently come under scrutiny by some authors. For instance, Goossens et al. (2009) investigated the nature of the $m = 1$ mode and demonstrated its existence in three widely different cases: a compressible pressure-less plasma, an incompressible plasma and a compressible plasma that emits MHD radiation. According to Goossens et al. (2009), classifying the kink mode as 'fast' is incorrect, as fast waves are wholly absent in incompressible plasmas, or in other words, a pressure gradient does not exist across the plasma and so magnetic tension is the only restoring force. Goossens et al. (2009) further proposed that, due to the coupled nature of MHD modes in non-uniform plasmas, a more suitable description would be the term 'Alfvénic'. In fact, the mixed behaviour of MHD waves in a cylindrical waveguide can simply be deduced from the bottom panel of Figure 1.13 where we show the frequency as a function of wavenumber. Although the internal (blue) and external (red) Alfvén modes are not exact solutions to Equation (1.31), one can simply infer from
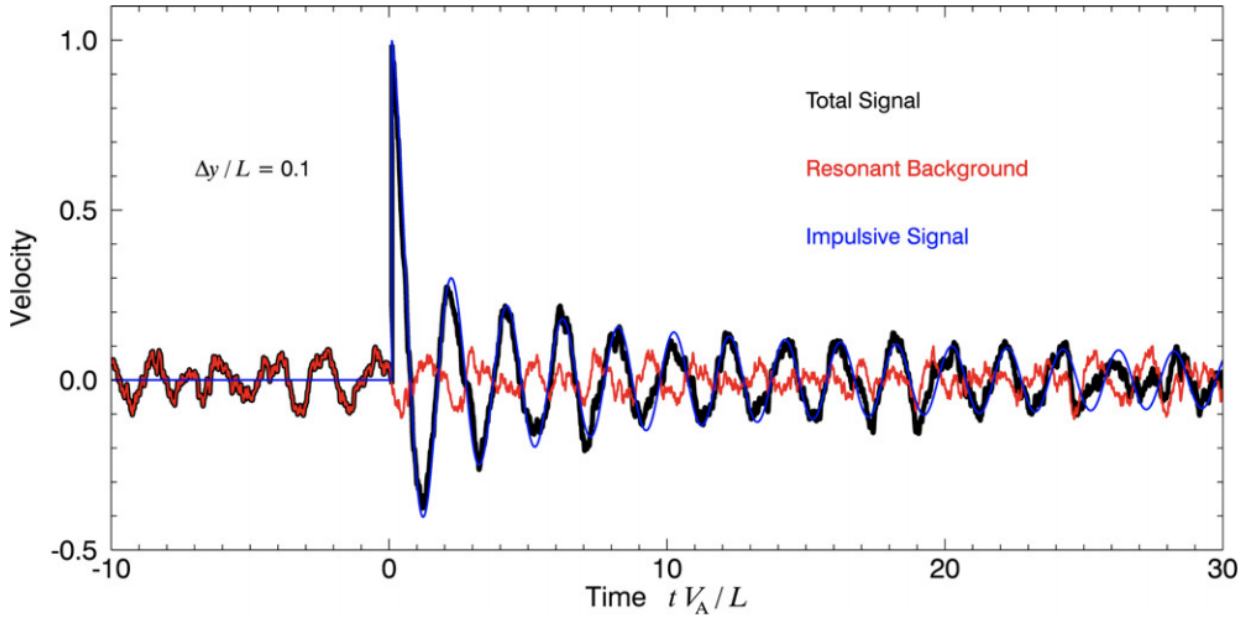
Figure 1.14: Example time series of a 2D coronal loop wave cavity excited by two fast wave sources: a broadband driver that generates ambient background oscillations and an impulsive source that induces a sudden pulse followed by wave interferences throughout the arcade. The red lines show signals from the ambient background driver excited by a white source. The blue curve corresponds to the impulsive driver (e.g. a flare) with an observational point located near the driver. The resultant waveform shown in black is then a superposition of the background and the impulsive signals. The dominant frequency excited by the background source corresponds to the eigenmode of the 2D arcade with waves propagating parallel to the magnetic field. Image from Hindman and Jain (2014).

Figure 1.13 that all three modes essentially tend to a similar frequency of oscillation in the long wavelength limit.

More recently, several studies have even called into question the validity of the 1D model for the use of seismic inferences. For instance, Jain and Hindman (2012) considered a typical flux tube model and found that the direct sensitivity of its eigenmodes to density is weak and, ultimately, loops with the same kink speed but different densities are seismically indistinguishable. Hindman and Jain (2014) suggested that the waveguide of a visible loop may be compromised of the entire arcade that continuously interact with their surroundings and the wave cavity is likely to be multi-dimensional. An example time series of this wave cavity is shown in Figure 1.14. Hindman and Jain (2015) developed a 3D model of coronal loop oscillations and showed that magnetic arcades can trap MHD fast waves. Within the 3D model of Hindman and Jain (2015), it was shown that both magnetic pressure and tension act as restoring forces, as opposed to the standard 1D model wherein magnetic tension is the primary force. Moreover, since both forces are present, the eigenmodes of the arcade evince oscillations from waves propagating both parallel and transverse to the magnetic

field. It is no doubt that these studies have been highly promising for our understanding of the true nature of coronal loop oscillations detected from observations. An immediate question that arises from these studies is the following: how reliable is this basic model for interpreting all observations of loop oscillations for seismic inferences? A recent study by Hindman and Jain (2021) attempted to answer this question by demonstrating that this simple model neglects the effects of the surrounding coronal plasma, and often the arcade resonances can masquerade as a single loop resonance. In what we have introduced so far, we now understand that coronal loops are far from static, isolated, monolithic structures. Their observed behaviour is, in fact, significantly more complicated. As we will see, the identification of wave modes from coronal loop oscillations can be non-trivial.

1.5 Instrumentation

1.5.1 Geostationary Operational Environment Satellites

The Geostationary Operational Environment Satellites (GOES), operated and archived by the National Oceanic and Atmospheric Administration (NOAA), are a series of geostationary satellites that provide time series of soft X-ray fluxes from the Sun, in addition to its meteorological observations of the Earth. Their trajectories are designed in such a way to ensure there are continuous uninterrupted X-ray measurements. Since the launch of the first GOES satellite (GOES-1) on 16 October 1974 the spacecraft series has progressed up to GOES-17, which was launched on 17 March 2018. The advancement of these spacecrafts has also provided additional imaging capabilities for solar observations, especially for the detection of solar flares. The GOES 12-15 spacecrafts, which most are decommissioned now, had soft X-ray imaging capability and GOES 16-17 currently have EUV capability. Further technical details of the recent GOES solar instruments can be found in Lemen et al. (2004), Hill et al. (2005), Pizzo et al. (2005), Väänänen et al. (2009), Evans et al. (2010) and Neupert (2011).

The detected X-ray flux arise from distinct two wavelength bands of 0.5-4 Å and 1-8 Å, which are extensively used for the classification of solar flares. The observed X-ray fluxes are characterised logarithmically and are labelled with the letters A, B, C, M and X, denoting an order of magnitude increase from $10^{-8} - 10^{-4}$ W m^{-2}. Each class can also be sub-divided to include an additional digit used to differentiate between the relative flaring strength of the same class (e.g. an X3.1 class flare has an flux of 3.1×10^{-4} W m^{-2}). A summary of the flare classifications is shown in Table 1.1.

Table 1.1: Solar flare classifications based on the GOES X-ray flux detected in the wavelength band 1-8 Å. These are categorised in increasing order, where the starting class, A, denotes the weakest and X the strongest flaring magnitude.

Class	Flux [$\mathrm{W\,m^{-2}}$]
A	$< 10^{-7}$
B	$\geq 10^{-7} < 10^{-6}$
C	$\geq 10^{-6} < 10^{-5}$
M	$\geq 10^{-5} < 10^{-4}$
X	$> 10^{-4}$

1.5.2 Solar Dynamics Observatory/Atmospheric Imaging Assembly

NASA's Solar Dynamics Observatory (SDO) is, to date, one of the most pre-eminent space-borne telescopes (Pesnell et al. 2012). The capabilities of SDO surpasses that of its predecessors due to its ability of observing 'all the Sun, all the time.' SDO's major scientific goals were to provide the first insight into the interconnectivity of the Sun-Earth system, and with the hope of developing the ability of predicting conditions within the interplanetary medium. Launched on 11 February 2010, SDO's geosynchronous view of the Sun is the first solar detector to provide continuous high-resolution, full-disk, multi-wavelength observations of our parent star. On board SDO are three main instruments, namely, the Atmospheric Imaging Assembly (AIA, Lemen et al. 2012), the Extreme Ultraviolet Variability Experiment (EVE, Woods et al. 2012), and the Helioseismic and Magnetic Imager (HMI, Scherrer et al. 2012). Each instrument operates in different wavelength domains, including from the EUV to the visible range. In total, SDO produces ∼1.5 Tb of data per day and can be readily downloaded from the SDO processing centre[7].

The AIA instrument (Lemen et al. 2012) on board SDO is an array of four telescopes that provide multiple simultaneous high-resolution images from the upper chromosphere to the hot flaring atmosphere. Its unprecedented spatial and temporal resolutions present a view of the Sun like never before. AIA captures continuous 4096 × 4096 pixel full-disk images in ten distinct wavelengths, three of which are in UV and the remaining seven are EUV bandpasses. Characteristically, each AIA bandpass corresponds to a range of temperatures emitted from plasma radiated along the line-of-sight. Out of the seven EUV wavebands, six are centred on strong Fe lines, namely: Fe XVII (AIA 94 Å), Fe IX (171 Å), Fe VIII, XXI (131 Å), Fe XII, XXIV (193 Å), Fe XIV (211 Å) and Fe XVI (335 Å). The remaining bandpass, 304 Å, corresponds to He II, which to this day remains a poorly understood chemical line (e.g. Del Zanna et al. 2011). Overall, these EUV wavebands cover a temperature distribution

---

[7] http://jsoc.stanford.edu/
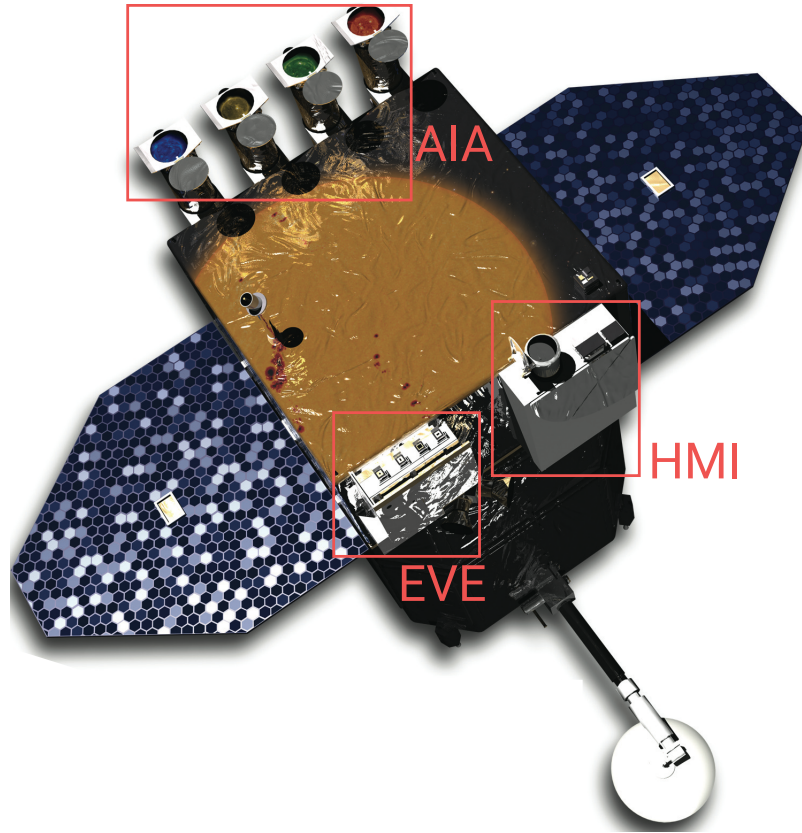
Figure 1.15: A schematic diagram of SDO, highlighting all three instruments (AIA, EVE and HMI) on board the spacecraft. The high-gain antennas are used to track the ground station. The arrays of are used as solar panels, producing power of up to 1500 W. Image adapted from Pesnell et al. (2012).
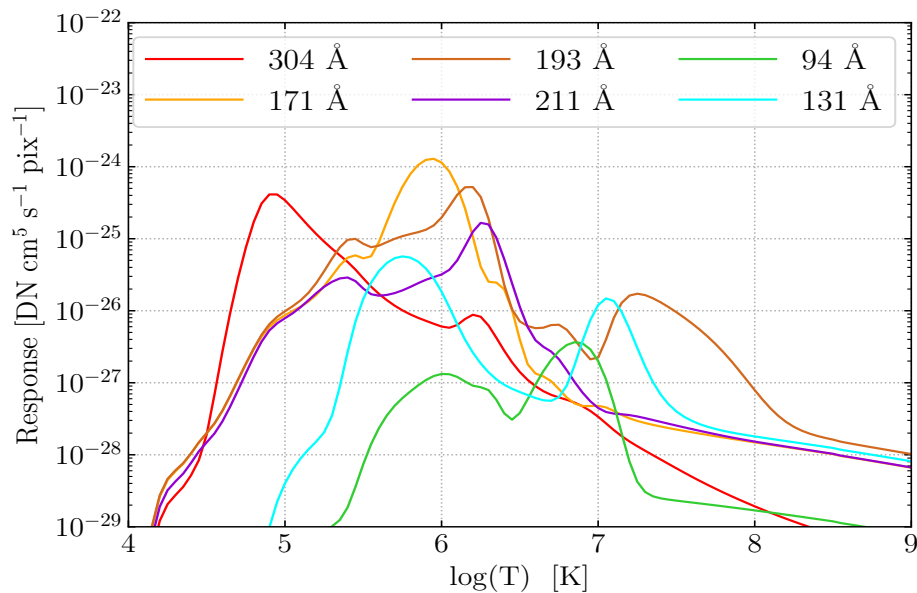
Figure 1.16: Temperature response functions for the six common EUV wavebands following Boerner et al. (2012), calculated from the CHIANTI v.8 model of solar emissivity (Del Zanna et al. 2015).
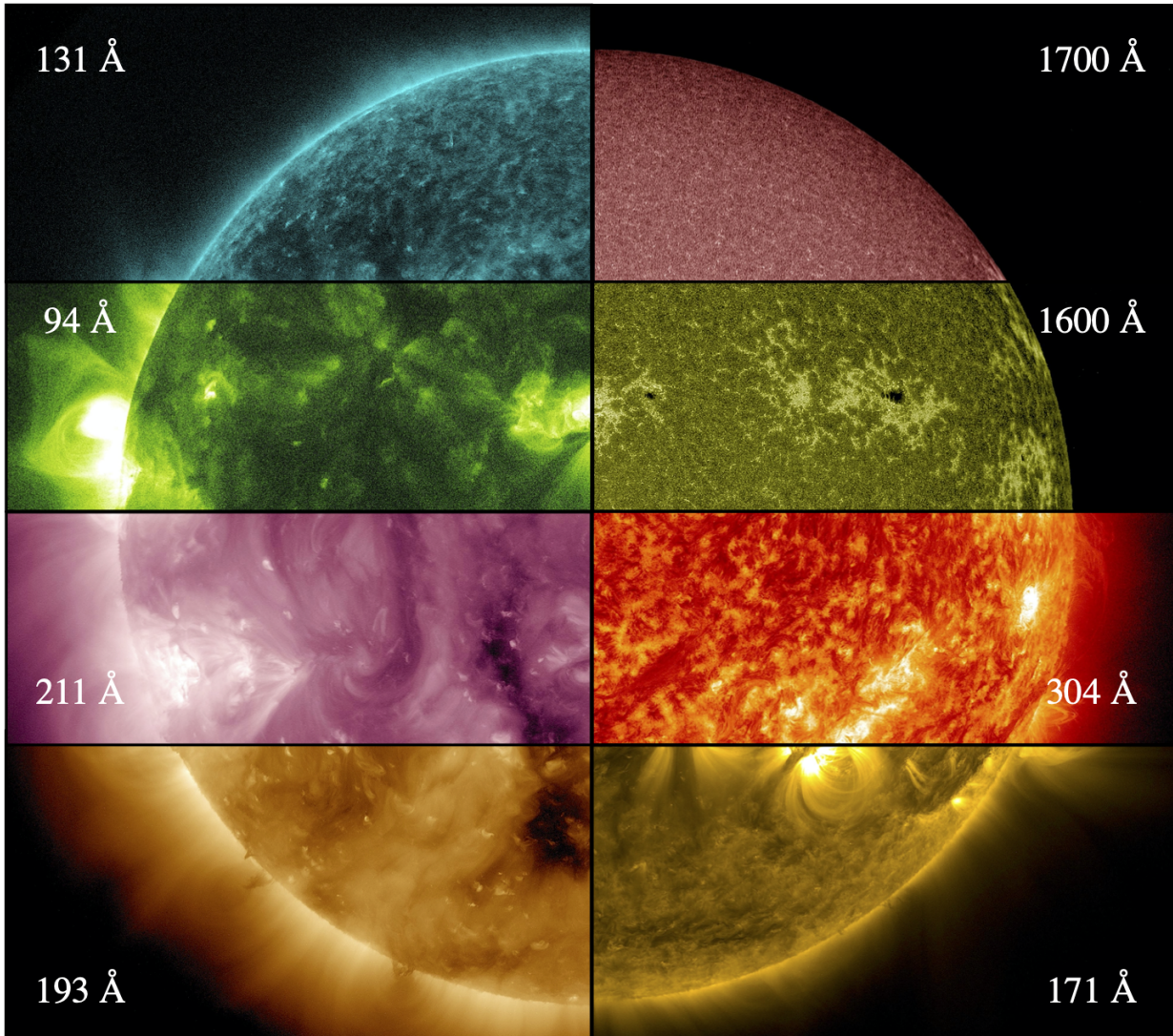
Figure 1.17: Typical images of the Sun captured by the SDO/AIA instrument on 2013 May 20. Each panel shows the Sun near-simultaneously observed in a distinct wavelength of light ranging from 1700 Å to 131 Å. Starting from the top right panel, the corresponding plasma temperature increases in a clockwise direction. The rosy pink glow of the 1700 Å bandpass corresponds to the temperature minimum of $4,500$ K at the photosphere. Chromospheric plasma with temperatures of around $50,000$ K are shown in the 304 Å bandpass in a vibrant red. Coronal plasmas with temperatures ranging from 1 to 10 million K are shown in the 171, 193, 211, 94 and 131 Å wavebands. The AIA 4500 Å and 335 Å filters are missing from this image. All images are false-coloured, with the brightest region corresponding to CCD pixels with the highest number of photon counts. Data courtesy of the SDO/AIA science teams.

Table 1.2: The main ion contributions observed by each AIA bandpass and the corresponding region of the solar atmosphere. The majority of wavebands are dominated by iron. The temperature range spans nearly three orders of magnitude (Lemen et al. 2012).

Channel (Å)	Primary Ion(s)	Region of Atmosphere	Char. $\log(T)$ [K]
4500	Continuum	Photosphere	3.7
1700	Continuum	Temperature minimum, photosphere	3.7
304	He II	Chromosphere, Transition region	4.7
1600	C IV + cont.	Transition region, upper photosphere	5.0
171	Fe IX	Quiet corona, upper transition region	5.8
193	Fe XII, XXIV	Corona, hot flare plasma	6.2, 7.3
211	Fe XIV	AR corona	6.3
335	Fe XVI	AR corona	6.4
94	Fe XVIII	Flaring corona	6.8
131	Fe VIII, XXI	Transition region, flaring corona	5.6, 6.7

ranging from 6×10^4 to 2×10^7 K. A diagnostic of the temperature response functions for six AIA wavebands are shown in Figure 1.16. The contribution from the primary ions of each wavelength band, characteristic temperatures and corresponding observed regions of the solar atmosphere are provided in Table 1.2.

All EUV wavebands also have an exceptional time resolution, consisting of a sampling interval (cadence) of about 12 seconds. A mechanical shutter regulates the time of exposure for each image every 2-3 seconds. The high spatial and temporal resolution of AIA, together with its continuous coverage, provides the currently best way of studying the magnetic waves and oscillations throughout the solar corona. The data from SDO/AIA are generally in Level 1.0 format, relative to the raw Level 0 data, meaning that the images have been processed to remove artefacts such as bad pixels, de-spiking and flat-fielding. Level 1.5 data contains additional calibration including translation, rotation and scaling for a more robust and accurate comparison between EUV bandpasses. Although not readily available, Level 2.0 data can be estimated by essentially removing SDO/AIA's point spread function (see Poduval et al. 2013). Examples of Level 1.5 processed SDO/AIA observations of the Sun on 2013 May 20 are shown in Figure 1.17. Once the stages of data acquisition and initial processing has been completed, the scientific analysis may begin.

1.6   Thesis Motivation

It is no question that the field of coronal seismology offers a unique chance to better under-
stand the Sun's corona. In this thesis, we investigate multiple events of transverse coronal
loop oscillations observed by SDO/AIA. In Chapter 3, we introduce a new procedure to
reveal the presence of wave signals that are otherwise indiscernible. In Chapter 4, we in-
vestigate the waveform of a loop oscillating with a single frequency and ask the question of
whether it is possible to identify the high-frequency modes of an oscillating loop. Chapter 5
presents an analysis on a rare event of transverse oscillations excited by consecutive flares.
Finally, Chapter 6 summarises the main conclusions before exploring possible future work.

2

Spectral Methods for Solar Coronal Data Analysis

"If you wish to find the secrets of the Universe,
  think in terms of energy, frequency and vibration."

— Nikola Tesla

This chapter provides a mathematical and practical background to the common time series techniques used to analyse oscillatory phenomena in the solar corona. We begin by introducing general integral transformations, including the convolution and correlation operators. We then extend the formalism to the two most important spectral methods in solar physics, namely, the Fourier and wavelet transforms. Their procedures are outlined and examples using artificial signals are provided. The Empirical Mode Decomposition algorithm is also detailed before summarising the key points.

2.1 Introduction to the Chapter

The Sun's highly dynamic corona is now well understood to host various Alfvénic waves and oscillatory phenomena, which are believed to play integral roles in several physical processes throughout its atmospheres. As we have already learned, the signals detected from observed wave phenomena can be utilised to provide critical information about the medium in which they reside by means of seismology (e.g. Roberts et al. 1984). However, analysing signals of solar origin is often non-trivial because, for example, they can be dominated by unwanted noise. Several basic data analysis techniques exist that can be used to reveal the underlying signal of interest. For instance, if the data from an observed structure contains signatures of background jitter, then integrating over consecutive frames (in time or space) can mitigate their contribution. On the other hand, a time variability of an image can be created by subtracting each frame from a previous time step. One obvious drawback these two techniques have in common is that the resultant data may still retain intensity contributions from undesired sources. In other words, they cannot isolate different time scales of an observed signal and identify the noise with clarity. To deal with these shortcomings, a common approach is to transform the data in such a way that the signal can be more easily distinguished from the noise. A following important step is to perform a statistical analysis in order to validate the significance of the detected signals. Thus, it is imperative to first gain a solid understanding of how such signal processing and statistical analysis tools operate before attempting to identify their wave behaviour for seismological purposes.

2.2 Integral Transformations

Wave phenomena in the solar atmosphere are often observed through a series of time-dependent variations in light intensity. To be able to extract meaningful information from such signals and reveal the underlying physical mechanisms requires careful processing. The foundation of signal processing relies upon the ability of transforming a noisy time-domain signal into another domain, with the objective of identifying the signal characteristics (such as the periodicity) that is otherwise difficult to analyse. Mathematically, this can be achieved by representing the transformation as an infinite sum of a real input signal, $s(t)$, multiplied by some a priori defined function, given by:

$$c(\tau) = \int_{-\infty}^{\infty} s(t)K(t,\tau)dt = s(\tau) * K(\tau), \qquad (2.1)$$

where $K(t,\tau)$ is the kernel of transformation, or also often termed the basis function. Equation (2.1) is a mapping from the input domain, t, to an output domain, τ and can also be understood as an inner (dot) product for infinite (finite) dimensional vectors. In the simplest

case where the kernel $K(t,\tau) \equiv K(\tau - t)$, i.e. some time-reversed and shifted function, this type of transformation is called a convolution. By applying this operation on an input signal, the output is essentially a measure of the similarity of the two functions. In the analyses of solar data, a convolution is often applied to 'smooth' the data and therefore, depending on the choice of kernel, this operation can mitigate any unwanted background jitter. The amount of which the data is smoothed is defined by the size of the convolution kernel.

2.2.1   Cross-correlation

Another important transformation is the correlation operation. In statistics and wider disciplines, the word 'correlation' is used to describe the mutual relationship between two or more parameters. This intuition can also be used in the processing of signals. In other words, a correlation measures the degree of similarity between two signals and, depending on whether the two signals are equivalent or different, the correlation function comes in two types: the cross-correlation and autocorrelation. We now introduce the former. The cross-correlation expresses the similarity of the input signal with a pre-defined function, $K(t,\tau) \equiv K(t+\tau)$:

$$c(\tau) = \int\limits_{-\infty}^{\infty} s(t)K(t+\tau)dt, \tag{2.2}$$

where τ is the time lag. The choice of the basis function depends on the application, however, its functional form will generally be known. The resultant transformation will then show strong peaks corresponding to times where the two signals are identical. For instance, in gravitational wave studies, the basis functions (or templates) are theoretically derived and are chosen as the candidate signals that are expected to exist in the observed data and so computing the cross-correlation function can yield the best matched waveform (e.g. Allen et al. 2012). Note that the only difference between a cross-correlation and convolution is that, for the cross-correlation, the input signal is not reversed, or $c(\tau) = s(-t) * K(t)$.

2.2.2   Autocorrelation

In the special case where basis is the input signal itself, i.e. $K(t,\tau) = s(t+\tau)$, the transformation is termed the autocorrelation ('auto' meaning 'self' in Latin). The signal's self-similarity may be revealed by summing the product of the signal with a time-shifted copy of itself. In a similar way as the cross-correlation, high magnitudes in the autocorrelation suggests that the signal is strongly correlated but with itself. For periodic signals, the autocorrelation peaks at time lags corresponding to the dominant period of the signal. On the other hand, a random process that is purely white (Gaussian) noise will be uncorrelated for all time lags, except at the the value $\tau = 0$. Signals exhibiting other forms of random noise, such as red noise (Markov processes), will evince an autocorrelation at time lags greater than zero.
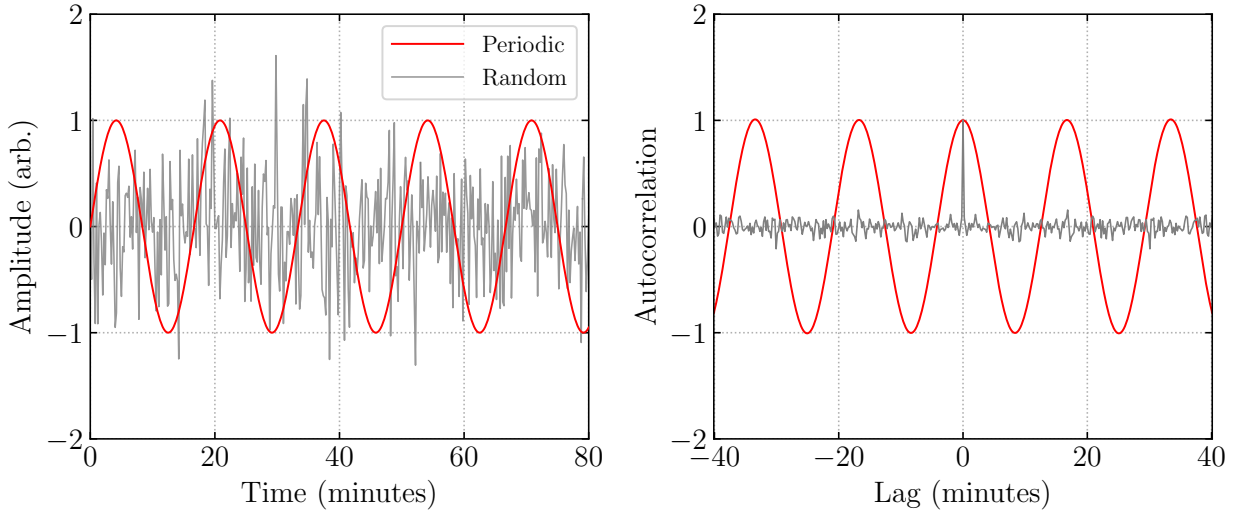
Figure 2.1: Examples of autocorrelation functions of two distinct cases: a periodic signal (red) and a random signal consisting of pure white noise (grey). The periodic signal has an amplitude of 1 and a linear frequency of 1 mHz. Both autocorrelations are symmetric and have been normalised with respect to their respective variance. The random signal is uncorrelated for all time lags, except at $\tau = 0$.

Furthermore, a key property of the autocorrelation is that $c(\tau = 0) \geqslant c(\tau)$ and, hence, the autocorrelation may be normalised such that $C(\tau) = c(\tau)/c(0)$ and so $|C(\tau)| \leqslant 1$ for all τ. This provides a consistent measure of the autocorrelation values and highlights any features of the signal. In comparison to the cross-correlation which is an odd function, the autocorrelation is even and therefore has a symmetrical property such that $C(-\tau) = C(\tau)$.

To illustrate some of the basic properties of the autocorrelation, consider the simple example of a sinusoid with amplitude A_0, angular frequency ω_0 and phase offset, ϕ_0 written as: $s(t) = A_0 \sin(\omega_0 t + \phi_0)$. Then following Equation (2.2) the autocorrelation may be calculated as:

$$c(\tau) = \frac{A_0}{2} \cos(\omega_0 \tau), \tag{2.3}$$

and we see that the autocorrelation of a periodic signal is also periodic (see Figure 2.1). Also, note that the autocorrelation of this signal is independent of ϕ_0. In Chapter 3, we show that the two-dimensional autocorrelation, however, can retain the initial phase information of the signal. Furthermore, due to the finite extent of the data, numerical approximations of the autocorrelation function involve padding the data with zeros (e.g. Harris et al. 2020), which introduces an artificial 'decay'. Since the objectives of observational studies are to estimate the time series parameters, such as periodicity and decay rate of a given signal, this effect must be correctly accounted for by calculating an unbiased autocorrelation. This is another important point that is further discussed in Chapter 3.

One common application of the autocorrelation function is to reveal periodic behaviour within observational data of physical systems. A more specific example of this may be found in several astroseismology studies (see the recent review by García and Ballot 2019) where the autocorrelation function is commonly used for correctly identifying the rotational period from stellar light curves of both short and long durations - contrary to traditional Fourier-based methods (see Figures 30 and 31 of García and Ballot 2019). As we will see, each spectral technique has their own benefits and disadvantages, especially in the analysis of solar signals; however, in this thesis we argue that it is important to perform analyses using multiple independent methods.

2.3 The Fourier Transform

Up until now, we have only introduced transformations that are restricted in the time domain and, hence, we do not have information about the constituent frequencies that make up a given signal. One way of circumventing this problem is by applying the Fourier transform - arguably the most widely used signal processing tool in science. Discovered by Joseph Fourier in the early 1800s (Fourier 1878), Fourier proposed that 'any arbitrary function, continuous or with discontinuities, defined in a finite interval by an arbitrarily capricious graph, can always be expressed as a sum of sinusoids'. This type of transformation is called the Fourier transform and it can be understood as an alternative representation of the input function. In the same notation introduced in Section 2.2, the Fourier transform of a given signal is defined as,

$$\hat{S}(\omega) = \int_{-\infty}^{\infty} s(t) \underbrace{e^{-i\omega t}}_{\text{Kernel}} dt = A(\omega) + iB(\omega), \tag{2.4}$$

where $i \equiv \sqrt{-1}$ denotes the imaginary unit, $\omega = 2\pi f$ is the angular frequency, f is the linear frequency and A and B are the real and imaginary Fourier coefficients, respectively. The corresponding inverse Fourier transform can also be defined as,

$$s(t) = \frac{1}{2\pi} \int_{-\infty}^{\infty} \hat{S}(\omega) e^{+i\omega t} d\omega. \tag{2.5}$$

For convenience, we may also define the operator $\mathcal{F}$, such that $\mathcal{F}\{s\} = \hat{S}$ and $\mathcal{F}^{-1}\{\hat{S}\} = s$. Hence, the Fourier transform decomposes an input signal into an infinite series of sinusoids of various amplitudes and frequencies.

We may proceed and define further important terminologies that will prove useful in this thesis. Firstly, if we compute the magnitude squared of the resultant transformation in Equation (2.4), we obtain a quantity called the power spectrum:

$$P(\omega) \equiv |\hat{S}(\omega)|^2. \tag{2.6}$$

The power spectrum of a given function provides a measure of the strength of each frequency within the overall signal. If the input function $s(t)$ is real, which is always the case for solar time series, then it can be shown that the power spectrum is even, i.e. $P(\omega) = P(-\omega)$. It must be also noted that this quantity is distinct from the amplitude spectrum of a signal, which is defined as $\sqrt{P(\omega)}$, though these terms are used interchangeably in the literature. Secondly, the phase spectrum of a signal can be written as,

$$\Delta\phi(\omega) \equiv \arctan\left(\frac{B(\omega)}{A(\omega)}\right). \tag{2.7}$$

Equation (2.7) quantifies the relative importance of the real (even) and imaginary (odd) Fourier coefficients, and represents the 'delay' of a signal. However, this quantity is often discarded in Fourier analysis and can be better understood using, for instance, the cross-correlation.

At this stage, one can identify clear similarities between the auto/cross-correlation introduced in Section 2.2 and the Fourier transform. Indeed, we can show this by taking the Fourier transform of Equation (2.2):

$$\mathcal{F}\left[\int_{-\infty}^{\infty} s(t)K(t+\tau)dt\right] = \int_{-\infty}^{\infty}\int_{-\infty}^{\infty} s(t)K(t+\tau)e^{-i\omega\tau}dtd\tau. \tag{2.8}$$

A simple change of variables $t' = t + \tau$ yields the following expression:

$$\mathcal{F}\left[\int_{-\infty}^{\infty} s(t)K(t+\tau)dt\right] = \int_{-\infty}^{\infty} s(t)e^{i\omega t}dt \int_{-\infty}^{\infty} K(t')e^{-i\omega t'}dt', \tag{2.9}$$
$$= \overline{\mathcal{F}\{s\}}\,\mathcal{F}\{K\},$$

where $\overline{[\cdot]}$ denotes the complex conjugate. Hence, a correlation (or convolution) in the time-domain is mathematically equivalent to a multiplication in the frequency domain. This property is particularly important, as it reduces the process of multiplying and integrating functions, to multiplication only. Furthermore, from the exact same procedure, the Fourier transform of the autocorrelation function yields,

$$\mathcal{F}\left[\int_{-\infty}^{\infty} s(t)s(t+\tau)dt\right] = \int_{-\infty}^{\infty} s(t)e^{i\omega t}dt \int_{-\infty}^{\infty} s(t')e^{-i\omega t'}dt', \tag{2.10}$$
$$= |\mathcal{F}\{s\}|^2,$$

which is just the power spectrum of the input signal. This relation is more formally known as the Wiener-Khinchin theorem (e.g Wiener 1930).

Another important property of the Fourier transform is the conservation of total power, or otherwise known as Parseval's theorem (Parseval 1806). We may show this mathematically by considering the frequency representation of the time series $s(t)$ and computing its magnitude squared:

$$|s(t)|^2 = s(t)\,\overline{s(t)} = \frac{1}{(2\pi)^2}\int\limits_{-\infty}^{\infty}\hat{S}(\omega)e^{i\omega t}d\omega\int\limits_{-\infty}^{\infty}\overline{\hat{S}(\omega')}\,e^{-i\omega't}d\omega'. \qquad (2.11)$$

Integrating both sides of Equation (2.11) with respect to time yields the following expressions,

$$\begin{aligned}\int\limits_{-\infty}^{\infty}|s(t)|^2dt &= \frac{1}{(2\pi)^2}\int\limits_{-\infty}^{\infty}\hat{S}(\omega)d\omega\int\limits_{-\infty}^{\infty}\overline{\hat{S}(\omega')}\,d\omega'\int\limits_{-\infty}^{\infty}e^{i(\omega-\omega')t}dt,\\[2mm] &= \frac{1}{2\pi}\int\limits_{-\infty}^{\infty}\hat{S}(\omega)d\omega\int\limits_{-\infty}^{\infty}\overline{\hat{S}(\omega')}\,\delta(\omega-\omega')d\omega',\\[2mm] &= \frac{1}{2\pi}\int\limits_{-\infty}^{\infty}|\hat{S}(\omega)|^2d\omega,\end{aligned} \qquad (2.12)$$

where

$$\delta(\omega-\omega') = \frac{1}{2\pi}\int\limits_{-\infty}^{\infty}e^{i(\omega-\omega')t}dt \qquad (2.13)$$

is the Dirac delta function. Note that we have assumed a finite energy signal, i.e.

$$\int\limits_{-\infty}^{\infty}|s(t)|^2dt < \infty. \qquad (2.14)$$

Thus, we can see that the Fourier transform conserves the total power of the input signal, as expected.

2.3.1 Key Properties of the Fourier Transform

We will now provide a summary of the basic Fourier transform properties that will be useful in later chapters.

Linearity

For any two arbitrary signals $s_1(t)$ and $s_2(t)$ and a constant A, the Fourier transform is a linear operation:

$$\mathcal{F}\{s_1(t) + s_2(t)\} = \mathcal{F}\{s_1(t)\} + \mathcal{F}\{s_2(t)\},$$
$$\mathcal{F}\{As_1(t)\} = A\mathcal{F}\{s_1(t)\}. \tag{2.15}$$

Translation

A time shift of a signal causes a phase change in the frequency domain, but the resultant amplitude remains unaffected:

$$\mathcal{F}\{s(t - t')\} = \mathcal{F}\{s(t)\}e^{-i\omega t'}. \tag{2.16}$$

Symmetry

If $s(t)$ is real, then its transform is symmetric in frequency:

$$\mathcal{F}\{s(t)\} = \hat{S}(\omega) = \overline{\hat{S}(-\omega)}. \tag{2.17}$$

Scaling

For a signal that is time-scaled by some constant, a, its transform obeys the following:

$$\mathcal{F}\{s(at)\} = \frac{1}{|a|}\mathcal{F}\left\{\frac{\omega}{a}\right\}. \tag{2.18}$$

Differentiation

Finally, the transform of the nth derivative imparts a scaling proportional to frequency to the power n:

$$\mathcal{F}\left\{\frac{d^n}{dt^n}s(t)\right\} = (-i\omega)^n\mathcal{F}\{s(t)\}. \tag{2.19}$$

2.3.2 Common Fourier Pairs

It is now instructive to introduce some of the basic Fourier pairs to understand their representation in the frequency domain. Figure 2.2 provides a visualisation of five common Fourier pairs: a sinusoid oscillating with a periodicity T, a top-hat of width T, a Dirac comb spaced equally in an interval T, a Gaussian of standard deviation σ and a double-sided exponential with decay rate, a. In all of these examples, there is a reciprocal relationship between a time domain signal and its corresponding Fourier transform. That is, a signal with characteristic time T will, in general, possess a Fourier transform of scale T^{-1}. Such properties are central to many areas of science, ranging from quantum theory to astrophysics. In this thesis, as we will see, these properties will be important for analysing oscillations in the solar corona.
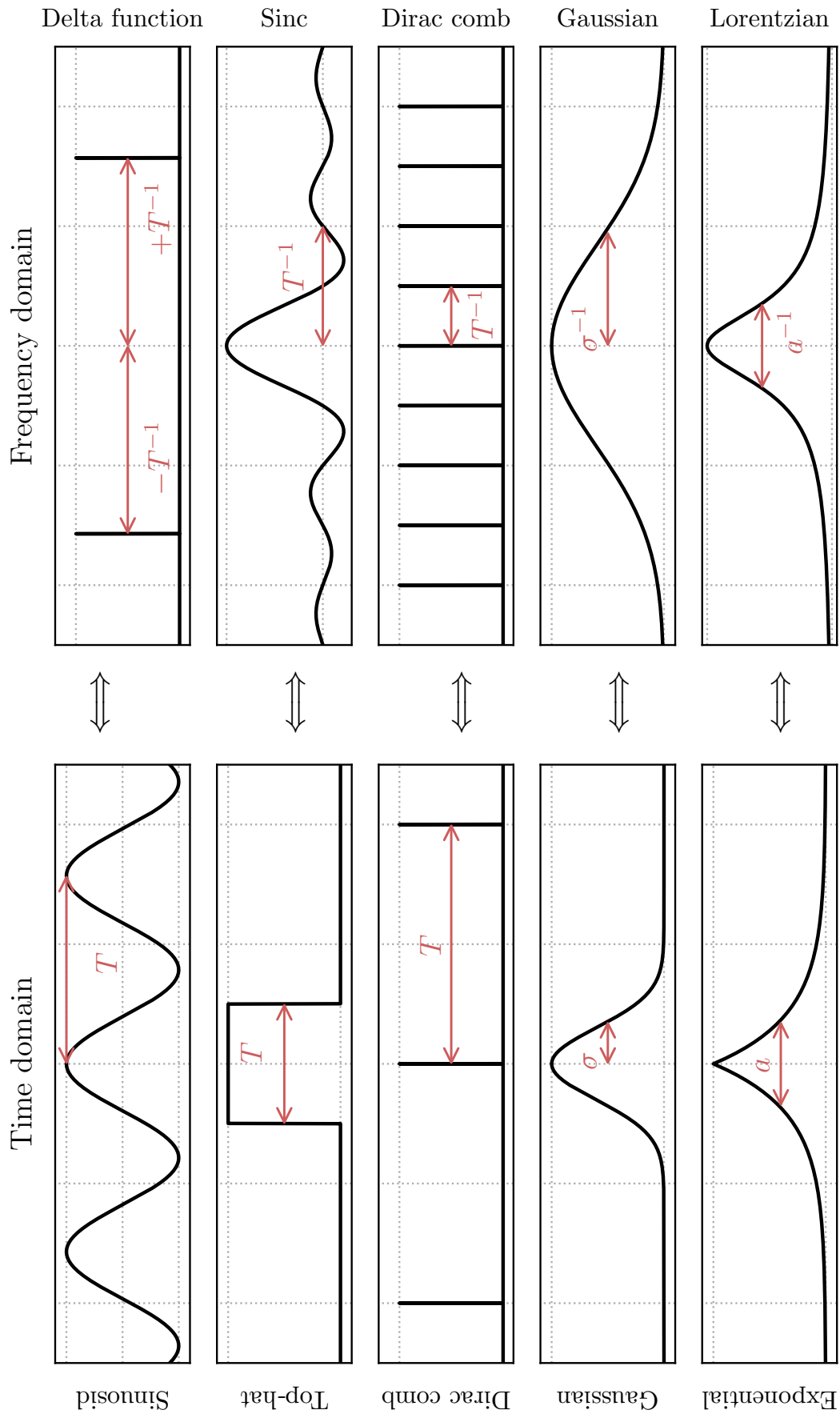
Figure 2.2: Illustration of some of the common Fourier pairs. The left panel shows the time domain representation, whereas the right panel shows the corresponding frequency domain form. Starting from the top left, the Fourier transform of a sinusoid oscillating with a periodicity of T yields two, symmetric Dirac delta functions at $\pm T^{-1}$. A top-hat of with T transforms to an a periodic sinc $(\sin(x)/x)$ function. The transform of a Dirac comb equally spaced in an interval T results in another Dirac comb with spacing $1/T$. A thin Gaussian of width σ transforms to a wide Gaussian. Finally, a double-sided exponential of decay rate a transforms to a Lorentzian of reciprocal width.

2.3.3 The Discrete and Fast Fourier Transforms

The Fourier transform is clearly an indispensable tool for analysing continuous signals that are well defined for times $-\infty < t < \infty$. Of course, real-world observations are not continuous but are discrete, with the data being acquired over some finite number of frames, N, at a given sampling rate, Δt. If we suppose we have observed a continuous signal, $s(t)$, at a regular interval then it follows that the resultant signal can be thought of as a multiplication of the continuous signal and a Dirac comb sampled regularly at times $n\Delta t$, where $n \in [0, N-1]$. Thus, the continuous Fourier transform (Equation (2.4)) can be written in a discrete form, namely the discrete Fourier transform (DFT):

$$\hat{S}(k\Delta f) = \sum_{n=0}^{N-1} s(n\Delta t)e^{-2\pi i f_k n\Delta t}, \tag{2.20}$$

where $k = 0, 1, 2, \ldots, N-1$, $\Delta f = 1/(N\Delta t)$ is the sampling frequency and $f_k = k/(N\Delta t)$ are the equally spaced frequency components. Similarly, the inverse DFT may be written as:

$$s(n\Delta t) = \frac{1}{N}\sum_{n=0}^{N-1} \hat{S}(k\Delta f)e^{+2\pi i f_k n\Delta t}. \tag{2.21}$$

The reciprocity between DFT and inverse DFT makes it possible to filter specific frequency bands of a given signal. In general, there exist three types of filtrations: low-pass, high-pass and bandpass filters. A low-pass filter mitigates high frequencies, whereas a high-pass filter diminishes low frequencies. A combination of low and high pass filters can be used to create a bandpass filter, allowing only a specified range of frequencies. Broadly speaking, subtracting a time series frames corresponds to a high-pass filter whilst a summation correspond to a low-pass filter (also see Appendix A). In coronal imagery, an example of a high-pass filter is the running-difference technique, where the time series in each pixel is subtracted from the previous time frame, removing trends and allowing high-frequency waves and oscillations to be viewed more clearly. Similarly, summing consecutive time frames in each pixel removes the contribution from high-frequency jitter. However, any frequency filtration must be done with care and justification, as the DFT's assumption of stationary signals can yield physically meaningless results if too narrow frequency bands are used for reconstructions. Alternative approaches for signal decompositions using more robust spectral techniques is discussed below.

It is also important to stress that in approximating both the DFT and inverse DFT, there exists an implicit top-hat function of width $T = N\Delta t$ that multiplies the observed signal. As we already know, this function will result in a sinc function in the frequency domain that will cause a 'leakage' of frequencies within neighbouring components. This property of the DFT has two important consequences: we must consider a way of minimising this leakage

with some other appropriate function (also sometimes called apodization) and that there exists a frequency criterion such that $\Delta f \geqslant 1/(N\Delta t)$. In fact, to capture all of the signal information correctly, it is vital to sample the frequencies according to the Nyquist criterion, which states that:

$$\Delta f \geqslant 2f_{\max}, \tag{2.22}$$

where $f_{\max}$ is the maximum frequency (Nyquist frequency) that can be observed. Hence, the equally spaced sampled frequencies are represented by $f_k \in [0, f_{max})$. Any signal containing frequencies greater than the Nyquist frequency cannot be accurately represented. If the frequencies are sampled any lower than the Nyquist criterion, then it is said that the frequencies are aliased and must be appropriately accounted using, for example, a low-pass filter. Moreover, it is also clear that increasing the sampling frequency does not increase the Nyquist frequency, which is usually set by the detector resolution. For the EUV wavebands onboard SDO/AIA, the sampling time (Nyquist frequency) is 12 seconds ($\approx$ 41.67 mHz), although, previous instruments such as TRACE have suffered from non-uniformly sampled data (see Handy et al. 1999). In this case, it is possible to construct a Lomb-Scargle periodogram (Lomb 1976; Scargle 1982), which is essentially a discrete power spectrum of unevenly sampled observations. However, it is well understood that several difficulties may arise, such as aliasing problems and defining a correct Nyquist frequency (e.g. VanderPlas 2018).

Furthermore, as we have already learned, the DFT of a signal of finite duration results in a leakage of frequencies due its implicit assumption that the signal is infinitely periodic. To minimize this spectral effect, the signal must be multiplied by a 'window' function prior to taking the DFT. This is mathematically equivalent to convolving in the frequency domain (see Equation (2.9)). The chosen window function should, ideally, have the form that it starts at zero, approaches a maximum in the middle, before reaching zero again at the end of the signal. Examples of typical window functions used in solar data analysis include: the Hann window (or $\cos^2$ bell curve), the Gaussian window and the Hamming window. The exact choice of window function depends on the application, though it is generally advised to select one that minimizes leakage without altering the raw data. Throughout this work, we apodize our data with the well-established Hann window (see Blackman and Tukey 1958).

Although the DFT is an indispensable processing tool, its computational time can be costly for large N. In fact, a naive implementation of the DFT described by Equations (2.20) and (2.21) implies that for N data points its computational time is $\mathcal{O}(N^2)$. This led Cooley and Tukey (1965) to develop a Fast Fourier Transform (FFT) algorithm based on the DFT and, ultimately, reducing its computational time to $\mathcal{O}(N \log N)$. The efficiency and robustness of the FFT algorithm has made it a regular mainstay of modern science.

Finally, it should be mentioned that not all programming languages use the same definition of the DFT/FFT shown in Equations (2.20) and (2.21). The commonly used software in solar physics is the Interactive Data Language (IDL) and, to date, a vast majority of the literature have been conducted using this software. However, implicit in such studies is that the IDL software uses the standard definitions of the DFT/FFT described above[1], which may cause problems in later stages of analyses, such as incorrectly normalising the power spectrum and establishing a null hypothesis. This can be seen by considering Parseval's theorem for the DFT equations described above. In this case, the following expression is obtained:

$$\sum_{n=0}^{N-1} |s(n\Delta t)|^2 = \frac{1}{N} \sum_{n=0}^{N-1} |\hat{S}(k\Delta f)|^2. \tag{2.23}$$

On the other hand, the (forward) DFT in IDL contains a factor of $1/N$ and so Parseval's theorem for the DFT has the following form:

$$\sum_{n=0}^{N-1} |s(n\Delta t)|^2 = N \sum_{n=0}^{N-1} |\hat{S}(k\Delta f)|^2. \tag{2.24}$$

Although this distinction might seem inconsequential, erroneous normalisations of power spectra will undoubtedly yield inconsistencies. It is suggested that, where possible, the DFT definition be confirmed and stated in future literature.

2.4 The Wavelet Transform

2.4.1 General Formalism

One major drawback of traditional Fourier methods is it cannot effectively deal with non-stationary signals, that is, signals that exhibit a modulation in frequency or amplitude. It is also unable to provide a picture of how frequencies varies in time. Coronal waves and oscillations can often observed to have short-lived and transient behaviour, occasionally deeming a standard Fourier approach insufficient to analyse the signal. A work-around this could be to use a short-time Fourier transform, where window functions are used to transform the data in smaller segments. An obvious disadvantage of the short-time Fourier transform is that it possesses a fixed resolution in both time and frequency. If the signal is multi-periodic, then the short-time Fourier transform must be used more than once, with windows of different sizes to reveal each component, which is computationally extensive. The wavelet transform (WT) was introduced to overcome each of these issues and is one of the most widely used processing tools in solar physics (Farge 1992; Torrence and Compo 1998).

---

[1] See the IDL FFT documentation www.l3harrisgeospatial.com/docs/fft.

We now introduce the general formalism of the WT in the context of solar data analysis.

Given a wavelet basis function, $\Psi_0(\eta)$, that depends on a non-dimensional time parameter η of zero mean and is localised in time and frequency, it is possible to define the (continuous) wavelet of an N-point time series, $f(t)$, with equal spacing δt at times $t = 0, \dots, (N-1)\delta t$ as the convolution of the input function with a translated and scaled version of the basis function:

$$W(s,t) = \frac{1}{\sqrt{N}} \sum_{t'=0}^{(N-1)\delta t} f(t') \left(\frac{\delta t}{s}\right) \bar{\Psi}_0 \left(\frac{t'-t}{s}\right), \qquad (2.25)$$

where s is the wavelet scale parameter and Ψ_0 is normalised to unit energy. Hence, by varying s and convolving the wavelet basis in time, the resultant transformation yields a 2D output of the signal amplitude as a function of the scale parameter and time.

There exists a number of wavelet basis functions $\Psi_0(\eta)$ with various properties and their use depends on the application. These can be broadly categorised into complex and real basis functions and are ideal for capturing oscillatory or steady-state signals, respectively. The spectral resolution is dictated by the width of the wavelet itself, such that a narrow function in frequency has good frequency resolution but a poor time resolution and, similarly, a broad function in frequency has poor frequency resolution but good time resolution. The two common wavelet basis functions used in solar physics are the Morlet and Paul wavelets. The Morlet wavelet is simply a sinusoid modulated with a Gaussian:

$$\Psi_0(\eta) = \pi^{-1/4} e^{i\omega_0 \eta} e^{-\eta^2/2}, \qquad (2.26)$$

where ω_0 is the non-dimensional frequency and is equal to 6 throughout this thesis. The Morlet wavelet has an e-folding time of $\sqrt{s}$ and is related to the Fourier period as $T = 4\pi/(\omega_0 + \sqrt{(2 + \omega_0^2)})$. Similar relationships of the Paul and the Derivative of Gaussian wavelets can be found in Torrence and Compo (1998).

In the same fashion as the FFT, the wavelet power spectrum is defined as the square modulus of the WT, $|W(s,t)|^2$. The wavelet power at a given instant in time can be taken by slicing the 2D function, such that an average of the wavelet power spectrum within the observational time interval yields the global wavelet spectrum (GWS), defined as:

$$|\widetilde{W}(s)|^2 = \frac{1}{N} \sum_{t=0}^{(N-1)\delta t} |W(s,t)|^2. \qquad (2.27)$$

It is worth noting that one should not expect equivalent power spectra between the FFT and WT. In fact, given a time series of two sine waves of the same amplitude but different frequencies, the FFT power spectrum yields the correct strengths at each of the two

frequencies, whereas in the global wavelet spectrum the high-frequency peak is significantly smaller than that of the low-frequency peak. This is effectively due to the selective width of the wavelet filter. In other words, for small scales (high frequencies), the wavelet is broad in frequency, which smooths out the peaks in the power spectrum, whereas at large scales (low frequencies) the wavelet is narrower and the peaks have a larger amplitude. Hence, in this case, the wavelet spectrum is biased and fails to determine the relative magnitude of the two signals. This ambiguity was noted by Torrence and Compo (1998) and the authors warn about the correct usage of a wavelet analysis in such a scenario on their webpage[2].

It is also possible to use the WT as a bandpass filter and reconstruct a given signal within a specified frequency band. The wavelet reconstructed time series can be obtained by summing the real part of the WT over specified scales:

$$f(t) = \frac{\delta j \delta t^{1/2}}{C_\delta \Psi_0(0)} \sum_{i=j_1}^{j_2} \frac{\mathrm{Re}\{W(s_j, t)\}}{s_j^{1/2}}. \tag{2.28}$$

Here, δj is the spacing between the scales, defined as $s_j = s_0 2^{j\delta j}, j = 0, 1, \ldots J$ and $J = \delta j^{-1} \log_2(N\delta t / s_0)$. The parameter s_0 defines the smallest resolvable scale (also called the Nyquist-Shannon scale) and J determines the largest scale. For the Morlet wavelet, $\delta j = 0.125$, $C_\delta = 0.776$ and $\Psi_0(0) = \pi^{-1/4}$.

2.4.2 Cone of Influence

Due to the finite length of an observed time series, unwanted edge effects arise at the beginning and end of the wavelet power spectrum because the transformation assumes the data is periodic. By padding the data with zeros and removing their contribution afterwards, it is convenient to define the regions where discontinuities enter the analysis using the cone of influence (COI). The COI is defined as the length of the time series where the power spectrum drops by a factor of e^{-2}, ensuring edge effects are minimal inside the COI.

2.4.3 Fourier and Wavelet Significance Levels

To test any peaks in the either FFT or wavelet power for statistical significance, it is necessary to choose an appropriate background model. For instance, if one assumes a background (Gaussian) white noise model, then the expected power is a constant function of frequency and is equal to 1 using the normalization $N\sigma_0{}^2$, where N is the total number of time frames and $\sigma_0{}^2$ is the variance. This scaling provides a measure of the power relative to white noise. Torrence and Compo (1998) established a null hypothesis for the significance of the wavelet power by comparing Monte Carlo simulations to theoretically derived models and

---

[2] paos.colorado.edu/research/wavelets

showed that both the wavelet and FFT power spectra are χ^2_D distributed with D degrees of freedom where $D = 2$. From this property, it is then possible to construct a noise model for FFT power by multiplying the background spectrum with a specified percentile of the χ^2 distribution. If we suppose that the signal is dominated by white noise, we can estimate a significance threshold in the FFT power by calculating the following:

$$P_{\text{white noise}} = N\sigma_0^2 \frac{\chi^2(p)}{2}. \tag{2.29}$$

where p is the desired level of significance. A similar argument can be used to construct confidence levels in the wavelet power (see Equation 23 of Torrence and Compo (1998)) for signals that are dominated by red noise instead. In the case of solar signals, studies have shown the (FFT or WT) power spectrum of a given time series can include power law behaviour, which suggest the inadequacy of such basic models may yield false positives (e.g. Vaughan 2005; Auchère et al. 2014; Ireland et al. 2015). To take the probability of multiple outcomes into account, Monte Carlo simulations can be used to derive more suitable confidence levels for time series containing coloured noise. An alternative approach is to utilise the Bonferroni correction, which can be applied when two or more different statistical analyses have been performed on the same dataset, though some studies argue that this correction can be unnecessary (e.g. Perneger 1998).

In this thesis, we take a significance level of 5% (95% confidence level) in both the Fourier and wavelet power using both white and coloured noise models unless otherwise stated. In Chapter 4, we demonstrate that often the observed power law behaviour of solar signals can be merely an artefact that arises due to the assumptions of the FFT. We further argue that the limitations of the spectral techniques must be thoroughly understood before performing such statistical tests.

2.4.4   Tests on Artificial Signals

We will now describe a test case of the FFT and WT techniques on an artificial time series that mimics the behaviour of oscillatory phenomena commonly observed in EUV data. The objective here is to build a picture of how these tools operate before exploring the questions we aim to address in this work. Suppose we observe a noisy signal that is a combination of a 'true' periodic component and a noise source within a single AIA pixel:

$$s(t) = \sin(2\pi f t) + 2n(t), \tag{2.30}$$

where $f = 1$ mHz is the frequency of oscillation of the underlying signal. The signal is buried in a background of noise that is sampled from a (Gaussian) white noise with an amplitude twice that of the underlying signal. The sampling time is taken to be equal to the AIA cadence. The procedure to analyse a given times series using the FFT can be summarised
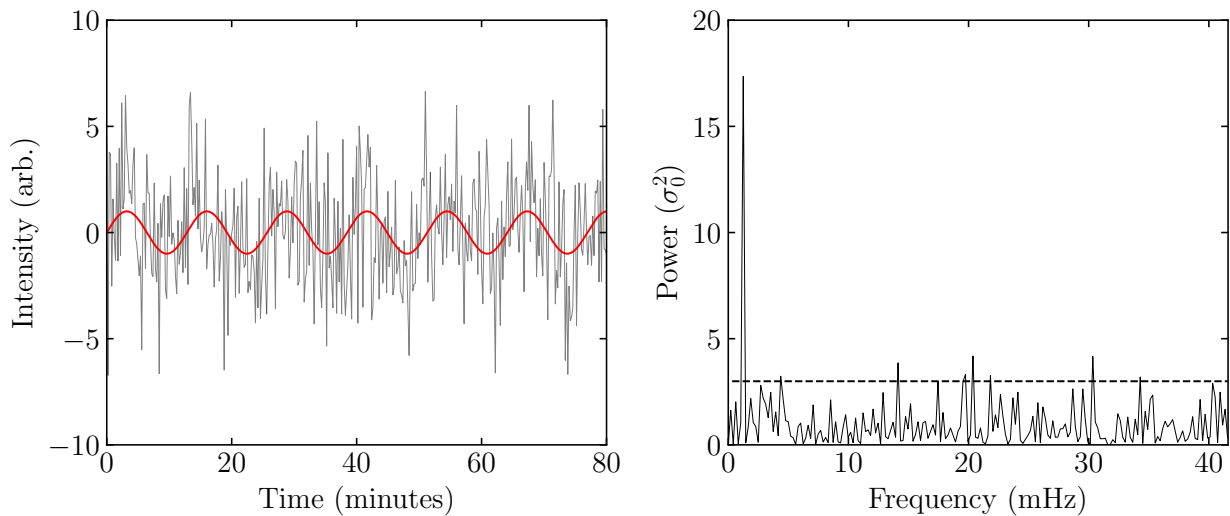
Figure 2.3: Example of the FFT on an artificial time series. Left panel: an observed signal (black) that is dominated by white noise with an underlying periodic signal of frequency 1 mHz (red). Right panel: the resultant FFT power spectrum normalised with respect to the signal variance. The dashed black lines show the 95% confidence level estimated from the theoretical white noise spectrum in Equation (2.29). The spectrum has one statistically significant frequency at 1 mHz, corresponding to that of the underlying periodic signal.
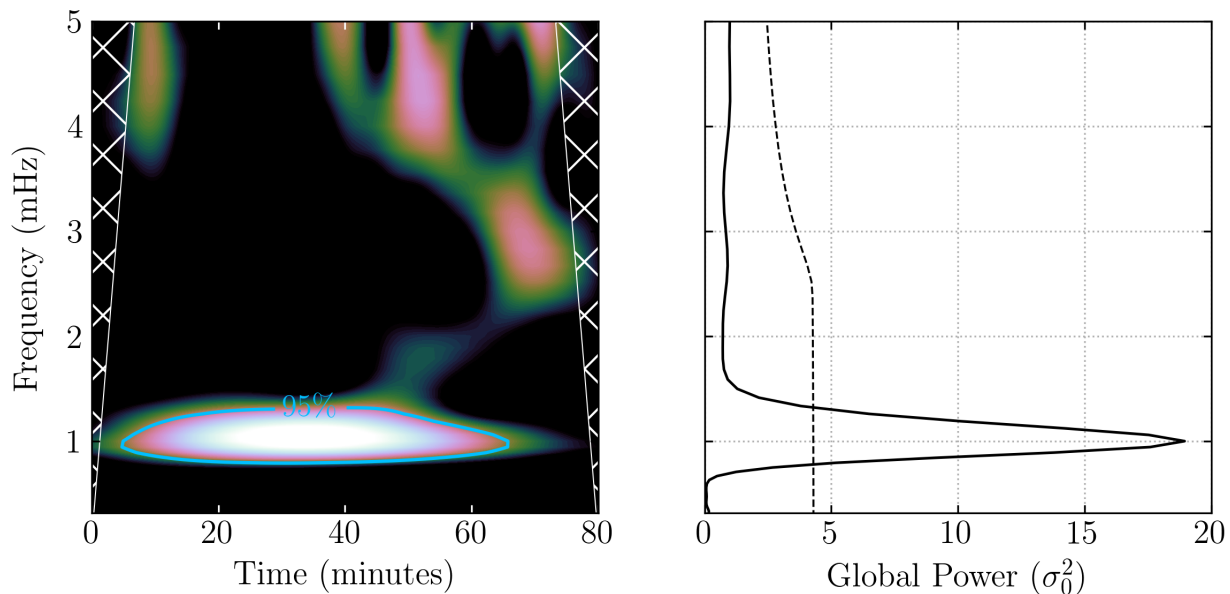
Figure 2.4: Wavelet analysis on the noisy time series shown in the left panel of Figure 2.3. Left panel: wavelet power of the signal as a function of time and frequency. The white hatched lines indicate the COI and the blue contour encircles the 95% statistically significant component at 1 mHz. Right panel: The (time averaged) global wavelet power normalised with respect to the signal variance. The dashed line denotes the 95% global confidence level. Note the similar scale in the FFT and wavelet power in this example.

as follows:

1. Detrend the signal by removing the mean or any long term variability, though the latter must be justified.

2. Apodize the signal with an appropriate window function to mitigate edge effects.

3. Compute the FFT and power spectrum.

4. Calculate a confidence level using an appropriate background noise model.

The procedure for a wavelet analysis is best described in Torrence and Compo (1998) though the methods are similar to those listed above.

Figures 2.3 demonstrates the FFT on an artificial time series described by Equation (2.30), that is, a periodic signal of 1 mHz frequency embedded in a background of noise. The signal has a time cadence equal of 12 seconds. The resultant power spectrum shows a strong peak at a frequency corresponding to the underlying signal and the small jitters arise from the added white noise. A similar result is shown in Figure 2.4 by performing a wavelet analysis of the signal. In this case, it can be seen that the signal is fairly stationary (i.e. no change in frequency) as a function of time. Unfortunately, the assumption of stationary signals in EUV observations is not always realistic due to the transient nature of coronal structures and, therefore, it is often required to use multiple methods to confirm their veracity. In the following section, we introduce a relatively new technique commonly used to identify oscillatory phenomenon in the solar corona.

2.5   Empirical Mode Decomposition

The complex physical behaviour of coronal structures often mean that their signals from observations can be non-linear (e.g. non-sinusoidal) and non-stationary. Although a wavelet analysis overcomes the issue of non-stationary signals, both the wavelet and FFT techniques operate under the assumption that the signal is a sum of linear harmonic basis functions. As a consequence, the analysis of non-linear signals require a technique that is basis independent. The Empirical Mode Decomposition (EMD) was introduced by Huang et al. (1998) with the objective of analysing both non-linear and non-stationary signals. EMD is essentially an algorithm that decomposes a given signal empirically from the data itself. Fundamentally, EMD operates under the assumptions that the input signal contains different modes of oscillations that possess the same number of extrema and zero crossings, and are symmetric with respect to the local mean. These are called Intrinsic Mode Functions (IMF). Each IMF is characterised if the following two criteria are met: (1) the number of extrema and zero-crossings must differ at most by one within the entire signal and (2) the mean of the envelopes of the local maxima and minima is zero. A single IMF represents a mode of oscillation with variable amplitude and frequency as a function of time. The exact procedure of extracting

an IMF is called 'sifting'. Specifically, this involves extracting the lower and upper envelopes of the signal and obtaining their mean, m_1. The difference between the signal and the envelopes' mean is computed as:

$$h_1(t) = s(t) - m_1(t). \tag{2.31}$$

In the following steps, a 'sifting' process is created by treating $h_1(t)$ as the data and the previous step is repeated, yielding:

$$h_{11}(t) = h_1(t) - m_{11}(t). \tag{2.32}$$

By iterating this process k times, we are left with $h_{1k}(t) = h_{1(k-1)}(t) - m_{1k}(t)$, which is taken as an IMF. Here, $m_{1k}(t)$ is the kth mean of the sifting process. Subsequently, the component,

$$c_1(t) = h_{1k}(t) \tag{2.33}$$

is then defined as the first IMF component of the signal. This first IMF contains oscillations near the Nyquist frequency, which is generally used as a benchmark for noise. The entirety of the sifting process is repeated until a stopping criterion $\sigma = \sigma_{\text{max}}$ is met by a standard deviation of consecutive siftings, calculated as:

$$\sigma = \sum_{t=0}^{T} \left[\frac{|h_{k-1}(t) - h_{1k}(t)|^2}{h_{k-1}^2(t)} \right]. \tag{2.34}$$

Equation (2.34) is a measure of the standard deviation between consecutive sifting processes. Huang et al. (1998) suggested that the stopping criterion values can lie in the range $0.2 - 0.3$, however, this must be tested accordingly on the data.

It is also possible to separate (filter) $c_1(t)$ from the data by calculating the residual, $r_1(t)$:

$$r_1(t) = s(t) - c_1(t). \tag{2.35}$$

If the data still contains longer period components, then $r_1(t)$ is treated as the new data and undergoes the same sifting process described above until the stopping criterion is met and the resultant IMF and residuals are given by:

$$r_2(t) = r_1(t) - c_2(t), \tag{2.36}$$

$$r_3(t) = r_2(t) - c_3(t) \tag{2.37}$$

. . .

$$r_n(t) = r_n - 1(t) - c_n(t). \tag{2.38}$$

From Equations (2.35) - (2.38), it can be inferred that a summation of all IMFs recovers the original signal:

$$s(t) = \sum_{j=1}^{n} c_j + r_n, \tag{2.39}$$

where n is the number of IMFs and r_n is the residual trend of the overall signal. Therefore, a decomposition of the data into n empirically derived modes of oscillation are achieved, which separates any time scales present in the data. The benefit of this kind of filtration, in comparison to FFT or wavelet methods introduced above, is that EMD preserves the non-linearity and non-stationarity of the raw data (Huang et al. 1998).

Since its initial development, EMD has received significant attention due to its adaptive nature, with applications in many areas of science and particularly in solar physics (e.g. Terradas et al. 2004; Morton et al. 2011, 2012; Kolotkov et al. 2016). For instance, Terradas et al. (2004) first employed EMD to reveal the spatial distribution of propagating and standing waves in a coronal loop using TRACE data. Morton et al. (2011) performed EMD analysis on observations of magnetoacoustic sausage modes within magnetic pores to identify oscillatory periods that range from 30 to 450 seconds. Morton et al. (2012) investigated intensity oscillations associated with a blowout solar jet and employed EMD to extract periodicities of 50, 100, 200 and 300 seconds using SDO/AIA. A study of large-scale fast MHD waves in the solar corona by Long et al. (2017) used EMD to characterise the oscillations of trans-equatorial coronal loops and estimate a seismologically-derived magnetic field strength of $|\mathbf{B}| \approx 5.5 \pm 1.5$ G. Kolotkov et al. (2016) used EMD on SDO/AIA data to reveal the statistical properties of physical processes from the upper photosphere and lower corona, and demonstrated that such EUV signals can exhibit random behaviour. The statistical results obtained by Kolotkov et al. (2016) using EMD on EUV data are also in accordance with previous studies that employ Fourier methods (e.g. Ireland et al. 2015).

Despite the popularity of EMD within the solar community, there are several drawbacks to this technique. For instance, the major issue with EMD is its lack of a rigorous mathematical formalism, which causes difficulties in defining a unique set of basis functions. This is because the sifting procedure is heavily dependent on the input parameters and still remains an open optimisation problem. Another difficulty with the EMD arises in establishing viable statistical tests for non-stationary signals and remains a subject of intense debate (see Huang 2014). Nevertheless, EMD is a promising tool that can be used in addition to

the aforementioned spectral methods to analyse the wave behaviour of coronal structures.

It is important to stress that the removal of background trends from observations of coronal loop oscillations is subjective because an exact physical model that incorporates long time scales, for instance from local heating events or footpoint buffeting motions, remains unknown (see Aschwanden et al. 2002). Within observational data, background trends may be removed using various methods (e.g. Verwichte et al. 2004; Aschwanden 2011). For example, Aschwanden et al. (2002) detrended their time series using polynomials with trends of order 1 – 6. White et al. (2012) used a third order polynomial for the background trend. Pascoe et al. (2016b) detrended the time series by employing a spline interpolation to the maxima and minima of the data. However, as stated above, unjustified detrending of time series can result in complications and erroneous estimations in later stages of analyses. This is because detrending essentially removes the underlying physics of a process that could be present. Similar conclusions were reached by Vaughan (2005) in the use of significance testing of Fourier periodograms, and by Auchère et al. (2014) for wavelet analyses of coronal time series. One benefit of detrending signals using Fourier techniques, as opposed to polynomial fittings, is that all frequency bins are equally affected and does not introduce preferential bias into the detrended data. Further discussions on detrending and our justification for using a high-pass filter is provided in Appendix A.

2.6   Summary

The purpose of this chapter was to provide a background into the various time series techniques currently used in solar physics, which will be employed to investigate the oscillatory behaviour of coronal loops in later chapters. The decision of exploring multiple analysis methods was twofold: to confirm the results of each technique, but also to go beyond their respective capabilities and qualitatively explore the MHD wave frequencies that may exist from our observations. As we have seen, theoretical models have predicted the existence of Alfvénic waves in the solar atmosphere (e.g. Alfvén 1942) and, often, observational studies aim to interpret the wave behaviour from such models. While these techniques have formed the cornerstone of solar data analysis for decades, there remain unanswered questions in the context of coronal seismology. In the following chapters, we employ each of the methods described above to unreported observations of coronal loop oscillations and discuss their physical implications.

3

Autocorrelations of Complex Coronal Loop Oscillations[1]

"The scientist does not study nature because it is useful; he studies it
because he delights in it, and he delights in it because it is beautiful.
If nature were not beautiful, it would not be worth knowing,
and if nature were not worth knowing,
life would not be worth living."

— Henri Poincaré

We present a novel technique to detect oscillations in complex arcades by means of auto-correlations. We show proof-of-principle tests of our method in 1D and 2D using SDO/AIA datasets to obtain the wavefield parameters of coronal loops. Applications include EUV images with poor contrasts where weak oscillations are confidently revealed. Possible signatures of fast MHD waves propagating in a 2D coronal arcade are discussed.

3.1 Introduction to the Chapter

The modern era of EUV imagers has presented observers with an opportunity to study the Sun's atmospheres like never before. In particular, the exceptional spatial and temporal resolutions of SDO/AIA (Pesnell et al. 2012; Lemen et al. 2012) has made the study of waves and oscillations a regular mainstay of coronal physics, owing to their seismological capabilities (e.g. Nakariakov and Verwichte 2005). However, analysing solar data and searching for oscillatory signals can often be non-trivial because such phenomena can exist near the threshold of the detector. This has necessitated a myriad of observational efforts to develop image analysis techniques and algorithms to confidently reveal oscillatory signatures in the corona. For instance, Nakariakov and King (2007) developed an automated detection of wave and oscillatory phenomena in the corona by constructing FFT 'periodmaps' using TRACE data. Sych and Nakariakov (2008) introduced a method to determine the spatial, temporal and phase behaviour of propagating and non-propagating waves based upon the continuous wavelet transform. More recently, Anfinogentov and Nakariakov (2016) proposed a technique for 'magnifying' oscillations using SDO/AIA data, which may exist on the brink of the detector's resolutions. Weberg et al. (2018) developed an automated algorithm for identifying and tracking transverse waves in open field configurations, which can be used to better quantify the statistical properties of solar structures.

In the context of coronal loop oscillations, the analysis often requires an initial visual inspection of images (e.g. Zimovets and Nakariakov 2015). Subsequently, the wave parameters can be more accurately estimated by manually fitting a (damped) sinusoid to the position of peak brightness as a function of time (see below for further details). Such traditional techniques have proved to be indispensable in the past for coronal loops that appear bright within the image foreground (e.g. Nisticò et al. 2013; Pascoe et al. 2016a), however, fails in cases of loops possessing relatively faint emissions embedded within the image background or if the loop cross section is not well-defined. Moreover, fitting the observed data with an a priori defined function may introduce seismic biases because not all loops, even within the same field of view, oscillate exactly according to the prescribed function. Thus, it is of great scientific importance to implement and advance observational analysis techniques that can be used to robustly detect oscillations from faint and bright coronal structures.

In this chapter, we present a novel analysis technique that utilises autocorrelations of the original data to extract properties of the wave-field within the coronal arcade. This method has the salutary feature that it can be successfully applied to loops and arcades for which the traditional method would fail because of a poor image contrast. We first validate our new technique by applying the autocorrelation function to visually identify oscillatory regions in a coronal arcade that may be otherwise difficult, in the context of 'coronal correlation maps'. We then extend our idea to obtain the spatio-temporal behaviour of the transverse

loop oscillations. To validate this, we measure the period of coronal loop oscillations using both our new procedure and the traditional time–distance method. We then compare the parameters measured with the two methods. Finally, we demonstrate the utility of the autocorrelation method in the detection of an additional periodicity in the form of small-amplitude oscillations that exist both long before and after the flares.

3.2 Data

3.2.1 Event Overview

For this study, we obtained a sequence of EUV images of coronal loop oscillations on 2014 January 27 as observed by SDO/AIA. Each image has a pixel resolution of about 0.6 arcsec and a cadence of 12 s. The loops appeared as part of a larger magnetic arcade, which belonged to a multipolar active region (AR) situated near the southerneasten limb of the solar disk. The entire AR emerged a day later exhibiting a sunspot with a complex ($\beta - \delta$ Hale classification) magnetic configuration, and is believed to be an amalgamation of the old AR NOAA 11944 (S09, L=101; see http://www.aurora-service.eu). The coronal arcade was predominantly visible in the 171, 193, and 211 Å channels, and appeared as a bundle of illuminated arched threads extending from the solar limb. This dataset was chosen due to the off-limb nature of the arcade, where the loops exhibited a higher visibility contrast against the dark background. For the entirety of our study, we analysed 12 hrs (3600 time frames) of SDO/AIA images, commencing on 2014 January 26 at 20:00 UT and concluding on 2014 January 27 at 08:00 UT. A sub field of view with dimensions 350×350 arcsec containing the arcade was extracted to begin the analysis.

Figure 3.1 displays the active region NOAA 11967 observed through the 304, 171, 193 and 211 Å EUV wavebands. The loops were most reliably observed in the 171 Å waveband. An initial analysis showed that the loops embedded in the arcade were oscillating and overlapping with localized variations in amplitude before, during, and after the initiation of two major flares of GOES-class M1.0 and M1.1 that initiated at approximately 01:05 UT and 02:02 UT, respectively. The epicenters of both flaring activity were also located near the southeastern limb and was recorded in X-rays by the GOES instruments. We aim to analyse the morphology of coronal loop oscillations induced by the flaring activity. As such, we separated the 12 hour data into three four-hour time intervals: 20:00 - 00:00 UT, 00:00-04:00 UT and 04:00-08:00 UT and hereafter refer these intervals as 'pre-flare', 'during-flare' and 'post-flare', respectively.

Figure 3.2 shows the recorded X-ray flux by GOES in $0.5 - 4.0$ and $1.0 - 8.0$ Å wavebands during all three intervals. The top and bottom panels correspond to the pre and post flares, where little activity is detected and the middle panel is the impulsive phase showing
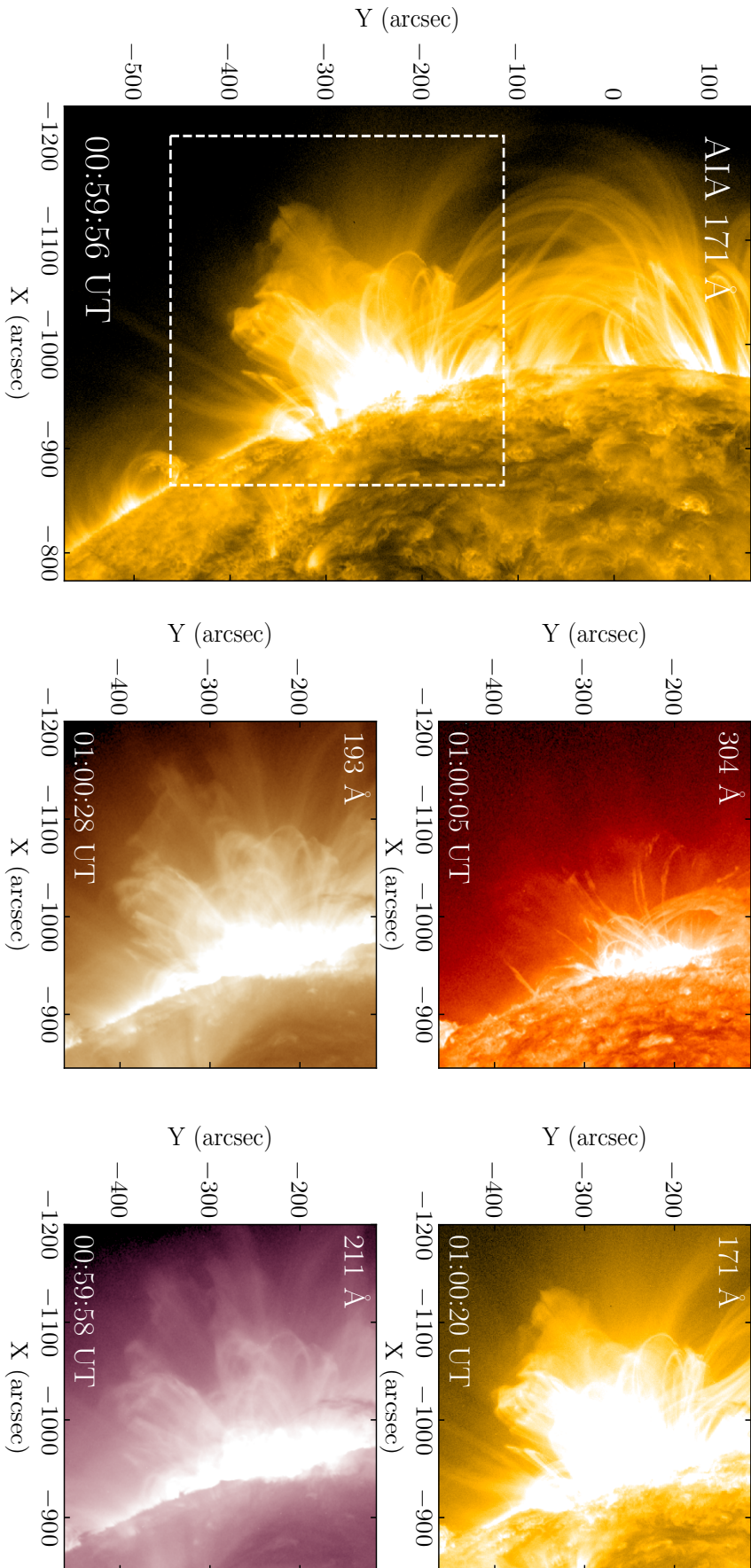
Figure 3.1: Near-simultaneous snapshots of the AR NOAA 11967 observed by SDO/AIA in four EUV wavebands on 2014 January 27. All images were recorded just before the flare onset. The dashed white box highlight the the subfield of view used to extract for further analysis. The coronal loop arcade is best visible in the 171 Å waveband.
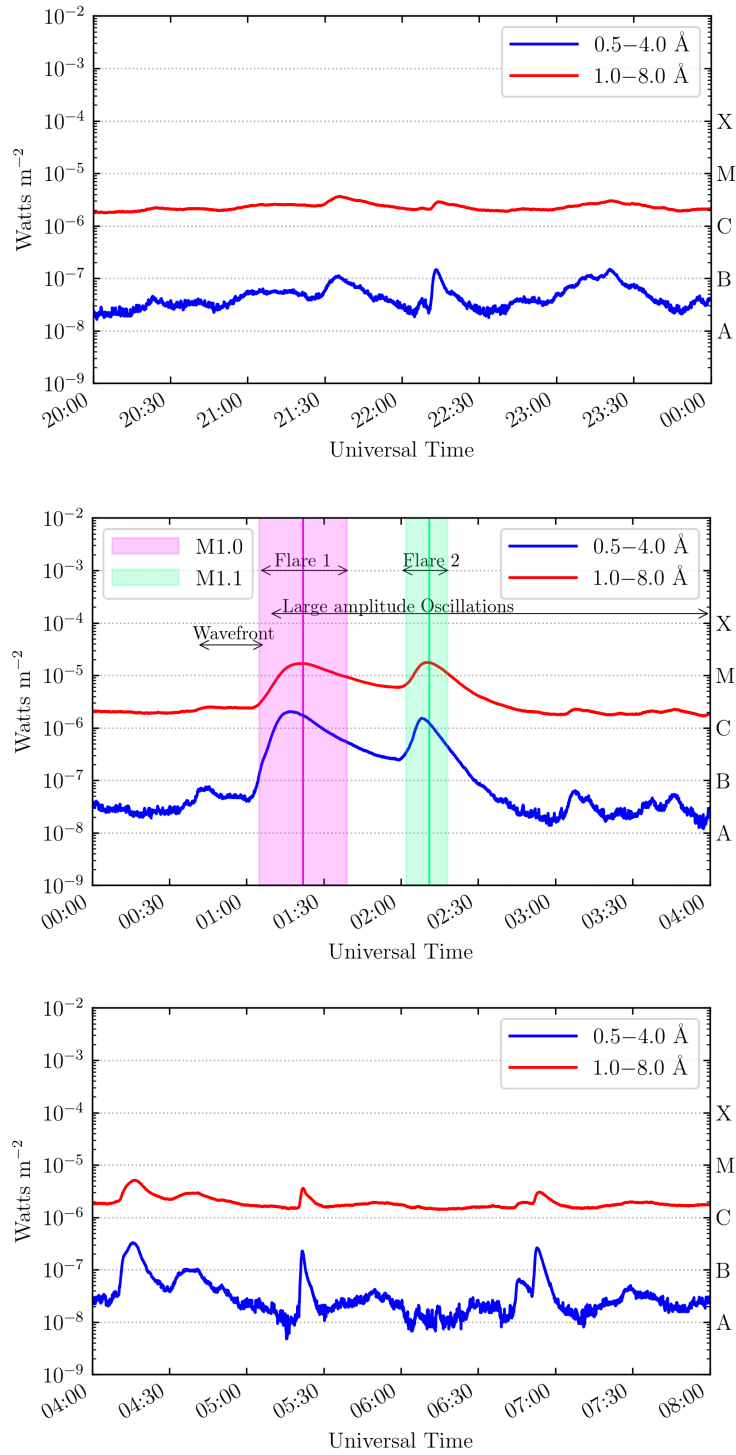
Figure 3.2: Energy fluxes of the three intervals used in this study. The red and blue lines correspond to the $0.5 - 4.0$ Å and $1.0 - 8.0$ Å wavebands, respectively. The top and bottom panels shows the pre-flare and post-flare phases where little flaring activity is recorded. The middle panel is the during-flare phase showing two M-class flares. The shaded areas correspond to the onset and final flare times. The duration of the wavefront and the coronal loop oscillations are also indicated by arrows.
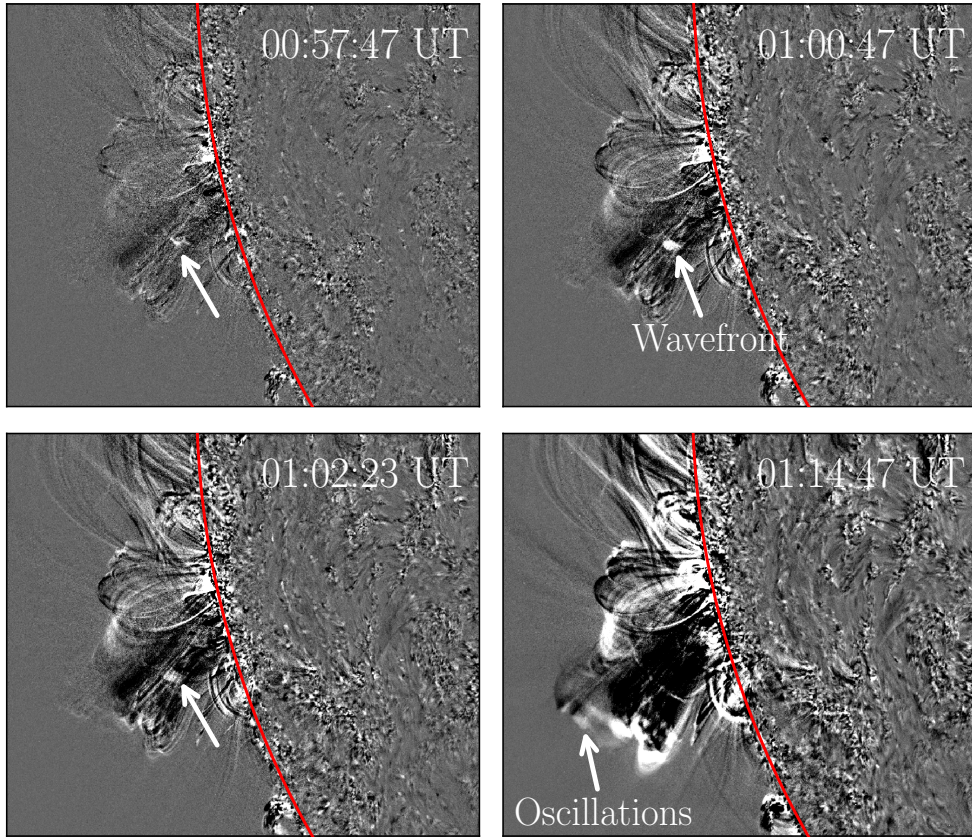
Figure 3.3: Base difference images of the arcade in the 171 Å waveband revealing a small propagating wavefront before the flare initiation. The wavefront excited oscillations in its wake, which is highlighted by arrows. The wavefront emerges around 00:57:47 UT and suddenly traverses the arcade before disappearing around 01:02:23 UT. The red line indicates the solar limb.

Table 3.1: Chronological summaries of the impulsive events that occurred in NOAA 11967 as observed by SDO/AIA.

Event	Duration (UT)	Comment
Wavefront	00:55-01:05	Visible in all EUV wavebands.
1st Flare	01:05-01:39	M1.0 class.
2nd Flare	02:02-02:18	M1.1 class.
Large-amplitude Oscillations	01:10-04:00	Predominant in 171, 193 and 211 Å.

two major M-class flares. The first flare, located at a heliographic latitude 16° south and longitude 88° east, was an M1.0 class flare, with a start time at 01:05 UT, a peak at 01:22 UT, and an end time at approximately 01:39 UT. After this an M1.1 class flare, at latitude 13° south and longitude 88° east, initiated at 02:02 UT, peaked at 02:11 UT, and ended at about 02:18 UT. Just before the first flare, a small wavefront was also seen propagating away from the limb and throughout the arcade. Initially, the wavefront appeared near the
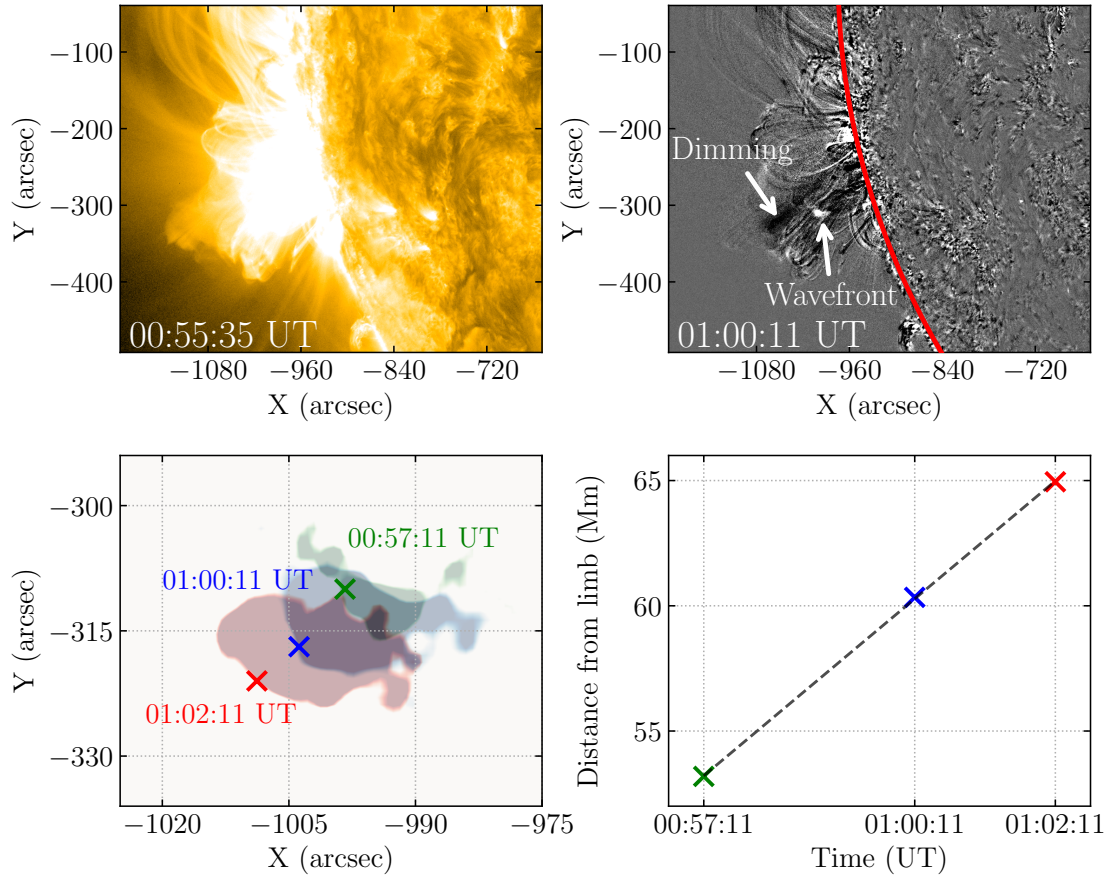
Figure 3.4: Analysis of the propagating wavefront. The top left panel shows the reference image taken at 00:55:35 UT that is used to create the base difference image. The base difference image used to reveal the wavefront and dimming regions of the arcade is shown in the right panel. The bottom left panel shows composite snapshots of the wavefront's location at three different times. The green cross marks the crest of the wavefront at a time 00:57:11 UT, the blue cross for 01:00:11 UT and the red for 01:02:11 UT. The projected distance from the solar limb as a function of time is shown in the resultant bottom right panel using the marked locations.

limb around 00:40 UT, and became evident about 01:00 UT when it started moving. The initial motion of the wavefront from the flare site was visible in the AIA images within all six EUV wavelengths. The life-time of the wavefront, as seen in the 171 Å bandpass, is also marked in the middle panel of Figure 3.2 with a double-headed arrow. A summary of the major events are shown in Table 3.1.

After its initial stage of propagation, the wavefront was obscured by a bundle of several loops in the line of sight and so it was not possible to track it further. This is demonstrated in Figure 3.3. By carefully inspecting difference images at smaller time increments, as shown in Figure 3.4, we measure the distance the wavefront travelled from the limb at three different times (see the bottom right). We estimated the wavefront to have an initial projected

propagation speed of about 40 kms^{-1} from the slope of the line shown in the right panel. As seen in the EUV image sequence, it appears that the wavefront propagated away from the limb, followed by the first M-class flare, exciting transverse oscillations in its wake.

3.2.2 Initial Processing

Before examining the transverse oscillations of the loops in detail, we wish to understand the global oscillations of the entire coronal arcade. This will also provide an idea of the pixel locations (and orientation) we may use to create time-distance maps in a later stage of analysis. A common technique that can be used to gain a sense of the global oscillations that may exist is to identify peaks in the FFT spectrum (Nakariakov and King 2007). However, as we have demonstrated in Chapter 2, computing the FFT of coronal signals can often result in spurious detections and, for example, can be sensitive to the duration of the time series. Thus, an alternative technique that is as computationally efficient and robust at detecting global oscillations in EUV images would prove a useful initial data analysis tool. In this subsection, we propose a new method of detecting global oscillations in the solar corona by means of the autocorrelation function.

Prior to computing the autocorrelation, the data must be carefully pre-processed to sharpen the visibility of oscillating loops and mitigate unwanted long-term trends (e.g. from local heating events). This can be accomplished by removing a background intensity in each pixel using a temporal high-pass filter. We investigated various detrending techniques on our AIA data and their characteristics are explored in Appendix A. For our purposes, we opted for the widely used (linear) Gaussian filter, with a known frequency response (another Gaussian) and a standard deviation of $\sigma = 10$ time frames to produce a high-pass filter:

$$\widetilde{I}(t) = I(t) - I_b(t), \tag{3.1}$$

where $I_b(t) = I(t) * \exp(-t^2/2\sigma^2)$ and t is the time coordinate. Following this procedure, the filtered time series in each pixel $\widetilde{I}(t)$ is now fairly stationary as a function of time and may be used for further analysis.

3.3 Coronal Correlation Maps

We may now calculate the autocorrelation within each spatial domain as a function of time lag:

$$c(\Delta t) = \int\limits_{-\infty}^{\infty} \widetilde{I}(t)\widetilde{I}(t + \Delta t)dt, \tag{3.2}$$

where t is AIA time coordinate. We first zero-pad the time-domain signals and then generate a normalised autocorrelation function defined as $C(\Delta t) \equiv c(\Delta t)/c(0)$ (see Section 2.2.2). Thus, within each pixel, the dominant periodicity of a signal are revealed by a strong autocorrelation at the corresponding time lag.

We can also calculate the statistically significant components in the autocorrelation function at various time lags. Although the spatially averaged coronal time series have been shown to follow a power law (e.g. Ireland et al. 2015), it is likely that the individual pixels exhibit a dominant white noise source (see Chapter 4 for details). Thus, we construct a 95% confidence level using a null hypothesis test based on a white noise autocorrelation, with zero autocorrelation at lag $\Delta t > 0$ except at $\Delta t = 0$ (for details, see Bartlett 1946; Taylor 1984). Similar to that of a WT/FFT significance test (see Chapter 2), 95% confidence level can be estimated by multiplying the standard deviation of the autocorrelation with the 95th percentile value of the normal distribution. If the autocorrelation at each time lag is above the 95% confidence level, the white noise null hypothesis is rejected.

Figure 3.5 shows the correlation map of the arcade viewed in the 171 Å waveband for time lags $\Delta t \in [2, 14]$ minutes, integrated within a 2-minute interval for the flaring dataset (though a root-mean-square approach can also be applied). We can clearly see the pixel locations corresponding to strongly correlated signals exist throughout the entire arcade. On the other hand, the arcade vicinity where no loop structures can be reliably observed possesses almost zero correlation for all time lags, as one would expect for a random white source. An immediate finding from this initial analysis is that the arcade could exhibit highly localised and multi-periodic signals ranging from around 4-14 minutes. For these loops, it appears that the dominant periodicities were around 10 minutes. Such broadband frequencies were first theoretically predicted by Hindman and Jain (2014) who demonstrated that the signals from a realistic multi-dimensional arcade waveguide can evince a range of frequencies excited around its dominant low-order resonant mode. Although it is possible that various kinds of waves and oscillation (e.g. propagating, standing, transverse, longitudinal) may be present during the waveguide in this interval, it is difficult to define the exact nature of the signals using just this approach alone, and will require additional techniques and simultaneous observations, such as Doppler imaging (e.g. Tomczyk and McIntosh 2009).

We can also see fine-detailed structuring exists within localised regions predominantly around the arcade tip where transverse oscillations were reliably observed (see Figure 3.3), occupying around $\sim 10 - 100$ arcsec of the field of view. The fine structuring of coronal loops has been known for decades (e.g. Aschwanden et al. 2000; Reale and Peres 2000) and has been an important topic of debate for heating models of the solar atmosphere (also see Williams et al. 2020a). Though this property is often overlooked in seismic studies. The results presented here highlight the strong inhomogeneity of coronal loops and the range of wave periods they support. It is clear that nearby pixels oscillate at various different periodicities
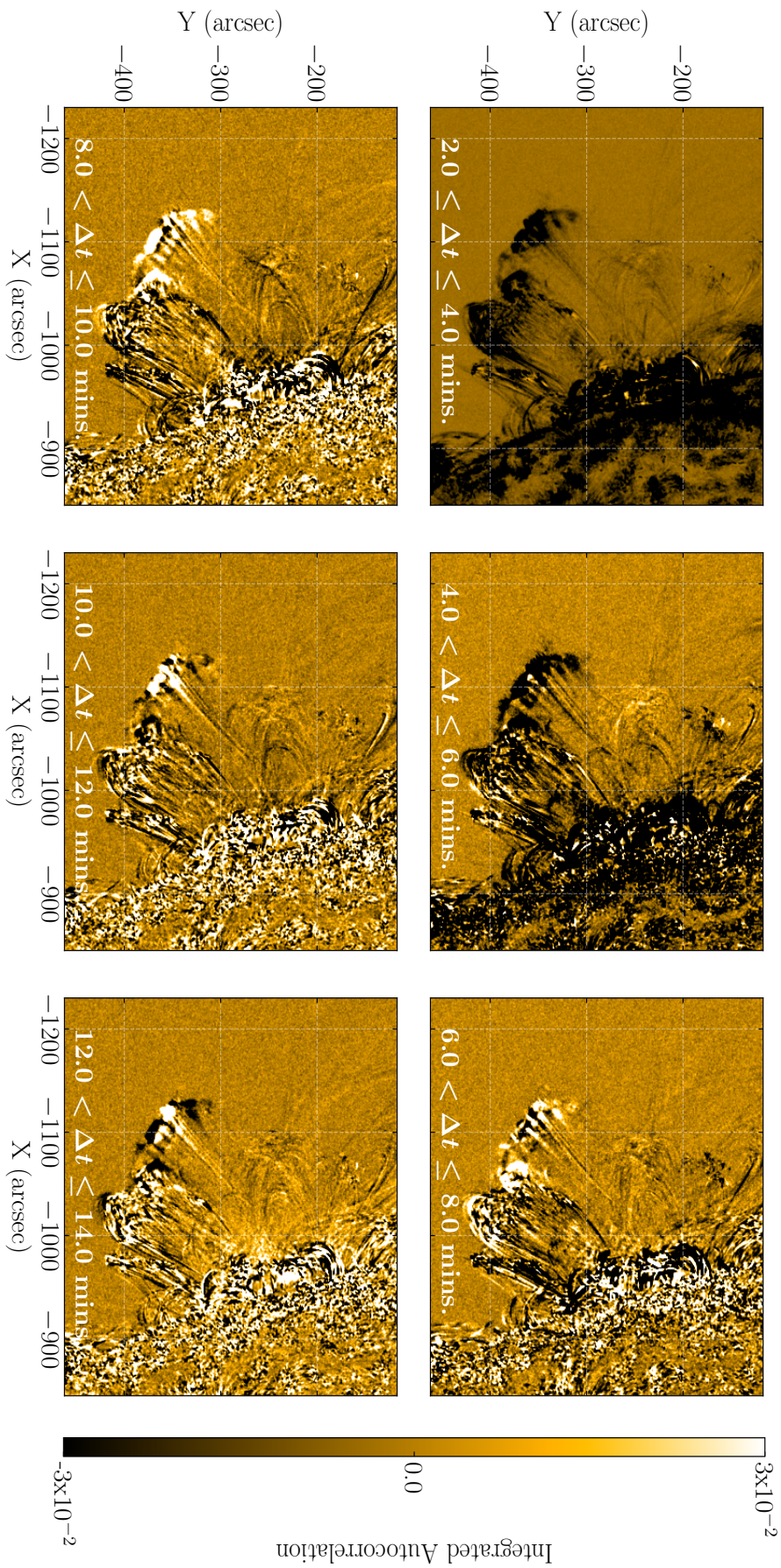
Figure 3.5: Coronal correlation maps for the flaring dataset observed in the 171 Å waveband during time interval 00:00 - 04:00 UT on 2014 January 27. The correlation maps are integrated within a two-minute band and are shown during the range 2-14 minutes. Dark regions correspond to locations in the arcade where the wave signals are negatively correlated, and the bright regions indicate positively correlated signals. Uncorrelated (random) signals possess a zero autocorrelation for all time lags greater than first lag. For this dataset, the loops show strong autocorrelations within a dominant periodicity range of 4-14 minutes.
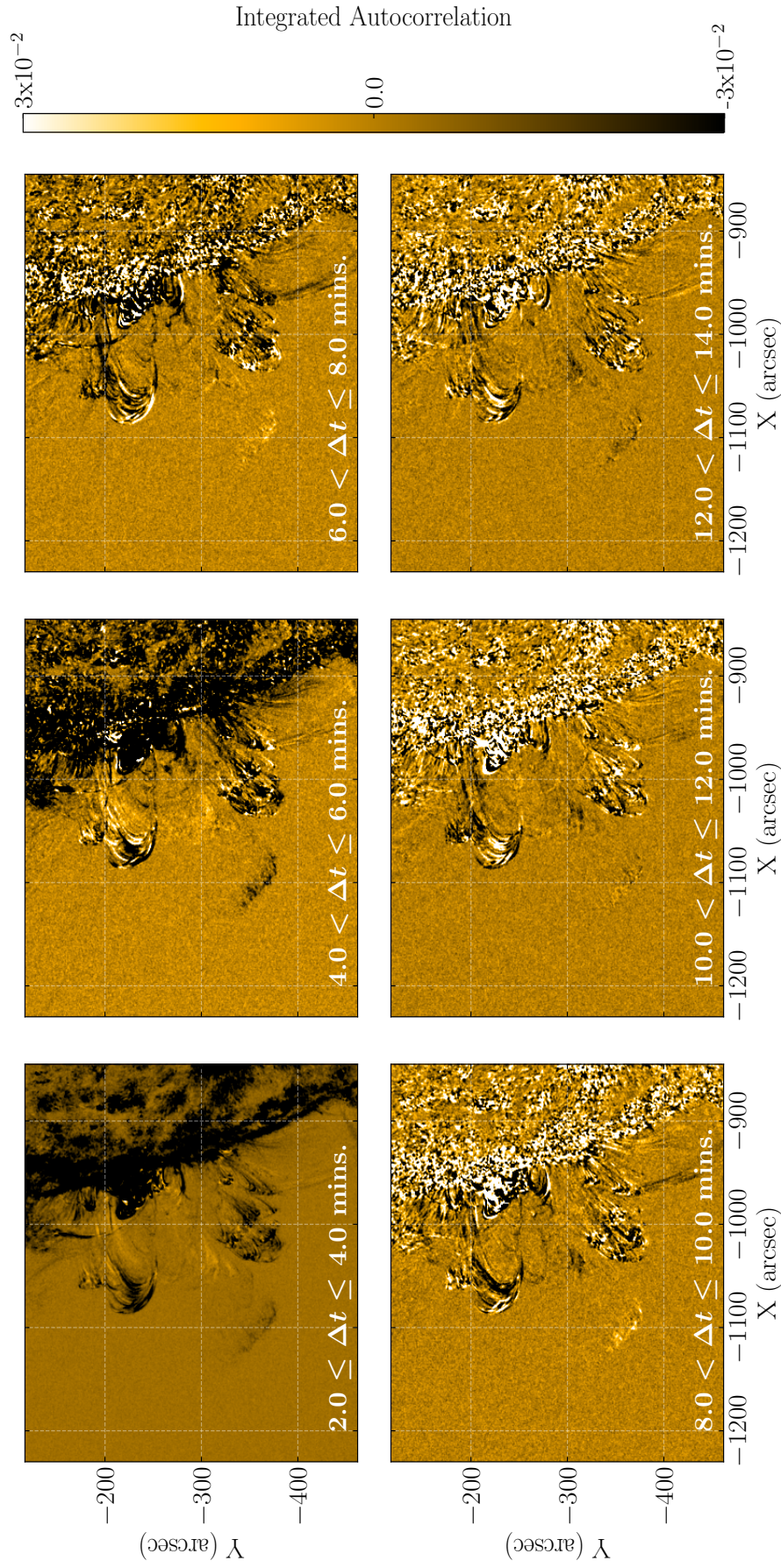
Figure 3.6: Same as Figure 3.5 but for the pre-flaring dataset during the time interval 20:00 - 23:59 UT on 2014 January 26. The range of dominant periodicity for this dataset is around 4-10 minutes. Signatures of ambient oscillations in the arcade before the flaring activity are shown by a strong autocorrelation at each time lag interval.

and only certain 'threads' exhibit rather weak signatures of monochromatic signals. It is also surprising that not all parts of the coronal arcade (the middle grid surrounding the coordinate $(x, y) = (-1050, -250)$ arcsec) exhibits as strong oscillations, though it is possible that observational effects, such as line-of-sight integration, may be responsible for the lack of correlated signals from these regions. It is could also be possible that the trajectory of the propagating wavefront exhibited little interference with the loops in those regions and, as a result, did not perturb them as forcefully. Observations of such small wavefronts (or 'puffs') have been previously reported to propagate along closed field line configurations (e.g. Bemporad et al. 2005; Alzate and Morgan 2016), which could explain the preferential excitation of loop oscillations we observe in this event.

We also computed the correlation maps of the arcade in the absence of the flaring activity and compared the morphology of the oscillations due to the flares. Figure 3.6 shows the 2-minute integrated correlation maps for the pre-flare arcade for the same time lag interval as the flaring case. The correlation maps show ambient oscillations with relatively lower autocorrelation values in the absence of any flaring activity. We see that the pre-flare arcade exhibits a similar behaviour, that is, with negatively correlated values at short periods (2-4 minutes) and positive correlations around 6-10 minutes. In contrast to the flaring dataset, it appears that the pre-flare oscillations lack the spatial coherence that the flare-induced oscillations possess. However, to validate this, a computation of the autocorrelation function in both time and space will be required. This will be further investigated in the following section using a spatio-temporal autocorrelation analysis. Nevertheless, we have demonstrated that the coronal correlation maps have proved to be useful in revealing the expected oscillatory behaviour of the arcade, and the pixel locations that require further attention. A comparison against the standard FFT power maps can also be made in Appendix B.

3.4 Transverse Oscillations

3.4.1 Traditional Time-Distance Fitting

Now that we have established the pixel locations of the transverse loop oscillations and their expected periodicities, we will investigate the wave properties in further detail. The approach to study transverse oscillations involve extracting a 'slit' of the data's spatial coordinates as a function of time. The resultant transformation (or time-distance map) produces a 2D image where the horizontal and vertical axes correspond to the time and spatial coordinates, respectively. Following this, a time series analysis is required to extract oscillatory parameters (such as the periodicity or displacement amplitude) of the loop, commonly using least-squares minimisation (linear/non-linear regression) and is well established in for the analysis of loop oscillations (e.g. Aschwanden et al. 2002; Verwichte et al. 2004; Jain et al.
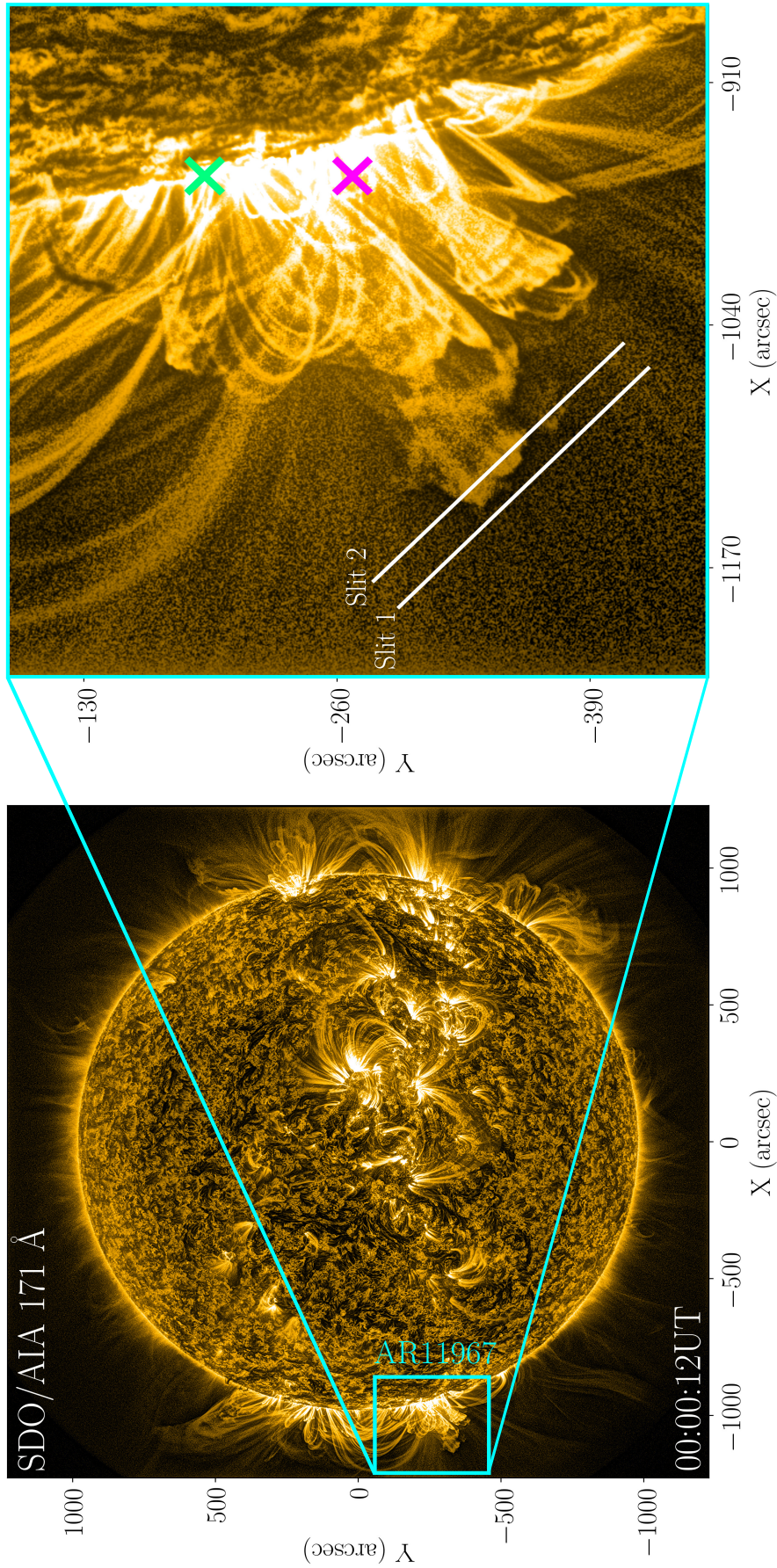
Figure 3.7: EUV image at the beginning of the dataset on 2014 January 27 00:00:12UT observed with SDO/AIA 171 Å. Left panel: full-disk image indicating the active region of interest. Right panel: zoomed-in view of the area contained in the box. The solid white lines correspond to a 130 Mm slit placed transverse to the apparent arcade. The magenta and green crosses correspond to the approximate positions of the flaring activity. The analyses of the loop oscillations are performed separately on each of these two numbered slits. Note that this image has been enhanced with the multiscale Gaussian normalization (Morgan and Druckmüller 2014)

2015). The functional form of the model will be either derived empirically or theoretically using the MHD framework (see Section 1.12). The purpose of this procedure is to find the curve that best fits the data given an input model by minimising the statistic:

$$\chi^2 = \sum_{i=1}^{N} \left(\frac{y_i - f(x_i; \mathbf{c})}{\sigma_i} \right)^2 , \tag{3.3}$$

where y_i is the observed data points and f is the model, which is some linear or non-linear function of the independent variable x_i, σ_i are the associated uncertainties and $\mathbf{c} = (c_1, c_2, \ldots, c_n)$ represents a constant vector. Equation (3.3) is then minimised by ensuring the condition $\partial \chi^2 / \partial \mathbf{c} = 0$ is satisfied. This procedure in the context of time-distance oscillations involves fitting a Gaussian (or parabola) at each time step to estimate the position of peak brightness. Once the positions are returned, the same technique can be used to fit an oscillatory function (typically a damped sinusoid) to the estimated data points for all time frames, enabling estimations of the wave parameters of the loop.

It must be highlighted that the choice of a fitting function is non-unique and several functions have been previously used to test theoretical hypothesis of wave propagation in coronal loops. In particular, there has recently been keen interest to identify the damping time (τ) profile of oscillating loops. Examples of such functional forms include exponential decaying ($e^{-t/\tau}$) (Aschwanden et al. 1999, 2002), Gaussian damping ($e^{-t^2/2\tau}$) (Hood et al. 2013; Pascoe et al. 2016b), and the dissipation of waves in the wake of a travelling pulse ($t^{-\alpha}$ where $\alpha = 0.5$) (Uralov 2003; Terradas et al. 2004; Abedini 2018). A study by Morton and Mooroogen (2016) demonstrated the unsuitability of using the χ^2 statistic to compare the exponential and Gaussian damping functions and highlighted the importance of incorporating more robust statistical techniques for model comparisons.

To date, coronal loop oscillations have been analysed by the time series fitting technique described above (e.g. Verwichte et al. 2009; Jain et al. 2015; Weberg et al. 2018). We first carry out a similar procedure to extract the oscillatory parameters in the AIA 171 and 193 Å channels along an approximately 130 Mm long slit, indicated by Slit 1 in Figure 3.7, and also shown by the white line in Figure 3.8 (left panel). The slit was placed perpendicular to the axis of the arcade where transverse motions were observed, and the time–distance images were created by temporally stacking the intensity along the slit at the AIA cadence. In order to remove small spatial-scale noise, we increase the signal-to-noise by smoothing the intensity over a width of about 2 Mm on either slide of the slit. The resultant intensity variations are shown in the right panels of Figure 3.8, where the origin of the time–distance image corresponds to the bottom right point of Slit 1. The upper and lower panels correspond to the 171 Å and the 193 Å bandpasses, respectively. From these maps, we believe it is evident that the second flare did not excite further loop oscillations above this AR. Though, this event was later studied by Pascoe et al. (2020) in the 171 Å waveband using their new loop
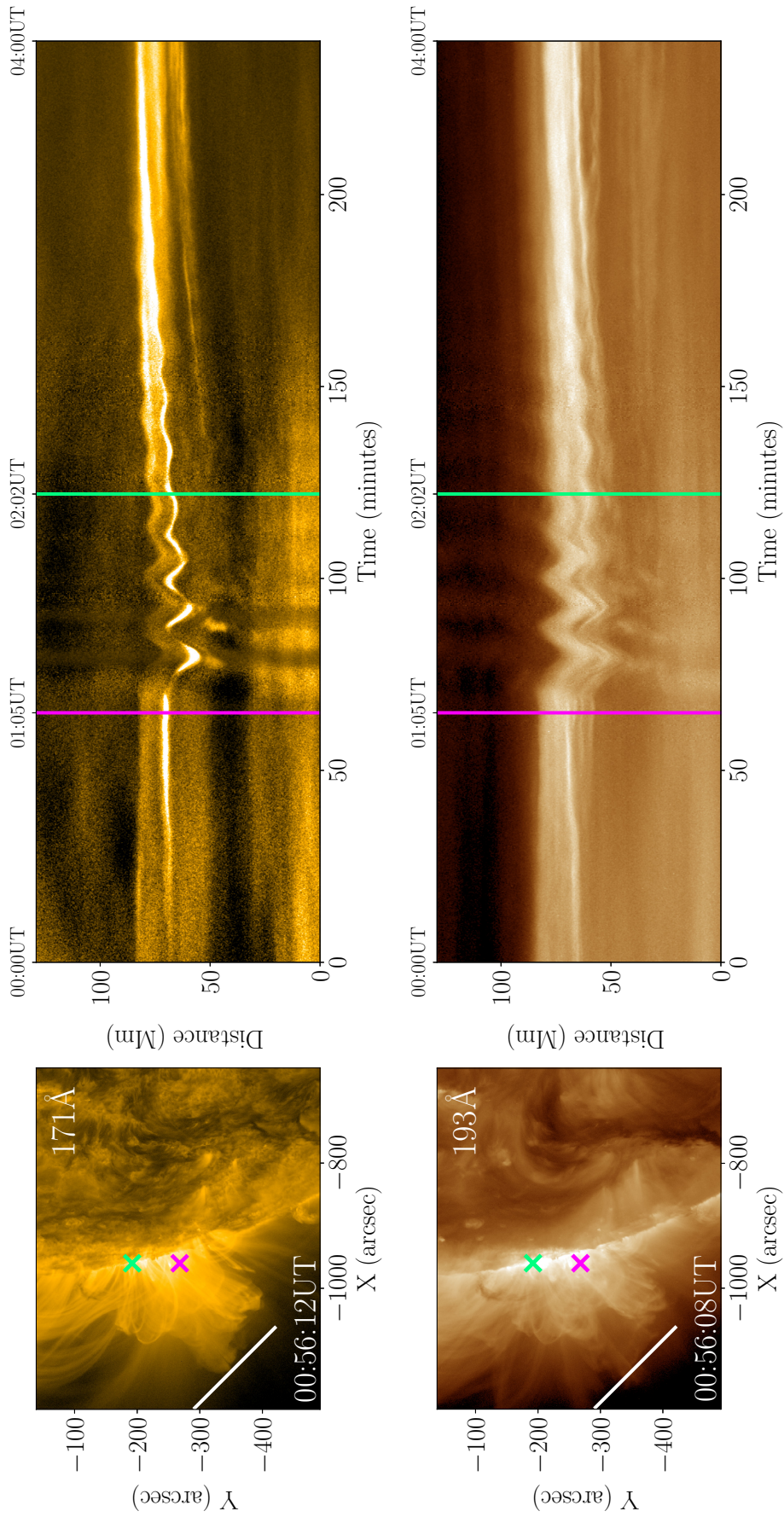
Figure 3.8: Coronal arcades and oscillations. Left panels: EUV snapshots in the 171 Å (top) and 193 Å (bottom) channels, with Slit 1 indicated by the white line. The magenta and green lines indicate the onset times of the flares. Right panel: the corresponding intensity variations along Slit 1 in the aforementioned channels as a function of time.
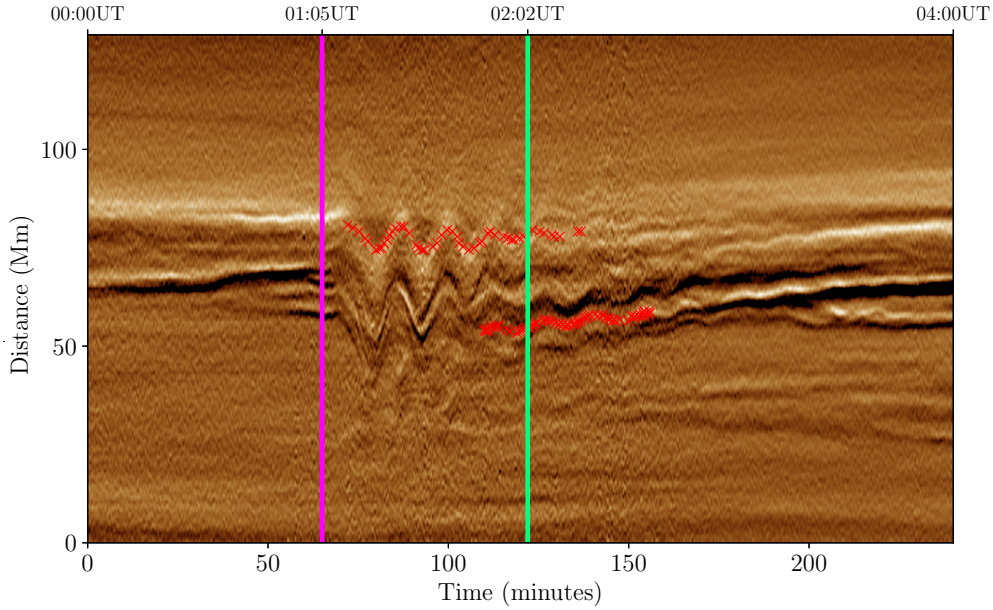
Figure 3.9: Convolved time–distance image for the intensity variations as seen in the 193 Å bandpass, shown in Figure 3.8. The red crosses overplotted on top of the time–distance image are from the resultant time series fits.

tracking method, who claimed to have detected relatively weaker oscillations from the second flare in support of the Kelvin-Helmholtz instability occurring. However, it is not made clear how the number of threads is chosen in their method and further criteria, such as the Akaike Information Criterion (Akaike 1974), must be incorporated to ensure over-fitting does not occur. Furthermore, it is important to highlight that the phase relations of oscillations observed within time-distance maps may be dependent on the orientation. Studies of 3D coronal loop reconstructions have demonstrated that, due to projection effects, the choice of a slit is not trivial and cannot be guaranteed to be along the projected displacement of a loop bundle (e.g. Verwichte et al. 2009).

To accurately extract the oscillatory properties with detail using the traditional time-distance method, the waveforms must be seen clearly with well-defined amplitude boundaries. This can be achieved by taking a derivative in the spatial direction (e.g. White et al. 2012; Nisticò et al. 2014). In order to accomplish this, we enhanced the time-distance maps by convolving each image with a weighted 3×3 kernel of the form:

$$\begin{pmatrix} 1 & 2 & 1 \\ 0 & 0 & 0 \\ -1 & -2 & -1 \end{pmatrix}. \tag{3.4}$$

This convolution performs a triangular temporal smoothing to the time–distance images and takes a numerical derivative with respect to the spatial position along the slit. As a result, the contrast is enhanced at the loop edges. Figure 3.9 presents the processed time–distance

Table 3.2: Fitted parameters from the traditional time-distance method.

Wavelength (Å)	Amplitude (Mm)	Period (min.)	Damping time (min.)	Phase (°)
171 (large-amplitude)	(5.20 ± 0.75)	(13.00 ± 0.06)	(34.43 ± 11.12)	(65.99 ± 3.73)
193 (large-amplitude)	(3.30 ± 0.76)	(13.02 ± 0.12)	(48.30 ± 2.70)	(-98.98 ± 6.57)
193 (small-amplitude)	(0.68 ± 0.12)	(14.03 ± 0.21)	$\ldots$	(20.38 ± 10.31)

image for the 193 Å bandpass, highlighting a variety of oscillating loops. These oscillations are also clearly visible in 171 and 211 Å but less so in the 94, 131 and 304 Å wavebands.

The dominant loop featured in Figure 3.9 undergoes a large-amplitude decaying oscillation. Interestingly, in addition to this, there were weaker small-amplitude oscillations that commenced near the onset of the second flare. These weaker oscillations appear near the bottom of the bundle of main loops. By fitting a Gaussian locally to the intensity of each pixel and carefully propagating the associated uncertainties, we find the position of maximum brightness as a function of time and generate the time series. Here, we fit the time series with appropriate damped sinusoidal functions of the form $\mathcal{A} \exp(-t/\tau) \cos(2\pi t/T + \phi)$, where $\mathcal{A}$ is an amplitude, T is a period, τ is a damping time, and ϕ is a wave phase using the minimisation technique described above. The resultant fits are shown in Figure 3.9 as a sequences of red crosses and the fitting parameters are summarized in Table 3.2. To better describe the fit of the small-amplitude oscillations, the decay rate τ^{-1} was fixed to zero.

3.4.2 Spatio-temporal Autocorrelation Analysis

The intensity variations within traditional time–distance images contain an abundance of information about bright loops. However, the standard time–distance method cannot capture these oscillations when the loops are not well-defined. For example, oscillations in the presence of complex, overlapping, and faint loops will result in inaccuracies of the time series fitting parameters. In such a circumstance the loops cannot be fitted with fidelity and the method fails. As we have already explored in Section 3.3, by computing the autocorrelation function of the observed intensity variations in time for each pixel, we were able to locate regions that showed strong periodicities. In this subsection, we extend the concept of the one 1D correlation map to a 2D spatio-temporal autocorrelation. As we will see, this new technique reveals the periodicities that remain 'hidden' in the traditional time–distance approach. In a similar manner as the 1D case, the 2D autocorrelation may now be calculated as:

$$c(\Delta t, \Delta x) = \int \int \widetilde{I}(t, x) \widetilde{I}(t + \Delta t, x + \Delta x) dt dx, \tag{3.5}$$

where the autocorrelation is now a function of both time lag and spatial offset Δx, and is normalised as $C(\Delta t, \Delta x) \equiv c(\Delta t, \Delta x)/c(0, 0)$. In principle, this 2D autocorrelation should
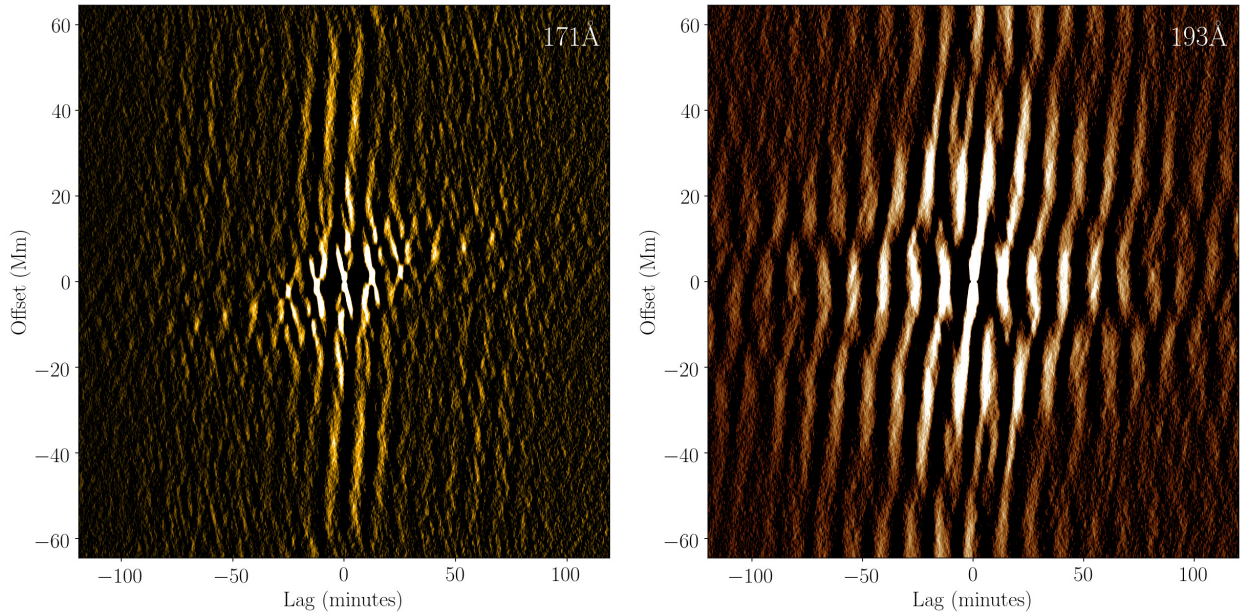
Figure 3.10: Spatio-temporal autocorrelations of the time–distance images in Figure 3.8, generated as a function of spatial offset (Mm) and time lag (minutes). The left image is for the 171 Å waveband and the right is for the 193 wavebands.

also reveal the propagation speed of waves across the time-distance map.

Figure 3.10 displays the autocorrelation as a function of spatial offset (measured in Mm) and time lag (measured in minutes) for the 171 Å (left) and 193 Å (right) wavelength bandpass. As expected, the maximum correlation occurs at zero time lag. The near-vertical streaks have a slope due to the phase shift that exists among the multitude of oscillating loops sampled along the slit. Very noticeable X-like features are aligned in a sequence across time-lag with a different shallower slope. These Xs are most prominent in the 171 Å channel and nearly invisible in the 193 Å bandpass.

In order to understand the origin of the various slopes and features evinced by these autocorrelations, we created a synthetic dataset that consists of a bright oscillating loop embedded in a background of fainter dispersed loops that are also oscillating. The upper-left panel of Figure 3.11 shows the time–distance image of the bright loop in isolation. This bright loop starts oscillating, decays rapidly, and slowly drifts upward along the slit as time passes. The upper right panel reveals the 2D autocorrelation of this bright loop. We immediately see that the X-like structures that we observed in the autocorrelation of the coronal imagery is due to a bright oscillating loop correlating with itself. Furthermore, the slope in the line passing through the centres of the sequence of Xs is caused by the temporal drift of the loop along the slit, possibly due to a moving driver or the wavefront.

The middle left panel of Figure 3.11 shows the background of dispersed faint loops and the middle-right panel shows their autocorrelation. These figures make it clear that
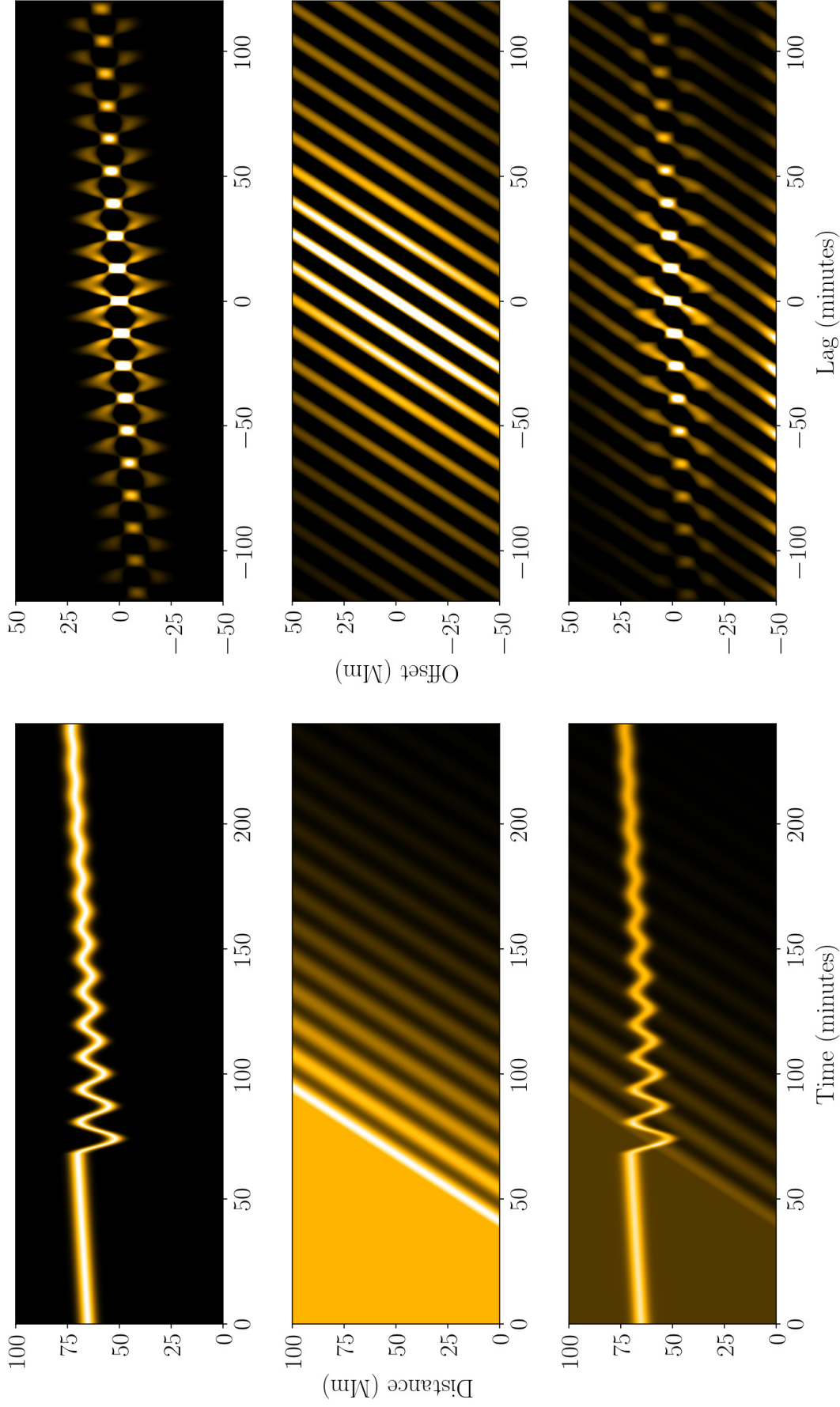
Figure 3.11: Artificial time–distance images (left) and their autocorrelations (right). Top panel: bright loop that suddenly begins oscillating, undergoes temporal decay, and slowly drifts along the slit. The autocorrelation of the bright loop with itself reveals a set of Xs whose centers are sloped according to the linear drift of the loop along the slit. Middle panel: background of faint loops that begin oscillating at different times thus introducing a phase shift that varies along the slit. The autocorrelation of the bundle of faint loops reveals tilted streaks whose slopes are fixed by the spatially varying phase between the different slit positions. Bottom panel: bright and faint loop background superimposed. The prominence of the Xs depends on the relative brightness of the bright loop to the bundle of faint loops.

81
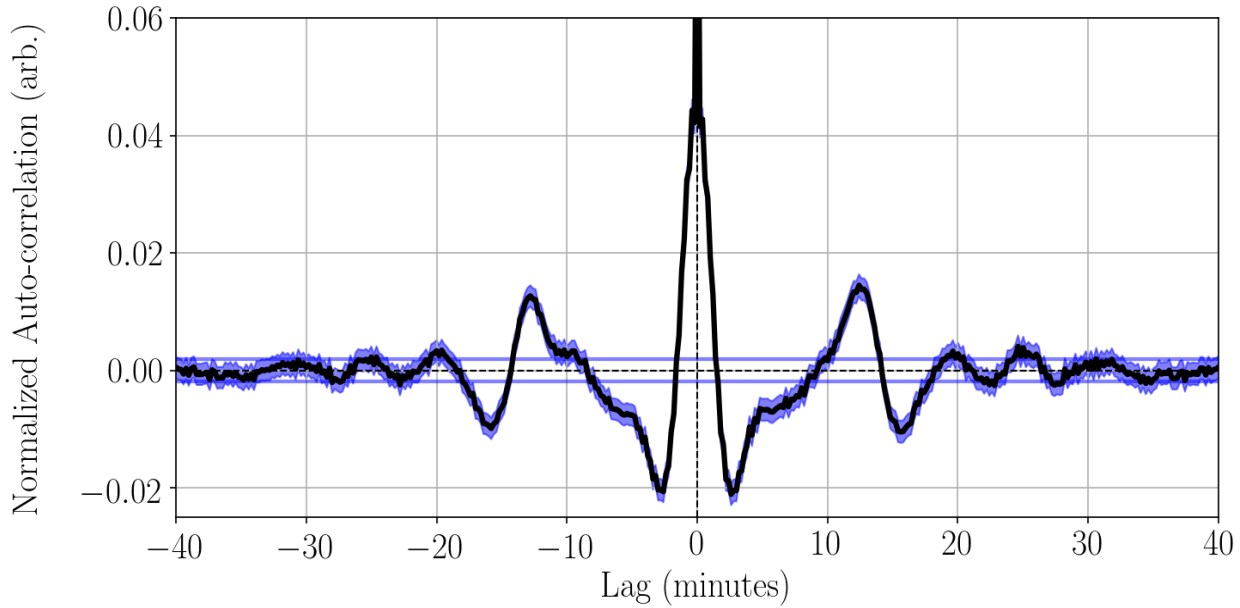
Figure 3.12: Autocorrelations of the time-distance images generated as a function of spatial offset (Mm) and time lag (minutes) for Slit 1 in the 171 Å (left) and 193 Å wavebands. Normalised autocorrelations averaged over a narrow range of spatial offsets (between -3.5 and 3.5 Mm) and plotted vs. time lag. Each X-like feature in Figure 3.5 (left panel) produces a peak of positive correlation. The time lag of peak correlation for the first set of side lobes (to the right and left of the central correlation) corresponds to the dominant period of oscillation. The 95% confidence levels are shown with the solid blue lines.

the tilted vertical streaks in Figure 3.10 are due to the bundle of faint loops inherent in the background of the image. The slope of the streaks arises from a phase shift between these loops in the bundle where the phase changes slowly along the slit. Finally, in the lower left panel of Figure 3.11 we show the superposition of the time–distance image for the bright loop and the bundle of faint loops. The corresponding autocorrelation in the lower right panel demonstrates that the prominence of the X-like features depends on the relative brightness contrast between the bright loop and the faint loop background and the relative phase shift. Note that in Figure 3.8 there is a clear bright loop in the 171 Å channel (upper right panel) with a well-defined amplitude and period; however, due to the relative contrast and the presence of a background of multiple faint loops, the same bright loop viewed in the 193 Å bandpass appears only marginally brighter (lower right panel). For this reason, the sequence of Xs is not so obvious in the autocorrelation of the time–distance image of the 193 Å bandpass.

3.4.3   Comparison of the Two Methods

The autocorrelation contains a plethora of information about the oscillations, e.g., the phase coherence of the primary oscillations over multiple periods, whether the oscillation periods

drift with time, phase relations between different oscillating structures, etc. However, at the moment, we will extract only the period of the dominant periodicity so that we can verify that our autocorrelation procedure and the traditional time series fitting method generate consistent results.

The dominant period of oscillation can be obtained by measuring the location of the peaks (centers of the Xs) in the autocorrelation immediately to the left and right of the central peak at a time lag of zero (see Figure 3.5). To reveal these peaks, we average the autocorrelation over a band of spatial offsets, $\Delta x \in [-3.5\,\mathrm{Mm}, 3.5\,\mathrm{Mm}]$. This average is performed separately at each time lag Δt and the result is shown in Figure 3.12. The central peak arises from the correlation of the signal with itself at the same time. The peaks to the right and left come from correlating the current period with either the previous or the following period in the oscillation. Thus, the autocorrelation peaks at a time lag that corresponds to the wave period.

By fitting a Gaussian to the time lag of maximum correlation for the first side peaks we deduce that the dominant oscillation within Slit 1 has a period of (12.31 ± 0.02) minutes, a number consistent with the 13 minute period measured using the traditional method. If the oscillations were long-lived with steady periods, we would expect to see peaks at each multiple of the period as well and the amplitude of each peak would attenuate only slowly with time lag. That is clearly not the case here. We do see enhanced correlation at 25–26 minutes but the autocorrelation value drops rapidly from peak to peak, as one would expect for a quickly decaying oscillation for which the higher multiples have fewer periods over which to correlate.

3.4.4 Application of the Autocorrelation Method to Complex Arcades

One of the advantages of the autocorrelation procedure is its ability to analyse loop systems for which the standard fitting method would fail. In particular, the autocorrelation procedure presented here can analyse bundles of loops that are poorly differentiated and criss-cross each other. As an illustration, we will analyse the intensity variations on Slit 2, which samples the arcade closer to the limb. On this slit many loops coexist in a complicated overlapping pattern. Furthermore, we will analyse oscillations in periods that lie well before the initiating flares and well after. The goal is to seek low-amplitude 'decayless' oscillations that would be too weak to otherwise fit.

In Figure 3.13, we show the intensity variations as they appeared on Slit 2 in AIA 171 Å (see Figure 3.7 for the location of Slit 2). The upper panel shows the time–distance diagram for a pre-flare phase that spans the 4 hour immediately prior to the analyses presented previously in this work (20:00–23:59 on 2014 January 26). The middle panel displays the
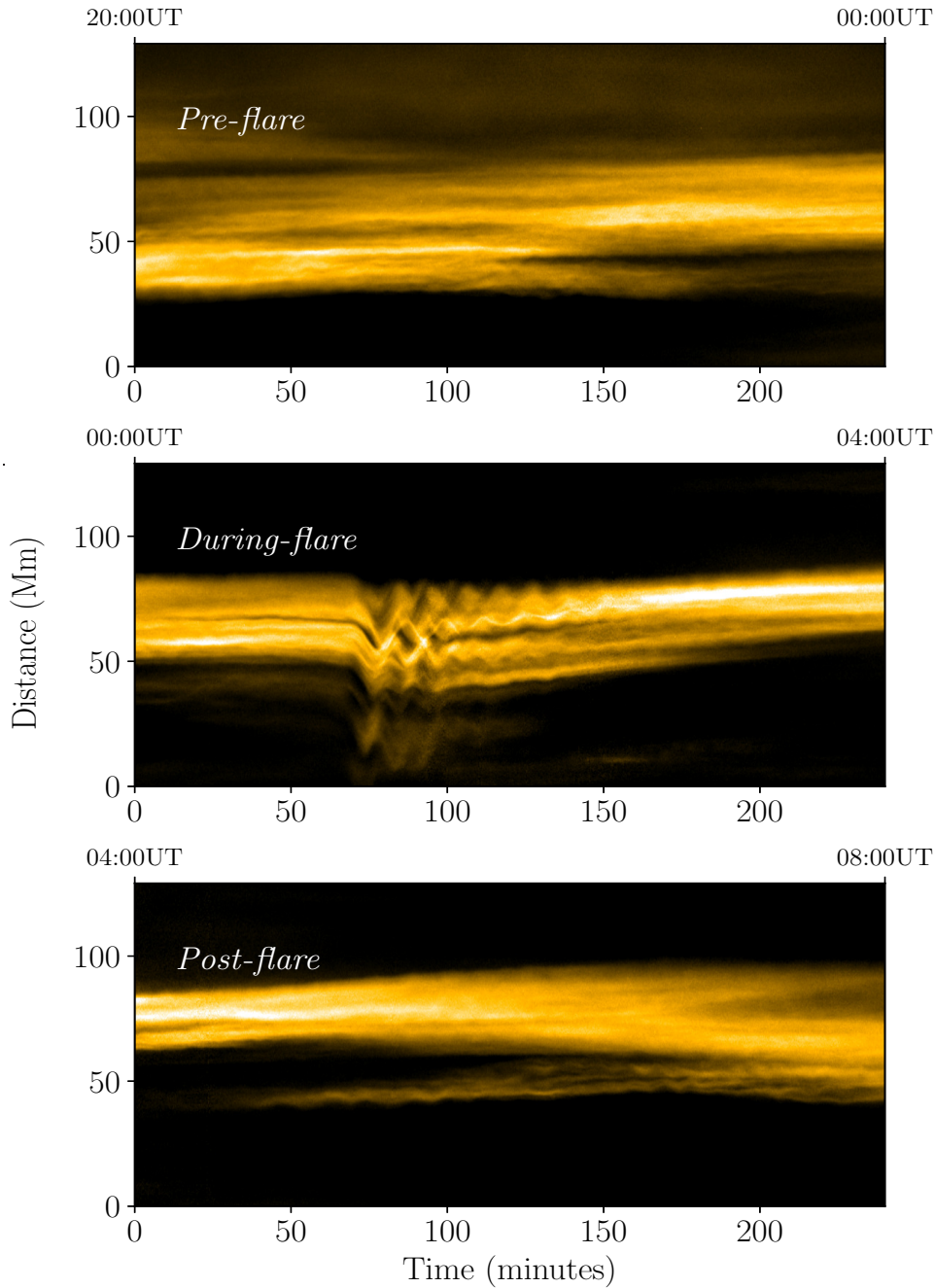
Figure 3.13: Intensity variations in 171 Å waveband as observed on Slit 2 closer to the limb. Top panel: the time–distance diagram for a pre-flare phase (20:00–23:59 on 2014 January 26). Middle panel: intensity variations during a phase coeval with the flares (0:00–04:00 on 2014 January 27). This interval is identical to the one used to analyse the oscillations on Slit 1 (see Figure 3.8). Bottom panel: the time–distance diagram for a post-flare phase (04:00–08:00 on 2014 January 27). Small-amplitude 'decayless' oscillations are present before and after the flares, but their displacements cannot be fitted due to the complex structure of the loop bundle. During the flaring phase, large-amplitude flare-induced oscillations exist, but once again the overlapping loops make the fitting of those loops problematic.
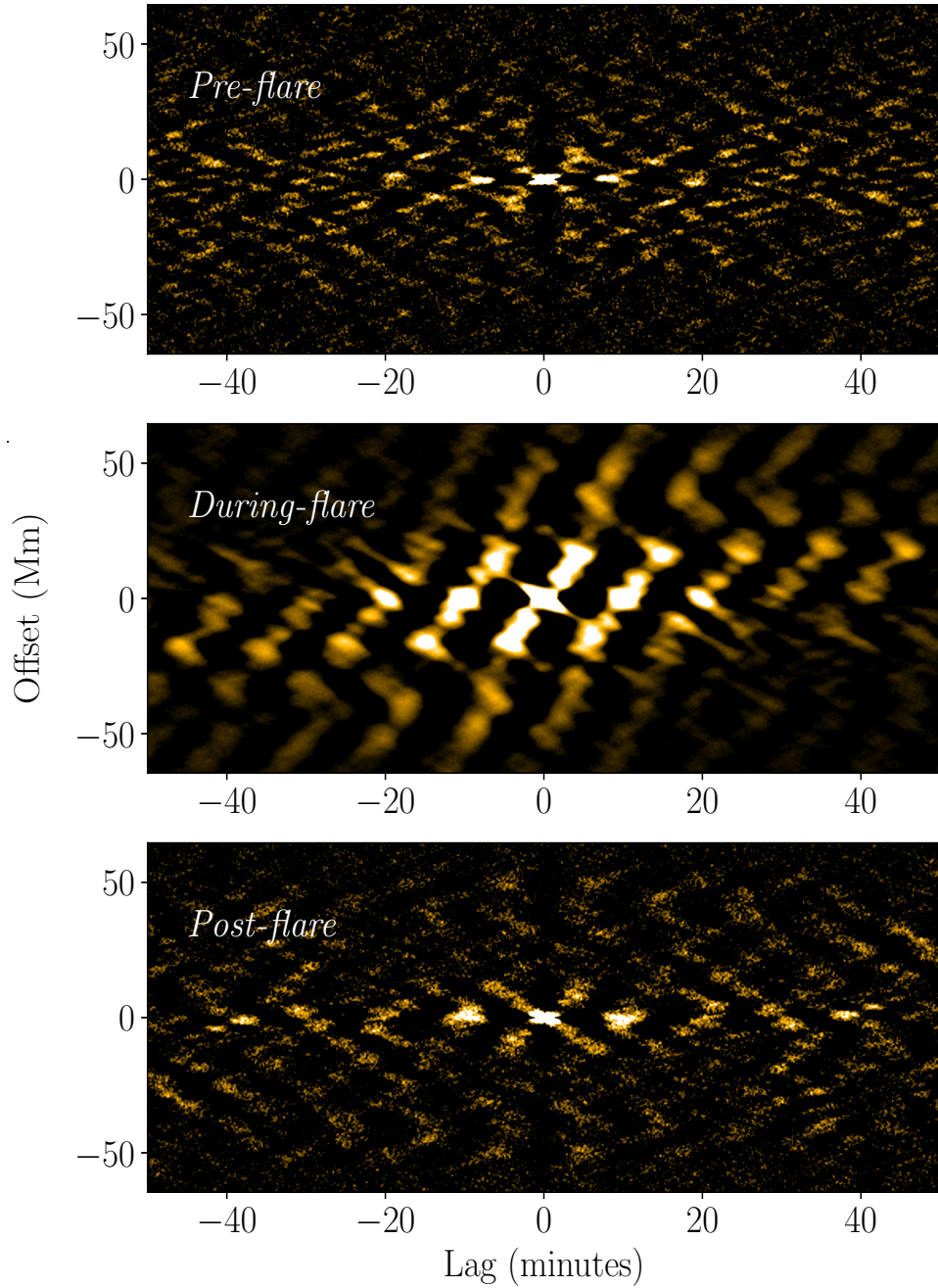
Figure 3.14: 2D autocorrelations of time–distance diagrams appearing in Figure 3.13 obtained for Slit 2. Top panel: the autocorrelation for the pre-flare phase. Middle panel: the autocorrelation for the flaring phase (from 00:00 to 04:00 UT on 2014 January 27). Bottom panel: autocorrelation of the post-flare phase (from 04:00 to 08:00 UT on 2014 January 27). All are for the 171 Å wavebands. The pre-flare and post-flare images reveal the existence of decayless oscillations whose lack of long spatial correlations indicate that different loops oscillate incoherently. Furthermore, the presence of only one or two side lobes on each side of the central correlation indicate poor phase coherence with time.
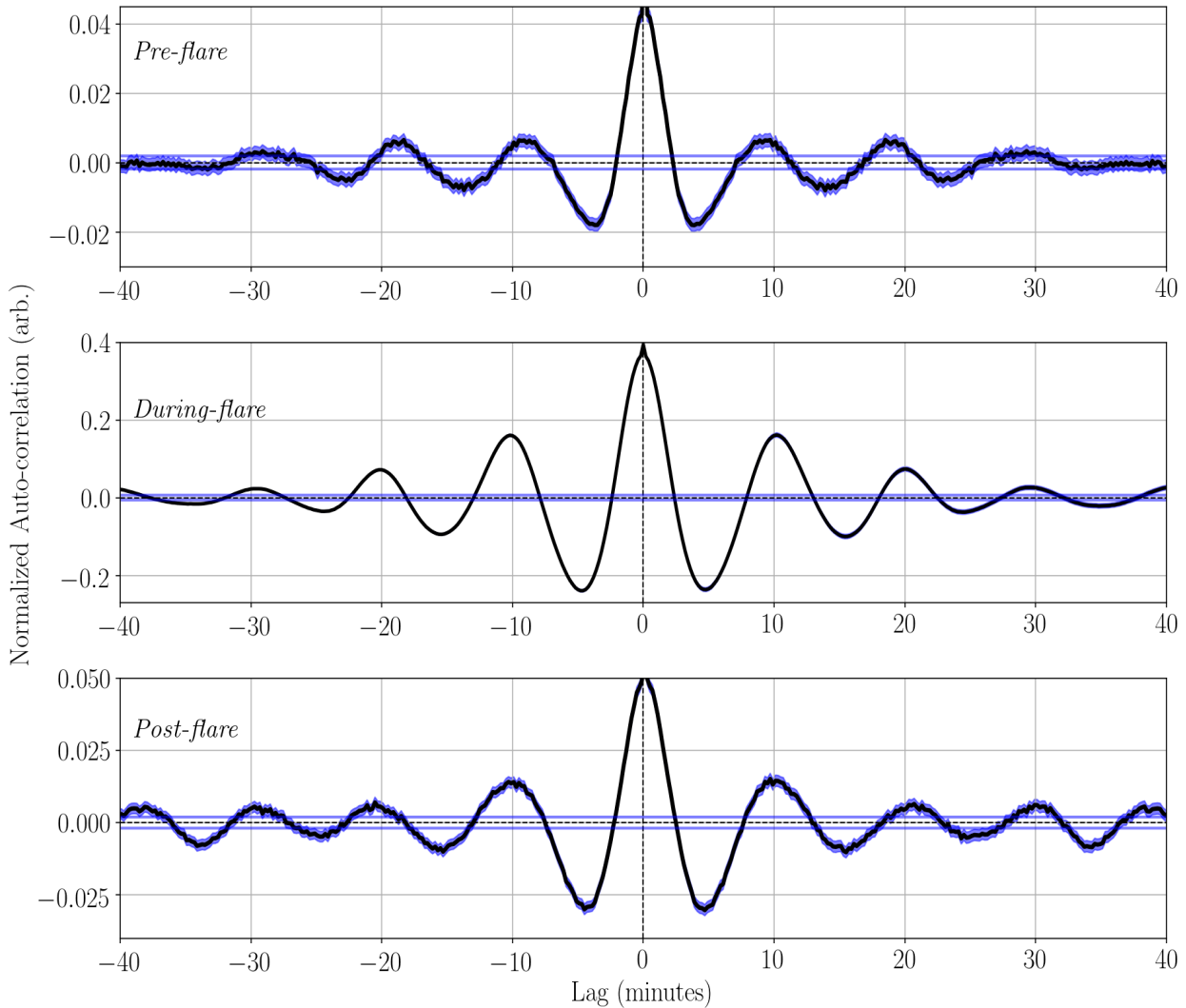
Figure 3.15: Normalised autocorrelation function generated in the same manner as Figure 3.12. The autocorrelations used to generate each panel are those shown in Figure 3.14. Top panel: autocorrelation for the pre-flare phase. Middle panel: autocorrelation for the flaring phase. Bottom panel: autocorrelation for the post-flare duration. The blue lines indicate the 95% confidence intervals derived from a white noise null hypothesis test.

flaring phase (00:00–04:00 on 2014 January 27), which identically matches the 4 hour period that was previously examined in detail for Slit 1. The bottom panel presents the post-flare phase, which is the subsequent 4 hour interval (04:00–08:00 on 2014 January 27). Recall that the duration of flare activity reported by GOES was from 01:05 to 01:39 UT on 2014 January 27. Note that weak oscillation signatures (due to the 'decayless oscillations') do appear in the pre- and post-flare phases. However, the loop structure is complicated and the oscillation amplitudes are relatively weaker that it is not possible to extract the parameters by the standard fitting procedure as outlined earlier in Section 3.4.1.

Figure 3.14 shows the autocorrelation functions derived from the three time durations

indicated in Figure 3.13. The top, middle, and bottom panels correspond to the pre-flare phase, during-flare phase, and post-flare phase, respectively. The oscillations illustrated in the middle panel correspond to the same flare-induced oscillations discussed previously, but viewed at a position closer to the limb. There is a primary period and multiples of that period. All of the loops along the slit oscillate in concert, but do so with a phase shift that changes roughly linearly along the slit (as discussed in Section 3.5). Furthermore, the lack of prominent Xs indicates that the entire bundle of faint loops are oscillating, as opposed to an isolated bright loop.

In the pre- and post-flare duration (top and bottom panel of Figure 3.14), we see that the correlation has little signals for spatial offsets of much more than 5 Mm. There is a slight slope to the correlation that corresponds to a drift of the loop system along the slit as time passes. However, the concentration of signal near a spatial offset of zero indicates that loops do not correlate well with each other. We do, however, find that the temporal correlation possesses structure. For the pre-flare phase we see a central lobe at zero time lag and a single obvious side-lobe to each side of the central lobe. For the post-flare phase, there are additional side lobes located at multiples of the time lag of the primary side lobes. The simplest interpretation of these observations is that there is a primary frequency of oscillation at which each loop oscillates. However, different loops along the slit lack coordination and oscillate at essentially random phases, suggesting that the temporal phase coherence of these small-amplitude oscillations are poor. In the pre-flare phase the amplitude is sufficiently low that only correlations with the immediately preceding or following phase is possible before noise (or another periodicity) dominates. In the post-flare phase the amplitude is larger, and we can see correlations arising from shifts of two or more wave periods.

The exact periods of oscillation can be extracted from line plots of the autocorrelation at zero spatial offset. Averaging over a width containing the Xs, one obtains the correlations shown in Figure 3.15. The dominant period of oscillation in the flaring phase is (10.05 ± 0.01) minutes and (9.81 ± 0.08) minutes in the post-flare phase. The dominant period is slightly shorter in the pre-flare phase at (9.13 ± 0.10) minutes.

3.4.5   2D Fitting Function of a Faint Oscillating Coronal Arcade

As we have already shown, the autocorrelation function can successfully reveal oscillations from loops with low emission. Here, we provide a mathematical derivation of a 2D fitting function that can we used to determine the time series parameters of an observed coronal loop wavefield.

To begin, suppose the loops on a time-distance slit suddenly oscillate in response to some driver, for instance, a flare. Each loop begins to oscillate at different times and the excitation time moves along the slit at a constant speed, c. Furthermore, the arcade oscillates with

frequency $\widetilde{\omega}$ and dampens exponentially with time rate, γ. For simplicity, we also assume the brightness of the arcade is Gaussian across the slit. The total observed brightness may then be written as:

$$S(x, t') = A_0 H(t')e^{-\gamma t'} \cos(\widetilde{\omega}t' + \phi)e^{-x^2/2\delta^2}, \tag{3.6}$$

where A_0 is the initial signal amplitude, $H(t')$ is the Heaviside step function, δ is the brightness spatial width, ϕ is the phase at excitation and t' is the retarded time defined as $t' \equiv t - x/c$. Now, using the Wiener-Khinchin theorem, the auto-correlation can be obtained by computing the inverse Fourier Transform of the power spectrum (see Chapter 2). Note that we use the wave propagation convention of the Fourier transform given by $e^{i(kx - \omega t)}$.

Firstly, we may compute the temporal Fourier transform:

$$
\begin{aligned}
S(x, \omega) &= \frac{A_0 e^{-x^2/2\delta^2}}{2\pi} \int_{-\infty}^{\infty} H(t')e^{-\gamma t'} \cos(\widetilde{\omega}t' + \phi)e^{-i\omega t}dt, \\
&= \frac{A_0 e^{-x^2/2\delta^2}}{2\pi} \int_{0}^{\infty} e^{-\gamma t'} \cos(\widetilde{\omega}t' + \phi)e^{-i\omega t'}e^{-i\omega x/c}dt'.
\end{aligned}
\tag{3.7}
$$

The cosine term may be expanded[2] to obtain two integrals, I_1 and I_2:

$$
\begin{aligned}
I_1 &= \int_{0}^{\infty} e^{-\gamma t'} \cos(\widetilde{\omega}t')e^{-i\omega t'}dt', \\
&= \int_{0}^{\infty} e^{-t'(\gamma + i\omega)} \cos(\widetilde{\omega}t')dt', \\
&= \mathcal{L}(\cos(\widetilde{\omega}t')), \\
&= \frac{\gamma + i\omega}{\widetilde{\omega}^2 + (\gamma + i\omega)^2},
\end{aligned}
\tag{3.8}
$$

where $\mathcal{L}$ is the Laplace transform operator. Similarly for I_2, we have:

$$
\begin{aligned}
I_2 &= \int_{0}^{\infty} e^{-t'(\gamma + i\omega)} \sin(\widetilde{\omega}t')dt' \\
&= \mathcal{L}(\sin(\widetilde{\omega}t'))
\end{aligned}
\tag{3.9}
$$

---

[2] The trigonometric identity used is $\cos(\alpha \pm \beta) = \cos(\alpha)\cos(\beta) \mp \sin(\alpha)\sin(\beta)$.

$$= \frac{\widetilde{\omega}}{\widetilde{\omega}^2 + (\gamma + i\omega)^2},$$

and the temporal Fourier transform is therefore given by:

$$S(x, \omega) = \frac{A_0 e^{\frac{-i\omega x}{c}} e^{\frac{-x^2}{2\delta^2}}}{2\pi} \Theta(\omega), \tag{3.10}$$

where

$$\Theta(\omega) = \frac{((\gamma + i\omega)\cos\phi - \widetilde{\omega}\sin\phi)}{(\omega^2 - \widetilde{\omega}^2 - \gamma^2 - 2i\gamma\omega)}. \tag{3.11}$$

Now, taking the Fourier transform in the space coordinate yields:

$$
\begin{aligned}
S(k, \omega) &= A_0 \frac{\Theta(\omega)}{(2\pi)^2} \int_{-\infty}^{\infty} e^{-x^2/2\delta^2} e^{i(k-\omega/c)x} dx, \\
&= A_0 \frac{\Theta(\omega)}{(2\pi)^2} \int_{-\infty}^{\infty} e^{-(x^2/2\delta^2 - ik'x)} dx.
\end{aligned}
\tag{3.12}
$$

where $k' = k - \omega/c$. We may rewrite Equation (3.12) by completing the square in the argument of the exponential:

$$S(k, \omega) = A_0 \frac{\Theta(\omega)}{(2\pi)^2} e^{\delta^2(ik')^2/2} \int_{-\infty}^{\infty} e^{-(x+i\delta^2 k')^2/2\delta^2} dx. \tag{3.13}$$

By letting $x' = x + i\delta^2 k'$ and using a Gaussian integral identity, we arrive at the following expression:

$$S(k, \omega) = A_0 \frac{\Theta(\omega)}{(2\pi)^2} \sqrt{2\pi} \delta e^{-\delta^2(k-\omega/c)^2/2}. \tag{3.14}$$

Hence, the power spectrum is simply

$$|S(k, \omega)|^2 = A_0 \frac{|\Theta(\omega)|^2}{(2\pi)^4} (2\pi)\delta^2 e^{-\delta^2(k-\omega/c)^2}, \tag{3.15}$$

where

$$|\Theta(\omega)|^2 = \Theta\overline{\Theta} = \frac{(\omega^2 + \gamma^2)\cos^2\phi + \widetilde{\omega}^2\sin^2\phi - 2\gamma\widetilde{\omega}\cos\phi\sin\phi}{[\omega^2 - (\widetilde{\omega}^2 + \gamma^2)]^2 + 4\gamma^2\omega^2}. \tag{3.16}$$

We may now compute the autocorrelation, c, by taking the inverse Fourier Transform of Equation (3.15). For the space coordinate, we have:

$$C(\Delta x, \omega) = \frac{A_0 \delta^2}{(2\pi)^3} |\Theta(\omega)|^2 \int_{-\infty}^{\infty} e^{-\delta^2(k-\omega/c)} e^{-ik\Delta x} dk. \tag{3.17}$$

Using a change of variables and completing the square, we arrive at:

$$C(\Delta x, \omega) = \frac{A_0 \delta^2}{(2\pi)^3} |\Theta(\omega)|^2 e^{-i\omega\Delta x/c} e^{-\Delta x^2/4\delta^2} \int_{-\infty}^{\infty} e^{-\delta^2(k'+i\Delta x/2\delta)^2} dk', \tag{3.18}$$

which can be reduced to,

$$C(\Delta x, \omega) = \frac{A_0 \delta^2}{(2\pi)^3} |\Theta(\omega)|^2 \frac{\sqrt{\pi}}{\delta} e^{-i\omega\Delta x/c} e^{-\Delta x^2/4\delta^2}. \tag{3.19}$$

The inverse Fourier transform in the time coordinate is:

$$\begin{aligned}
C(\Delta x, \Delta t) &= \frac{A_0 \delta \sqrt{\pi}}{(2\pi)^3} e^{-\Delta x^2/4\delta^2} \int_{-\infty}^{\infty} |\Theta(\omega)|^2 e^{i\omega(\Delta t - \Delta x/c)} d\omega, \\
&= \frac{A_0 \delta \sqrt{\pi}}{(2\pi)^3} e^{-\Delta x^2/4\delta^2} \int_{-\infty}^{\infty} |\Theta(\omega)|^2 e^{i\omega\Delta t'} d\omega,
\end{aligned} \tag{3.20}$$

where $\Delta t' \equiv \Delta t - \Delta x/c$. Equation (3.20) must be solved by contour integration due to the poles in denominator of $\Theta(\omega)$. The poles of $\Theta(\omega)$ are calculated by setting the denominator to zero:

$$[\omega^2 - (\widetilde{\omega}^2 + \gamma^2)]^2 + 4\gamma^2\omega^2 = 0. \tag{3.21}$$

Equation (3.21) is a quadratic in ω^2 and has four simple poles (see Figure 3.16):

$$\omega_1 = -\widetilde{\omega} + i\gamma, \qquad \omega_2 = -\widetilde{\omega} - i\gamma, \qquad \omega_3 = \widetilde{\omega} + i\gamma, \qquad \omega_4 = \widetilde{\omega} - i\gamma.$$

We now choose a closed contour[3] such that $|e^{i\omega\Delta t'}| = |e^{-\text{Im}(\omega)\Delta t'}|$ tends to zero. Therefore, for $\text{Im}(\omega) < 0$ and $\Delta t' > 0$, the exponential vanishes as $|\omega| \to \infty$ and we close the contour in the upper-half plane. The two residues we pick up are at ω_1 and ω_3. The denominator of $\Theta(\omega)$ has poles at:

$$[\omega^2 - (\widetilde{\omega}^2 + \gamma^2)]^2 + 4\gamma^2\omega^2 = (\omega - \omega_1)(\omega - \omega_2)(\omega - \omega_3)(\omega - \omega_4), \tag{3.22}$$

and at ω_1 we have

---

[3] By Jordan's lemma, we may take $\oint_C f(z)e^{iaz} dz = \int_{C_1} f(z)e^{iaz} dz + \int_{C_2} f(z)e^{iaz} dz$ where $C = C_1 + C_2$ is a closed contour.
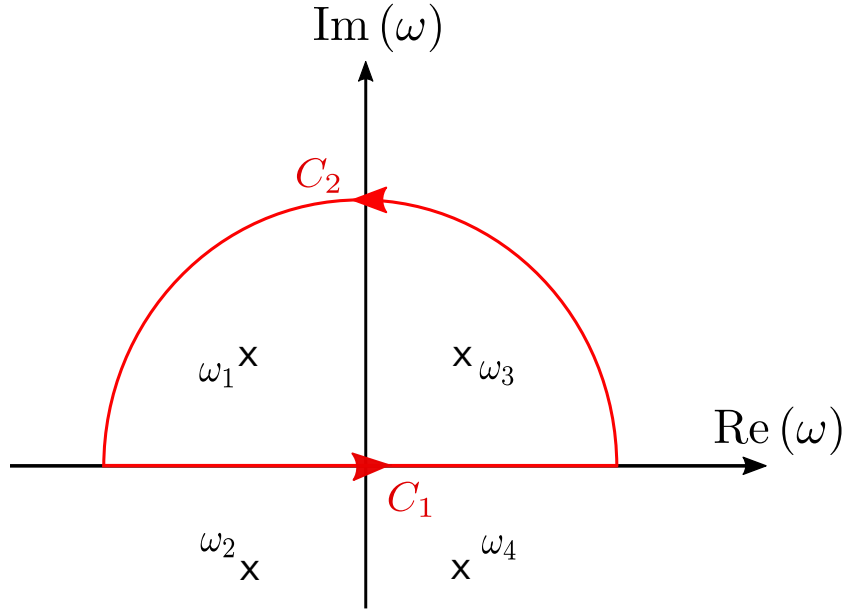
Figure 3.16: All four residues of Equation (3.20) indicated by crosses in the ω-plane. The red semi-circle depicts the closed inversion contour used to pick up the two residues for $\Delta t' > 0$. The symmetry of the residues yield a symmetric autocorrelation function for $\Delta t' < 0$.

$$\frac{[\omega^2 - (\widetilde{\omega}^2 + \gamma^2)]^2 + 4\gamma^2\omega^2}{(\omega - \omega_1)} = (\omega_1 - \omega_2)(\omega_1 - \omega_3)(\omega_1 - \omega_4),$$

$$= 8i\gamma\widetilde{\omega}(\widetilde{\omega} - i\gamma). \tag{3.23}$$

The corresponding numerator of $\Theta(\omega)$ at ω_1 is:

$$\widetilde{\omega}^2 - \gamma\widetilde{\omega}\sin 2\phi - 2i\gamma\widetilde{\omega}\cos^2\phi, \tag{3.24}$$

and hence

$$\Theta(\omega_1) = \frac{\widetilde{\omega} - \gamma\sin 2\phi - 2i\gamma\cos^2\phi}{8i\gamma(\widetilde{\omega} - i\gamma)}. \tag{3.25}$$

Therefore, the residue at the pole $\omega = \omega_1$ is accounted by:

$$\frac{\widetilde{\omega} - \gamma\sin 2\phi - 2i\gamma\cos^2\phi}{8i\gamma(\widetilde{\omega} - i\gamma)}e^{i\omega_1\Delta t'}. \tag{3.26}$$

Carrying out the same analysis at the the pole, $\omega = \omega_3$, we calculate the residue to be:

$$\frac{\widetilde{\omega} - \gamma\sin 2\phi + 2i\gamma\cos^2\phi}{8i\gamma(\widetilde{\omega} + i\gamma)}e^{i\omega_3\Delta t'}. \tag{3.27}$$

91

Thus, by the residue theorem we have:

$$\oint_{-\infty}^{\infty} |\Theta(\omega)|^2 e^{i\omega\Delta t'} d\omega = 2\pi i e^{-\gamma\Delta t'} \left[\frac{\widetilde{\omega} - \gamma\sin 2\phi - 2i\gamma\cos^2\phi}{8i\gamma(\widetilde{\omega} - i\gamma)} e^{-i\widetilde{\omega}\Delta t'} + \frac{\widetilde{\omega} - \gamma\sin 2\phi + 2i\gamma\cos^2\phi}{8i\gamma(\widetilde{\omega} + i\gamma)} e^{i\widetilde{\omega}\Delta t'} \right]$$

(3.28)

The terms in the square brackets can be rewritten as:

$$\frac{1}{8i\gamma(\widetilde{\omega}^2 + \gamma^2)} \left[(\alpha - i\beta)(\widetilde{\omega} + i\gamma)e^{-i\widetilde{\omega}\Delta t'} + (\alpha - i\beta)(\omega - i\gamma)e^{i\widetilde{\omega}\Delta t'} \right],$$

(3.29)

where $\alpha = \widetilde{\omega} - \gamma\sin 2\phi$ and $\beta = 2\gamma\cos^2\phi$. This expression can be further simplified by expanding the terms and using Euler's identity:

$$= \frac{1}{8i\gamma(\widetilde{\omega}^2 + \gamma^2)} [(\alpha\widetilde{\omega} + i\gamma\alpha - i\beta\widetilde{\omega} + \beta\gamma)(\cos(\widetilde{\omega}\Delta t') - i\sin(\widetilde{\omega}\Delta t'))$$
$$+ (\alpha\widetilde{\omega} - i\gamma\alpha - i\beta\widetilde{\omega} - \beta\gamma)(\cos(\widetilde{\omega}\Delta t') + i\sin(\widetilde{\omega}\Delta t'))]$$
$$= \frac{1}{4i\gamma(\widetilde{\omega}^2 + \gamma^2)} \left[(\widetilde{\omega}^2 + 2\gamma^2\cos\phi^2 - \gamma\widetilde{\omega}\sin 2\phi)\cos(\widetilde{\omega}\Delta t') - (\gamma\widetilde{\omega}\cos 2\phi + \gamma^2\sin 2\phi)\sin(\widetilde{\omega}\Delta t') \right].$$

(3.30)

The expression in the square brackets of Equation (3.30) is in the form:

$$A\cos\theta - B\sin\theta.$$

If we let

$$R\cos(\widetilde{\omega}\Delta t' + \theta) = R\cos(\widetilde{\omega}\Delta t')\cos(\theta) - R\sin(\widetilde{\omega}\Delta t')\sin(\theta),$$

(3.31)

then by comparing the coefficients of Equations (3.30) and (3.31), we observe that:

$$R\cos(\theta) = \widetilde{\omega}^2 + 2\gamma^2\cos^2\phi - \gamma\widetilde{\omega}\sin 2\phi, \qquad R\sin(\theta) = \gamma\widetilde{\omega}\cos 2\phi + \gamma^2\sin 2\phi,$$

where

$$R^2 = (\widetilde{\omega}^2 + 2\gamma^2\cos^2\phi - \gamma\widetilde{\omega}\sin 2\phi)^2 + (\gamma\widetilde{\omega}\cos 2\phi + \gamma^2\sin 2\phi)^2,$$

and

$$\tan\theta = \frac{\gamma\widetilde{\omega}\cos 2\phi + \gamma^2\sin 2\phi}{\widetilde{\omega}^2 + 2\gamma^2\cos\phi^2 - \gamma\widetilde{\omega}\sin 2\phi}.$$

Hence, the integral in Equation (3.28) reduces to:

$$\oint_{-\infty}^{\infty} |\Theta(\omega)|^2 e^{i\omega\Delta t'} d\omega = \frac{\pi}{2\gamma(\widetilde{\omega}^2 + \gamma^2)} e^{-\gamma\Delta t'} R\cos(\widetilde{\omega}\Delta t' + \theta). \tag{3.32}$$

The autocorrelation function derived from the contour in the upper-half plane is given by the expression:

$$c(\Delta x, \Delta t') = \frac{A_0 \delta R}{2^4 \pi^{3/2} \left(\widetilde{\omega}^2 + \gamma^2\right)\gamma} e^{-\Delta x^2/4\delta^2} e^{-\gamma\Delta t'} \cos(\widetilde{\omega}\Delta t' + \theta). \tag{3.33}$$

On the other hand, if $\Delta t' < 0$ we would close downwards and pick up the residues at ω_2 and ω_4. The contour integrals around these poles are clockwise so the residue theorem would give $-2\pi i \sum$ residues and a symmetric result is obtained, as expected for the autocorrelation function. Therefore, a normalised autocorrelation ($C(\Delta x, \Delta t') = c(\Delta x, \Delta t')/c(0,0)$) that is valid for a symmetric $\Delta t'$ is described by the following:

$$C(\Delta x, \Delta t') = Ae^{-\Delta x^2/4\delta^2} e^{-\gamma|\Delta t'|} \cos(\widetilde{\omega}|\Delta t'| + \theta), \tag{3.34}$$

where $A = \sec\theta$ is a constant.

Now that we have derived a 2D function describing the autocorrelation of the faint background loops, we aim to fit this model to the observed data. Our objective is to successfully extract the time series parameters such as the periodicity and phase speed of the flare-induced oscillations. We further demonstrate the advantage of the spatio-temporal autocorrelation by performing our analysis on the 171 Å data where there are signatures of faint oscillations surrounding the visible bright loop, and also on the 304, 193 and 211 Å datasets were no prominent bright structure can be readily observed.

Figure 3.17 shows the spatio-temporal autocorrelations for the 304, 171, 193 and 211 Å wavebands, and the white lines indicate the best fit to the data using non-linear least squares fitting. The estimated time series parameters are listed in Table 3.3. We find that the background loops clearly oscillate in all four wavebands. The periodicity of the background loops in the 304, 193 and 211 Å waveband is around 14 minutes, whereas the 171 Å waveband possesses a shorter component of around 10 minutes. The spatial decay of the waveforms are approximately 22 Mm for the 304, 17 and 211 Å channels and about 17 Mm for the 193 Å, suggesting that the signals possess a strong spatial coherence across all four EUV wavebands. On the other hand, the estimated waveform decay times have values of around 15-23 minutes, which implies that the waves have decayed relatively quickly in only cycle, with the exception of the 304 Å channel. Although both of the spatial and temporal decay quantities have not received significant attention in theoretical studies, we believe they can be important for characterising the wave behaviour in coronal loops. Furthermore, it is clear that 171 Å channel exhibits the fastest propagation of signals with a value around
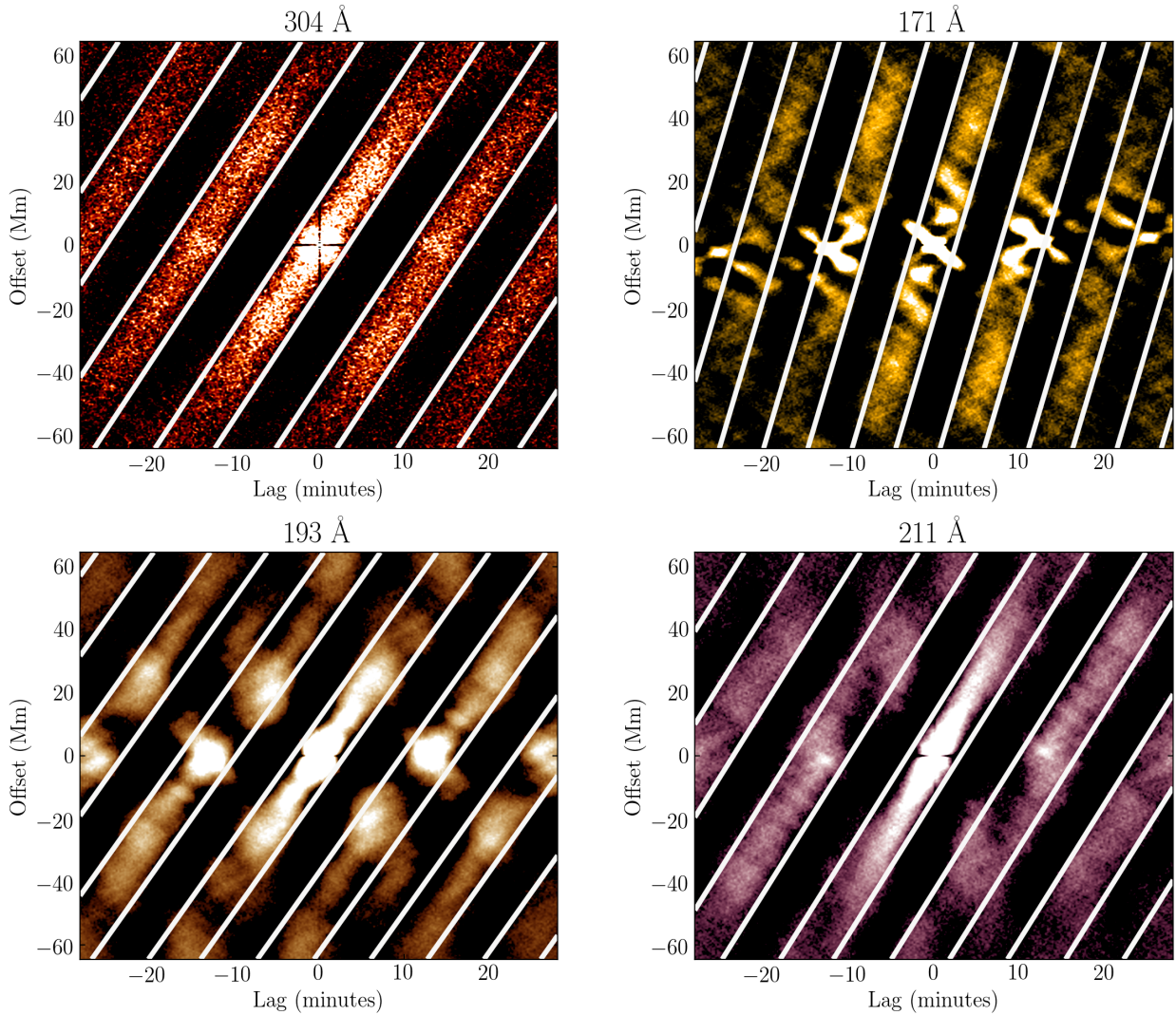
Figure 3.17: Same as Figure 3.10 but including the diffuse 304 and 211 Å wavebands for the flaring dataset. The solid white lines indicate the best fits to the data using our derived 2D fitting function. All datasets have been pre-processed with a high-pass filter using a Gaussian kernel of width $\sigma = 10$ frames, except for the 304 Å waveband, which has been filtered using a kernel of width $\sigma = 15$ frames.

153 kms^{-1}, whereas the 304, 193 and 211 Å data possess a relatively slower propagation speed. This may reflect the fact that the wavefront was most clearly observed in the 171 Å channel and, hence, the disturbance originated in the lower transition region, as opposed to the hotter, upper layers of the corona. Our interpretation is consistent with Conde et al. (2020) who studied this event on the following day using spectrographic and Doppler velocity observations, and found evidence of simultaneous oscillations propagating from the lower photosphere to the upper corona.

Table 3.3: Estimated wavefield parameters of oscillations in 304, 171, 193 and 211 Å wavebands shown in Figure 3.17 using our 2D fitting function. The associated 1σ errors are obtained from the covariance matrix.

Waveband (Å)	Decay length (Mm)	Period (mins.)	Decay time (mins.)	Phase speed (kms^{-1})	Phase (deg)
304	22.56 ± 0.09	14.27 ± 0.01	23.45 ± 0.19	68.48 ± 0.07	-5.15 ± 0.22
171	22.89 ± 0.09	10.36 ± 0.01	14.37 ± 0.09	152.96 ± 0.26	-0.01 ± 0.01
193	17.35 ± 0.27	13.29 ± 0.01	16.23 ± 0.05	63.56 ± 0.03	28.64 ± 0.53
211	21.76 ± 0.47	13.59 ± 0.01	15.59 ± 0.04	72.22 ± 0.03	1.14 ± 0.87

3.5 Discussion

3.5.1 Oscillations During the Flares

The primary period of oscillation of the flare-induced waves in the 171 Å is clearly a function of the position of the slit. The oscillations observed on Slit 1, the slit furthest from the limb, possessed a dominant period of 12.31 minutes, while the slit closer to limb, Slit 2, had a shorter period, 10.05 minutes. Without performing similar analyses along a plethora of slits, we cannot ascertain whether the dominant period is a smooth function of height above the limb.

Hindman and Jain (2015) have argued that the bundles of magnetic loops in an arcade oscillate together and that the true cavity is multidimensional as opposed to an individual loop. Figures 3.8 and 3.9 clearly suggest this. Nearby loops are likely to have similar lengths, magnetic field strengths, and densities and so we expect the entire arcade to oscillate with similar periods in response to the driver. Loops at different positions along the slit oscillate with phase shifts relative to each other and those phases change roughly linearly along the slit. If the waves propagate both along the field and transverse to the field, then we must entertain the possibility that magnetic pressure also plays a role, even if magnetic tension is the main restoring force. The motions studied here, are clearly transverse to the magnetic field lines and the phase shift appears to be travelling across the magnetic field lines. This suggests that there is a compression of magnetic field lines, perhaps, indicating the presence of fast MHD waves.

To test this idea further, we measure the speed of phase propagation along the slit directly from the slope of the near-vertical streaks in the autocorrelation diagrams. Doing so produces a phase speed of 153 kms^{-1} for the 171 Å bandpass and about 63 kms^{-1} for the 193 Å channel. Both slits generate similar phase speed values with the 171 Å being around twice as large. Both of these speeds are sufficiently slow compared to the local Alfvén speed that if the phase shift was caused by cross-field propagation the wave vector would need to be strongly radial, with only a small component aligned with the slits. A more likely interpretation for such a phase shift is a moving driver. Recall that the initial

propagation speed of the wavefront was 40 kms^{-1} as projected on the plane of the sky (see Figure 3.4). The similarity of this speed with that of the propagation of the wavefront may be coincidental, but it may also suggest that the wavefront acted as a moving wave-excitation source. This conclusion is further supported by the observation that the large-amplitude flare-induced oscillations appear to have been excited slightly before the peak of the X-ray flux from the first flare that was recorded by the GOES observatories (see Figure 3.2).

3.5.2 Oscillations Before and After the Flares

Along Slit 2, we see oscillations before, during, and after flaring activity. Prior to the flares the dominant period appears to be 9.13 minutes and each strand of the bundle of loops appears to oscillate rather incoherently with more distant strands. This can also be confirmed in our initial analysis using the correlation maps (see Figure 3.6). Well after the flares, around 12 hours later, the primary period appears to be 9.81 minutes and, once again, the individual loops that are well-separated oscillate somewhat incoherently. The correlation length in both cases is roughly 5 Mm. We reiterate and emphasize that the low-amplitude oscillations presented here would be laborious to fit with the traditional time–distance fitting method with fidelity due to the complexity of overlapping loops. The autocorrelation method presented here is a promising tool for analysing small-amplitude waves in coronal arcades at all times. Detailed studies of the prevalence of such complex small-amplitude oscillations can now be conducted with the key advantages of being simpler to implement and being able to form parts of automated search tools.

It is possible that the difference in dominant period between the pre-flare and post-flare phases (9.13 minutes and 9.81 minutes, respectively) indicates a change in the arcade's resonant structure. The heating induced by the flares may have initiated a change in Alfvén speed along the loops under analysis. We note, however, that a similar change in apparent frequency may arise from a change in the distribution of waves with different cross-field wavenumber. Hindman and Jain (2015, 2018) have demonstrated that coronal arcades can act as waveguides, with resonances only in the radial direction (radial to the limb) and in the direction parallel to the field lines. The direction along the axis of the arcade (in this case parallel to the slit), may be unquantized. Each axial wavenumber has a different frequency and when the energy is redistributed among this continuum of wavenumbers, the distribution of energy among modes with different periods is also changed. One piece of evidence that supports this latter scenario is that the large-amplitude oscillations that were initiated during the flaring activity also have a dominant period of 10 minutes along Slit 2. It could very well be that the post-flare phase is dominated by waves initiated during the flare that have decayed in amplitude. Therefore, the intensity variations in the post-flare phase may be a superposition of oscillations with periodicities of 9 and 10 minutes.

3.6 Summary

In this chapter, we presented a new observational technique that can successfully reveal the waveforms present within EUV data by means of autocorrelations. We firstly showed that the 1D autocorrelation in each spatial domain can successfully reveal the global oscillations of the active region. This method has the key advantage that it can be used as an initial analysis to probe for regions where oscillations are expected, and it can be easily applied to form parts of automated search tools, together alongside, for example, the coronal period maps technique (Nakariakov and King 2007) and pixelised wavelet filtering method (Sych and Nakariakov 2008). A benefit of the autocorrelation technique is its fast computation time, which would also make it an auspicious tool for the future generation of high-resolution solar detectors.

We further investigated transverse oscillations within a 12 hour dataset where the traditional Gaussian fitting technique can fail due to a poor image contrast. We demonstrated the utility of the spatio-temporal autocorrelation, which can reveal the phase coherence of both flare-induced and non-flaring waveforms. We found that the small-amplitude oscillations lack a spatial and temporal phase coherence, adding credence to the multi-dimensional arcade framework by Hindman and Jain (2014). The periods of oscillations were found to be 9 minutes before the flare, 9-14 minutes during the flare, and around 10 minutes after the flare. We suggested that the intensity variations in the post-flare regime could be due to a superposition of waves from the pre-flare and flaring events. Lastly, we demonstrated that the autocorrelation method can also be used to confidently reveal the background waveforms in various EUV wavebands. This provided observational evidence that the signals in distinct wavelengths exhibit different properties, enabling us to distinguish that these oscillations were likely to be triggered in the transition region-lower corona region.

It is clear that the autocorrelation is a highly promising tool for analysing oscillations in the solar corona. However, despite the advantages we have highlighted, there remains several drawbacks to the method. For instance, one major problem is the initial filtering of signals. It has been shown that coronal time series can be highly non-stationary (e.g. Kolotkov et al. 2016) and can exhibit long term modulations in periodicity and amplitude. To confidently reveal the true periodic motion, the time series must be made stationary prior to the analysis. Although this is also a common preliminary step in FFT and wavelet analysis (see Chapter 2), filtering any frequency component essentially removes parts of the underlying physics and the choice of filtering is non-unique. In other words, the amount of detrending will generally depend the quality of the observational data (e.g. wavelength channel, signal-to-noise ratio), and does contain a manual element. Nevertheless, once the filter properties have been established (see Appendix A), the method can be successfully automated to multiple datasets. Another challenge of the autocorrelation technique is the

choice of a significance test. In this work, we employed a test based on a white noise null hypothesis, however, evidence of power-law behaviour in coronal time series has been previously reported (e.g. Ireland et al. 2015). Therefore, an advancement of the technique presented here would be to incorporate more realistic significance tests. For this, the reader is forwarded to the papers by Bartlett (1946) and Taylor (1984). Lastly, we reiterate that the 2D fitting function of the background oscillations we derived is also likely to be not unique for all observations. For example, in our derivation we assumed an exponential decay time, whereas a handful of studies have suggested that a Gaussian decay may be more appropriate (Hood et al. 2013; Pascoe et al. 2016b; Morton and Mooroogen 2016). The fitting function can still be improved to include more complicated waveforms, although this will probably have to be numerically computed. Despite this distinction, we believe that this would not drastically change our results presented here.

4

Is it Possible to Identify the High-frequency MHD waves of an Oscillating Coronal Loop?[1]

> "Here it is standing: atoms with consciousness; matter with curiosity.
> Stands at the sea, wonders at wondering:
> I, a universe of atoms, an atom in the universe."

— Richard P. Feynman.

We investigate the high frequency component of an oscillating coronal loop by performing a spectral analysis using the Fast Fourier Transform (FFT) and Wavelet Transform (WT) on our observation and compare our results with basic simulations. We find that both spectral methods incorrectly identify signatures of a second harmonic superposed on to the dominant frequency of the loop. We demonstrate that the second harmonic, and several higher order harmonics, are artificial and arise due to the non-uniform brightness of the loop. Possible signatures of beat phenomenon in coronal loops are discussed.

4.1 Introduction to the Chapter

Coronal loops are often observed to oscillate in the plane of the sky. To date, substantial efforts involving theory, simulations, and observations of these oscillatory phenomena have been made to extract the inaccessible yet imperative physical properties of the loops by MHD seismology. The commonly accepted model describes the transverse perturbations as the free, instantaneous, and non-axisymmetric (kink) eigenmodes of a cylindrical waveguide (e.g. Roberts et al. 1984). However, alternative frameworks consisting of an entire magnetic arcade also exist (Hindman and Jain 2014, 2015, 2018). A recent review of MHD waves and oscillations can be found in Nakariakov and Kolotkov (2020).

Initially, the spatially resolved motion of coronal loops was discovered by TRACE in EUV wavelengths as periodic displacements induced by flaring activity (Aschwanden et al. 1999). Since then, further studies have shown that these periodicities range from a few to several tens of minutes (Aschwanden et al. 2002) and are found to be strongly correlated with the length of the loop (Goddard et al. 2016). However, their excitation mechanism is debated. Hudson and Warmuth (2004) suggested that a fast-mode shock wave expelled from a flaring epicentre may be important. In a more recent observational catalogue of 58 events, Zimovets and Nakariakov (2015) found that the majority (57 events) of transverse oscillations are perturbed from an equilibrium by nearby impulsive eruptions, instead of shock waves. Zimovets and Nakariakov (2015) also reported that 53 of these events were associated with flares, which may imply a relationship between these two types of magnetic activities. Although it is agreed that flares play an important role in the excitation of loop oscillations, why certain frequencies are enhanced over others in nearby loops remains unknown.

In addition to impulsive loop oscillations, observational efforts have revealed ambient, small-amplitude oscillations that persist in the absence of any (obvious) driver without a significant decay (Wang et al. 2012; Nisticò et al. 2013; Anfinogentov et al. 2015; Duckenfield et al. 2018). Their periods of oscillation are similar to the impulsive regime and different segments of the loop, from the footpoints to the apex, have been shown to oscillate in phase (Anfinogentov et al. 2013). Even though it is agreed that their source of oscillation must be small scale and likely broadband (Hindman and Jain 2014), their precise excitation mechanism is also unknown and several theories have been proposed. Nakariakov et al. (2016) considered small-amplitude oscillations as self-oscillatory processes due to the interaction between quasi-steady flows at the loop footpoints. Afanasyev et al. (2020) suggested that a broadband frequency-dependent driver at the loop footpoints can lead to the excitation of several waveguide modes. A recent and comprehensive 3D MHD simulation by Kohutova and Popovas (2021) demonstrated that a harmonic footpoint driver is not a prerequisite for the excitation of loop oscillations.

Both regimes of transverse loop oscillations are found to predominantly exhibit the fundamental mode, that is, with nodes at the footpoints of the loop and an anti-node at its apex. Higher-order modes can also be excited; however, their presence is rare in comparison (e.g. Verwichte et al. 2004). The primary interest in understanding the mode of oscillation of a loop lies in its seismological capability when used in tandem with 1D models (Andries et al. 2005). Often, the approach is to compute the ratio of a loop's observed fundamental period P_1 to its nth overtone, that is P_1/nP_n (Duckenfield et al. 2018, 2019). For a dispersion-less oscillation, it is believed that any deviation of this period ratio from unity may suggest a plasma density stratification within the loop (Andries et al. 2009). On the contrary, Jain and Hindman (2012) demonstrated using sensitivity kernels for a cylindrical waveguide that this period ratio only contains broad spatial averages of the wave speed and is highly insensitive to the loop density. Jain and Hindman (2012) suggested that it is necessary to obtain inversions of several frequency modes and additional non-seismic observations are needed to infer about the density.

A clear verification of the existence of higher-order modes however can be difficult to detect from observations. It is well understood that the emission from coronal plasmas in EUV wavelengths is optically thin. Observationally, this means that a particular coronal loop is preferentially illuminated owing to a superposition of emission along the line of sight from local heating processes. This unfortunate property the of optically thin corona introduces a particularly challenging task of disentangling the emission from nearby loops with fidelity, including for mode verification (De Moortel and Pascoe 2012). To date, observational studies of transverse loop oscillations have excluded the high frequencies in favour of the signal whose intensity is brightest in the image foreground for seismological purposes with 1D models (e.g. Nakariakov and Ofman 2001). Two common techniques for separating a dominant periodic signal from its background include filtering frequencies within the data spectrum (e.g. Terradas et al. 2004; Morton et al. 2012) and tracking the peak intensity as a function of time (Li et al. 2017). The foreground signal is calculated by creating a time series of the maximum intensity of a loop (typically modelled as a Gaussian) within a time-distance map and is often interpreted as the resonant kink modes of a 1D isolated waveguide (e.g. Pascoe et al. 2016a, 2020).

However, there are now multiple lines of evidence that show oscillations are not only confined to the visible loop and therefore a propagation of waves across the magnetic arcade must be present (e.g. Jain et al. 2015; Allian et al. 2019; Conde et al. 2020). Noting the cross-field propagation from observations, Hindman and Jain (2014) and Hindman and Jain (2015) argued that the true nature of a coronal loop wave cavity is multidimensional, and an examination of the power spectrum of the waveform is imperative for understanding the origin of signals from observational data. In particular, Hindman and Jain (2014) demonstrated that the presence of ambient, high-frequency signals from a coronal arcade may be indicative

of a stochastic excitation mechanism. Within their 2D framework, a source consisting of a broad range of frequencies embedded in the background can excite fast MHD waves, which are trapped standing waves longitudinal to the field, while propagating perpendicular to the arcade. Moreover, Hindman and Jain (2014) postulated that an observed impulsive waveform is therefore a superposition of waveguide modes from an ambient background source and an impulsive driver (see Figure 1.14). Thus, in principle, the power spectrum of an observed coronal loop time series contains seismic information about the excitation mechanism and the arcade waveguide.

In a broader context, several studies have also revealed that the power spectrum of dynamical processes in the solar corona can follow a power-law distribution (Aschwanden 2011; Auchère et al. 2014; Ireland et al. 2015; Kolotkov et al. 2016). Aschwanden (2011) initially proposed that the power-law behaviour of random processes in solar time series could be due to the superposition of several small energy deposition events. Auchère et al. (2014) analysed 917 events of EUV intensity pulsations and found power laws with frequencies ranging from $0.01 - 1$ mHz. Similarly, Ireland et al. (2015) revealed power-law properties from active regions in the 171 Å and 193 Å wavebands. These authors argued that the power-law spectra of coronal time series must be considered for the automation of detection algorithms, the correct interpretation of the underlying physical processes and coronal seismological inferences. Ireland et al. (2015) also cast doubt on how frequencies can be extracted from data due to the unknown efficacy of a priori defined background noise models. While much attention has been given to the power-law distribution of solar time series and their associated noise models, a careful investigation into how the standard analysis techniques may lead to artefacts in the context of coronal seismology remains to be satisfactorily addressed.

The hypothesis of our study presented in this chapter is as follows: If a coronal loop is observed to oscillate with a single frequency, then diminishing the strength of that signal should accentuate the presence of ambient wave frequencies, if they exist. We test this by performing a spectral analysis on the waveform of an observed coronal loop oscillating with a single frequency and compare our results with a synthetic loop embedded in a background of noise. We show that the identification of wave frequencies from an observed oscillating loop is non-trivial and the shape of the waveform indirectly influences the detected frequencies.

4.2 Observations and Techniques

4.2.1 Event Overview

For this study, we utilise the same observational event described in Chapter 3. From our results presented in the previous chapter, we found dominant periodicities ranging from 9-13 minutes between loops in proximity during the flare, which was later confirmed by Pascoe
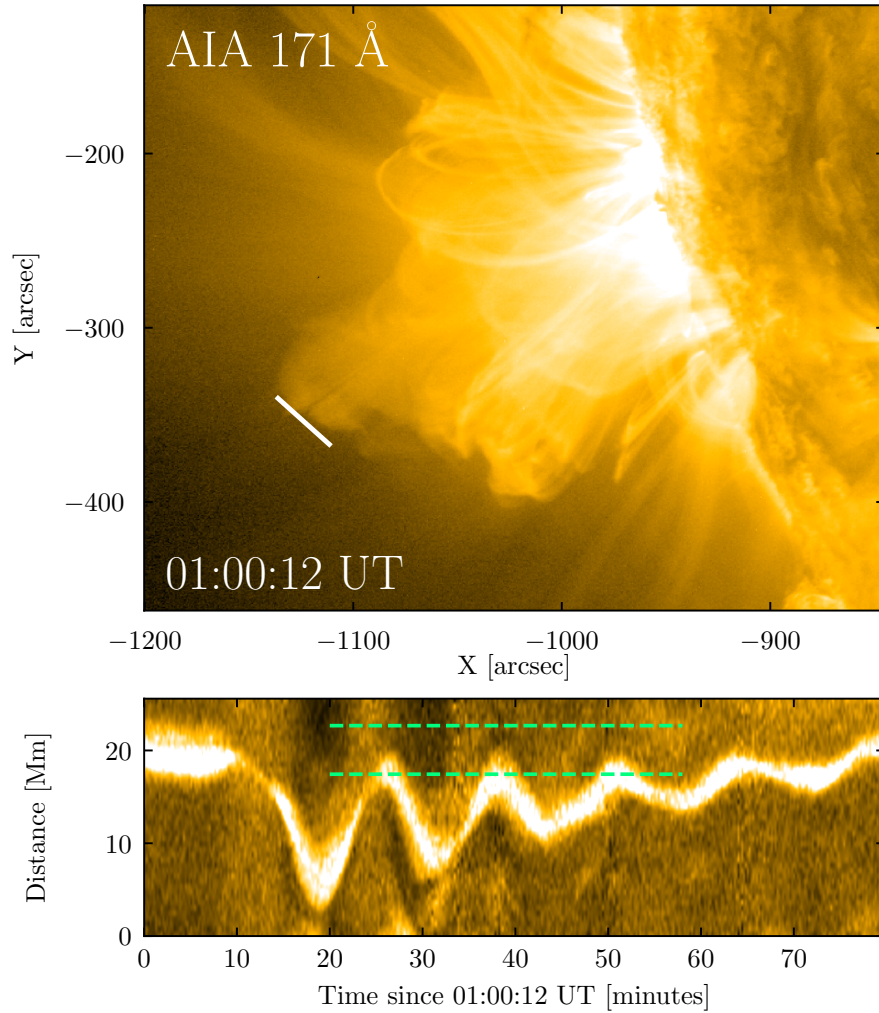
Figure 4.1: Top panel: Snapshot of our region of interest observed by SDO/AIA at 01:00:12 UT. The origin of our slit corresponds to $(x, y) = (-1111, -366)$ arcsec. Bottom panel: Time-distance map of a bright coronal loop exhibiting clear transverse oscillations with a dominant periodicity of $\sim$13 minutes. The dashed green lines highlight the two pixel locations used for further analysis.

et al. (2020). Pascoe et al. (2020) also reported the absence of a higher frequency component from this event. In this study, we use a combination of spectral techniques to investigate whether such high-frequency oscillations exist. The coronal loop of interest was observed on 2014 January 27 off the south eastern limb of the Sun with AIA (Lemen et al. 2012) on board SDO (Pesnell et al. 2012). Our analysis utilises AIA 171 Å data, with a pixel resolution of $0.6''$ pixel^{-1} ($\approx$0.435 Mm) and temporal cadence of 12 s. This dataset was chosen due to the high-quality and well-contrasted observable conditions of a bright coronal loop in the image foreground. A nearby M1.0 class flare initiated around 01:05:12 UT and perturbed the apex of several loops. The top panel of Figure 4.1 shows the region of interest in which transverse oscillations took place at the arcade apex and the slit (white line) used to create

the time-distance map. The resultant time-distance map we use for our study is shown in the bottom panel of Figure 4.1. Prior to the flare onset, the loop appears as a compact shape with non-uniform brightness, which spans a projected distance of approximately 3 Mm within the slit. Thereafter, the loop exhibits a clear transverse oscillation with a dominant periodicity of ~13 minutes.

4.2.2   Methods

Our aim is to investigate the frequency content of the raw data in search of a high-frequency component superposed onto the bright loop shown in the bottom panel of Figure 4.1. To do this, we firstly employed an FFT of the time-distance map. The data is apodized in time and space with a $\cos^2$ curve to mitigate frequency leakage before computing the FFT along each dimension (see Chapter 2 for further details). Other window functions were tested for verification and produced similar results; which, for brevity, is omitted. The power spectrum is then calculated as the magnitude squared of the FFT spectrum and is normalised with respect to the signal variance, $\sigma_0{}^2$ (Torrence and Compo 1998). Full details on analysis procedure is described in Chapter 2. It is worth noting that, apart from the standard procedure outlined above, no detrending or smoothing is applied to the data. Time-distance maps of loop oscillations are often averaged within neighbouring pixels to increase the signal-to-noise ratio of the data (e.g. Pascoe et al. 2016a), and therefore any high-frequency signal is decimated, causing bias in the interpretation of the power spectrum. In this work, we do not perform any smoothing and the full cadence and pixel resolution of the original data is retained to obtain any fine-detail intensity variation of waves that may be present. This data has temporal (ν_{max}) and spatial Nyquist (k_{max}) frequencies of approximately 41.67 mHz and 1.15 Mm^{-1}, respectively.

To assess the significance of wave components in the FFT spectrum, we carefully selected an appropriate background noise model. The theoretical study of Hindman and Jain (2014) demonstrated that a white noise source can excite fast MHD waves, which travel throughout the arcade waveguide. As the aim of our study is to isolate such background frequencies, which are likely to have a constant amplitude for all frequencies, we use a null hypothesis test based on a theoretical white noise spectrum and calculate the 5% significance threshold (95% confidence level) from the data using Equation (2.29) (see Torrence and Compo 1998). Frequencies with power greater than the significance threshold are identified as real signals from waves traversing the coronal loop. Further justification for choosing such a background noise model is corroborated with a basic simulation, which is described in Section 4.3.2.

Furthermore, we validate our initial FFT analysis and account for any non-stationary signals that may be present within the data by performing a wavelet analysis (Torrence and Compo 1998). This technique is often preferred over a traditional FFT analysis in coronal seismic studies owing to its ability to distinguish both the frequency and temporal content of
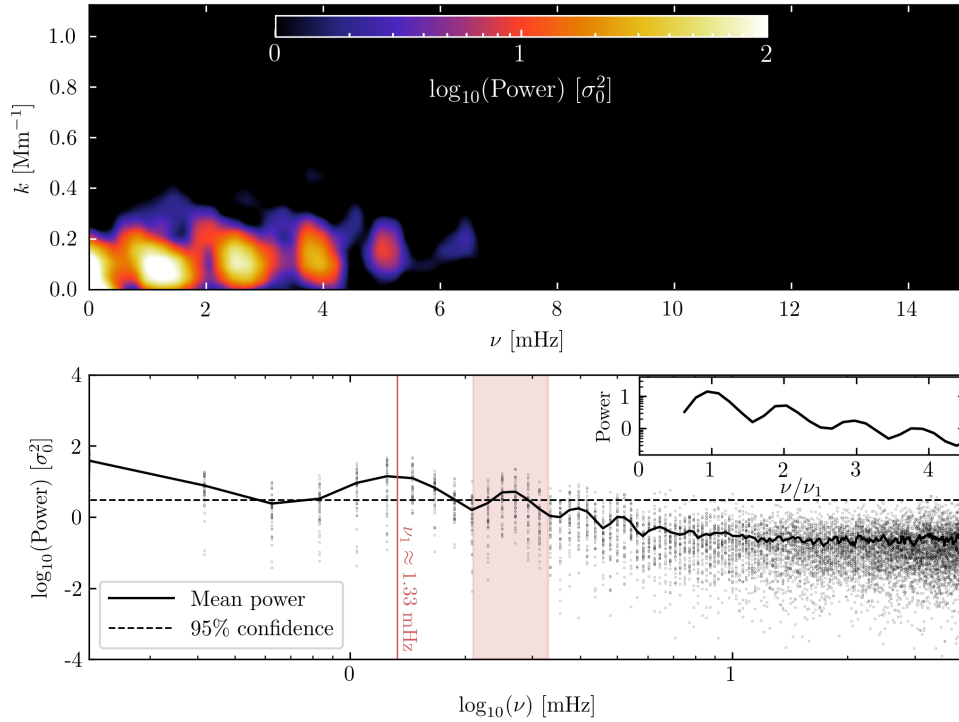
Figure 4.2: Top panel: Two-dimensional FFT power spectrum of the time-distance map shown in the bottom panel of Figure 4.1 as a function of spatial frequency, k, and temporal frequency, ν. The power is normalised with respect to the variance of the time series signal within each pixel. The peak power occurs at a fundamental frequency of $\nu_1 \approx 1.33$ mHz, corresponding to the dominant 13 minutes period of the loop. Signatures of high-frequency components are also present at $\nu > \nu_1$ with decreasing power. Bottom panel: Log-log plot of the FFT power as a function of frequency. The black dots represent the distribution of spectral power within each pixel domain. The solid black line indicates the mean power and the dashed line indicates the 95% confidence level estimated from the theoretical white-noise spectrum. The shaded red region highlights a secondary significant frequency band with a peak at ~2.67 mHz.

a given signal (e.g. Duckenfield et al. 2019; Pascoe et al. 2020). We also relax the assumption of a white noise background in our wavelet analysis to account for any frequency dependence from the data and estimate the corresponding 95% confidence levels of the wavelet power.

4.3 Spectral Analysis

4.3.1 Observed Waveform

The top panel of Figure 4.2 shows the resultant 2D FFT power spectrum of the oscillating coronal loop data as a function of temporal frequency, ν, and spatial frequency, k. As expected, the peak power occurs at the fundamental temporal frequency $\nu_1 \approx 1.33$ mHz, corresponding to that of the dominant period of the loop (~13 minutes). Surprisingly, we

also find significant power at frequencies greater than the fundamental mode of the loop following a near-linear ridge, suggesting that the observed 13 minutes waveform is almost dispersion-less. The relatively low power of the flare-induced high frequencies ($\nu \gtrsim 10$ mHz) is currently unclear and has been previously reported (Liu et al. 2011). One obvious possibility is that the signals produced by the flaring driver at these frequencies exist, but are much weaker in strength. Hindman and Jain (2014) demonstrated that the presence of ambient power at high frequencies can be attributed to fast MHD waves propagating across finer spatial structures of a coronal arcade, and could be due to ambient stochastic sources embedded within the background.

The log-log FFT power of each pixel domain and their mean is shown in the bottom panel of Figure 4.2. The distribution of power in each pixel appears flat at high frequencies. Noticeably, the peak frequencies are equidistant with decreasing strength, as we would expect to observe from a signal whose harmonics have been excited. This pattern is seen more clearly in the inset plot of Figure 4.2, showing the mean power distribution as a function of a frequency ratio (normalised with respect to ν_1). Evidently, the power peaks at several integer multiples of the fundamental frequency. Pascoe et al. (2020) state that they found no evidence of a higher frequency component in search for overtones from these loops. However, we can clearly see that signatures of such high-frequency harmonics exist within the raw data. A white noise hypothesis test supports our initial claim that the second harmonic ($\sim$2.67 mHz) is significant and present within the waveform, based on the estimated 95% confidence level. At this initial stage of analysis, it could be possible to identify this frequency as the higher-order overtone of the loop. A more thorough treatment, of course, requires a multitude of time-distance maps spanning the projected loop in search of a clear phase difference. From this method, we were also unable to find convincing evidence of phase change from this loop. As shown in this work, however, the intensity variations corresponding to the harmonics of an oscillating loop cannot be easily distinguished within coronal time series.

To study the observed waveform shown in the bottom panel of Figure 4.1 in greater detail, we considered two cases: a pixel located on the bright loop where the transverse oscillations appeared most prominent, and another located away from the loop where the transverse oscillations were not as visible. Our objective is to isolate any high-frequency waves that may be superposed on the bright loop. We now describe the first case. Following the oscillation start time at approximately 01:10:12 UT, the bright loop exhibits a contraction that causes it to drift off the slit before beginning its dominant 13 minute cycle. As a result, we extracted a shorter time series ($x = 18$ Mm) of $\sim$40 minute duration starting from 01:20:12 UT, where the loop appeared most stable for three cycles before decaying and examined the raw AIA waveform. This is also motivated by our expectation of the relatively short-lived duration of high-frequency waves, whose presence can go unnoticed within longer duration time series. The top left panel of Figure 4.3 shows the extracted
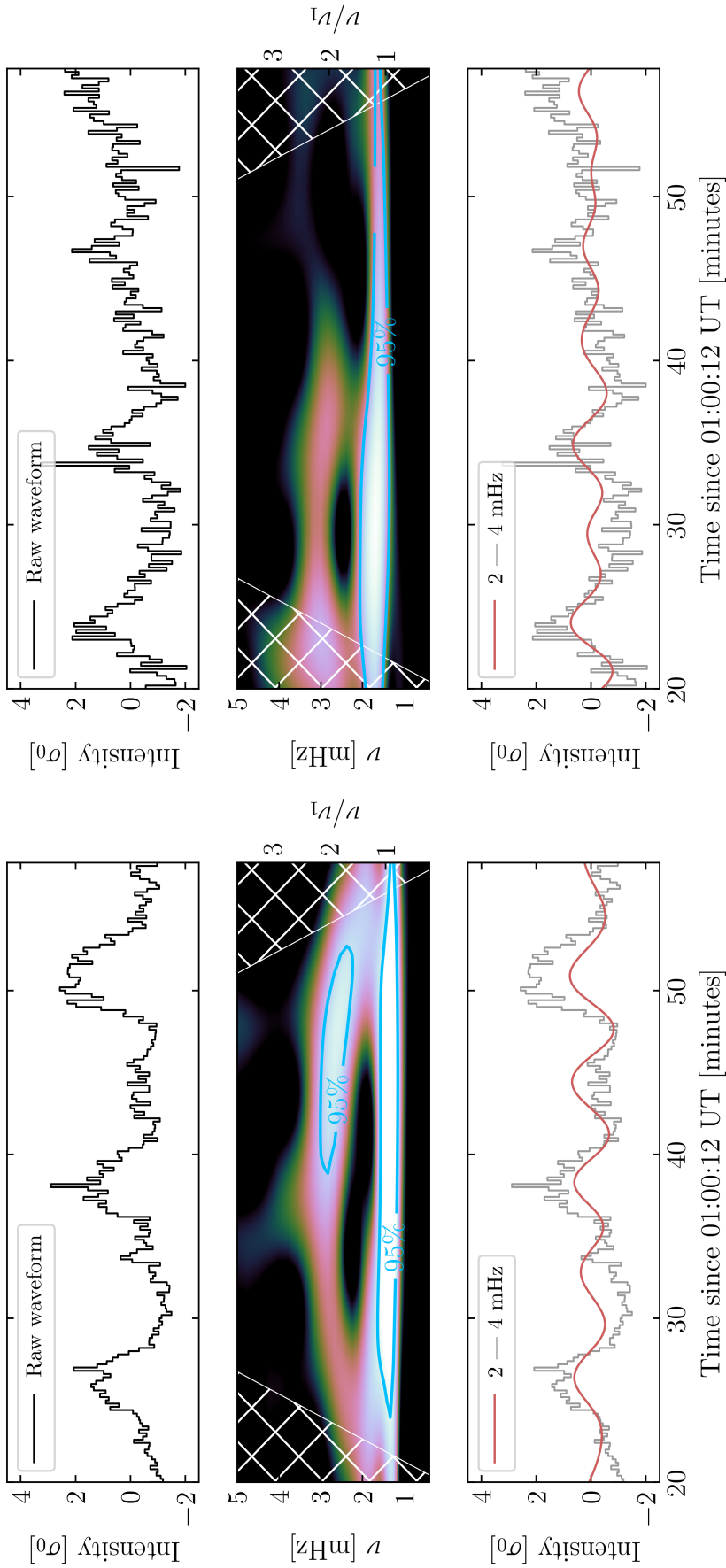
Figure 4.3: Analysis of the observed waveforms from the bright loop (left) and the faint oscillatory region (right) highlighted by the green lines in the bottom panel of Figure 4.1. The top panels show the raw waveforms normalised with respect to the standard deviation. Ambient signatures of high-frequency signals are present in addition to the dominant 13 minutes oscillations. The middle panels shows the wavelet power of the raw signals. For the bright loop, two statistically significant oscillatory frequencies are present at approximately 1.33 mHz and 2.67 mHz, which is highlighted by the blue contours. The bottom panels show the 2–4 mHz bandpass filtered signals (red) overlaid onto the observed waveforms (grey). There are signatures of ∼6 minutes periodic signals superposed on the raw waveforms.

waveform, which is normalised with respect to the standard deviation (σ_0) of the signal. In addition to the pronounced 13 minute waveform, there is a clear presence of ambient, high-frequency jitter embedded within three cycles of the flare-induced waves (see Allian et al. 2019). The wavelet power of the observed waveform is shown in the middle of Figure 4.3 as a function of frequency and time. We find that the WT of this time series also results in two statistically significant frequencies (using a red noise background model) at ~1.33 mHz and its second harmonic (~2.67 mHz), in accord with our initial FFT analysis. At present, we posit that the ~2.67 mHz frequency component with relatively low power is either due to the presence of an ambient stochastic driver superposed onto the dominant flare-induced waves or a weak signature of the overtone of a neighbouring loop. In an attempt to isolate the ~2.67 mHz component, we applied a bandpass filter to the raw AIA waveform between 2-4 mHz. The bottom left panel of Figure 4.3 presents the filtered signal that we suspect to be embedded within the loop, which is over plotted to provide a comparative visualisation relative to the total observed waveform. Clearly, these ~2.67 mHz (6 minute) oscillations permeate throughout the coronal loop, however, their presence within the raw data is practically indiscernible as a result of the high-power contribution from the dominant ~1.33 mHz component. A similar waveform is shown in the right panel of Figure 4.3 for the faint region case ($x = 23$ Mm) in the same duration. Signatures of ~2.67 mHz frequencies are still present in the wavelet power; however, this component falls below the 95% confidence interval likely because of the relatively poor signal-to-noise ratio of the waveform. The frequency content for all pixels can also be inferred by assessing the distribution of FFT power shown in the bottom panel of Figure 4.2.

The amplitude of the 2-4 mHz reconstructed signal from the bright loop is approximately 25% of the total intensity. We estimated the uncertainty of this reconstructed signal by calculating the expected noise level of our observed waveform. Following Yuan and Nakariakov (2012), the noise level in the 171 Å waveband is calculated according to Poisson statistics to be:

$$\sigma_{\text{noise}}(I) \approx (0.06I + 2.3)^{1/2}, \tag{4.1}$$

where I is the overall intensity in units of DN. For typical intensity values within the bright loop (~150 DN), this yields an error of ±3 DN. This value is around ±$0.1\sigma_0$ in the standardized units of intensity. The intensity of the reconstructed signal is around two to three times higher than this estimated noise level, and we are left to believe that the 2.67 mHz component represents some real mechanism. However, as we demonstrate with a basic simulation in the following section, this component is an artefact that arises because of the non-uniform brightness of the observed coronal loop.
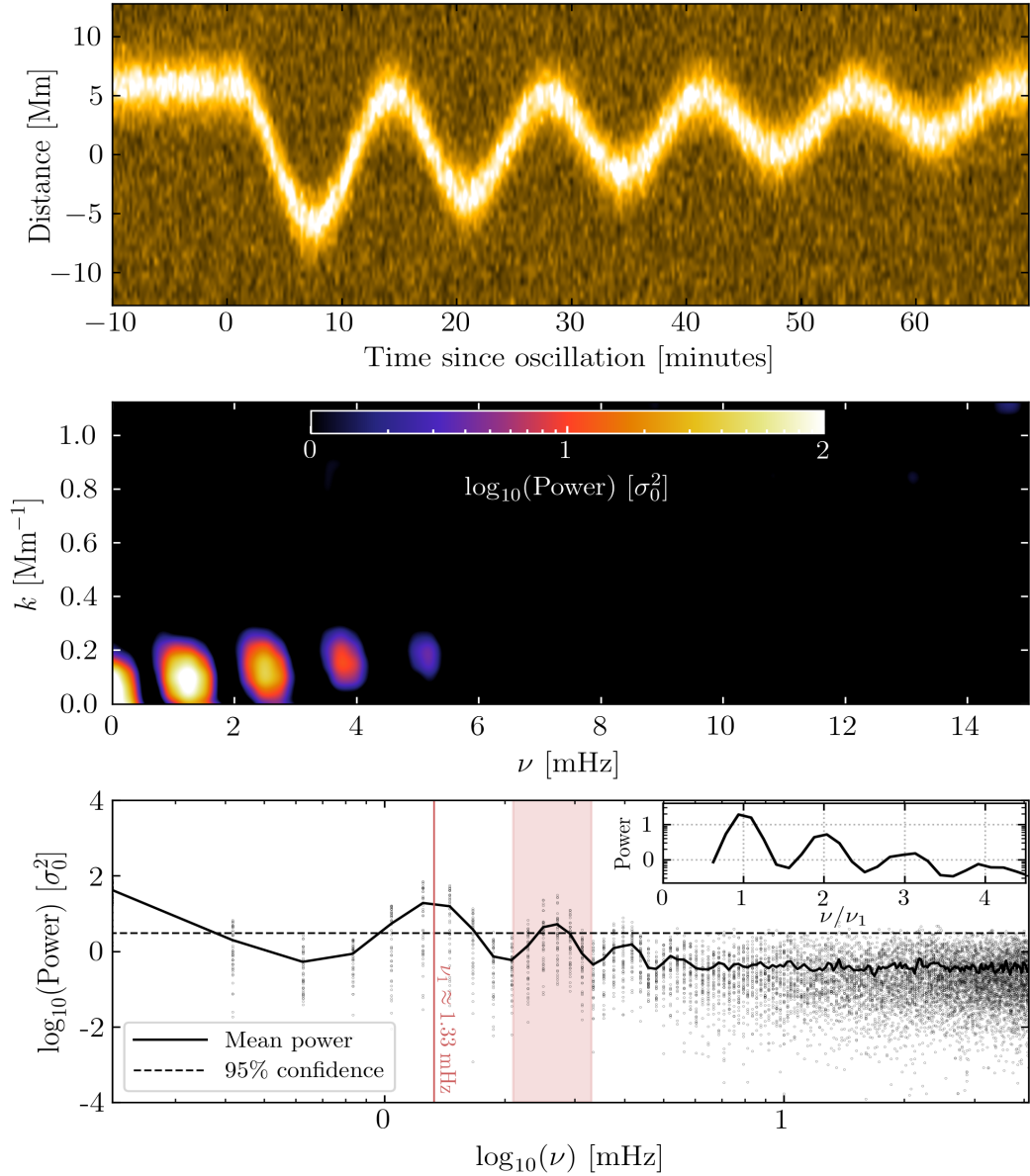
Figure 4.4: Basic simulation of a coronal loop that suddenly oscillates with a single periodicity of 13 minutes, embedded within a uniform background of noise. Top panel: Synthetic time-distance map of a loop oscillating with a single periodicity that exhibits a slow exponential decay and linear drift along the slit. Poisson noise and white noise sources have been included. Middle panel: Two-dimensional FFT power of the simulated waveform shown in the above panel. The pattern of frequencies is akin to the observed waveform shown in Figure 4.2, that is the power peaks at 1.33 mHz and at several of its harmonics. Bottom panel: Log-log plot of the FFT power of the synthetic waveform. The symbols and colours are the same as in Figure 4.2.

4.3.2 Synthetic Waveform

Now that we have carefully examined the spectral content of the observed waveform, we perform a basic simulation of a coronal loop oscillating with a single periodicity. Our goal is
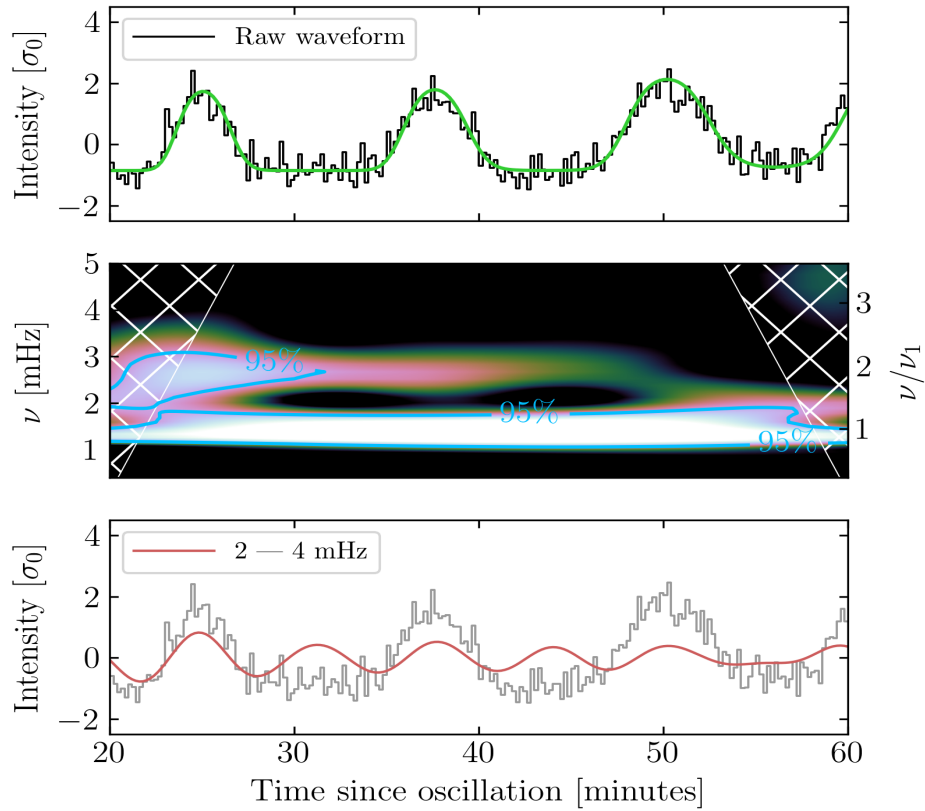
Figure 4.5: Same as Figure 4.3 but for the synthetic loop waveform. The green line overlaid in the top panel represents the 13 minute synthetic waveform in the absence of any noise. The presence of the second harmonic ($\sim$2.67 mHz component) in the wavelet power is artificial and arises as a result of the periodic but non-uniform (Gaussian) brightness of the loop.

to better understand the presence of the harmonics observed in the raw AIA data. To this end, we synthesised a time-distance map of a coronal loop oscillating with a single periodicity (13 minute) observed at the AIA cadence and pixel resolution. The loop is simulated in a 45×400 domain, which represents a 25 Mm long slit observed for a duration of 80 minute, respectively. For simplicity, we assume that the loop cross-sectional brightness is Gaussian across the slit and that the amplitude and width of the loop are constant throughout its lifetime. The loop oscillates sinusoidally with a single frequency as

$$y(t) = \xi_0 \cos(2\pi\nu t + \phi)e^{-t/\tau} + \text{trend}, \qquad (4.2)$$

where ξ_0 is the displacement amplitude of the loop, ν is the frequency of oscillation, and ϕ is the phase offset. The sinusoid is modulated with an exponential decay term with a decay time τ, as is commonly expected for flare-induced transverse waves. A linear trend is also included across the slit to account for the observed growth in the time-distance map in Figure 4.1, perhaps resulting from a change in the magnetic field topology from the flare.

Finally, we include a constant background intensity that consists of contributions from both Poisson noise and artificial white noise at their expected levels. The former is added to mimic photon noise within each AIA pixel and the latter to account for any additional broadband source that may be present (Hindman and Jain 2014).

Figure 4.4 demonstrates the different analysis stages we used to infer about the waveform of the synthetic loop. The top panel shows the time-distance map of a simulated loop oscillating with a single periodicity embedded within a uniform background of noise. The displacement amplitude of the loop is 5 Mm with a 13 minute periodicity that suddenly oscillates. The loop displacement decays with an e-folding time of 45 minutes. The middle panel shows the 2D FFT power spectrum of the synthesised time-distance map. We immediately find that the synthetic power spectrum reflects a striking resemblance to that of the observed loop in Figure 4.2. Similarly, the bottom panel of Figure 4.4 shows the log-log plot of the FFT power as a function of temporal frequency, where there is a significant power enhancement around 2.67 mHz in addition to the expected 1.33 mHz. The high-frequency tail of the power spectrum is also uniformly distributed, reinforcing our claim that the observed waveform is likely to be dominated by a white-noise source. A close inspection of the bottom panel in Figure 4.4 reveals that the FFT power decreases as $\nu^{-1.5}$ for at least three harmonics before tending to a more uniform distribution at higher frequencies, suggesting a power-law model might be appropriate within the low-frequency range. This is particularly suspect since the synthetic waveform was created with only a dominant white-noise source contribution. Hence, the overall shape of a 1D FFT spectrum can be indirectly dictated by the observed shape of the waveform itself (also see Figure 4.6). Nevertheless, it is clear that the $\sim$2.67 component of the synthetic waveform is also significant and requires further investigation.

We now proceed to analyse the time series of the synthetic waveform of the bright loop in the same manner as described in Section 4.2.1. The top panel of Figure 4.5 shows the raw synthetic waveform in which both noise sources are included. The green lines overlaid onto the raw waveform represents that of the noise-free loop. The wavelet power in the middle panel of Figure 4.5 shows a significant power enhancement at $\sim$2.67 mHz throughout the duration of the time series, and the corresponding bandpass filtered signal in the bottom panel also shows signatures of $\sim$2.67 mHz signals embedded within the loop waveform. We reiterate that no wave frequency other than the 1.33 mHz component was included in our set-up.

The presence of the high-frequency harmonics in Figure 4.4 and Figure 4.5 can be explained as follows. Consider the waveform within a single pixel, such as that in the top left panel of Figure 4.5. Since the loop has a non-uniform width that is defined by its brightness, or density inhomogeneity, then the time series from a single pixel contains information about the loop periodicity and the lifetime of brightness within that pixel. In other words, we may
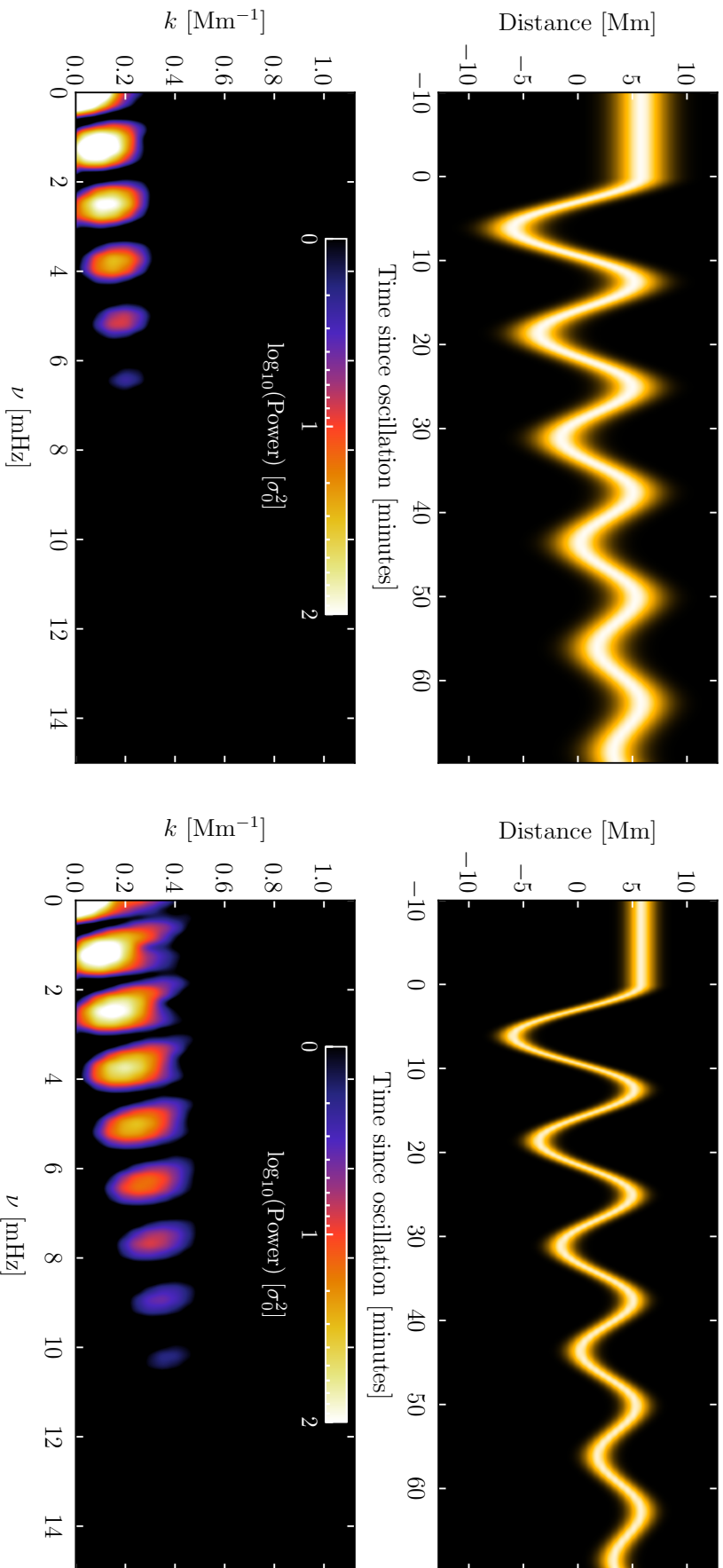
Figure 4.6: Simulated, noise-free time–distance maps (top) and their 2D power spectrum (bottom). Left panel: A thick (FWHM = 3.0 Mm) coronal loop oscillating at a single frequency of 1.33 mHz. Right panel: Equivalent to the left panel but for a thin (FWHM = 1.5 Mm) loop. The relative increase in power at high frequencies, compared to the thick loop, arises due to the Fourier transform of a narrow Gaussian. In both cases, the harmonics arise owing to the periodic but non-sinusoidal waveform of the loop.

think of the resultant waveform as convolution with a Dirac comb spaced every ~13 minutes in time and a Gaussian shape that is defined by the loop of width σ_x traversing a single pixel. Therefore, the power spectrum of such a waveform yields another Dirac comb with a frequency of $\nu_1 \approx 1.33$ mHz multiplied by another Gaussian of width proportional to σ_x^{-1} and the spectral power of the time series decreases like a Gaussian. We can also demonstrate the presence of the artificial harmonics mathematically. Consider a non-uniformly bright loop described by the following expression:

$$I(x,t) = A_0 \exp\left(-(x - y(t))^2/2\sigma^2\right). \tag{4.3}$$

For simplicity, we may assume that the loop oscillates with a single frequency $\widetilde{\omega}$ and exhibits no decay, trend, change in brightness and change in width:

$$y(t) = A_1 \cos\left(\widetilde{\omega}t\right), \tag{4.4}$$

where $\widetilde{\omega} = 2\pi\nu$ is the angular frequency of oscillation and A_1 is the displacement amplitude of the loop. Taking the Fourier transform in space (using the properties described in Chapter 2) and dropping the constants for tractability we obtain:

$$\hat{I}(\kappa,t) \propto e^{-\frac{\sigma^2\kappa^2}{2}} e^{-i\kappa y(t)}. \tag{4.5}$$

where κ is the wavenumber. Equation (4.5) can be rewritten as a sum of complex exponentials:

$$\hat{I}(\kappa,t) \propto e^{-\frac{\sigma^2\kappa^2}{2}} \sum_{n=0}^{\infty} (-i\kappa)^n \left(e^{i\widetilde{\omega}t} + e^{-i\widetilde{\omega}t}\right)^n. \tag{4.6}$$

Expanding the exponential term and taking the Fourier transform in time gives:

$$\hat{I}(\kappa,\omega) \propto e^{-\frac{\sigma^2\kappa^2}{2}} \sum_{n=0}^{\infty}\sum_{r=0}^{n} \delta\left(\omega - (n-2r)\widetilde{\omega}\right) (-i\kappa)^n. \tag{4.7}$$

Now, by letting $m = n - 2r$ and taking positive frequencies ($\omega \geqslant 0$) yields the following transformation as a function of wavenumber and frequency:

$$\hat{I}(\kappa,\omega) \propto e^{-\frac{\sigma^2\kappa^2}{2}} \sum_{m=-2r}^{\infty}\sum_{m=0}^{n} \delta\left(\omega - m\widetilde{\omega}\right) (-i\kappa)^{m+2r}. \tag{4.8}$$

Hence, from Equation (4.8), we can see that the Fourier transform of a non-uniformly bright coronal loop oscillating with a single frequency of $\widetilde{\omega}$ contains frequencies at integer multiples of $\widetilde{\omega}$, i.e. a Dirac comb (e.g. Hartmann 2007). Moreover, the Dirac comb is modulated with a Gaussian envelope, which causes the relative strength of each harmonic to decrease like
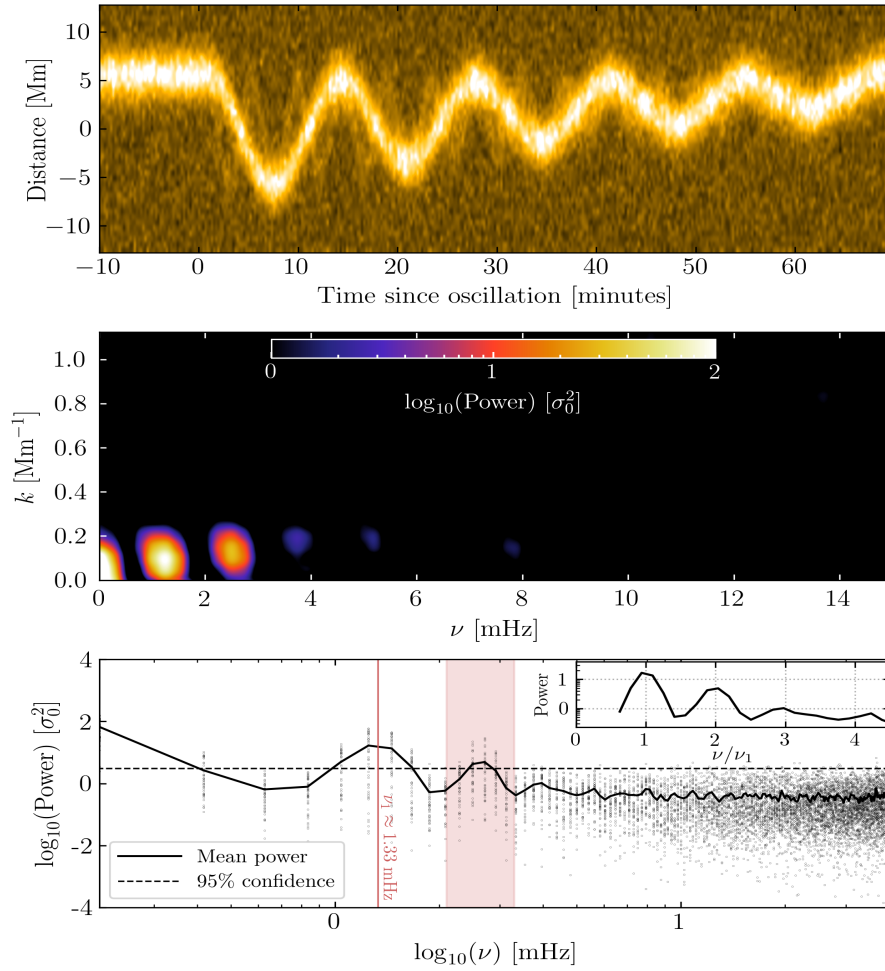
Figure 4.7: Same as Figure 4.4 but for a faint background loop superposed onto the bright loop. The fundamental frequency of the faint loop (4 mHz) is 3 times that of the bright loop. The 1D FFT spectrum is almost identical to that of the single loop in Figure 4.4. However, the 2D spectrum shows deviations at different k from the expected single loop, suggesting a high-frequency signal may be present.

a Gaussian. The presence of the non-linear $(-i\kappa)$ term also means that each harmonic will drift in wavenumber. As a result, frequencies greater than ν_1 are essentially aliases of this mode. In reality, an observed coronal waveform contains more time-dependent features that are non-trivial to simulate and may cause further difficulty in interpreting the frequency content, for instance, from a change in width or periodicity of the structure. Note that the wavelet power of the waveform contains only up to the second harmonic, as opposed to the FFT spectrum, which is primarily due to the resolution of the wavelet filter itself (see Torrence and Compo 1998).
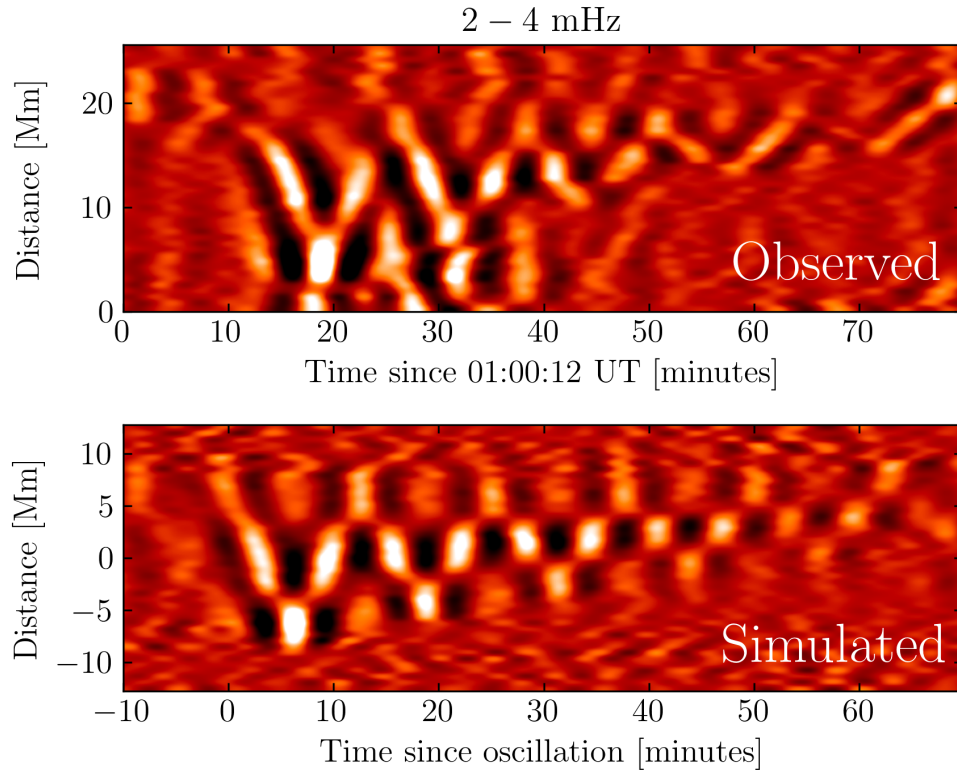
Figure 4.8: Reconstructed coronal loop waveforms (2-4 mHz) of the observed (top) and synthetic data (bottom). The dominant oscillatory (1.33 mHz) pattern is still visible despite diminishing its frequency. Signatures of small-scale oscillatory behaviour are also present. In both cases, these oscillations are completely artificial and arise owing to the non-uniform brightness of the loop in the presence of noise.

4.3.3 Comparison of the Two Waveforms

It is now instructive to return to the observed and synthetic waveforms to better visualise the high-frequency oscillatory behaviour (or lack thereof) in the entire spatial domain. Figure 4.8 shows a comparison of the 95% significant 2-4 mHz signals from the observed (top) and synthetic (bottom) data. Visibly, the dominant 13 minute component of the loop is still present in both cases despite diminishing its strength. This reinforces our previous claim that frequencies greater than the dominant mode ($\nu > \nu_1$) of the loop are essentially aliases and arise as a result of the periodic but non-sinusoidal shape of the thick coronal loop waveform. This result has severe consequences for coronal seismology, as we demonstrated with unambiguous examples that one can only confidently infer about the dominant frequency of a given signal. Moreover, attempts of isolating or filtering a specified frequency band of a coronal waveform can lead to artificially enhanced oscillations and cannot be used as evidence of high-frequency behaviour. The presence of high-frequency oscillations can be supported by examining the 2D power spectrum as a function of k and ν. This is because a high-frequency component of a coronal loop results in a shift in spatial frequency that is not

evinced within a 1D spectrum (see Figure 4.7). To re-emphasise, our results suggest that these frequencies are artefacts that arise because of the inability of the spectral techniques to distinguish periodic but non-sinusoidal signals.

4.3.4 Beat Phenomenon in Faint Coronal Loop Threads?

In the previous section, we demonstrated that both the FFT and WT suffer from harmonic distortions, possibly due to the non-linear signals of the observed waveform. Therefore, we now turn to the adaptive Empirical Mode Decomposition (EMD) algorithm (see Chapter 2 for details) and attempt to determine whether a high-frequency component can be successfully extracted (Huang et al. 1998). Briefly, EMD decomposes an input time series into n empirically-derived, time-scaled basis functions (see Equation (2.39)), or an Intrinsic Mode Function (IMF), and hence does not filter signals by means of reconstructions, as in the FFT and WT techniques. Each IMF represents a variety of time scales present within the original data. For AIA observations, the first IMF, $c_1(t)$, contains the highest frequency component of the signal near the temporal Nyquist frequency. It must be emphasised that due to the adaptive basis of the EMD algorithm, it is not possible to decompose signals according to their exact time scales and crosstalk between each extracted IMF is expected. Therefore, for the interests of our study, we aim to diminish the strength of the dominant 13 minute oscillation to accentuate the presence of high frequency signals. We therefore focus on the second IMF, $c_2(t)$, i.e. the next attainable high-frequency oscillations given the AIA cadence. We further assessed the change in periodicity and power of the filtered signal using wavelet analysis. Note, this analysis is focussed on only isolating a high-frequency component that may be superposed on to the waveform of the bright loop, and we suggest a more thorough study of the relationship between the various IMFs extracted from coronal loop waveforms for future work.

The EMD analysis was performed on the observed AIA waveform, which we extracted from a pixel located on the bright loop (bottom green line of Figure 4.1). Figure 4.9 shows our EMD analysis on this extracted waveform. The decomposed IMF (IMF2) shows ambient, non-sinusoidal, periodic intensity variations embedded within the background of the original waveform. A wavelet analysis of the filtered time series, similar to that described in Section 4.3.1, is shown in the bottom panel of Figure 4.3 suggesting that the background plasma of the loop oscillates with a dominant periodicity of ~2 minutes. Visibly, the filtered time series is modulated with an envelope (highlighted by the red lines) that oscillates in-phase with the same periodicity as the bright loop, suggesting a possibility of beat phenomenon taking place. It is well known that the superposition of two (quasi) harmonic signals at periodicities P_1 and P_2 produces a 'beat' at the period $1/P_b = |1/P_1 - 1/P_2|$. The FFT power spectrum of the filtered signal (right panel of Figure 4.9) shows two dominant peaks at $P_1 = 2.16$ minutes and $P_2 = 2.66$ minutes, yielding a beat period of $P_b \simeq 11.5$ minutes. This beat period is
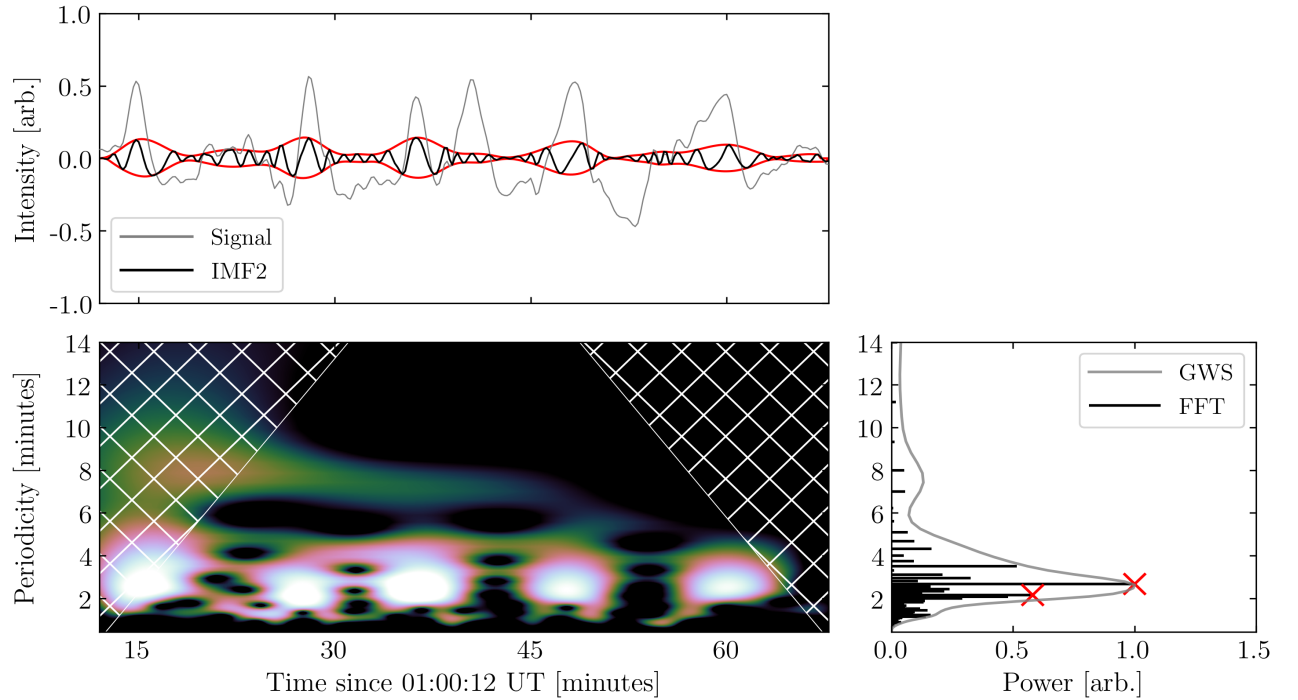
Figure 4.9: Top panel: Time series of the bright coronal loop in the bottom panel of Figure 4.1 taken at a cut at $x = 18$ Mm. The grey line indicates the AIA waveform, which has been detrended for illustrative purposes. The black line shows the second IMF of the original signal obtained using EMD, with a periodicity of ∼2 minutes. The red line highlights the envelope of the original signal. The filtered signal exhibits a clear beat period ($\simeq 11.5$ at approximately the dominant periodicity of the bright loop minutes), despite attempting to diminish the contribution from the low-frequencies. Bottom panels: Wavelet analysis of the filtered time series. The white hatched lines show the COI. The GWS and FFT power is shown in the right panel. The signal beats due to the periodicities at 2.16 and 2.66 minutes marked by the red crosses. Note, the beat period will not be present within the power spectra.

consistent with the dominant period of the loop (∼13 minutes) but with a lower intensity. The GWS of the filtered time series also shows slightly enhanced power at 8 minutes, but these are likely to be cross contamination from the EMD procedure. It must be noted that the spectrum of a signal exhibiting beats should not show any significant power at the beat period. Instead, its spectrum will only consist of the two harmonic signals with periodicities of P_1 and P_2, which produce the beating pattern. This is indeed what we find from both the FFT and GWS spectra in Figure 4.9. Moreover, in the time-domain, the amplitude of the beat period will be significantly lower than that of the fundamental mode since the harmonic signals that create the beat period have a lower spectral power, which can be easily inferred from Figure 4.2. Thus, despite attempting to remove the dominant frequency of the loop, the filtered time series using EMD still contains background intensity variations at a beat period approximately equivalent to the fundamental mode of the loop, but with a
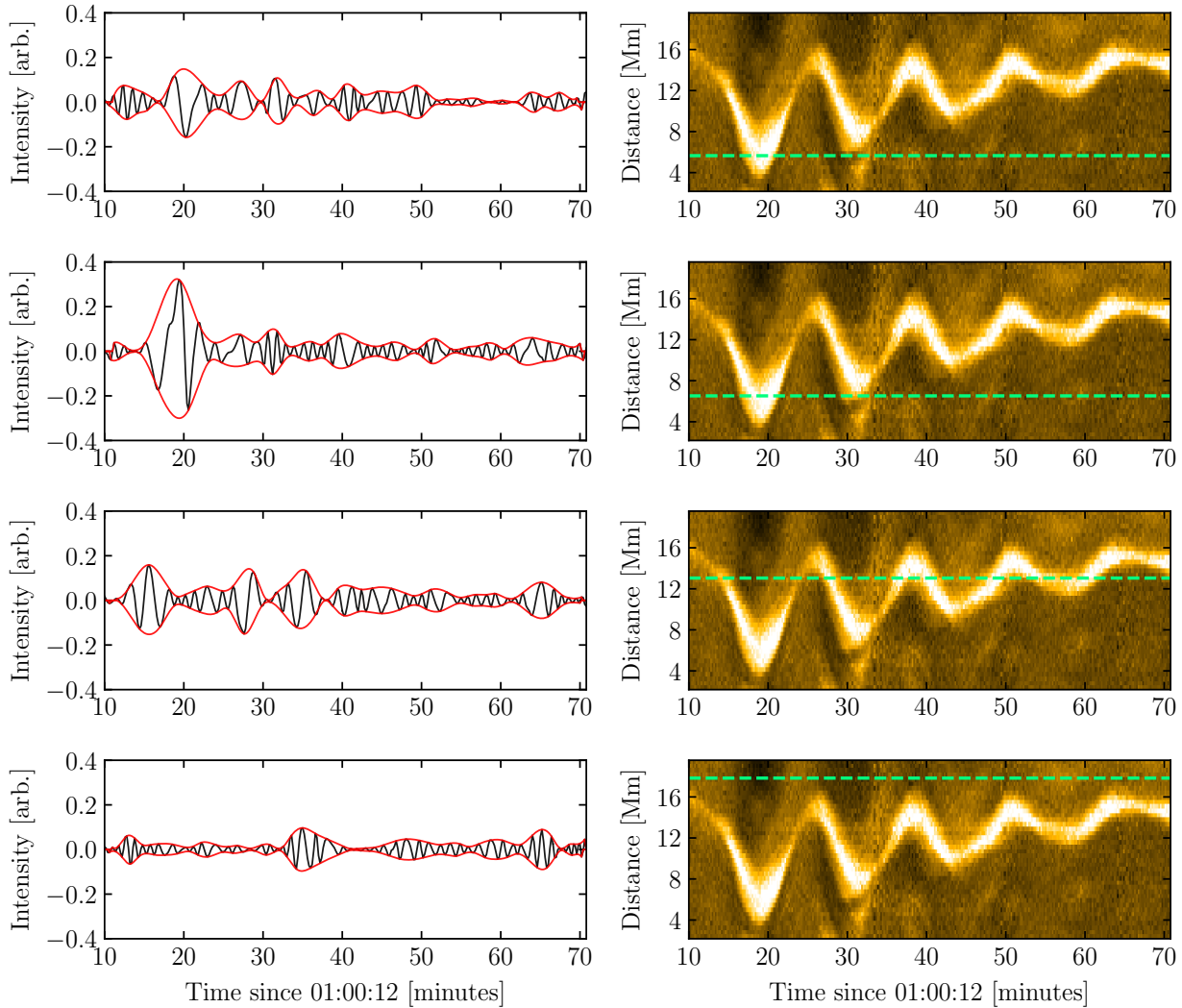
Figure 4.10: EMD analysis (left) on different pixel locations of the time-distance map in Figure 4.1 (right). The black lines show the IMF2 components. Beating patterns (shown in red) are artificially produced by the EMD method in the presence of noise. The dashed green lines show the pixel locations of each intensity slice on the left panel.

weaker amplitude, due to the periodicities at 2.16 minutes and 2.66 minutes. This is precisely the main problem we found from our FFT and wavelet analysis, which suggests that the EMD algorithm may also suffer from distinguishing high-frequency components from the observed coronal loop waveform, and is artificially producing beating effects. Further tests on neighbouring pixels showing artificial beat patterns are highlighted in Figure 4.10.

4.3.5 Line-of-sight Intensity Profile of a Bright Coronal Loop

The presence of the bright loop in the decomposed IMF2 of the loop intensity is surprising and requires further investigation. As such, we now wish to examine the intensity profile of the bright loop. Recall that the intensity of the bright loop spans a distance of ∼3 Mm of the
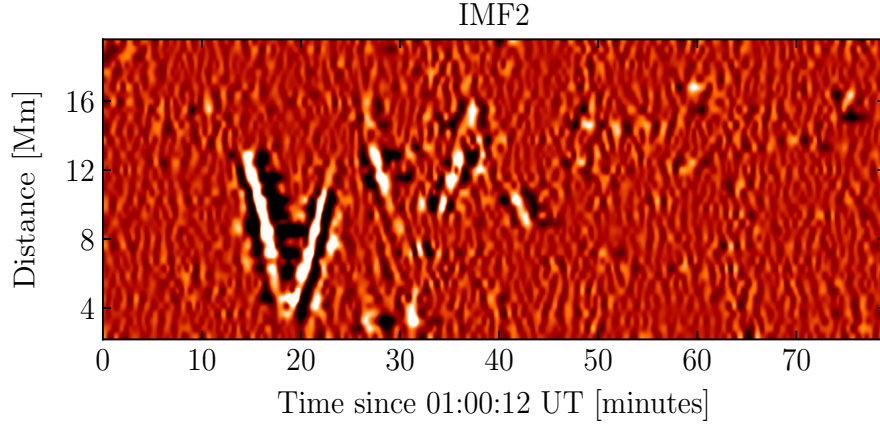
Figure 4.11: Same as Figure 4.8 but using the EMD algorithm to extract the second IMF within each pixel. Again, the dominant 13 minute oscillation can still be seen, however, finer threads of the bright loop can be observed within the time-distance map.

time-distance map shown in Figure 4.1. This brightness is likely to contain plasma emission from the observational line-of-sight, or from several adjacent threads, that contribute to the overall intensity. Thus, as a simple illustrative example, we modelled the bright intensity profile of the bright loop as a linear sum of Gaussians (also see Williams et al. 2020a):

$$I(x) = \sum_{i=1}^{N} A_i \exp\left(-(x - y_i)^2/(2\sigma_i{}^2)\right). \tag{4.9}$$

Here, the parameters A and y are the modelled amplitude and peak location, respectively, x is the cross-sectional spatial coordinate and σ is the root mean square width.

We solve Equation (4.9) by linear regression and pre-defining the total number of Gaussians, $N = 6$. This value is completely arbitrary and is chosen for illustrative purposes only. Figure 4.12 shows an example of the cross-sectional intensity profile of the loop at 01:10:12 UT. Clearly, this intensity profile contains an obvious main lobe centred at 3.5 Mm with additional side lobes on either side, indicating the presence of relatively low-emission threads nearby. Each fitted Gaussian (red, dashed lines) yields a profile that produces the overall observed intensity accurately (red, solid line), suggesting this loop may consist of substructure along the integrated line-of-sight. This could also explain why we can clearly see the fine-structuring and inhomogeneity of several oscillating loops in the IMF2 filtered data in Figure 4.11. Thus, it is possible that our observed beat phenomenon arises due to the high-frequency oscillations of two, or perhaps more, faint threads nearby or embedded within the bright loop itself.
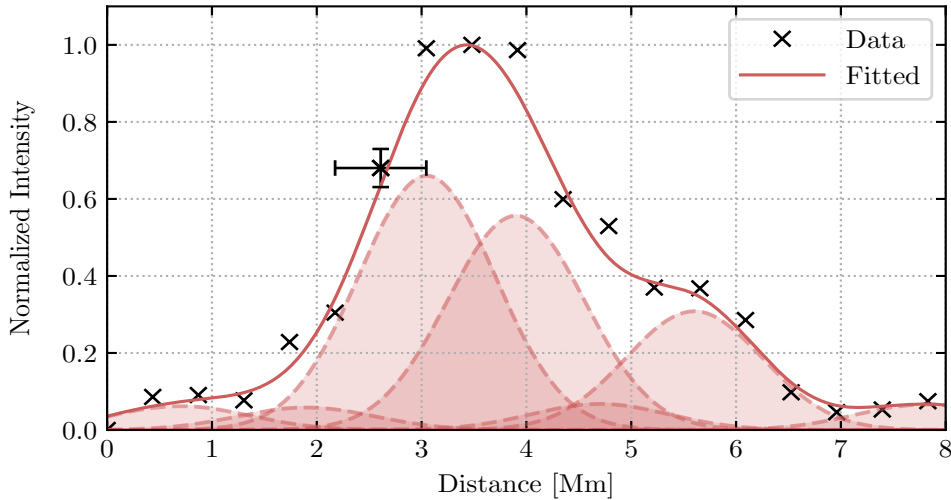
Figure 4.12: An illustration of the cross-sectional intensity profile of the bright coronal loop in Figure 4.1 at 01:10:12 UT. The intensity data points are shown as black crosses. The generated Gaussian profiles (dashed) and the resultant fit (solid) are shown in red. A typical error bar is also shown.

4.4   Discussion

We have performed a spectral analysis of an observed coronal loop oscillating with a dominant periodicity of 13 minute ($\sim$1.33 mHz) in search of a high-frequency component. Using a combination of FFT and wavelet analysis, we 'found' evidence of a significant second harmonic component ($\sim$2.67 mHz) embedded within the dominant mode of oscillation of the loop. A basic simulation of the loop revealed that this component, including frequencies greater than the fundamental component, is artificial. These high-frequency harmonics arise as a result of periodic but non-sinusoidal oscillations, the shape of which is defined by the non-uniform brightness of the coronal loop itself. We argued that, with just these techniques alone, high-frequency signals from an oscillating loop cannot be identified with fidelity. We demonstrated that the power spectrum of an observed coronal waveform and its frequency dependency may be better understood by inspecting the 2D spectrum as a function of spatial and temporal frequency. In reference to our initial hypothesis, it is now clear that diminishing the strength of the dominant frequency cannot confidently reveal the existence of high-frequency waves. Despite using two common and independent analysis techniques in coronal seismology, and adjusting our background noise assumption, these signals are still identified as real signals from both methods. In the following subsections, we explore the plausibility of detecting high-frequency oscillations and the implications for coronal seismology.

4.4.1   High-frequency Oscillations: Real or Artificial?

Our observed results presented in Section 4.3.1 demonstrates ambient signatures of the second harmonic (∼2.67 mHz) of a coronal loop superposed onto the dominant mode of oscillation of the loop, using two independent analysis techniques in coronal seismology. The FFT and wavelet spectrum identified this component as a 'real' signal from their corresponding 95% confidence levels. Only by examining the 2D FFT spectrum together with a basic simulation (see Section 4.3.2) were we able to rule out the possibility of a genuine signal being present. However, interestingly, the periodicity of this signal (∼6 minute) and its persistence is comparable to that of the loop several hours before the impulsive flare, which was shown to exhibit small-amplitude 9 minute oscillations and may indicate a stochastic driver (see Allian et al. 2019). Our interpretation is similar to that of Nisticò et al. (2013) who derived an empirical model of transverse loop oscillations as the response to two distinct drivers: a continuous non-resonant source and an impulsive driver. A more rigorous mathematical framework developed by Hindman and Jain (2014) suggested that fast MHD waves emanating from a stochastic (white) source can excite the resonant modes of an arcade waveguide (see Figure 1.14). Within the 2D model of Hindman and Jain (2014), the primary role of the flare is to enhance the power of frequencies that are already present within the background of the arcade. Although the FFT and wavelet power of this component from the observed loop waveform (left panel of Figure 4.3) is slightly more enhanced than that of the synthetic waveform (Figure 4.5), we believe insufficient evidence remains to suggest the presence of a continuous, resonant source superposed on the bright loop within the duration of the flaring activity.

It is also natural to question whether these artificial harmonics arise due to the basis functions (complex sinusoids) of the FFT and, by extension, the WT. It is well known that the FFT suffers from the distortion of non-sinusoidal signals. We speculate that a more suitable approach of analysing solar coronal waveforms could be accomplished using the adaptive EMD algorithm, which we demonstrated in Section 4.3.4, and only a handful of other studies previously have explored (e.g. Huang et al. 1998; Terradas et al. 2004; Morton et al. 2012; Kolotkov et al. 2016). For instance, Terradas et al. (2004) employed EMD filtering on TRACE observations of coronal loops oscillations to obtain the spatial distribution of propagating and standing waves of periods 5 and 10 minutes, respectively. Terradas et al. (2004) suggested that the intensity fluctuation of the EMD filtered 10 minute period may be indicative of the radial overtone of the loop being excited. While we demonstrate in this work that filtering a frequency band of an observed waveform can result in artificial frequencies, even with appropriate significance testing, it is clear that further work is needed to explore the applicability of the EMD algorithm in solar applications.

Our initial analysis using the EMD on our data revealed that the background plasma of the bright loop may be oscillating at a periodicity nearly 7 times lower than that of its

dominant component. We also demonstrated that the EMD algorithm produces artificial beating effects, and in one example, we found two signals of periodicities 2.16 and 2.66 minutes produced an overall beat period approximately at the dominant mode of the bright loop. In general, the presence of beats is attributed to the interference of waves with two similar periodicities. Theoretical studies of transverse loop oscillations have shown that their the interference of fast waves can produce beat patterns (Hindman and Jain 2014). Though, it is worth remarking that such beat patterns are not unique to MHD waves. This phenomenon is also commonly detected in acoustic studies wherein the time series of a sound source, whose fundamental frequency, ν_1, has been filtered, beats at this mode (Rossing 2002, p. 126). More specifically, a signal with no spectral component at ν_1 can yield a 'phantom' perception of this mode due to the beating of spectral components at $n\nu_1, (n+1)\nu_1, \ldots, (n+m)\nu_1$ for integers $n, m > 1$. This may explain why we can still observe the dominant oscillation, despite attempting to remove the fundamental frequency.

However, it is more likely that the beat patterns produced by the EMD algorithm are also artificial and the method is extremely sensitive to cross-contamination of frequencies within the original data. This should be expected, since the EMD algorithm essentially operates as a quasi-bandpass (dyadic) filter (see Flandrin et al. 2004). Nevertheless, we believe that the EMD method with a correct understanding of its drawbacks may be used as a more robust signal decomposition tool, alongside additional techniques.

4.4.2 Implications for Coronal Seismology

The discussion of Section 4.4.1 explores whether the background oscillatory signals of an observed waveform are genuine or not. To date, seismological inferences have heavily relied upon the standard FFT and WT techniques, and less so with the EMD algorithm, to extract the frequencies of oscillating coronal loops. Our results highlight the dangers of over-interpreting signatures of high frequencies from observed coronal waveforms and add to the complexity of their nature reported in previous works. Ireland et al. (2015) highlighted the importance of incorporating the power-law distribution of coronal waveforms including appropriate background noise models for the correct seismological inference and the automation for oscillatory detection algorithms. While our work has focussed on large-amplitude oscillatory signals, Ireland et al. (2015) analysed quiet-sun regions, including loop footpoints. However, several studies have shown the prevalence of small-amplitude oscillations that persist from the loop footpoints to their apex in quiet-sun regions (Anfinogentov et al. 2013, 2015). Recent high-resolution observations have also revealed fine-scale coronal loop strands from the Hi-C instrument, which are almost unresolvable by SDO/AIA (see Aschwanden and Peter 2017; Williams et al. 2020a,b) and, as a result, the emission from nearby strands are likely to contribute to the overall emission of what we perceive as the visible coronal loop. From our results presented in this work, it is now clear that the power spectrum of

signals from coronal structures may consist of artefacts, such as higher harmonics and power-law behaviour solely from the width of the observed loop waveform. Although the power spectrum of small-amplitude oscillations is almost comparable to the background noise, we believe they can contribute to the overall spectrum and can result in biases, particularly when applying image processing techniques or any non-linear manipulation of the raw data. However, as we have demonstrated, it is possible to rule these frequencies out by consulting the 2D FFT and wavelet power of the waveform in tandem with a basic simulated model. We also note that while our work has focussed on the oscillation of a coronal loop, our inference applies to any transversely oscillating structure that consists of a non-uniform brightness.

While our basic simulation has successfully elucidated the presence of high-frequency components from the observed data, a more realistic set-up is required to model how the emission of EUV plasmas evolve in space and time. We suggest that a forward modelling approach of an entire 3D coronal arcade may be prudent to account for more complex configurations (e.g. Peter et al. 2006). Similarities from the observed and 3D modelled waveforms may then be revealed, for instance, using cross-correlation analysis. A significant improvement in the spatial and temporal resolutions of the detector may also be necessary to convincingly identify high-frequency modes from observations.

Finally, we comment on the validity of searching for loop overtones from observations (e.g Pascoe et al. 2016a; Duckenfield et al. 2019). Such studies extract the dominant (foreground) signal before conducting a spectral analysis using either FFT or WTs by estimating the position of peak brightness as a function of time where the projected loop exhibits a clear phase difference (also see Verwichte et al. 2009). From this, we find non-negligible signatures of up to the artificial second harmonic of the loop due to the sampling from its non-uniform brightness in the FFT power. On the other hand, the wavelet power retains the fundamental mode but generally smooths out the presence of the artificial second harmonic. Thus, from this approach, a wavelet analysis with appropriate significance testing can be suitably used in seismic studies as others have envisioned.

4.5 Summary

In this chapter, we performed a detailed spectral analysis of a bright coronal loop oscillating with a single periodicity in search for a high-frequency component. We employed two common and independent methods in coronal seismology in order to reveal the existence of such waves. We found that the FFT and WT incorrectly identified a significant component of 2.67 mHz superposed onto the dominant mode of oscillation of the loop (1.33 mHz). We demonstrated that such harmonics in the data spectrum arise due to the inability of the spectral techniques to distinguish periodic but non-sinusoidal signals, and that filtering specific frequency bands gives rise to false oscillatory behaviour. We further argued that the

1D FFT power spectrum may be better understood by inspecting the 2D spectrum, as a function of temporal and spatial frequencies. Furthermore, we tested whether the basis independent EMD algorithm can also reveal such signals. It was found that the EMD algorithm is also unable to confidently accentuate these signals, and the method also introduces artificial beating patterns. Therefore, we believe it is important to develop more robust analysis techniques, such as 3D forward model of a coronal arcade, in addition to these standard spectral techniques to successfully identify high-frequency waves.

5

Successive Transverse Oscillations in a Magnetic Arcade

"Remember to look up at the stars and not down at your feet.
Try to make sense of what you see, and wonder about what
makes the universe exist."

— Stephen Hawking

We present multi-wavelength observations into a rare event of transverse loop oscillations induced by consecutive flares. Evidence is provided for both flares inducing transverse oscillations, including horizontal and vertical modes, and small amplitude decayless (oscillations) that have only been observed in non-flaring systems. The periods of oscillation range from 8-20 minutes. We demonstrate that the second flare decreased the period of a coronal loop from 23.5 to 21.0 minutes, which may reflect a change in its physical structure. Possible explanations for the existence of multiple simultaneous excitation sources are discussed.

5.1   Introduction to the Chapter

Magnetohydrodynamic (MHD) waves and oscillations routinely govern the dynamics of solar coronal loops. The first observation of transverse loop oscillations served as an example of MHD coronal seismology (Aschwanden et al. 1999; Nakariakov et al. 1999). By now, there has been much observational evidence accumulated that show such MHD waves and oscillations are excited suddenly in response to a flare or plasma eruption (Zimovets and Nakariakov 2015; Nechaeva et al. 2019). Loop oscillations with displacement amplitudes on the order of a few Mm are termed large amplitude. On the other hand, oscillations in the absence of impulsive events have amplitudes around an order of magnitude smaller and are called small amplitude (decayless) oscillations (Anfinogentov et al. 2015). Both types of oscillations have been intensively studied because of their diagnostic potential they offer for estimating the local plasma properties (e.g. Roberts 2000; Nakariakov and Ofman 2001; Sarkar et al. 2016; Anfinogentov and Nakariakov 2019).

Despite the progress in theoretical models and observational studies, several properties of loop oscillations remain largely debated. For instance, the exact mechanism(s) by which a flare excites oscillations is not fully understood. Terradas et al. (2004) analytically studied the dynamics of transverse oscillations in a magnetic slab as the response to a spatially localised transient fast wave. Terradas et al. (2004) demonstrated that the time signature of a loop perturbed by a transient wave initially oscillates at a high frequency and its eigenfrequency is reached asymptotically. A similar phenomenon was also demonstrated by Hindman and Jain (2014) who considered the response of fast MHD waves of loops within a realistic arcade model. There have also been observations that show the displacement amplitudes of some oscillations grow, suggesting that the driving mechanism responsible may be spatially and temporally prolonged (e.g. Wang et al. 2012). Furthermore, the spatial location of the driver relative to the loop generally governs the loop polarisation (Selwa et al. 2010). Perturbations perpendicular to the loop plane are termed horizontal oscillations, whereas the motion in the loop plane are termed vertical oscillations (e.g. Wang and Solanki 2004; Wang et al. 2008; White et al. 2012).

During a flare (or any transient event), it is also believed that the removal of energy within a given volume of the corona should cause an implosion (Hudson 2000). This phenomenon arises because of the removal of magnetic energy density (magnetic pressure), which in turn, creates a partial vacuum that pulls in the surrounding plasma. Nowadays, such events have been confidently detected (e.g. Wang et al. 2018) and have also been proposed to be connected to oscillations during flares (Russell et al. 2015).

However, up until now, the vast majority of observational studies of transverse loop oscillations have been concerned with a single driver (i.e. one visible flare). There has recently been interests in the phenomenology of consecutive flares on transverse oscillations,

but reports of their presence are currently scarce in the literature (e.g. Allian et al. 2019; Pascoe et al. 2020; Zhang et al. 2020). For instance, in Chapter 3 (and in Allian et al. (2019)), we considered transverse oscillations induced by successive flares using our newly developed autocorrelation technique, and argued that the second flare did not excite further impulsive oscillations. However, Pascoe et al. (2020) claimed to have found oscillations from the second flare in support of the Kelvin-Helmholtz instability using their loop tracking technique. It is currently unclear whether the secondary oscillations found by Pascoe et al. (2020) from the second flare were not an artefact of their tracking method and further independent tests are required. Therefore, reports of similar events would greatly benefit our understanding of the effects of successive flares on transverse loop oscillations.

The present study is focused on our multi-wavelength observation of successive flares on coronal loop oscillations on 2014 June 11. Both flares were associated with a coronal mass ejection (CME) and are unambiguously observed to excite transverse oscillations. In Section 5.2, we describe the evolution of events in our observation. Section 5.3 presents our results demonstrating successive transverse oscillations. Finally, in Section 5.4 we give a summary of our key findings.

5.2 Observations

This study is focused on the coronal loop arcade above AR NOAA 12087 on 2014 June 11. The AR was situated near the southeastern solar disk (S18E68) and exhibited a complex sunspot configuration (β-δ Hale classification)[1]. This AR was prone to a number of flares over several hours, including an M3.0 GOES X-ray class flare peaking at approximately 08:09 UT, which was subsequently followed by a major X1.0 class flare almost an hour later at 09:03 UT. Both flares were recorded in hard X-rays (6-26 keV) by the Reuven Ramaty High Energy Solar Spectroscopic Imager (RHESSI) (Lin et al. 2002) with similar epicenter locations[2] and by the GOES detectors (see Figure 5.2). Each flare was also associated with a CME as observed by the C2 white light coronagraphs of the Large Angle Spectroscopic Coronagraph on board Solar and Heliospheric Observatory (SOHO)[3]. The flaring events were more clearly observed near-simultaneously with AIA (Lemen et al. 2012) onboard SDO (Pesnell et al. 2012) in UV (1600 Å) and EUV (304, 171, 193, 211 Å) wavebands. This event was selected due to the similar spatial locations of the AR as the event presented in Chapters 3 and 4 (see also Allian et al. 2019; Allian and Jain 2021).

To begin, we obtained a sequence of SDO/AIA images starting from 08:00-10:30 UT and extracted an 840×840 sub-field of view containing the AR, as highlighted in Figure 5.1. The

---

[1] See https://solarmonitor.org/20140611 for further details on the AR.
[2] https://hesperia.gsfc.nasa.gov/rhessi_extras/flare_images/20140611
[3] https://cdaw.gsfc.nasa.gov/CME_list
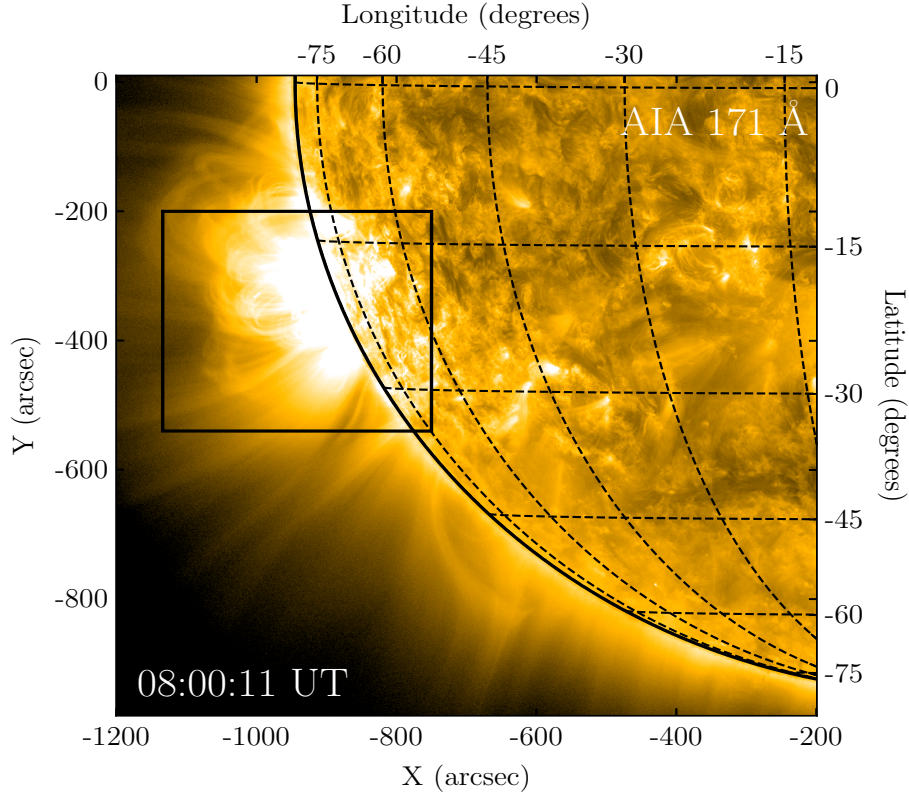
Figure 5.1: Snapshot of AR NOAA 12087 observed by SDO/AIA in the 171 Å waveband on 2014 June 11 at 08:00:11 UT. The AR is situated approximately 18 degrees south and 68 degrees east, relative to the central solar meridian. The black box highlights the region of interest we use for further analysis.

coronal arcade was predominantly illuminated in the 171 Å waveband, which was successively triggered by an M3.0 class flare that initiated at ≈ 08:00 UT and then by a X1.0 class flare at ≈ 08:58 UT. The entire arcade exhibited clear transverse oscillations by a visual inspection. This event was previously studied by Procházka et al. (2017) using RHESSI observations who reported evidence for the suppression of hydrogen emission from both flares. Here, our objective is to study the oscillatory behaviour of a coronal loop arcade induced by these two flares. This AR was also observed near the limb with the EUVI/STEREO-B spacecraft; however, it was not possible to confidently identify any individual loops observed by SDO/AIA. All AIA data were interpolated onto a uniform grid of spatial resolution 0.6″ and a nominal cadence of 12 seconds for the EUV wavebands using standard routines. An overview of the flaring events is shown in Figure 5.3 where three white slits used for our analysis are also indicated.

The evolution of this event is as follows. Following the onset of the first flare, a wavefront was clearly observed to propagate away from the AR core in the 171 Å waveband. Almost simultaneously, in the 304 Å band, a relatively cool chromospheric surge emerged from the
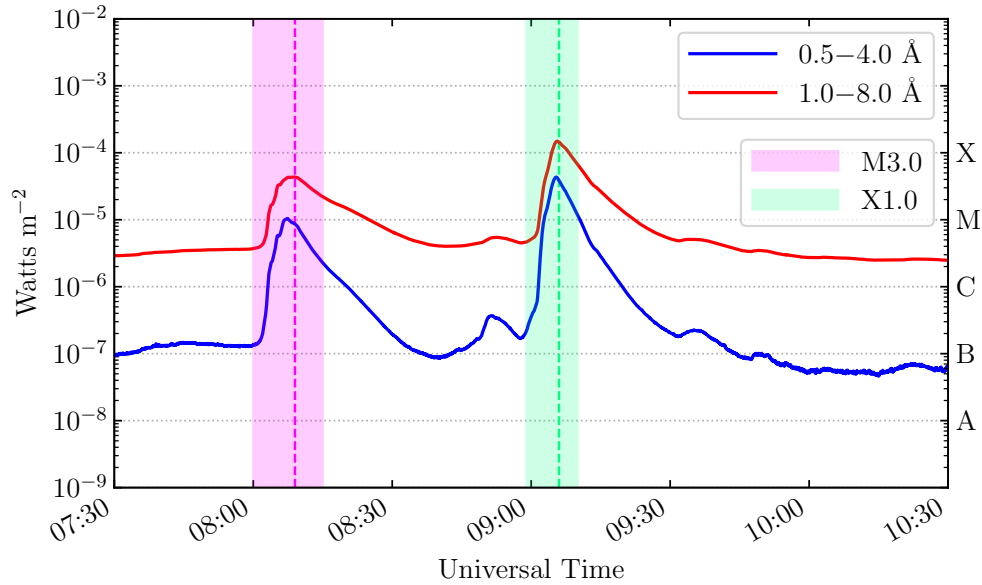
Figure 5.2: X-ray light curves detected by GOES in the 0.5-4.0 Å (blue) and 1.0-8.0 Å wavebands (red) illustrating two consecutive flares. The first flare was an M3.0 class flare that started around 08:00 UT, peaked at 08:09 UT, and decayed around 08:15 UT. The second flare was X1.0 class and initiated around 08:58 UT, peaked at 09:05 UT and started to decay at approximately 09:10 UT.

Table 5.1: Descriptions of evolutionary events that occurred in NOAA 12087.

Event	Duration (UT)	Comment	CME
1st Flare	08:00 - 08:14	M3.0 class.	Yes
Fast Wave	08:07 - 08:15	Visible in 171 Å.	-
Surge	08:07 - 08:28	Visible in 304 Å. Signatures present in 171 Å.	-
2nd Flare	08:58 - 09:10	X1.0 class. No eruption/ejection.	Yes
Large Amplitude Oscillations	08:10 - 10:30	Predominant in 171 Å.	-

AR core. Both features are highlighted in Figure 5.4 using difference images. The surge reached a peak height above the solar limb at approximately 08:14 UT before imploding back on to the solar disk, and triggered loop oscillations during its trajectory. We note that the implosion exhibited by the surge within the duration of the first flare may indicate a partial vacuum that provided energy to the second flare that is later observed (Hudson 2000). The plasma emission of the AR core is subsequently observed to increase in hotter 193 Å and 211 Å wavebands within only ~1 minute, suggesting the AR could have been locally heated. The difference images illustrate that the whole active region experienced topological changes from the first flare by virtue of the surge. Another prominent feature in the difference images shown in the bottom panel of Figure 5.4 where a propagating fast wave is observed in the 171 Å waveband. By carefully tracking the wave trajectory, as in Chapter 3, we estimate an instantaneous velocity of ≈ 775 kms^{-1} eastward. This value can
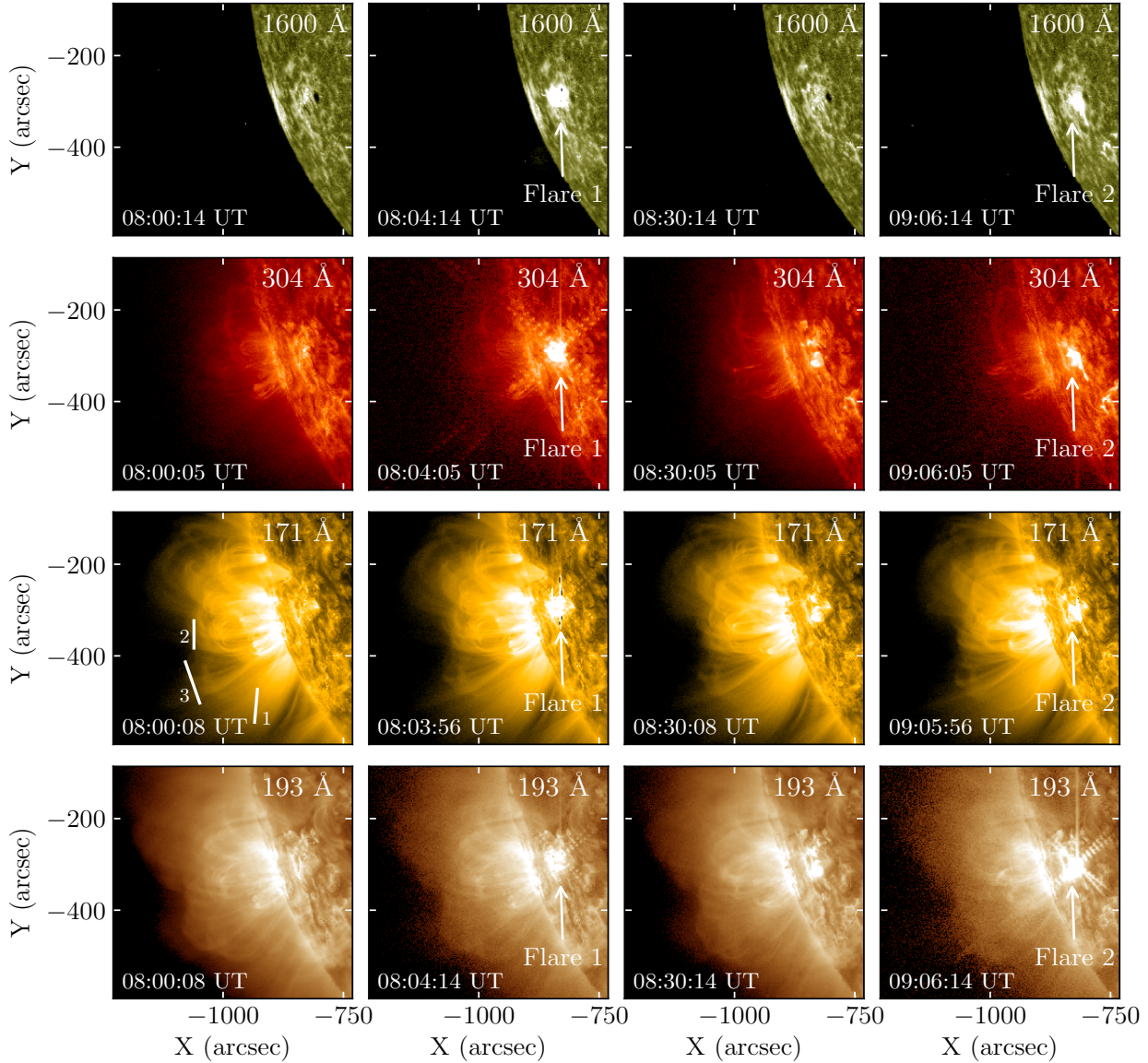
Figure 5.3: Overview of the consecutive flaring events observed by SDO/AIA displayed in UV (first row) and EUV (remaining rows) wavebands near-simultaneously for four different times spanning the duration of both flares. The flaring epicenters can be visibly identified in all wavelengths, as highlighted by the white arrows where the brightness is saturated. The oscillations of the coronal arcade are most reliably observed in the 171 Å waveband. In the first 171 Å image, the solid white lines indicate three slices we use to analyse the oscillatory behaviour of the arcade in detail.

be compared to the approximate sound speed of the 171 Å waveband, c_s, calculated as: $c_s = 147\sqrt{T_e/1\mathrm{MK}}$, which corresponds to a sound speed of ≈ 147 kms^{-1} (see Aschwanden 2004). Hence, the wave propagation speed is several times larger than the typical sound speed in the corona and we refer to this disturbance as a fast wave. A summary of the evolutionary events is given in Table 5.1.
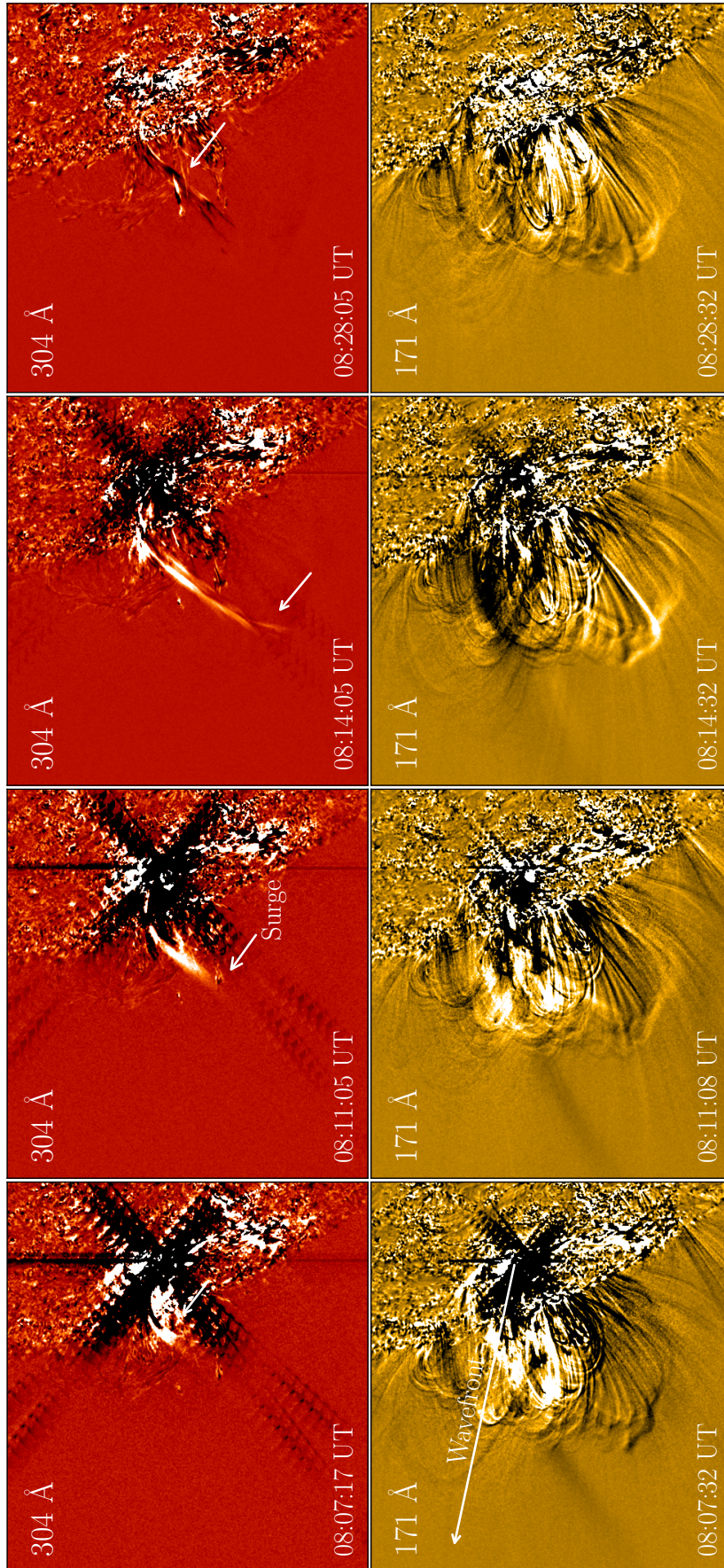
Figure 5.4: Eight near-simultaneous snapshots of difference images in AIA 304 Å (top panels) and 171 Å wavebands (bottom). The white arrows in the top panel highlights the trajectory of the chromospheric surge that exploded and imploded following the first flare. The white arrow in the bottom panel denotes the direction of a fast wave that preceded the surge. Both wavebands exhibit a dimming near the flaring vicinity of the AR. Loop oscillations are most prominent in 171 Å waveband.

Following the evolution of the first flare, the second flare initiated at around 08:59 UT, only this time without any additional (obvious) eruptive events. Despite the absence of eruptions/ejections, the entire arcade reverberated for a second time, displaying oscillations in almost all EUV wavebands, with 171 Å waveband exhibiting the most prominent. The bottom vicinity of the arcade seen in the 171 Å data also contains contorted fan-like loops in the image foreground with a similar brightness, which caused difficulty to reliably identify nearby oscillations. In what follows, we aim to analyse the oscillatory behaviour of the coronal arcade to distinguish any potential properties of the excitation mechanisms.

5.3 Results and Discussion

Now that we have provided an observational overview of our event, we proceed to analyse the arcade oscillations induced by the flares. In particular, we are interested in examining the global behaviour of the arcade and any transverse oscillations exhibited in response to the flares, as clearly viewed in the 171 Å data. The presence of these signals (or lack thereof) are important for understanding properties of the excitation mechanism(s) responsible. Furthermore, we aim to investigate if a loop undergoes a change in frequency of oscillation as excited by the two flares to better understand the role of the drivers.

5.3.1 Spatial Distribution of Wave Power

We first wish to understand the global characteristics of the coronal arcade to build a picture of the oscillatory regions that require further attention. This approach will also help us understand the global features of this AR and will allow us to qualitatively compare this event with those reported in Chapters 3 and 4 due to their similar phenomenological behaviours (i.e. consecutive flares). To this end, we computed the FFT within each 0.6×0.6 arcsec spatial domain and calculated the wave power spectrum (see Chapter 2 for details). The resultant power maps integrated within 2 minute intervals are shown in Figure 5.5. We find that, throughout the 2.5 hour time series (08:00-10:30 UT), the dominant power originates from spatially confined pixels located over the flaring core and is present in all frequency intervals. This is consistent with our findings in Chapter 3 from the AR NOAA 11967 (also see Appendix B). The enhancement of power within all frequency intervals may suggest that the signals expelled from the flaring core may be multi-periodic in nature. The pixel sizes of the enhanced flaring regions is roughly constant in each frequency range and spans a projected area of around 50×50 arcseconds of the AR, which is comparable with the size of the flaring core observed in X-Ray by RHESSI.

At low periods (high frequencies) we find relatively low power within the coronal arcade located above the flaring core in the intervals ranging from 2 to around 4 minutes, suggesting there may be a suppression of wave power from these frequencies. This is again consistent
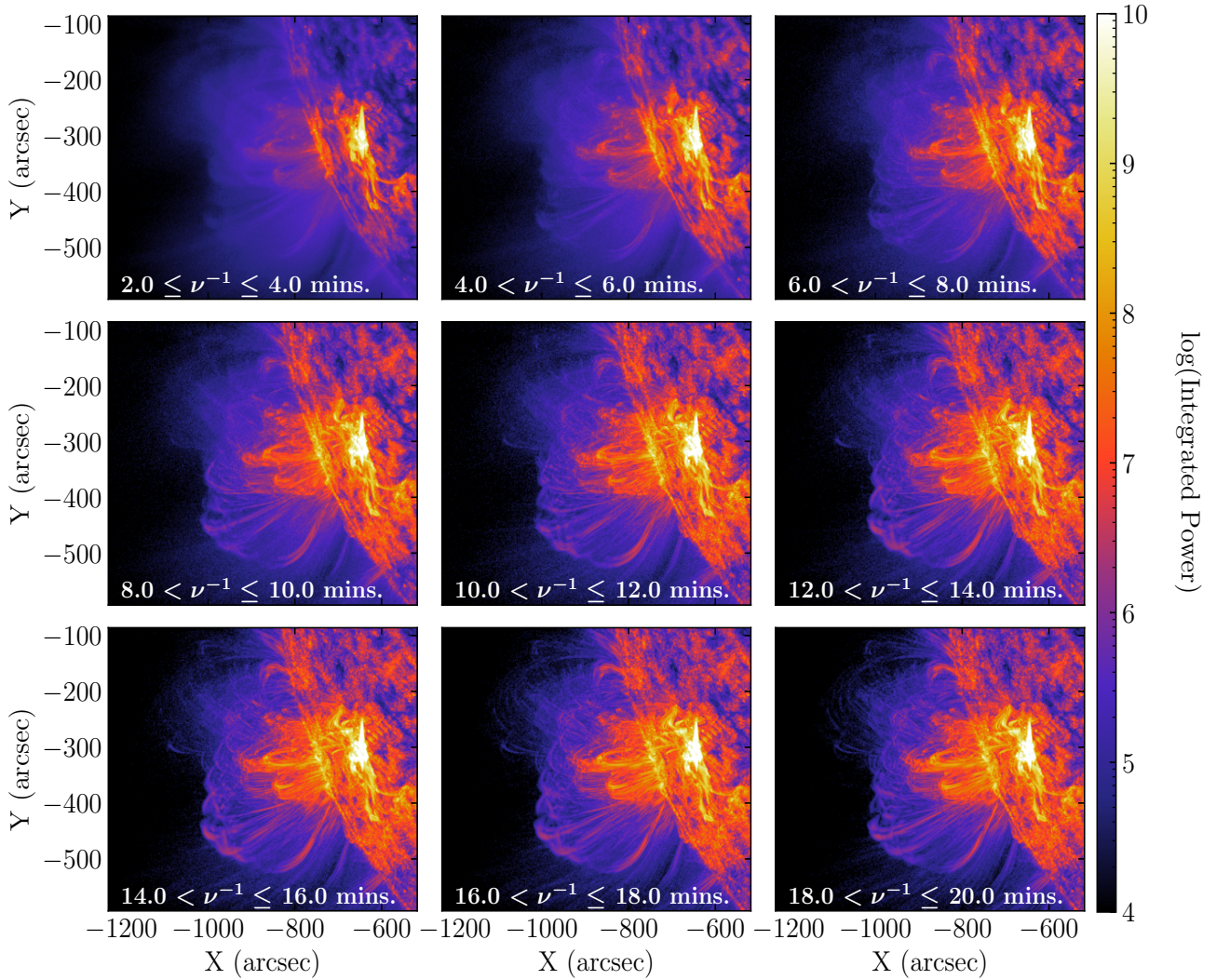
Figure 5.5: Spatial distributions of wave power for AR NOAA 11967 integrated within narrowband (2-minute) frequencies ranging from 2 to 20 minutes. The maximum power originates at the flaring core. At low periods (high frequencies) the coronal arcade appears diffuse with relatively low wave power. Coronal loops are visible with high power in the range of 14-20 minutes.

with AR NOAA 11967. On the other hand, for long periods (low frequencies) the arcade loops exhibit a power enhancement in the intervals ranging from 14 and 20 minutes (around the pixel locations $(X,Y) = (-1100, -450)$ arcsec). Similar to the flaring power maps of NOAA 11967 we find that the distribution of wave power within the coronal arcade is highly concentrated along only a relatively narrow distribution of pixels, which may reflect the multi-threaded nature of AR loops that has previously been reported (e.g. Aschwanden and Peter 2017). Furthermore, the most prominent locations of enhanced wave power occurs in three distinct regions of the arcade from which we wish to investigate in further detail (these regions are represented as white lines in Figure 5.3).

We note that although the power maps presented here are a powerful way of visualising the global spatial distribution of wave power in the arcade, further analysis is required to verify the correct wave nature of these frequencies. For instance, FFT power maps are often unable to differentiate between the pixel locations enhanced by the signals emitted from (quasi-periodic) waves and genuine oscillations. It is also possible that the FFT technique itself can produce spurious artificial signals due to the complicated period but non-sinusoidal waveforms exhibited by the loops, as demonstrated in Chapter 4. Furthermore, in this initial analysis we also did not attempt to separate the two flaring events for two reasons: Firstly, both flares were temporally extended (i.e. they had broad rise and decay times) and so a cross-contamination of wave signals from the first flaring event into the second event should be expected. This prevents us from being able to confidently reveal what effects (if any) the second flare had on the oscillation period of the AR loops, and must be studied with additional techniques. Secondly, creating a smaller time series for both flares would result in relatively poorer frequency resolutions since the FFT frequency bins are inversely proportional to the number of AIA time frames (see Chapter 2). Thus, in the following subsection, we expand on our initial analysis and investigate the oscillatory behaviour of three distinct coronal loops as they are manifested along three slits using time-distance analysis.

5.3.2 Time-distance Analysis

The spatial distribution of wave power in the 171 Å of AR NOAA 12087 presented in Section 5.3.1 provided compelling evidence that multiple wave frequencies exist throughout the coronal arcade. These oscillations are expected to have dominant periods of ∼10-20 minutes. To investigate these oscillatory locations in further detail, we map the raw AIA 171 Å data in the locations highlighted in Figure 5.3 to produce time-distance images at the AIA cadence of 12 s. The resultant three time-distance maps are shown in Figure 5.6. The slit lengths are 48 Mm, 41 Mm and 63 Mm long for Slits 1, 2 and 3, respectively.

We begin by first describing the oscillatory features of Slit 1, as shown in the top panel of 5.6. This slit was oriented parallel to the projected loop plane and therefore exhibits vertically polarised oscillations. Following the peak time of the first (M3.0 class) flare around 08:09 UT, the loop oscillated with a displacement amplitude of approximately 7 Mm and a dominant periodicity of ∼18 minutes before rapidly decaying within only 2-3 cycles. Subsequently, the loop exhibited a secondary large amplitude oscillation with an initiation time that almost coincided with the peak time of the second (X1.0 class) flare. During this phase, the loop oscillated with a shorter periodicity of approximately ∼14 minutes, which also abruptly decayed after 1-1.5 cycles. The periods of these oscillations show good agreement with our independent analysis using the FFT power maps shown in Figure 5.5. However, whether the second flare influenced the frequency of oscillation requires a more
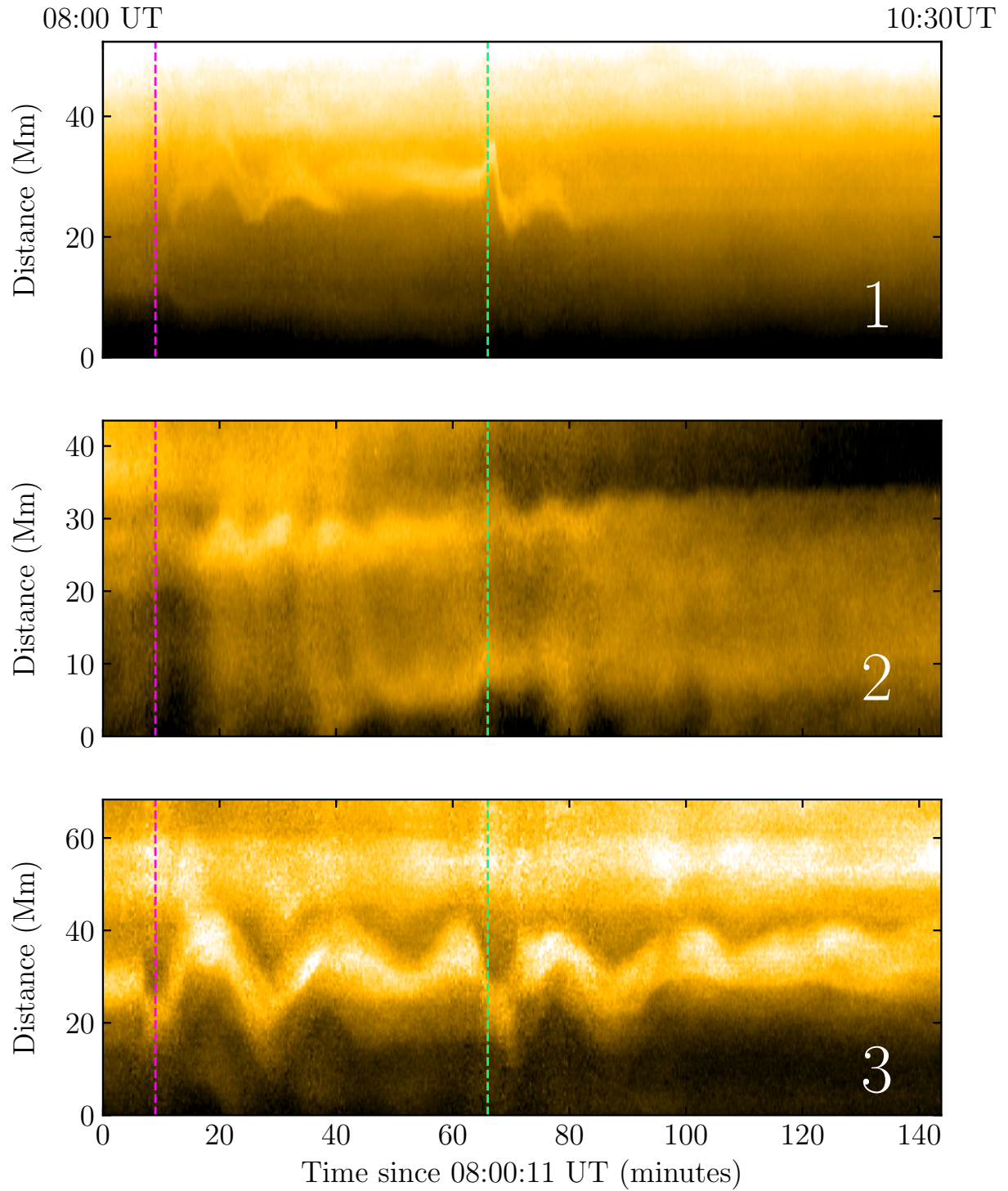
Figure 5.6: Time-distance maps of the three slits indicated in Figure 5.3. Top panel: Vertically polarised transverse oscillations. Middle panel: Signatures of small-amplitude (decayless) oscillations. Bottom panel: Large-amplitude (horizontally polarised) oscillations with a dominant periodicity of around 20 minutes. In all panels, the dashed magenta and green lines indicate the peak flare times as recorded by the GOES X-ray observatories.

careful analysis where the waveform is visually defined. This will be discussed below.

The middle panel of Figure 5.6 shows the time-distance map for Slit 2. The spatial distribution of wave power suggests that the loops recorded in these pixel locations should possess dominant periodicities of around ∼8-12 minutes. Surprisingly, in the corresponding time-distance map for this location, we find small amplitude (decayless) oscillations that have been commonly reported within non-flaring region loops (e.g. Anfinogentov et al. 2015). It can be seen that the loops in this time-distance map indeed exhibit a dominant periodicity of 8-12 minutes. It also appears that neither flare was able to excite the impulsive large amplitude oscillations we find in the top and bottom panels of Figure 5.6 within this region of the arcade. There still remains a debate on the selectivity of large amplitude oscillations, though Aschwanden et al. (2002) formulated a criterion based on a hypothetical exciter and suggested that loops with weaker magnetic fields strengths |**B**| have a higher likelihood of oscillating than strong ones. If it is true that only a subset of weak-field loops oscillate, then it is clear that current seismic models must be improved to incorporate more realistic scenarios (e.g. Hindman and Jain 2014, 2015, 2018). On the other hand, small amplitude oscillations have been shown to be prevalent in the corona (Anfinogentov and Nakariakov 2016). It is currently unclear why both oscillatory regimes (large and small amplitude) exist within this event due to the scarcity of reports in the literature. At present, we speculate that the presence of these small amplitude oscillations may arise due to the indirect impact of the fast wave propagating throughout the arcade. It is also possible that these small amplitude oscillations could be different to those reported in non-flaring systems, though confirmation is needed.

The most prominent signature of successive transverse oscillations from both flares are shown in the bottom panel of Figure 5.6 in Slit 3. Here, we unambiguously see the sudden influence of the flares that we believe impulsively induced both these oscillations. During the first flare, we can see an abrupt equilibrium shift that coincides with the peak flare time causing the loop to contract off the slit before oscillating. Although the contraction here is more subtle than those previously reported (e.g. Russell et al. 2015), this could be a result of the implosion following the first flare (see Section 5.2). The loop then oscillates with a dominant periodicity of around 19 minutes before rapidly attenuating within 2 cycles. Interestingly, the peak time of the second flare was almost coincident (in phase) with the oscillations induced by the first flare. We highlight that, in contrast to our analysis of NOAA 11967 presented in Chapter 3, we can say with certainty that the second flare indeed excited further oscillations. Albeit, the loop waveform induced by the second flare is more complicated and deviates far from a simple sinusoidal profile. This should be expected for loops excited by impulsively generated MHD waves expelled from flaring regions (Aschwanden et al. 2002).

We now wish to analyse Slit 3 in more detail, which contains the waveform with the
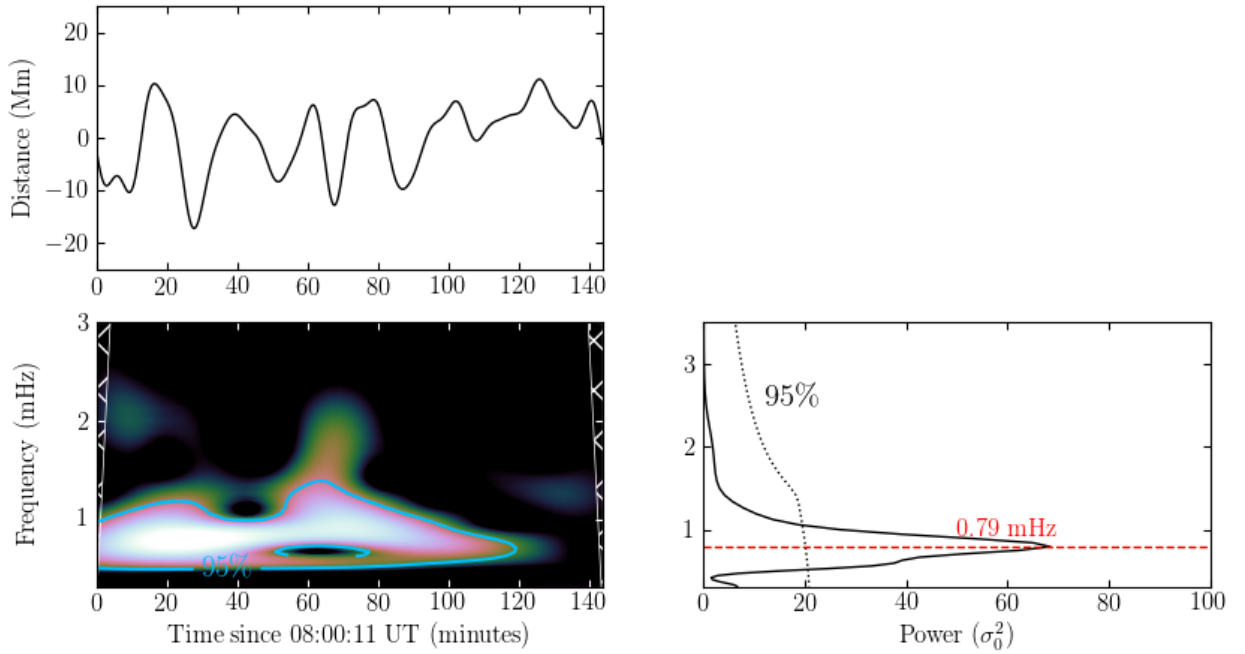
Figure 5.7: Wavelet analysis of the dominant waveform in Slit 3 shown in the bottom panel of Figure 5.6. Top panel: The time series generated using the Gaussian fitting technique with an initial amplitude of ∼11 Mm. Bottom left panel: Wavelet spectrum of the time series as a function of frequency and time. The signal frequency slightly increases at around 60 minutes. The hatched white lines show the cone of influence. The blue contours highlight the statistically significant regions. Bottom right panel: Global power spectrum. The dashed black line signifies a confidence level generated under a red-noise model. The red line demonstrates the peak of the power spectrum at a frequency of 0.79 mHz.

best signal-to-noise ratio out of the three time-distance maps. To track the oscillation of the dominant wave signal, we fit a Gaussian to the cross-sectional flux at each time step, as described in Chapter 3. We stress that although this technique is well established in studies of coronal loop oscillations (e.g. Aschwanden et al. 2002; Jain et al. 2015), it is often difficult to determine whether an observed waveform of a thick loop, such as that in the bottom panel of Figure 5.6, is not an amalgamation of finer threads oscillating coherently along the line-of-sight (see Allian and Jain 2021). Nevertheless, we may proceed and analyse the foreground signal using this technique as a zero-order approximation.

A subsequent step in this method involves fitting a model that best describes the waveform of the generated time series. However, the waveform exhibited by the loop in this instance is relatively complex and an exact expression of its time-dependent dynamical behaviour under the assumption of a particular physical mechanism is likely to be mathematically tedious. As a result, we do not attempt to fit a model but instead analyse the oscillations using wavelet analysis (Torrence and Compo 1998). Our aim is simply to understand if the loop underwent a change in frequency owing to the second flare.
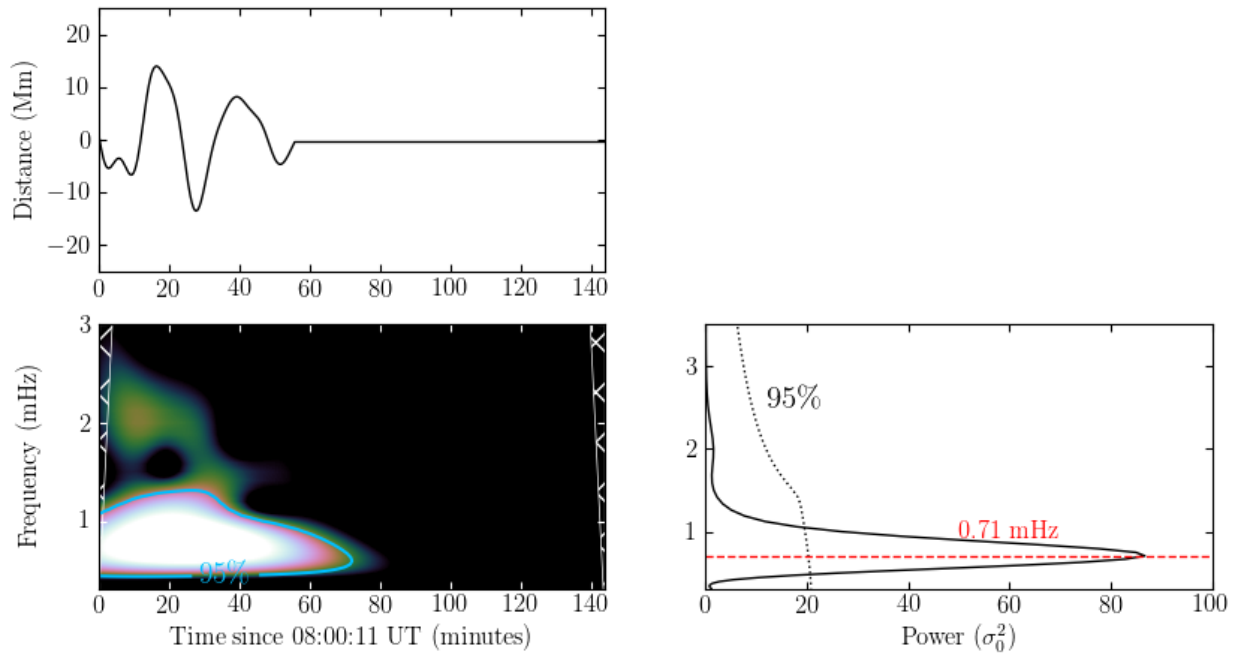
Figure 5.8: Same as Figure 5.7 but for the duration of the first flare. The frequency is almost constant as a function of time.
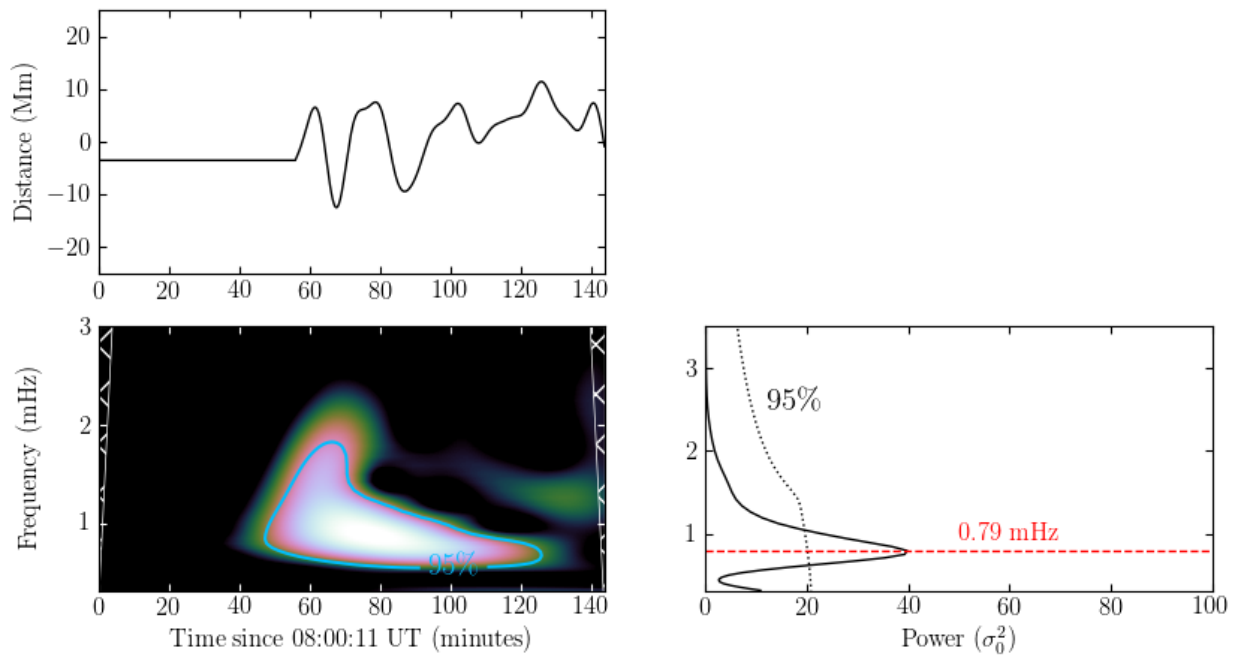
Figure 5.9: Same as Figure 5.7 but for the duration of the second flare. There are signatures of the frequency decreasing from around 1.50 to 0.79 mHz.

The top panel of Figure 5.7 shows the resultant time series of Slit 3, where the complexity loop waveform can be better seen. The bottom left panel shows the wavelet power spectrum of the generated signal as a function of frequency and time. It is clear that the frequency of oscillation is a function of time. Within the duration of the first flare (08:00 - 08:50 UT), the loop frequency is fairly stationary with decreasing power. Before the initiation of the second flare, there are signatures of the loop frequency increasing before plateauing out though this is not clear. The GWS shows that the dominant frequency for this loop within the 2.5 hour interval was around 0.79 mHz ($\sim$ 21 minutes). There is also a smaller 'bump' present at lower frequencies, which may indicate the presence of hidden signal.

In an attempt to understand the effects of the flares on the loop frequency, we separated the time series into two shorter intervals and carried out the same analysis described above. Now, we can confirm that the first two cycles induced by the first flare were indeed constant, whereas the second flare produced signatures of a high frequency component that rapidly attenuated. We also find that the first flare had a shorter dominant frequency (longer period) of 0.71 mHz (23.5 minutes), whereas the second flare exhibited a clear increase (decrease) in frequency (period) to 0.79 mHz (21.0 minutes). Such an observational feature was first predicted by Terradas et al. (2004), who considered the propagation of fast waves under coronal conditions (see Figure 2(b) of Terradas et al. (2004)) and demonstrated that the decrease of power and frequency in time can arise because of wave reflections within the waveguide. This behaviour was also predicted by Hindman and Jain (2014) using an arcade model, who argued that passing of a transient disturbance naturally leads to wave attenuation without any physical dissipation of energy. However, a quantitative study on the transmission and reflection coefficients of coronal loops is outside the scope of this work.

It is likely that the change in periodicity observed in this loop indicates that two distinct drivers were responsible in its excitation. Recall that the 304 Å data contained a chromospheric surge that perturbed the loop apex during the initiation of the first flare. If, for instance, we were to use only one wavelength (such as the 171 Å) for our analysis, we would interpret these oscillations as the response of the fast wave only. Therefore, future studies must incorporate multi-wavelength observations and, if possible, additional non-(E)UV wavelengths to confidently confirm the excitation sources (e.g. Conde et al. 2020).

Another possibility is that the change in periodicity reflects a change in the resonant structure of the loop. In Chapter 4, we discussed whether the change in periodicities observed from the post-flare small amplitude oscillations could be a superposition of waves from the non-flaring and flaring events, as revealed by our autocorrelation procedure (Allian et al. 2019). The same idea could explain the change in periodicity observed in this event from the two flares. In Figure 5.9, we can see a slight compression of the waveform that may indicate a difference in wave arrival times at the observational point (see Hindman and Jain 2014). If this is the case, then it is arguable whether such oscillations fit the profile of the

idealised fast kink modes routinely used for seismology. The present study, alongside the results presented in Chapter 3 and 4 implores for improvements in mathematical models, observational techniques and simulations to better understand the complex waveforms.

5.4 Summary

In this chapter, we reported rare multi-wavelength observations of successive transverse oscillations in a coronal loop arcade on 2014 June 11. Our main results can be summarised as follows. The first flare (M3.0 class) initiated at ∼08:00 UT took place within NOAA AR 12087 near the eastern solar limb. Following this, in EUV wavebands, a fast wave propagated with an instantaneous velocity of ≈775 kms^{-1} eastward before the initiation of a chromospheric surge that erupted upwards and perturbed the apex of several loops. The surge then imploded back onto the solar disk. The chromospheric implosion was interpreted as the response of a partial vacuum created by the removal of magnetic energy from the first flare. We also found evidence for multi-periodic oscillations throughout the entire arcade, with periodicities ranging from ∼8-20 minutes. At ∼08:59 UT, a second (X1.0) class flare initiated without any additional eruptions or waves. Both flares induced clear transverse oscillations with complicated, non-sinusoidal profiles. For the loop with the most prominent waveform, we found that the periodicity decreased from 23.5 minutes to 21.0 minutes. We argued that the change in periodicity may indicate the presence of multiple excitation sources and/or a change in the resonant structure of the loop. Further case studies with better quality, multi-wavelength and high-resolution observations are required to investigate the transmission and reflection of waves in the loop-arcade system and to understand these rare events with greater statistics. MHD simulations of successive flares in a coronal arcade are also encouraged to gain insight into the restoring forces and properties of successively induced transverse loop oscillations.

6

Conclusions and Outlook

"Imagination is more important than knowledge.
 Knowledge is limited. Imagination encircles the world."

— Albert Einstein

The main research findings of this thesis presented in Chapters 3 to 5 are summarised before discussing prospective ideas. Future work includes collating greater statistics of similar observational events, using the autocorrelation technique as parts of automated search tools and incorporating more realistic simulations and models into studies.

6.1 Overall Summary of this Thesis

The question of how the solar corona is heated to temperatures several thousand times hotter than the photosphere has remained unanswered since it was first proposed by Hannes Alfvén in the 1940s (Alfvén 1942). In more recent times, the high spatial and temporal resolutions of solar imagers have presented observers with irrefutable evidence that MHD waves and oscillations permeate throughout the solar corona. As we have demonstrated in this thesis, the conspicuous features of the bright and arching magnetic loops in the solar atmospheres are amongst one of the multifarious observational examples that can be used to investigate the mechanisms of coronal heating and magnetism in tandem with the MHD framework - giving birth to coronal seismology. The work presented in this thesis has strived to further the nascent field of coronal seismology and our key results can be summarised as follows.

Chap. 3: In this chapter, we developed a novel and robust observational technique for detecting periodicities within complex configurations of coronal loop oscillations by means of autocorrelations (Allian et al. 2019). We firstly introduced the 1D autocorrelation function in the context of 'coronal correlation maps'. We demonstrated that the correlation maps can confidently reveal the pixel locations within coronal loops where periodicities exist. The main purpose of the correlation map technique was described as an initial data analysis tool, which can be used to identify and probe regions required for further investigation. Secondly, we advanced the correlation map technique to 2D by incorporating both the spatial and temporal coordinates of coronal loop oscillations. More specifically, we demonstrated that the spatio-temporal autocorrelation function has the salutary feature of revealing properties of the coronal wave-field that may be otherwise unmeasurable. From this, we were able to detect a dominant periodicity of 12.31 ± 0.02 minutes from a large amplitude oscillation that was obscured by a faint background in the field-of-view. Our method was then found to successfully reveal small amplitude (decayless) oscillations (with a poor image contrast) within the same arcade with periodicities of 9.13 ± 0.08 and 9.81 ± 0.10 minutes before and after the flaring activity, respectively. It was argued that due to the relatively poor phase coherence of the small amplitude oscillations between nearby loops, a randomly driven fast wave source may be responsible for these oscillations, as was demonstrated by Hindman and Jain (2014) using an arcade model.

Chap. 4: This chapter is an extension of the work presented in Chapter 3 and is also published in Allian and Jain (2021). Here, we tested whether it was possible to identify high-frequency signals from an oscillating coronal loop using two common and independent analysis techniques; namely the FFT and WT. We found that both methods identified the presence of a second harmonic of a loop ($\sim$2.67 mHz) su-

perposed onto its dominant mode of oscillation (∼1.33 mHz). A basic simulation revealed that this harmonic, and several higher order modes, are completely artificial and the techniques erroneously identified these as genuine signals. It was demonstrated that these frequencies arise due to the inability of the spectral techniques to distinguish periodic but non-sinusoidal signals, which yields power at integer multiples of the fundamental frequency. The overall shape of the power spectrum is shown to be indirectly dictated by the width of the visible coronal loop. Most notably, we showed that the reconstruction of high frequency signals, particularly in the presence of noise, yields a false perception of oscillations that does not otherwise exist. In addition, we tested our initial hypothesis using the adaptive and basis independent EMD algorithm. We found that the second IMF reveals ambient oscillations with frequencies as high as ∼8 mHz (∼2 minutes) embedded within the dominant mode of oscillation of the loop. In particular, two components with periodicities of 2.61 and 2.66 minutes were revealed using EMD and was shown to exhibit a beat phenomenon. It was undetermined whether an isolated bright coronal loop could be a superposition of finer threads oscillating coherently along the line of sight. The study presented in Chapter 4 therefore highlights the requirement of more realistic simulations to be designed in tandem with observations to successfully determine whether high frequency signals can be identified.

Chap. 5: Finally, in this chapter, we investigated the effects of successive flares on transverse loop oscillations. The event was chosen due to the similar phenomenological features reported in previous chapters. The first flare (M3.0 class) initiated at ∼08:00 UT occurred near the eastern solar limb. We detected a propagating disturbance with an instantaneous velocity of ≈775 kms^{-1} before the initiation of a chromospheric surge that erupted upwards and perturbed the apex of several loops. This chromospheric implosion was interpreted as the response of a partial vacuum created by the removal of magnetic energy from the first flare. We also found evidence for multi-periodic oscillations throughout the entire arcade, with periodicities ranging from ∼8-20 minutes. Both flares induced clear transverse oscillations with complicated, non-sinusoidal profiles and we showed that the loop periodicity decreased from 23.5 minutes to 21.0 minutes. We argued that this change in frequency may indicate the presence of two distinct drivers.

6.2   Future Work and Perspectives

Looking towards the future, we may think about how the findings presented in this thesis could improve future studies, but also about how the results themselves could be improved.

Chap. 3: One of the major benefits of our autocorrelation technique presented in Chapter 3 is its simplicity in forming parts of automated search tools for oscillations in the solar corona. Given the vast amount of observational data readily available from SDO/AIA, and the importance of quantitative analyses for the rare events presented in this thesis, our method can be used to gain improved statistics using machine/deep learning routines. For instance, if a sufficiently rich sample of oscillatory events can be collated into training set, then a convolution neural network classifier can be trained and automatically applied to large datasets from any solar imager. This is a natural extension to our method because convolution neural networks are known to be effective at identifying patterns (such as the Xs shown in Figures 3.5) in image data that are otherwise difficult to quantify (e.g. LeCun et al. 2015; Goodfellow et al. 2016). Such image processing techniques and deep learning routines will also be paramount in the rise of new solar imagers with increased spatial and temporal resolutions, such as the Daniel K. Inouye Solar Telescope (DKIST, Rast et al. 2021).

Chap. 4: In Chapter 4, we demonstrated that often the analysis techniques used for seismic studies may reveal false oscillations that are merely an artefact of the method. It was shown that the FFT, WT and EMD suffer from distinguishing periodic but non-sinusoidal signals, and that using these techniques alone, it is not possible to confidently identify high frequency signals from an oscillating coronal loop. We argued that, alongside observations, realistic MHD simulations of a 3D coronal arcade must be consulted. As a result, we believe that future studies must incorporate simulations into their analysis to verify high frequency wave modes. In this instance, a cross-correlation of the observed and simulated waveforms will produce a peak at locations where the two spectra are similar (see Chapter 2). Another possibility would be to utilise spectral analysis techniques that are not dependent on the power spectrum of the waveforms. We speculate that a method involving the phase or coherence spectra of the waveforms may be able to better reveal high frequency signals. For this, the reader is forwarded to the article by Hayashi (1982).

Chap. 5: The major result from this chapter is that successive flares on transverse loop oscillations have properties that are very different from single flare events. Although our first analysis on this rare event was able to shed light onto some of their characteristics (e.g. periodicity decrease, complicated waveforms), the most obvious improvement for understanding these events comes with larger statistical studies. In terms of the excitation mechanism of both large and small amplitude oscillations, several open question remain. For instance: how are transverse oscillations precisely excited and what is the reason for the selectivity of excitations? Do neigh-

144

bouring loops 'feel' the effect of the surrounding plasma following an excitation? To answer these questions, future studies must incorporate multi-wavelength observations and, where possible using additional non-(E)UV observations, to better constrain the likely excitation mechanisms. We also believe that 3D MHD simulations of successive flares are worthwhile to better understand their characteristics.

With these recommendations in mind, it must be noted that these problems are subjective and are listed in terms of the progress of this thesis. However, we believe that those suggested above are central to understanding the long-standing questions of the nature of MHD wave propagation in the solar corona, which have direct consequences for unravelling the mysteries of the elusive coronal heating problem. There remains a wealth of observational data to be leveraged and the results produced in this thesis can put the data to good use. Thus, the fundamental scientific questions listed above are only waiting to be answered.

Bibliography

Abdurashitov, J. N., Gavrin, V. N., Gorbachev, V. V. et al., 2009, "Measurement of the solar neutrino capture rate with gallium metal. III. Results for the 2002-2007 data-taking period", *Phys. Rev. C*, **80**(1), 015807. [DOI], [ADS], [arXiv:0901.2200 [nucl-ex]]. (Cited on page 3.)

Abe, K., Hayato, Y., Iida, T. et al., 2011, "Solar neutrino results in Super-Kamiokande-III", *Phys. Rev. D*, **83**(5), 052010. [DOI], [ADS], [arXiv:1010.0118 [hep-ex]]. (Cited on page 3.)

Abedini, A., 2018, "Observations of Excitation and Damping of Transversal Oscillations in Coronal Loops by AIA/SDO", *Solar Phys.*, **293**(2), 22. [DOI], [ADS], [arXiv:1801.09217 [astro-ph.SR]]. (Cited on page 76.)

Afanasyev, A. N., Van Doorsselaere, T. and Nakariakov, V. M., 2020, "Excitation of decayless transverse oscillations of coronal loops by random motions", *Astron. Astrophys.*, **633**, L8. [DOI], [ADS], [arXiv:1912.07980 [astro-ph.SR]]. (Cited on page 100.)

Ahmad, Q. R., Allen, R. C., Andersen, T. C. et al., 2001, "Measurement of the Rate of ν_e + d –> p + p + e$^-$ Interactions Produced by ^{8}B Solar Neutrinos at the Sudbury Neutrino Observatory", *Phys. Rev. L*, **87**(7), 071301. [DOI], [ADS], [arXiv:nucl-ex/0106015 [nucl-ex]]. (Cited on page 3.)

Akaike, H., 1974, "A New Look at the Statistical Model Identification", IEEE Transactions on Automatic Control, **19**, 716–723. [ADS]. (Cited on page 78.)

Alfvén, H., 1942, "Existence of Electromagnetic-Hydrodynamic Waves", *Nature*, **150**(3805), 405–406. [DOI], [ADS]. (Cited on pages 24, 25, 27, 28, 62, and 142.)

Allen, Bruce, Anderson, Warren G., Brady, Patrick R., Brown, Duncan A. and Creighton, Jolien D. E., 2012, "FINDCHIRP: An algorithm for detection of gravitational waves from inspiraling compact binaries", *Phys. Rev. D*, **85**(12), 122006. [DOI], [ADS], [arXiv:gr-qc/0509116 [gr-qc]]. (Cited on page 45.)

Allian, Farhad and Jain, Rekha, 2021, "The need for new techniques to identify the high-frequency MHD waves of an oscillating coronal loop", *Astron. Astrophys.*, **650**, A91. [DOI], [ADS], [arXiv:2105.08189 [astro-ph.SR]]. (Cited on pages 127, 137, and 142.)

Allian, Farhad, Jain, Rekha and Hindman, B. W., 2019, "A New Analysis Procedure for Detecting Periodicities within Complex Solar Coronal Arcades", *ApJ*, **880**(1), 3. [DOI], [ADS], [arXiv:1902.06644 [astro-ph.SR]]. (Cited on pages 101, 108, 121, 127, 139, and 142.)

Alzate, N. and Morgan, H., 2016, "Jets, Coronal "Puffs," and a Slow Coronal Mass Ejection Caused by an Opposite-polarity Region within an Active Region Footpoint", *ApJ*, **823**(2), 129. [DOI], [ADS]. (Cited on page 74.)

Andries, J., van Doorsselaere, T., Roberts, B., Verth, G., Verwichte, E. and Erdélyi, R., 2009, "Coronal Seismology by Means of Kink Oscillation Overtones", *Space Sci. Rev.*, **149**(1-4), 3–29. [DOI], [ADS]. (Cited on pages 34 and 101.)

Andries, Jesse, Arregui, Inigo and Goossens, Marcel, 2005, "Determination of the Coronal Density Stratification from the Observation of Harmonic Coronal Loop Oscillations", *ApJL*, **624**(1), L57–L60. [DOI], [ADS]. (Cited on pages 34 and 101.)

Anfinogentov, S., Nisticò, G. and Nakariakov, V. M., 2013, "Decay-less kink oscillations in coronal loops", *Astron. Astrophys.*, **560**, A107. [DOI], [ADS]. (Cited on pages 22, 100, and 122.)

Anfinogentov, S. A., Nakariakov, V. M. and Nisticò, G., 2015, "Decayless low-amplitude kink oscillations: a common phenomenon in the solar corona?", *Astron. Astrophys.*, **583**, A136. [DOI], [ADS], [arXiv:1509.05519 [astro-ph.SR]]. (Cited on pages 22, 100, 122, 126, and 136.)

Anfinogentov, Sergey and Nakariakov, Valery M., 2016, "Motion Magnification in Coronal Seismology", *Solar Phys.*, **291**(11), 3251–3267. [DOI], [ADS], [arXiv:1611.01790 [astro-ph.SR]]. (Cited on pages 64 and 136.)

Anfinogentov, Sergey A. and Nakariakov, V. M., 2019, "Magnetohydrodynamic Seismology of Quiet Solar Active Regions", *ApJL*, **884**(2), L40. [DOI], [ADS], [arXiv:1910.03809 [astro-ph.SR]]. (Cited on page 126.)

Antiochos, S. K., Karpen, J. T., DeLuca, E. E., Golub, L. and Hamilton, P., 2003, "Constraints on Active Region Coronal Heating", *ApJ*, **590**(1), 547–553. [DOI], [ADS]. (Cited on page 19.)

Aschwanden, M. J., Fletcher, L., Schrijver, C. J. and Alexander, D., 1999, "Coronal Loop Oscillations Observed with the Transition Region and Coronal Explorer", *ApJ*, **520**, 880–894. [DOI]. (Cited on pages 20, 34, 76, 100, and 126.)

Aschwanden, Markus J., 2004, Physics of the Solar Corona: An Introduction with Problems and Solutions. [ADS]. [ADS]. (Cited on pages 24, 27, 28, and 130.)

Aschwanden, Markus J., 2011, Self-Organized Criticality in Astrophysics. [ADS]. [ADS]. (Cited on pages 20, 62, 102, 167, and 169.)

Aschwanden, Markus J. and Nightingale, Richard W., 2005, "Elementary Loop Structures in the Solar Corona Analyzed from TRACE Triple-Filter Images", *ApJ*, **633**(1), 499–517. [DOI], [ADS]. (Cited on page 19.)

Aschwanden, Markus J. and Peter, Hardi, 2017, "The Width Distribution of Loops and Strands in the Solar Corona—Are We Hitting Rock Bottom?", *ApJ*, **840**(1), 4. [DOI], [ADS], [arXiv:1701.01177 [astro-ph.SR]]. (Cited on pages 20, 122, and 133.)

Aschwanden, Markus J., Nightingale, Richard W. and Alexander, David, 2000, "Evidence for Nonuniform Heating of Coronal Loops Inferred from Multithread Modeling of TRACE Data", *ApJ*, **541**(2), 1059–1077. [DOI], [ADS]. (Cited on page 71.)

Aschwanden, Markus J., de Pontieu, Bart, Schrijver, Carolus J. and Title, Alan M., 2002, "Transverse Oscillations in Coronal Loops Observed with TRACE II. Measurements of Geometric and Physical Parameters", *Solar Phys.*, **206**(1), 99–132. [DOI], [ADS]. (Cited on pages 19, 20, 21, 22, 62, 74, 76, 100, 136, and 137.)

Aschwanden, Markus J., Winebarger, Amy, Tsiklauri, David and Peter, Hardi, 2007, "The Coronal Heating Paradox", *ApJ*, **659**(2), 1673–1681. [DOI], [ADS]. (Cited on pages 10 and 12.)

Astropy Collaboration, Price-Whelan, A. M., Sipőcz, B. M. et al., 2018, "The Astropy Project: Building an Open-science Project and Status of the v2.0 Core Package", *Astron. J.*, **156**(3), 123. [DOI], [ADS], [arXiv:1801.02634 [astro-ph.IM]]. (Cited on page iv.)

Auchère, F., Bocchialini, K., Solomon, J. and Tison, E., 2014, "Long-period intensity pulsations in the solar corona during activity cycle 23", *Astron. Astrophys.*, **563**, A8. [DOI], [ADS], [arXiv:1312.3792 [astro-ph.SR]]. (Cited on pages 57, 62, and 102.)

Aulanier, G., Janvier, M. and Schmieder, B., 2012, "The standard flare model in three dimensions. I. Strong-to-weak shear transition in post-flare loops", *Astron. Astrophys.*, **543**, A110. [DOI], [ADS]. (Cited on page 16.)

Babcock, H. W., 1961, "The Topology of the Sun's Magnetic Field and the 22-YEAR Cycle.", *ApJ*, **133**, 572. [DOI], [ADS]. (Cited on page 13.)

Baliunas, S. L., 2004, "Stellar magnetic cycles", in American Astronomical Society Meeting Abstracts #204, American Astronomical Society Meeting Abstracts, 204, [ADS]. (Cited on page 5.)

Bartlett, Maurice S, 1946, "On the theoretical specification and sampling properties of auto-correlated time-series", Supplement to the Journal of the Royal Statistical Society, **8**(1), 27–41. (Cited on pages 71 and 98.)

Basu, Sarbani and Antia, H. M., 2008, "Helioseismology and solar abundances", *Phys. Rept.*, **457**(5-6), 217–283. [DOI], [ADS], [arXiv:0711.4590 [astro-ph]]. (Cited on page 6.)

Bellan, P. M., 1994, "Alfvén 'resonance' reconsidered: Exact equations for wave propagation across a cold inhomogeneous plasma", Physics of Plasmas, **1**(11), 3523–3541. [DOI], [ADS]. (Cited on page 35.)

Bellan, P. M., 1996, "Comment on "On the Alfvén resonance and its existence" [Phys. Plasmas 2, 340 (1995)]", Physics of Plasmas, **3**(1), 435–436. [DOI], [ADS]. (Cited on page 35.)

Bemporad, A., Sterling, Alphonse C., Moore, Ronald L. and Poletto, G., 2005, "A New Variety of Coronal Mass Ejection: Streamer Puffs from Compact Ejective Flares", *ApJL*, **635**(2), L189–L192. [DOI], [ADS]. (Cited on page 74.)

Benz, Arnold O., 2008, "Flare Observations", Living Reviews in Solar Physics, **5**(1), 1. [DOI], [ADS]. (Cited on pages 15 and 17.)

Benz, Arnold O., 2017, "Flare Observations", Living Reviews in Solar Physics, **14**(1), 2. [DOI], [ADS]. (Cited on page 16.)

Bethe, H. A., 1939, "Energy Production in Stars", Physical Review, **55**(5), 434–456. [DOI], [ADS]. (Cited on page 2.)

Blackman, Ralph Beebe and Tukey, John Wilder, 1958, "The measurement of power spectra from the point of view of communications engineering—Part I", Bell System Technical Journal, **37**(1), 185–282. (Cited on page 53.)

Boerner, Paul, Edwards, Christopher, Lemen, James et al., 2012, "Initial Calibration of the Atmospheric Imaging Assembly (AIA) on the Solar Dynamics Observatory (SDO)", *Solar Phys.*, **275**(1-2), 41–66. [DOI], [ADS]. (Cited on pages xiv and 39.)

Borexino Collaboration, Bellini, G., Benziger, J. et al., 2014, "Neutrinos from the primary proton-proton fusion process in the Sun", *Nature*, **512**(7515), 383–386. [DOI], [ADS]. (Cited on page 3.)

Borexino Collaboration, Agostini, M., Altenmüller, K. et al., 2018, "Comprehensive measurement of pp-chain solar neutrinos", *Nature*, **562**(7728), 505–510. [DOI], [ADS]. (Cited on page 3.)

Brady, C. S. and Arber, T. D., 2005, "Damping of vertical coronal loop kink oscillations through wave tunneling", *Astron. Astrophys.*, **438**(2), 733–740. [DOI], [ADS]. (Cited on page 35.)

Bray, R. J., Cram, L. E., Durrant, C. and Loughhead, R. E., 1991, Plasma Loops in the Solar Corona. [ADS]. [ADS]. (Cited on page 19.)

Brueckner, G. E. and Bartoe, J. D. F., 1974, "The Fine Structure of the Solar Atmosphere in the Far Ultraviolet", *Solar Phys.*, **38**(1), 133–156. [DOI], [ADS]. (Cited on page 19.)

Cally, Paul S., 2017, "Alfvén waves in the structured solar corona", *Mon. Not. Roy. Astron. Soc.*, **466**(1), 413–424. [DOI], [ADS], [arXiv:1612.02064 [astro-ph.SR]]. (Cited on pages 6 and 23.)

Carmichael, H., 1964, "A Process for Flares", in NASA Special Publication, 50, [ADS]. (Cited on page 16.)

Carrington, R. C., 1859, "Description of a Singular Appearance seen in the Sun on September 1, 1859", *Mon. Not. Roy. Astron. Soc.*, **20**, 13–15. [DOI], [ADS]. (Cited on page 16.)

Carroll, Bradley W. and Ostlie, Dale A., 2007, An Introduction to Modern Astrophysics, 2nd (international) edn. [ADS]. (Cited on pages 3, 7, and 8.)

Chen, Francis F., 2016, Introduction to Plasma Physics and Controlled Fusion. [DOI], [ADS]. [ADS]. (Cited on pages 24 and 29.)

Conde, C, Sandra M., Jain, Rekha and Jatenco-Pereira, Vera, 2020, "Excitation Sources of Oscillations in Solar Coronal Loops: A Multi-wavelength Analysis", *ApJL*, **890**(2), L21. [DOI], [ADS]. (Cited on pages 94, 101, and 139.)

Cooley, James W and Tukey, John W, 1965, "An algorithm for the machine calculation of complex Fourier series", Mathematics of computation, **19**(90), 297–301. (Cited on page 53.)

De Moortel, I. and Nakariakov, V. M., 2012, "Magnetohydrodynamic waves and coronal seismology: an overview of recent results", Philosophical Transactions of the Royal Society of London Series A, **370**(1970), 3193–3216. [DOI], [ADS], [arXiv:1202.1944 [astro-ph.SR]]. (Cited on page 29.)

De Moortel, I. and Pascoe, D. J., 2012, "The Effects of Line-of-sight Integration on Multi-strand Coronal Loop Oscillations", *ApJ*, **746**(1), 31. [DOI], [ADS]. (Cited on page 101.)

Del Zanna, G., O'Dwyer, B. and Mason, H. E., 2011, "SDO AIA and Hinode EIS observations of "warm" loops", *Astron. Astrophys.*, **535**, A46. [DOI], [ADS]. (Cited on page 38.)

Del Zanna, G., Dere, K. P., Young, P. R., Landi, E. and Mason, H. E., 2015, "CHIANTI - An atomic database for emission lines. Version 8", *Astron. Astrophys.*, **582**, A56. [DOI], [ADS], [arXiv:1508.07631 [astro-ph.SR]]. (Cited on pages xiv and 39.)

Deubner, F. L., 1975, "Observations of low wavenumber nonradial eigenmodes of the sun.", *Astron. Astrophys.*, **44**(2), 371–375. [ADS]. (Cited on page 5.)

Díaz, A. J., Oliver, R., Ballester, J. L. and Roberts, B., 2004, "Fast MHD oscillations in line-tied homogeneous coronal loops", *Astron. Astrophys.*, **424**, 1055–1064. [DOI], [ADS]. (Cited on page 34.)

Dikpati, M. and Gilman, P. A., 2007, "Global solar dynamo models: simulations and predictions of cyclic photospheric fields and long-term non-reversing interior fields", New Journal of Physics, **9**(8), 297. [DOI], [ADS]. (Cited on pages xii, 14, and 15.)

Druckmüller, M. and National Science Foundation/NSO, 2013, "License: Creative Commons Attribution 4.0", [accessed: 2020-05-30]. (Cited on pages xii and 11.)

Duckenfield, T., Anfinogentov, S. A., Pascoe, D. J. and Nakariakov, V. M., 2018, "Detection of the Second Harmonic of Decay-less Kink Oscillations in the Solar Corona", *ApJL*, **854**(1), L5. [DOI], [ADS]. (Cited on pages 100 and 101.)

Duckenfield, T. J., Goddard, C. R., Pascoe, D. J. and Nakariakov, V. M., 2019, "Observational signatures of the third harmonic in a decaying kink oscillation of a coronal loop", *Astron. Astrophys.*, **632**, A64. [DOI], [ADS]. (Cited on pages 101, 105, and 123.)

Eddington, A. S., 1926, The Internal Constitution of the Stars, University Press Cambridge. [ADS]. (Cited on page 2.)

Eddy, John A., 1976, "The Maunder Minimum", Science, **192**(4245), 1189–1202. [DOI], [ADS]. (Cited on page 14.)

Edlen, B., 1943, "Die Deutung der Emissionslinien im Spektrum der Sonnenkorona. Mit 6 Abbildungen.", **22**, 30. [ADS]. (Cited on page 9.)

Edwin, P. M. and Roberts, B., 1983, "Wave Propagation in a Magnetic Cylinder", *Solar Phys.*, **88**(1-2), 179–191. [DOI], [ADS]. (Cited on pages 29 and 32.)

Einstein, A., 1905, "Ist die Trägheit eines Körpers von seinem Energieinhalt abhängig?", Annalen der Physik, **323**(13), 639–641. [DOI], [ADS]. (Cited on page 2.)

Evans, J. S., Strickland, D. J., Woo, W. K. et al., 2010, "Early Observations by the GOES-13 Solar Extreme Ultraviolet Sensor (EUVS)", *Solar Phys.*, **262**(1), 71–115. [DOI], [ADS]. (Cited on page 37.)

Farge, Marie, 1992, "Wavelet transforms and their applications to turbulence", Annual Review of Fluid Mechanics, **24**, 395–457. [DOI], [ADS]. (Cited on page 54.)

Fedun, V., Shelyag, S. and Erdélyi, R., 2011, "Numerical Modeling of Footpoint-driven Magneto-acoustic Wave Propagation in a Localized Solar Flux Tube", *ApJ*, **727**(1), 17. [DOI], [ADS]. (Cited on page 10.)

Flandrin, P., Rilling, G. and Goncalves, P., 2004, "Empirical mode decomposition as a filter bank", IEEE Signal Processing Letters, **11**(2), 112–114. (Cited on page 122.)

Fletcher, L., Dennis, B. R., Hudson, H. S. et al., 2011, "An Observational Overview of Solar Flares", *Space Sci. Rev.*, **159**(1-4), 19–106. [DOI], [ADS], [arXiv:1109.5932 [astro-ph.SR]]. (Cited on page 16.)

Fourier, Joseph, 1878, The analytical theory of heat, Cambridge University Press. [DOI]. (Cited on page 47.)

Fukuda, Y., Hayakawa, T., Inoue, K. et al., 1996, "Solar Neutrino Data Covering Solar Cycle 22", *Phys. Rev. L*, **77**(9), 1683–1686. [DOI], [ADS]. (Cited on page 3.)

García, Rafael A. and Ballot, Jérôme, 2019, "Asteroseismology of solar-type stars", Living Reviews in Solar Physics, **16**(1), 4. [DOI], [ADS], [arXiv:1906.12262 [astro-ph.SR]]. (Cited on page 47.)

Gary, G. Allen, 2001, "Plasma Beta above a Solar Active Region: Rethinking the Paradigm", *Solar Phys.*, **203**(1), 71–86. [DOI], [ADS]. (Cited on page 19.)

Gent, Frederick A., Snow, Ben, Fedun, Viktor and Erdélyi, Robertus, 2019, "Modelling 3D magnetic networks in a realistic solar atmosphere", *Mon. Not. Roy. Astron. Soc.*, **489**(1), 28–35. [DOI], [ADS], [arXiv:1904.11421 [astro-ph.SR]]. (Cited on page 10.)

Goddard, C. R., Nisticò, G., Nakariakov, V. M. and Zimovets, I. V., 2016, "A statistical study of decaying kink oscillations detected using SDO/AIA", *Astron. Astrophys.*, **585**, A137. [DOI], [ADS], [arXiv:1511.03558 [astro-ph.SR]]. (Cited on page 100.)

Goedbloed, J. P. Hans and Poedts, Stefaan, 2004, Principles of Magnetohydrodynamics. [ADS]. (Cited on page 24.)

Goldreich, P. and Keeley, D. A., 1977, "Solar seismology. II. The stochastic excitation of the solar p-modes by turbulent convection.", *ApJ*, **212**, 243–251. [DOI], [ADS]. (Cited on page 12.)

Goodfellow, Ian, Bengio, Yoshua and Courville, Aaron, 2016, Deep learning, MIT press. (Cited on page 144.)

Goossens, M., Andries, J. and Aschwanden, M. J., 2002, "Coronal loop oscillations. An interpretation in terms of resonant absorption of quasi-mode kink oscillations", *Astron. Astrophys.*, **394**, L39–L42. [DOI], [ADS]. (Cited on page 35.)

Goossens, M., Terradas, J., Andries, J., Arregui, I. and Ballester, J. L., 2009, "On the nature of kink MHD waves in magnetic flux tubes", *Astron. Astrophys.*, **503**(1), 213–223. [DOI], [ADS], [arXiv:0905.0425 [astro-ph.SR]]. (Cited on page 35.)

Gough, D., 1977, "Random Remarks on Solar Hydrodynamics", in IAU Colloq. 36: The Energy Balance and Hydrodynamics of the Solar Chromosphere and Corona, [ADS]. (Cited on page 6.)

Grotrian, W., 1939, "Zur Frage der Deutung der Linien im Spektrum der Sonnenkorona", Naturwissenschaften, **27**(13), 214–214. [DOI], [ADS]. (Cited on page 9.)

Hale, George E., 1908, "On the Probable Existence of a Magnetic Field in Sun-Spots", *ApJ*, **28**, 315. [DOI], [ADS]. (Cited on pages 5 and 7.)

Hampel, W. et al. [GALLEX], 1999, "GALLEX solar neutrino observations: Results for GALLEX IV", Phys. Lett. B, **447**, 127–133. [DOI]. (Cited on page 3.)

Handy, B. N., Acton, L. W., Kankelborg, C. C. et al., 1999, "The transition region and coronal explorer", *Solar Phys.*, **187**(2), 229–260. [DOI], [ADS]. (Cited on pages 19 and 53.)

Hanle, Wilhelm, 1924, "Über magnetische Beeinflussung der Polarisation der Resonanzfluoreszenz", Zeitschrift fur Physik, **30**(1), 93–105. [DOI], [ADS]. (Cited on page 8.)

Harris, Charles R., Millman, K. Jarrod, van der Walt, St'efan J. et al., 2020, "Array programming with NumPy", Nature, **585**(7825), 357–362. [DOI]URL: https://doi.org/10.1038/s41586-020-2649-2. (Cited on pages iv and 46.)

Hartmann, William, 2007, Acoustic Signal Processing, Springer New York. [DOI]URL: https://doi.org/10.1007/978-0-387-30425-0_14. [DOI]. (Cited on page 113.)

Hathaway, David H., 2010, "The Solar Cycle", Living Reviews in Solar Physics, **7**(1), 1. [DOI], [ADS]. (Cited on pages 12, 13, and 14.)

Hayashi, Yoshikazu, 1982, "Space-Time Spectral Analysis and its Applications to Atmospheric Waves", Journal of the Meteorological Society of Japan. Ser. II, **60**(1), 156–171. [DOI]. (Cited on page 144.)

Hill, S. M., Pizzo, V. J., Balch, C. C. et al., 2005, "The NOAA Goes-12 Solar X-Ray Imager (SXI) 1. Instrument, Operations, and Data", *Solar Phys.*, **226**(2), 255–281. [DOI], [ADS]. (Cited on page 37.)

Hindman, Bradley W and Jain, Rekha, 2014, "An Interpretation of Flare-induced and Decayless Coronal-loop Oscillations as Interference Patterns", *ApJ*, **784**(2), 103. [DOI], [ADS], [arXiv:1312.1922 [astro-ph.SR]]. (Cited on pages xiv, 35, 36, 71, 97, 100, 101, 102, 104, 106, 111, 121, 122, 126, 136, 139, and 142.)

Hindman, Bradley W. and Jain, Rekha, 2015, "Eigenmodes of Three-dimensional Magnetic Arcades in the Sun's Corona", *ApJ*, **814**(2), 105. [DOI], [ADS], [arXiv:1511.09411 [astro-ph.SR]]. (Cited on pages 35, 36, 95, 96, 100, 101, and 136.)

Hindman, Bradley W. and Jain, Rekha, 2018, "A Novel Approach to Resonant Absorption of the Fast Magnetohydrodynamic Eigenmodes of a Coronal Arcade", *ApJ*, **858**(1), 6. [DOI], [ADS], [arXiv:1803.08948 [astro-ph.SR]]. (Cited on pages 35, 96, 100, and 136.)

Hindman, Bradley W. and Jain, Rekha, 2021, "Do Coronal Loops Oscillate in Isolation?", *ApJ*, **921**(1), 29. [DOI], [ADS], [arXiv:2108.04362 [astro-ph.SR]]. (Cited on page 37.)

Hirayama, T., 1974, "Theoretical Model of Flares and Prominences. I: Evaporating Flare Model", *Solar Phys.*, **34**(2), 323–338. [DOI], [ADS]. (Cited on page 16.)

Hodgson, R., 1859, "On a curious Appearance seen in the Sun", *Mon. Not. Roy. Astron. Soc.*, **20**, 15–16. [DOI], [ADS]. (Cited on page 16.)

Hood, A. W., Ruderman, M., Pascoe, D. J., De Moortel, I., Terradas, J. and Wright, A. N., 2013, "Damping of kink waves by mode coupling. I. Analytical treatment", *Astron. Astrophys.*, **551**, A39. [DOI], [ADS]. (Cited on pages 76 and 98.)

Huang, N. E., Shen, Z., Long, S. R. et al., 1998, "The empirical mode decomposition and the Hilbert spectrum for nonlinear and non-stationary time series analysis", Proceedings of the Royal Society of London Series A, **454**(1971), 903–998. [DOI], [ADS]. (Cited on pages 59, 60, 61, 116, and 121.)

Huang, Norden E, 2014, "Introduction to the Hilbert–Huang transform and its related mathematical problems", in Hilbert–Huang transform and its applications, pp. 1–26, World Scientific. (Cited on page 61.)

Hudson, H. S., 2000, "Implosions in Coronal Transients", *ApJL*, **531**(1), L75–L77. [DOI], [ADS]. (Cited on pages 126 and 129.)

Hudson, H. S. and Warmuth, A., 2004, "Coronal Loop Oscillations and Flare Shock Waves", *ApJL*, **614**(1), L85–L88. [DOI], [ADS]. (Cited on pages 22 and 100.)

Hunter, J. D., 2007, "Matplotlib: A 2D graphics environment", Computing in Science & Engineering, **9**(3), 90–95. [DOI]. (Cited on page iv.)

Ireland, J., McAteer, R. T. J. and Inglis, A. R., 2015, "Coronal Fourier Power Spectra: Implications for Coronal Seismology and Coronal Heating", *ApJ*, **798**(1), 1. [DOI], [ADS], [arXiv:1410.2171 [astro-ph.SR]]. (Cited on pages 57, 61, 71, 98, 102, and 122.)

Jain, R. and Hindman, B. W., 2012, "What can be learned from the seismology of a coronal loop using only a handful of frequencies?", *Astron. Astrophys.*, **545**, A138. [DOI], [ADS]. (Cited on pages 36 and 101.)

Jain, Rekha, Maurya, Ram A. and Hindman, Bradley W., 2015, "Fundamental-mode Oscillations of Two Coronal Loops within a Solar Magnetic Arcade", *ApJL*, **804**(1), L19. [DOI], [ADS], [arXiv:1504.07822 [astro-ph.SR]]. (Cited on pages 76, 101, and 137.)

Kelvinsong, 2012, "License: Creative Commons Attribution-ShareAlike 3.0 Unported.", [accessed: 2020-04-27]. (Cited on pages xi and 4.)

Kohutova, P. and Popovas, A., 2021, "Excitation and evolution of coronal oscillations in self-consistent 3D radiative MHD simulations of the solar atmosphere", arXiv e-prints, arXiv:2101.06430. [ADS], [arXiv:2101.06430 [astro-ph.SR]]. (Cited on page 100.)

Kolotkov, D. Y., Anfinogentov, S. A. and Nakariakov, V. M., 2016, "Empirical mode decomposition analysis of random processes in the solar atmosphere", *Astron. Astrophys.*,

592, A153. [DOI], [ADS]. (Cited on pages 61, 97, 102, and 121.)

Kopp, R. A. and Pneuman, G. W., 1976, "Magnetic reconnection in the corona and the loop prominence phenomenon.", *Solar Phys.*, **50**(1), 85–98. [DOI], [ADS]. (Cited on pages 16 and 19.)

Kosovichev, Alexander G., 2012, "Local Helioseismology of Sunspots: Current Status and Perspectives", *Solar Phys.*, **279**(2), 323–348. [DOI], [ADS], [arXiv:1010.4927 [astro-ph.SR]]. (Cited on page 6.)

Kuridze, D., Mathioudakis, M., Morgan, H. et al., 2019, "Mapping the Magnetic Field of Flare Coronal Loops", *ApJ*, **874**(2), 126. [DOI], [ADS], [arXiv:1902.07514 [astro-ph.SR]]. (Cited on page 34.)

Kusano, Kanya, Iju, Tomoya, Bamba, Yumi and Inoue, Satoshi, 2020, "A physics-based method that can predict imminent large solar flares", Science, **369**(6503), 587–591. [DOI], [ADS]. (Cited on page 16.)

LeCun, Yann, Bengio, Yoshua and Hinton, Geoffrey, 2015, "Deep learning", nature, **521**(7553), 436–444. (Cited on page 144.)

Leibacher, J. W. and Stein, R. F., 1971, "A New Description of the Solar Five-Minute Oscillation", *ApJL*, **7**, 191–192. [DOI]. (Cited on page 5.)

Leighton, Robert B., Noyes, Robert W. and Simon, George W., 1962, "Velocity Fields in the Solar Atmosphere. I. Preliminary Report.", *ApJ*, **135**, 474. [DOI], [ADS]. (Cited on page 5.)

Lemen, James R., Duncan, Dexter W., Edwards, Christopher G. et al., 2004, "The Solar X-ray Imager for GOES", in *Proc. SPIE*, Society of Photo-Optical Instrumentation Engineers (SPIE) Conference Series, 5171, SPIE. [DOI]. [ADS]. (Cited on page 37.)

Lemen, James R., Title, Alan M., Akin, David J. et al., 2012, "The Atmospheric Imaging Assembly (AIA) on the Solar Dynamics Observatory (SDO)", *Solar Phys.*, **275**, 17–40. [DOI], [ADS]URL:
https://doi.org/10.1007/s11207-011-9776-8. (Cited on pages xxv, 38, 41, 64, 103, and 127.)

Levine, R. H. and Withbroe, G. L., 1977, "Physics of an active region loop system.", *Solar Phys.*, **51**(1), 83–101. [DOI], [ADS]. (Cited on page 19.)

Li, Hongbo, Liu, Yu and Vai Tam, Kuan, 2017, "Fundamental and Harmonic Oscillations in Neighboring Coronal Loops", *ApJ*, **842**(2), 99. [DOI], [ADS]. (Cited on page 101.)

Lin, R. P., Dennis, B. R., Hurford, G. J. et al., 2002, "The Reuven Ramaty High-Energy Solar Spectroscopic Imager (RHESSI)", *Solar Phys.*, **210**(1), 3–32. [DOI], [ADS]. (Cited

on page 127.)

Liu, Wei, Title, Alan M., Zhao, Junwei, Ofman, Leon, Schrijver, Carolus J., Aschwanden, Markus J., De Pontieu, Bart and Tarbell, Theodore D., 2011, "Direct Imaging of Quasi-periodic Fast Propagating Waves of $\sim$2000 km s^{-1} in the Low Solar Corona by the Solar Dynamics Observatory Atmospheric Imaging Assembly", *ApJL*, **736**(1), L13. [DOI], [ADS], [arXiv:1106.3150 [astro-ph.SR]]. (Cited on page 106.)

Lockwood, M., Harrison, R. G., Woollings, T. and Solanki, S. K., 2010, "Are cold winters in Europe associated with low solar activity?", Environmental Research Letters, **5**(2), 024001. [DOI], [ADS]. (Cited on page 14.)

Lockyer, J. Norman, 1868, "Spectroscopic Observation of the Sun, No. II.", Proceedings of the Royal Society of London Series I, **17**, 131–132. [ADS]. (Cited on page 8.)

Lomb, N. R., 1976, "Least-Squares Frequency Analysis of Unequally Spaced Data", *Astrophys. Space Sci.*, **39**(2), 447–462. [DOI], [ADS]. (Cited on page 53.)

Long, D. M., Valori, G., Pérez-Suárez, D., Morton, R. J. and Vásquez, A. M., 2017, "Measuring the magnetic field of a trans-equatorial loop system using coronal seismology", *Astron. Astrophys.*, **603**, A101. [DOI], [ADS], [arXiv:1703.10020 [astro-ph.SR]]. (Cited on page 61.)

Mann, Michael E., Zhang, Zhihua, Rutherford, Scott et al., 2009, "Global Signatures and Dynamical Origins of the Little Ice Age and Medieval Climate Anomaly", Science, **326**(5957), 1256. [DOI], [ADS]. (Cited on page 14.)

Maunder, E. Walter, 1904, "Note on the Distribution of Sun-spots in Heliographic Latitude, 1874-1902", *Mon. Not. Roy. Astron. Soc.*, **64**, 747–761. [DOI], [ADS]. (Cited on page 14.)

Maxwell, J. C., 1865, "A Dynamical Theory of the Electromagnetic Field", Philosophical Transactions of the Royal Society of London Series I, **155**, 459–512. [ADS]. (Cited on page 24.)

McWhirter, R. W. P., Thonemann, P. C. and Wilson, R., 1975, "The heating of the solar corona. II. A model based on energy balance.", *Astron. Astrophys.*, **40**(1-2), 63–73. [ADS]. (Cited on pages xi and 9.)

Mitalas, R. and Sills, K. R., 1992, "On the Photon Diffusion Time Scale for the Sun", *ApJ*, **401**, 759. [DOI], [ADS]. (Cited on page 3.)

Morgan, Huw and Druckmüller, Miloslav, 2014, "Multi-Scale Gaussian Normalization for Solar Image Processing", *Solar Phys.*, **289**(8), 2945–2955. [DOI], [ADS], [arXiv:1403.6613 [astro-ph.SR]]. (Cited on pages xvii and 75.)

Morton, R. J. and Mooroogen, K., 2016, "Model fitting of kink waves in the solar atmosphere:

Gaussian damping and time-dependence", *Astron. Astrophys.*, **593**, A59. [DOI], [ADS], [arXiv:1607.05905 [astro-ph.SR]]. (Cited on pages 76 and 98.)

Morton, R. J., Erdélyi, R., Jess, D. B. and Mathioudakis, M., 2011, "Observations of Sausage Modes in Magnetic Pores", *ApJL*, **729**(2), L18. [DOI], [ADS], [arXiv:1011.2375 [astro-ph.SR]]. (Cited on page 61.)

Morton, R. J., Srivastava, A. K. and Erdélyi, R., 2012, "Observations of quasi-periodic phenomena associated with a large blowout solar jet", *Astron. Astrophys.*, **542**, A70. [DOI], [ADS], [arXiv:1204.5033 [astro-ph.SR]]. (Cited on pages xiii, 30, 61, 101, and 121.)

Morton, R. J., Tomczyk, S. and Pinto, R., 2015, "Investigating Alfvénic wave propagation in coronal open-field regions", Nature Communications, **6**, 7813. [DOI], [ADS]. (Cited on page 23.)

Morton, R. J., Weberg, M. J. and McLaughlin, J. A., 2019, "A basal contribution from p-modes to the Alfvénic wave flux in the Sun's corona", Nature Astronomy, **3**, 223. [DOI], [ADS], [arXiv:1902.03811 [astro-ph.SR]]. (Cited on pages 6, 17, and 23.)

Mulu-Moore, Fana M., Winebarger, Amy R., Warren, Harry P. and Aschwanden, Markus J., 2011, "Determining the Structure of Solar Coronal Loops Using Their Evolution", *ApJ*, **733**(1), 59. [DOI], [ADS]. (Cited on pages 19 and 20.)

Mumford, S. J. and Erdélyi, R., 2015, "Photospheric logarithmic velocity spirals as MHD wave generation mechanisms", *Mon. Not. Roy. Astron. Soc.*, **449**(2), 1679–1685. [DOI], [ADS], [arXiv:1501.01871 [astro-ph.SR]]. (Cited on page 10.)

Murphy, R. J., Dermer, C. D. and Ramaty, R., 1987, "High-Energy Processes in Solar Flares", *Astrophys. J. Suppl.*, **63**, 721. [DOI], [ADS]. (Cited on page 17.)

Nakariakov, V. M. and King, D. B., 2007, "Coronal Periodmaps", *Solar Phys.*, **241**(2), 397–409. [DOI], [ADS]. (Cited on pages 64, 70, and 97.)

Nakariakov, V. M. and Ofman, L., 2001, "Determination of the coronal magnetic field by coronal loop oscillations", *Astron. Astrophys.*, **372**, L53–L56. [DOI], [ADS]. (Cited on pages 34, 101, and 126.)

Nakariakov, V. M., Ofman, L., Deluca, E. E., Roberts, B. and Davila, J. M., 1999, "TRACE observation of damped coronal loop oscillations: Implications for coronal heating", Science, **285**, 862–864. [DOI], [ADS]. (Cited on pages 20, 34, and 126.)

Nakariakov, V. M., Pilipenko, V., Heilig, B. et al., 2016, "Magnetohydrodynamic Oscillations in the Solar Corona and Earth's Magnetosphere: Towards Consolidated Understanding", *Space Sci. Rev.*, **200**(1-4), 75–203. [DOI], [ADS]. (Cited on pages 23 and 100.)

Nakariakov, Valery M. and Kolotkov, Dmitrii Y., 2020, "Magnetohydrodynamic Waves

in the Solar Corona", Annual Review of Astronomy and Astrophysics, **58**(1). [DOI], [https://doi.org/10.1146/annurev-astro-032320-042940]URL: https://doi.org/10.1146/annurev-astro-032320-042940. (Cited on page 100.)

Nakariakov, Valery M. and Verwichte, Erwin, 2005, "Coronal Waves and Oscillations", Living Reviews in Solar Physics, **2**(1). [DOI]URL: https://doi.org/10.12942/lrsp-2005-3. (Cited on pages 29 and 64.)

Nechaeva, Alena, Zimovets, Ivan V., Nakariakov, V. M. and Goddard, C. R., 2019, "Catalog of Decaying Kink Oscillations of Coronal Loops in the 24th Solar Cycle", *Astrophys. J. Suppl.*, **241**(2), 31. [DOI], [ADS]. (Cited on page 126.)

Neupert, W. M., Swartz, M. and White, W. A., 1968, "Observations of the Solar X-Ray and Extreme Ultraviolet Spectrum from OSO-III", The Astronomical Journal Supplement, **73**, 73. [ADS]. (Cited on page 12.)

Neupert, Werner M., 2011, "Intercalibration of Solar Soft X-Ray Broad Band Measurements from SOLRAD 9 through GOES-12", *Solar Phys.*, **272**(2), 319–335. [DOI], [ADS]. (Cited on page 37.)

Nisticò, G., Nakariakov, V. M. and Verwichte, E., 2013, "Decaying and decayless transverse oscillations of a coronal loop", *Astron. Astrophys.*, **552**, A57. [DOI], [ADS]. (Cited on pages 22, 64, 100, and 121.)

Nisticò, G., Anfinogentov, S. and Nakariakov, V. M., 2014, "Dynamics of a multi-thermal loop in the solar corona", *Astron. Astrophys.*, **570**, A84. [DOI], [ADS]. (Cited on page 78.)

Ofman, L. and Aschwanden, M. J., 2002, "Damping Time Scaling of Coronal Loop Oscillations Deduced from Transition Region and Coronal Explorer Observations", *ApJL*, **576**(2), L153–L156. [DOI], [ADS]. (Cited on page 35.)

Ossendrijver, Mathieu, 2003, "The solar dynamo", *Astron. Astrophys. Rev.*, **11**(4), 287–367. [DOI], [ADS]. (Cited on page 5.)

Owens, Mathew J., Lockwood, Mike, Hawkins, Ed, Usoskin, Ilya, Jones, Gareth S., Barnard, Luke, Schurer, Andrew and Fasullo, John, 2017, "The Maunder minimum and the Little Ice Age: an update from recent reconstructions and climate simulations", Journal of Space Weather and Space Climate, **7**, A33. [DOI], [ADS]. (Cited on page 14.)

Parseval, Marc-Antoine, 1806, "Mémoire sur les séries et sur l'intégration complète d'une équation aux différences partielles linéaires du second ordre, à coefficients constants", Mém. prés. par divers savants, Acad. des Sciences, Paris,(1), **1**, 638–648. (Cited on page 49.)

Pascoe, D. J., Goddard, C. R. and Nakariakov, V. M., 2016a, "Spatially resolved observation of the fundamental and second harmonic standing kink modes using SDO/AIA", *Astron.*

Astrophys., **593**, A53. [DOI], [ADS]. (Cited on pages 64, 101, 104, and 123.)

Pascoe, D. J., Goddard, C. R., Nisticò, G., Anfinogentov, S. and Nakariakov, V. M., 2016b, "Damping profile of standing kink oscillations observed by SDO/AIA", *Astron. Astrophys.*, **585**, L6. [DOI], [ADS]. (Cited on pages 62, 76, and 98.)

Pascoe, D. J., Smyrli, A. and Van Doorsselaere, T., 2020, "Tracking and Seismological Analysis of Multiple Coronal Loops in an Active Region", *ApJ*, **898**(2), 126. [DOI], [ADS]. (Cited on pages 76, 101, 103, 105, 106, and 127.)

Peres, G., Orlando, S., Reale, F., Rosner, R. and Hudson, H., 2000, "The Sun as an X-Ray Star. II. Using theYohkoh/Soft X-Ray Telescope-derived Solar Emission Measure versus Temperature to Interpret Stellar X-Ray Observations", *ApJ*, **528**(1), 537–551. [DOI], [ADS]. (Cited on page 17.)

Perneger, Thomas V, 1998, "What's wrong with Bonferroni adjustments", BMJ, **316**(7139), 1236–1238. [DOI], [https://www.bmj.com/content]URL:
https://www.bmj.com/content/316/7139/1236. (Cited on page 57.)

Pesnell, W. Dean, Thompson, B. J. and Chamberlin, P. C., 2012, "The Solar Dynamics Observatory (SDO)", *Solar Phys.*, **275**(1-2), 3–15. [DOI], [ADS]. (Cited on pages xiv, 38, 39, 64, 103, and 127.)

Peter, Hardi, Gudiksen, Boris V. and Nordlund, Åke, 2006, "Forward Modeling of the Corona of the Sun and Solar-like Stars: From a Three-dimensional Magnetohydrodynamic Model to Synthetic Extreme-Ultraviolet Spectra", *ApJ*, **638**(2), 1086–1100. [DOI], [ADS], [arXiv:astro-ph/0503342 [astro-ph]]. (Cited on page 123.)

Phillips, Kenneth J. H., 1992, Guide to the Sun, University Press Cambridge. [ADS]. (Cited on pages 3 and 8.)

Pizzo, V. J., Hill, S. M., Balch, C. C. et al., 2005, "The NOAA Goes-12 Solar X-Ray Imager (SXI) 2. Performance", *Solar Phys.*, **226**(2), 283–315. [DOI], [ADS]. (Cited on page 37.)

Poduval, B., DeForest, C. E., Schmelz, J. T. and Pathak, S., 2013, "Point-spread Functions for the Extreme-ultraviolet Channels of SDO/AIA Telescopes", *ApJ*, **765**(2), 144. [DOI], [ADS]. (Cited on page 41.)

Priest, E. R., 1986, "Magnetohydrodynamic Theories of Solar Flares", *Solar Phys.*, **104**(1), 1–18. [DOI], [ADS]. (Cited on page 10.)

Priest, Eric, 2014, "Magnetohydrodynamics of the Sun", [ADS]. (Cited on pages 7, 8, 10, 12, 24, and 28.)

Procházka, Ondřej, Milligan, Ryan O., Allred, Joel C., Kowalski, Adam F., Kotrč, Pavel and Mathioudakis, Mihalis, 2017, "Suppression of Hydrogen Emission in an X-class White-light

Solar Flare", *ApJ*, **837**(1), 46. [DOI], [ADS], [arXiv:1702.00638 [astro-ph.SR]]. (Cited on page 128.)

Rachmeler, Laurel A., Winebarger, Amy R., Savage, Sabrina L. et al., 2019, "The High-Resolution Coronal Imager, Flight 2.1", *Solar Phys.*, **294**(12), 174. [DOI], [ADS], [arXiv:1909.05942 [astro-ph.SR]]. (Cited on page 20.)

Rast, Mark P., Bello González, Nazaret, Bellot Rubio, Luis et al., 2021, "Critical Science Plan for the Daniel K. Inouye Solar Telescope (DKIST)", *Solar Phys.*, **296**(4), 70. [DOI], [ADS], [arXiv:2008.08203 [astro-ph.SR]]. (Cited on page 144.)

Reale, F. and Peres, G., 2000, "TRACE-derived Temperature and Emission Measure Profiles along Long-lived Coronal Loops: The Role of Filamentation", *ApJL*, **528**(1), L45–L48. [DOI], [ADS], [arXiv:astro-ph/9911096 [astro-ph]]. (Cited on page 71.)

Reale, Fabio, 2014, "Coronal Loops: Observations and Modeling of Confined Plasma", Living Reviews in Solar Physics, **11**(1), 4. [DOI], [ADS]. (Cited on page 17.)

Roberts, B., 1981, "Wave Propagation in a Magnetically Structured Atmosphere - Part One - Surface Waves at a Magnetic Interface", *Solar Phys.*, **69**(1), 27–38. [DOI], [ADS]. (Cited on pages 32 and 34.)

Roberts, B., 2000, "Waves and Oscillations in the Corona - (Invited Review)", *Solar Phys.*, **193**, 139–152. [DOI], [ADS]. (Cited on pages 29 and 126.)

Roberts, B., Edwin, P. M. and Benz, A. O., 1984, "On coronal oscillations", *ApJ*, **279**, 857–865. [DOI], [ADS]. (Cited on pages 29, 32, 34, 44, and 100.)

Rossing, Thomas D., 2002, The science of sound, Addison Wesley, San Francisco ; London, 3rd ed. edn. (Cited on page 122.)

Ruderman, M. S. and Roberts, B., 2002, "The Damping of Coronal Loop Oscillations", *ApJ*, **577**(1), 475–486. [DOI], [ADS]. (Cited on page 35.)

Ruderman, Michael S. and Erdélyi, Robert, 2009, "Transverse Oscillations of Coronal Loops", *Space Sci. Rev.*, **149**(1-4), 199–228. [DOI], [ADS]. (Cited on pages 29, 31, and 34.)

Ruderman, Michael S. and Roberts, Bernard, 2006, "Leaky and non-leaky kink oscillations of magnetic flux tubes", Journal of Plasma Physics, **72**(3), 285–308. [DOI], [ADS]. (Cited on page 33.)

Russell, A. J. B., Simões, P. J. A. and Fletcher, L., 2015, "A unified view of coronal loop contraction and oscillation in flares", *Astron. Astrophys.*, **581**, A8. [DOI], [ADS], [arXiv:1506.07716 [astro-ph.SR]]. (Cited on pages 126 and 136.)

Sarkar, S., Pant, V., Srivastava, A. K. and Banerjee, D., 2016, "Transverse Oscillations

in a Coronal Loop Triggered by a Jet", *Solar Phys.*, **291**(11), 3269–3288. [DOI], [ADS], [arXiv:1611.04063 [astro-ph.SR]]. (Cited on page 126.)

Scargle, J. D., 1982, "Studies in astronomical time series analysis. II. Statistical aspects of spectral analysis of unevenly spaced data.", *ApJ*, **263**, 835–853. [DOI], [ADS]. (Cited on page 53.)

Scherrer, P. H., Schou, J., Bush, R. I. et al., 2012, "The Helioseismic and Magnetic Imager (HMI) Investigation for the Solar Dynamics Observatory (SDO)", *Solar Phys.*, **275**(1-2), 207–227. [DOI], [ADS]. (Cited on page 38.)

Schmelz, J. T., Scopes, R. T., Cirtain, J. W., Winter, H. D. and Allen, J. D., 2001, "Observational Constraints on Coronal Heating Models Using Coronal Diagnostics Spectrometer and Soft X-Ray Telescope Data", *ApJ*, **556**(2), 896–904. [DOI], [ADS]. (Cited on page 19.)

Schrijver, Carolus J., 2009, "Driving major solar flares and eruptions: A review", Advances in Space Research, **43**(5), 739–755. [DOI], [ADS], [arXiv:0811.0787 [astro-ph]]. (Cited on page 16.)

Schrijver, Carolus J., Aschwanden, Markus J. and Title, Alan M., 2002, "Transverse oscillations in coronal loops observed with TRACE I. An Overview of Events, Movies, and a Discussion of Common Properties and Required Conditions", *Solar Phys.*, **206**(1), 69–98. [DOI], [ADS]. (Cited on page 22.)

Selwa, M., Murawski, K., Solanki, S. K. and Ofman, L., 2010, "Excitation of vertical kink waves in a solar coronal arcade loop by a periodic driver", *Astron. Astrophys.*, **512**, A76. [DOI], [ADS]. (Cited on page 126.)

Selwa, M., Solanki, S. K. and Ofman, L., 2011, "The Role of Active Region Loop Geometry. II. Symmetry Breaking in Three-dimensional Active Region: Why are Vertical Kink Oscillations Observed so Rarely?", *ApJ*, **728**(2), 87. [DOI], [ADS]. (Cited on page 20.)

Smith, J. M., Roberts, B. and Oliver, R., 1997, "Ducted fast waves in coronal loops: curvature effects.", *Astron. Astrophys.*, **317**, 752–760. [ADS]. (Cited on page 35.)

Spiegel, E. A. and Zahn, J. P., 1992, "The solar tachocline.", *Astron. Astrophys.*, **265**, 106–114. [ADS]. (Cited on page 5.)

Spruit, H. C., 1981, "Magnetic flux tubes.", in NASA Special Publication, (Ed.) Jordan, Stuart, 450, [ADS]. (Cited on page 34.)

Spruit, H. C., 1982, "Propagation Speeds and Acoustic Damping of Waves in Magnetic Flux Tubes", *Solar Phys.*, **75**(1-2), 3–17. [DOI], [ADS]. (Cited on page 29.)

Stenflo, J. O., 1982, "The Hanle Effect and the Diagnostics of Turbulent Magnetic Fields in the Solar Atmosphere", *Solar Phys.*, **80**(2), 209–226. [DOI], [ADS]. (Cited on page 8.)

Sturrock, P. A., 1966, "Model of the High-Energy Phase of Solar Flares", *Nature*, **211**(5050), 695–697. [DOI], [ADS]. (Cited on page 16.)

Sych, R. A. and Nakariakov, V. M., 2008, "The Pixelised Wavelet Filtering Method to Study Waves and Oscillations in Time Sequences of Solar Atmospheric Images", *Solar Phys.*, **248**(2), 395–408. [DOI], [ADS]. (Cited on pages 64 and 97.)

Taylor, Stephen J., 1984, "Estimating the Variances of Autocorrelations Calculated from Financial Time Series", Journal of the Royal Statistical Society. Series C (Applied Statistics), **33**(3), 300–308URL:
http://www.jstor.org/stable/2347707. (Cited on pages 71 and 98.)

Terradas, J. and Ofman, L., 2004, "Loop Density Enhancement by Nonlinear Magnetohydrodynamic Waves", *ApJ*, **610**(1), 523–531. [DOI], [ADS]. (Cited on page 28.)

Terradas, J., Oliver, R. and Ballester, J. L., 2004, "Application of Statistical Techniques to the Analysis of Solar Coronal Oscillations", *ApJ*, **614**(1), 435–447. [DOI], [ADS]. (Cited on pages 61, 76, 101, 121, 126, and 139.)

Terradas, J., Oliver, R. and Ballester, J. L., 2005, "The Excitation and Damping of Transversal Coronal Loop Oscillations", *ApJL*, **618**(2), L149–L152. [DOI], [ADS]. (Cited on page 35.)

The SunPy Community, Barnes, Will T., Bobra, Monica G. et al., 2020, "The SunPy Project: Open Source Development and Status of the Version 1.0 Core Package", The Astrophysical Journal, **890**, 68–. [DOI]URL:
https://iopscience.iop.org/article/10.3847/1538-4357/ab4f7a. (Cited on page iv.)

Tomczyk, Steven and McIntosh, Scott W., 2009, "Time-Distance Seismology of the Solar Corona with CoMP", *ApJ*, **697**(2), 1384–1391. [DOI], [ADS], [arXiv:0903.2002 [astro-ph.SR]]. (Cited on pages 23 and 71.)

Toriumi, Shin and Wang, Haimin, 2019, "Flare-productive active regions", Living Reviews in Solar Physics, **16**(1), 3. [DOI], [ADS], [arXiv:1904.12027 [astro-ph.SR]]. (Cited on page 14.)

Torrence, Christopher and Compo, Gilbert P., 1998, "A Practical Guide to Wavelet Analysis.", Bulletin of the American Meteorological Society, **79**(1), 61–78. [DOI], [ADS]. (Cited on pages 54, 55, 56, 57, 59, 104, 114, and 137.)

Uchida, Y., 1970, "Diagnosis of Coronal Magnetic Structure by Flare-Associated Hydromagnetic Disturbances", *Pub. Astron. Soc. Japan*, **22**, 341. [ADS]. (Cited on page 29.)

Ulrich, Roger K., 1970, "The Five-Minute Oscillations on the Solar Surface", *ApJ*, **162**, 993. [DOI], [ADS]. (Cited on page 5.)

Uralov, A. M., 2003, "The Resonant Excitation of Transverse Oscillations in Coronal Loops", Astronomy Letters, **29**, 486–493. [DOI], [ADS]. (Cited on pages 22, 35, and 76.)

Usoskin, I. G., Solanki, S. K. and Kovaltsov, G. A., 2007, "Grand minima and maxima of solar activity: new observational constraints", *Astron. Astrophys.*, **471**(1), 301–309. [DOI], [ADS], [arXiv:0706.0385 [astro-ph]]. (Cited on page 12.)

Väänänen, Mikko, Alha, Lauri and Huovelin, Juhani, 2009, "Cross-Calibration of SMART-1 XSM with GOES and RHESSI", *Solar Phys.*, **260**(2), 479–488. [DOI], [ADS]. (Cited on page 37.)

Van Doorsselaere, T., Nakariakov, V. M. and Verwichte, E., 2007, "Coronal loop seismology using multiple transverse loop oscillation harmonics", *Astron. Astrophys.*, **473**(3), 959–966. [DOI], [ADS]. (Cited on page 35.)

van Driel-Gesztelyi, Lidia and Green, Lucie May, 2015, "Evolution of Active Regions", Living Reviews in Solar Physics, **12**(1), 1. [DOI], [ADS]. (Cited on page 14.)

VanderPlas, Jacob T., 2018, "Understanding the Lomb-Scargle Periodogram", *Astrophys. J. Suppl.*, **236**(1), 16. [DOI], [ADS], [arXiv:1703.09824 [astro-ph.IM]]. (Cited on page 53.)

Vaughan, S., 2005, "A simple test for periodic signals in red noise", *Astron. Astrophys.*, **431**, 391–403. [DOI], [ADS], [arXiv:astro-ph/0412697 [astro-ph]]. (Cited on pages 57 and 62.)

Vernazza, J. E., Avrett, E. H. and Loeser, R., 1981, "Structure of the solar chromosphere. III. Models of the EUV brightness components of the quiet sun.", *Astrophys. J. Suppl.*, **45**, 635–725. [DOI], [ADS]. (Cited on pages xi and 9.)

Verth, G., Van Doorsselaere, T., Erdélyi, R. and Goossens, M., 2007, "Spatial magneto-seismology: effect of density stratification on the first harmonic amplitude profile of transversal coronal loop oscillations", *Astron. Astrophys.*, **475**(1), 341–348. [DOI], [ADS]. (Cited on page 35.)

Verwichte, E., Nakariakov, V. M., Ofman, L. and Deluca, E. E., 2004, "Characteristics of transverse oscillations in a coronal loop arcade", Solar Physics, **223**(1), 77–94. [DOI]URL: https://doi.org/10.1007/s11207-004-0807-6. (Cited on pages 22, 35, 62, 74, and 101.)

Verwichte, E., Foullon, C. and Nakariakov, V. M., 2006, "Seismology of curved coronal loops with vertically polarised transverse oscillations", *Astron. Astrophys.*, **452**(2), 615–622. [DOI], [ADS]. (Cited on pages 20 and 22.)

Verwichte, E., Aschwanden, M. J., Van Doorsselaere, T., Foullon, C. and Nakariakov, V. M., 2009, "Seismology of a Large Solar Coronal Loop from EUVI/STEREO Observations of its Transverse Oscillation", *ApJ*, **698**(1), 397–404. [DOI], [ADS]. (Cited on pages 76, 78, and 123.)

Virtanen, Pauli, Gommers, Ralf, Oliphant, Travis E. et al., 2020, "SciPy 1.0: Fundamental Algorithms for Scientific Computing in Python", Nature Methods, **17**, 261–272. [DOI], [ADS]. (Cited on page iv.)

Wang, Juntao, Simões, P. J. A. and Fletcher, L., 2018, "Unambiguous Evidence of Coronal Implosions during Solar Eruptions and Flares", *ApJ*, **859**(1), 25. [DOI], [ADS], [arXiv:1804.02354 [astro-ph.SR]]. (Cited on page 126.)

Wang, T. J. and Solanki, S. K., 2004, "Vertical oscillations of a coronal loop observed by TRACE", *Astron. Astrophys.*, **421**, L33–L36. [DOI], [ADS]. (Cited on pages 20 and 126.)

Wang, T. J., Solanki, S. K. and Selwa, M., 2008, "Identification of different types of kink modes in coronal loops: principles and application to TRACE results", *Astron. Astrophys.*, **489**(3), 1307–1317. [DOI], [ADS], [arXiv:0808.0685 [astro-ph]]. (Cited on page 126.)

Wang, Tongjiang, Ofman, Leon, Davila, Joseph M. and Su, Yang, 2012, "Growing Transverse Oscillations of a Multistranded Loop Observed by SDO/AIA", *ApJL*, **751**(2), L27. [DOI], [ADS], [arXiv:1204.1376 [astro-ph.SR]]. (Cited on pages 22, 100, and 126.)

Warren, Harry P., Winebarger, Amy R. and Brooks, David H., 2010, "Evidence for Steady Heating: Observations of an Active Region Core with Hinode and TRACE", *ApJ*, **711**(1), 228–238. [DOI], [ADS], [arXiv:0910.0458 [astro-ph.SR]]. (Cited on page 19.)

Warren, Harry P., Brooks, David H. and Winebarger, Amy R., 2011, "Constraints on the Heating of High-temperature Active Region Loops: Observations from Hinode and the Solar Dynamics Observatory", *ApJ*, **734**(2), 90. [DOI], [ADS], [arXiv:1009.5976 [astro-ph.SR]]. (Cited on page 19.)

Warrickball, 2017, "License: Creative Commons Attribution-ShareAlike 4.0 Unported.", [accessed: 2021-04-03]. (Cited on pages xi and 6.)

Weberg, Micah J., Morton, Richard J. and McLaughlin, James A., 2018, "An Automated Algorithm for Identifying and Tracking Transverse Waves in Solar Images", *ApJ*, **852**(1), 57. [DOI], [ADS], [arXiv:1807.04842 [astro-ph.SR]]. (Cited on pages 64 and 76.)

White, R. S., Verwichte, E. and Foullon, C., 2012, "First observation of a transverse vertical oscillation during the formation of a hot post-flare loop", *Astron. Astrophys.*, **545**, A129. [DOI], [ADS]. (Cited on pages 20, 62, 78, and 126.)

Wiener, Norbert, 1930, "Generalized harmonic analysis", Acta Mathematica, **55**(none), 117 – 258. [DOI]URL:
https://doi.org/10.1007/BF02546511. (Cited on page 49.)

Williams, Thomas, Walsh, Robert W., Peter, Hardi and Winebarger, Amy R., 2020a, "Evidence for and Analysis of Multiple Hidden Coronal Strands in Cross-sectional Emission Profiles: Further Results from NASA's High-resolution Solar Coronal Imager", *ApJ*,

902(2), 90. [DOI], [ADS], [arXiv:2009.02210 [astro-ph.SR]]. (Cited on pages 20, 71, 119, and 122.)

Williams, Thomas, Walsh, Robert W., Winebarger, Amy R. et al., 2020b, "Is the High-Resolution Coronal Imager Resolving Coronal Strands? Results from AR 12712", *ApJ*, **892**(2), 134. [DOI], [ADS], [arXiv:2001.11254 [astro-ph.SR]]. (Cited on pages 20 and 122.)

Wills-Davey, M. J. and Thompson, B. J., 1999, "Observations of a Propagating Disturbance in TRACE", *Solar Phys.*, **190**, 467–483. [DOI], [ADS]. (Cited on page 20.)

Woods, T. N., Eparvier, F. G., Hock, R. et al., 2012, "Extreme Ultraviolet Variability Experiment (EVE) on the Solar Dynamics Observatory (SDO): Overview of Science Objectives, Instrument Design, Data Products, and Model Developments", *Solar Phys.*, **275**(1-2), 115–143. [DOI], [ADS]. (Cited on page 38.)

Yuan, D. and Nakariakov, V. M., 2012, "Measuring the apparent phase speed of propagating EUV disturbances", *Astron. Astrophys.*, **543**, A9. [DOI], [ADS]. (Cited on page 108.)

Zeeman, P., 1897, "The Effect of Magnetisation on the Nature of Light Emitted by a Substance", *Nature*, **55**(1424), 347. [DOI], [ADS]. (Cited on page 7.)

Zhang, Q. M., Dai, J., Xu, Z., Li, D., Lu, L., Tam, K. V. and Xu, A. A., 2020, "Transverse coronal loop oscillations excited by homologous circular-ribbon flares", *Astron. Astrophys.*, **638**, A32. [DOI], [ADS], [arXiv:2005.02067 [astro-ph.SR]]. (Cited on page 127.)

Zimovets, I. V. and Nakariakov, V. M., 2015, "Excitation of kink oscillations of coronal loops: statistical study", *Astron. Astrophys.*, **577**, A4. [DOI], [ADS]. (Cited on pages 22, 64, 100, and 126.)

A

Frequency Response Curves of Differencing Filters

The purpose of this appendix is to qualitatively explore some of the most common filtering techniques used for solar coronal data analysis. Our objective is to select the one that optimises the signal-to-noise ratio without distorting the original data that is passed into the autocorrelation function in Chapter 3. Aschwanden (2011) proposed five distinct high-pass filters to enhance the contrast of oscillating loops, namely: a box-car smoothed image, a baseline difference $(I(t_i) - I(t_j), j = 5)$ image, a one-sided running difference scheme $(I(t_i) - I(t_{i-1}))$, a symmetric running difference filter $(I(t_i) - I[(t_{i-j} + t_{i+j})/2])$ and a running-minimum difference $(I(t_i) - \min[I(t_{i-j}, \ldots t_{i+j})], j = 5)$. As an example, consider the (one-
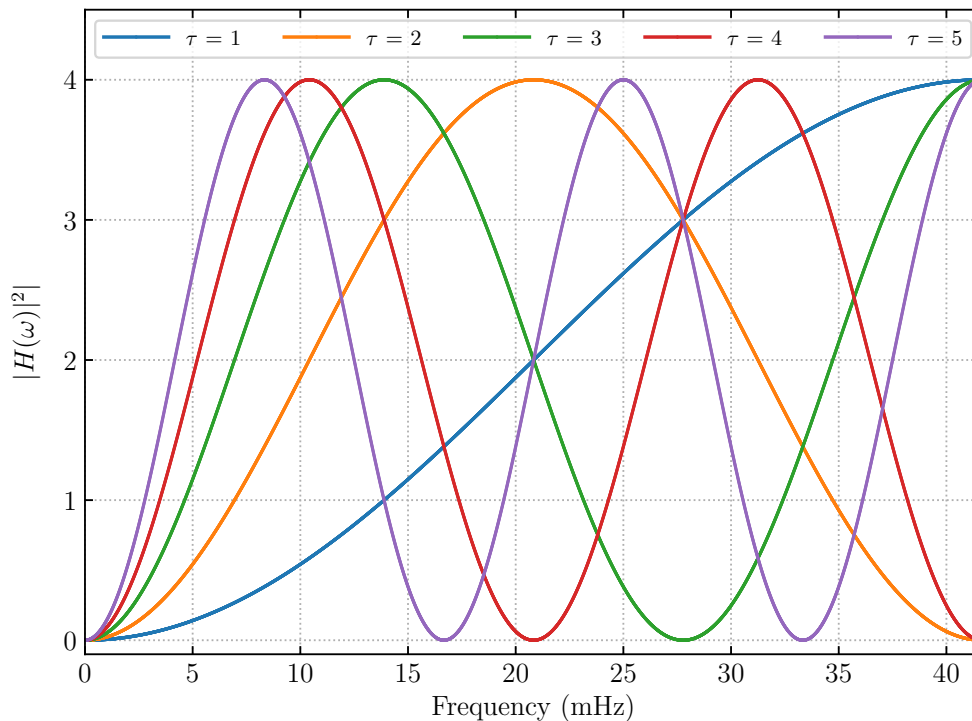
Figure A.1: Frequency responses (transfer functions) of common time derivative filters used in coronal loop studies. The value of $\tau = 1$ corresponds to a 'running-difference', where each frame is subtracted from the previous one, and is a true high-pass filter. Derivatives with time steps greater than 1 correspond to bandpass filters. The abscissa ranges from zero up to the AIA Nyquist frequency.

sided) running difference filter, which has the general following functional form:

$$\Delta I(t) = I(t) - I(t + \tau). \tag{A.1}$$

where τ is some previous time frame. Using the Fourier shift theorem, the power spectrum of the filter is described by the following expression:

$$|H(\omega)|^2 = 2\left(1 - \cos(\omega\tau)\right). \tag{A.2}$$

where $H(\omega) \equiv \Delta\widetilde{I}(\omega)/\widetilde{I}(\omega)$ is the transfer function of the filter.

Figure A.1 shows the frequency response curves for the running-difference high-pass filter for five different values of τ. It is clear that only the value of $\tau = 1$ corresponds to a true high-pass filter and all other values of the running-difference scheme result in a highly chromatic frequency response and are actually bandpass filters. If an observed time series within given pixel is multi-periodic, then it is evident that the application of this filter to the data will result in the enhancement of selective frequencies and must be used with caution.

Similar conclusions can be made about the other filters, though for the running-minimum difference which is the main filter used by Aschwanden (2011), the minimum operator is a non-linear manipulation and renders the frequency response undefined. Therefore, we opted for the more appropriate Gaussian filter, which has a known frequency response, i.e. another Gaussian.

B

Power Maps of Flaring and Non-flaring Arcades

In this appendix, we provide the FFT power maps of the flaring and non-flaring datasets that were used to compare the global oscillations of the arcade with the coronal correlation maps (see Figure 3.5) presented in Chapter 3. The power maps were integrated for the same two-minute interval, as in the correlation maps. Figure B.1 shows the integrated power maps of the flaring dataset. An immediate comparison of the FFT and correlation maps show that the autocorrelation appears to be more robust at detecting waveforms that have similar periodicies within a narrow band. This could be because of the relatively poor low-frequency resolution of the FFT.
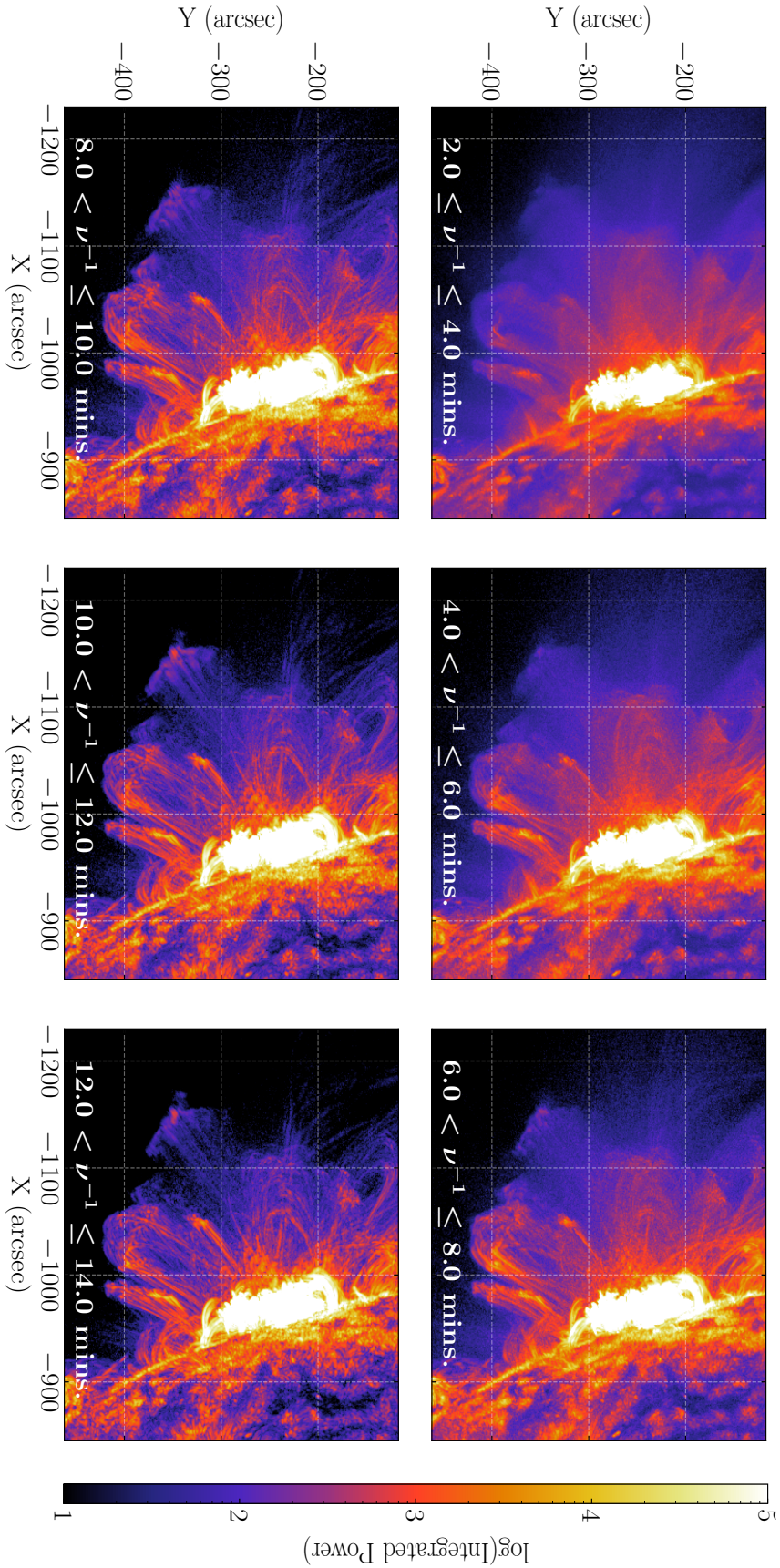
Figure B.1: FFT power maps of our region of interest integrated within a 2-minute interval. The FFT in each pixel was calculated following the procedure described in Chapter 2. As expected, the maximum power arises at the core of the active region, where the flaring activity is believed to have occurred. Similar to the correlation maps, we see that the dominant periodicities for this active region range between 4-14 minutes.
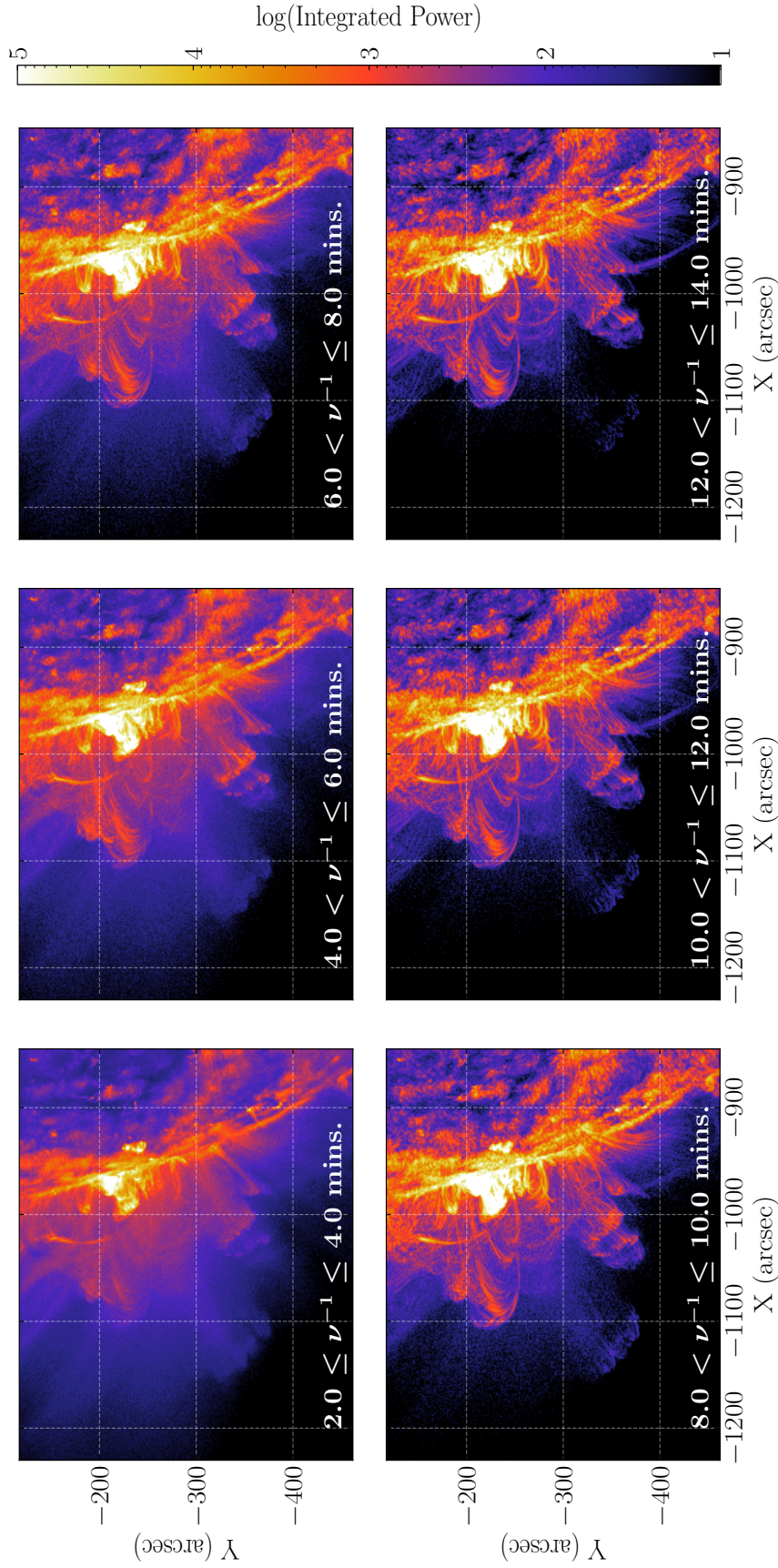
Figure B.2: Same as Figure B.1 but for the pre-flaring dataset.